JULIUS-MAXIMILIANS-UNIVERSITÄT WÜRZBURG
Fakultät für Mathematik und Informatik

The Total Variation on Surfaces and of Surfaces

Dissertation zur Erlangung
des naturwissenschaftlichen Doktorgrades
der Julius-Maximilians-Universität Würzburg

vorgelegt von

MARC HERRMANN
geboren in Lindenberg im Allgäu

Würzburg, 2021

1. Gutachter:	Dr. Stephan Schmidt Humboldt-Universität zu Berlin
2. Gutachter:	Prof. Dr. Christian Klingenberg Julius-Maximilians-Universität Würzburg
3. Gutachter:	Prof. Dr. Roland Herzog Technische Universität Chemnitz

---

Eingereicht am 04.12.2020

Abstract

This thesis is concerned with applying the total variation (TV) regularizer to surfaces and different types of shape optimization problems. The resulting problems are challenging since they suffer from the non-differentiability of the TV-seminorm, but unlike most other priors it favors piecewise constant solutions, which results in piecewise flat geometries for shape optimization problems.The first part of this thesis deals with an analogue of the TV image reconstruction approach [Rudin, Osher, Fatemi (Physica D, 1992)] for images on smooth surfaces. A rigorous analytical framework is developed for this model and its Fenchel predual, which is a quadratic optimization problem with pointwise inequality constraints on the surface. A function space interior point method is proposed to solve it. Afterwards, a discrete variant (DTV) based on a nodal quadrature formula is defined for piecewise polynomial, globally discontinuous and continuous finite element functions on triangulated surface meshes. DTV has favorable properties, which include a convenient dual representation. Next, an analogue of the total variation prior for the normal vector field along the boundary of smooth shapes in 3D is introduced. Its analysis is based on a differential geometric setting in which the unit normal vector is viewed as an element of the two-dimensional sphere manifold. Shape calculus is used to characterize the relevant derivatives and an variant of the split Bregman method for manifold valued functions is proposed. This is followed by an extension of the total variation prior for the normal vector field for piecewise flat surfaces and the previous variant of split Bregman method is adapted. Numerical experiments confirm that the new prior favours polyhedral shapes.

Zusammenfassung

Die vorliegende Arbeit beschäftigt sich mit der Anwendung der totalen Variation (TV) als Regularisierung auf Oberflächen und in verschiedenen Problemen der Formoptimierung. Die daraus entstehenden Optimierungsprobleme sind aufgrund der TV-Seminorm nicht differenzierbar und daher eine Herausforderung. Allerdings werden dadurch, im Gegensatz zu anderen Regularisierungen, stückweise konstante Lösungen favorisiert. Dies führt bei Problemen der Formoptimierung zu stückweise flachen Geometrien. Der erste Teil dieser Arbeit widmet sich der Erweiterung des Ansatzes zur mathematischen Bildverarbeitung [Rudin, Osher, Fatemi (Physica D, 1992)] von flachen Bildern auf glatte Oberflächen und deren Texturen. Für das damit verbundene Optimierungsproblem wird das Fenchel präduale Problem hergeleitet. Dies ist ein quadratisches Optimierungsproblem mit Ungleichungsrestriktionen für dessen Lösung ein Innere-Punkte-Verfahren in Funktionenräumen vorgestellt wird. Basierend auf einer Quadraturformel, wird im Anschluss eine diskrete Variante (DTV) der TV-Seminorm für global unstetige und stetige Finite-Elemente-Funktionen auf triangulierten Oberflächen entwickelt. (DTV) besitzt positive Eigenschaften, wie eine praktische duale Darstellung. Im letzten Teil wird zuerst ein TV-Analogon für die Oberflächennormale von glatten Formen in 3D gezeigt und mit Hilfe von Differentialgeometrie analysiert. Danach wird eine mögliche Erweiterungen für stückweise glatte Oberflächen vorgestellt. Zur Lösung von beiden Regularisierungen wird eine Variante des Split-Bregman-Verfahrens für Funktionen mit Werten auf Mannigfaltigkeiten benutzt.

Acknowledgements

First of all, I would like to thank my supervisor Dr. Stephan Schmidt for offering me a doctoral position, supervising my thesis and supporting me throughout the last years. He introduced my to the topic of shape optimization and related topics. From the very beginning of my work he was always willing to discuss any problems and question and gave many valuable ideas.
At the same time, I would like to thank my project partners Prof. Dr. Roland Herzog and Dr. José Vidal-Núñez for their co-authorship in our papers and for their significant helpful advices and ideas.
In addition, I would like to express my gratitude to all the members of the institute of mathematics at the Julius-Maximilians-Universität Würzburg. In particular, I want to thank all my colleagues from the workgroup mathematical fluid mechanics, especially Prof. Dr. Christian Klingenberg. From the first day, I felt always warmly welcomed into his group and enjoyed a lot of celebrations at his home.
Finally, I would like to thank my family and friends for their constant support throughout the last years, and I would also like to acknowledge the financial support by the German Research Foundation (DFG) under the grant number SCHM 3248/2–1 within Priority Program SPP 1962.

List of Symbols and Abbreviations

Abbreviations

a.e.	almost everywhere
ADMM	alternating direction method of multipliers
e.g	exempli gratia (for example)
EIT	Electrical impedance tomography
FE	finite element
PDE	partial differential equation
TV	total variation

General Notation

$\Gamma \subset \mathbb{R}^3$	smooth surface
Γ_h	discrete surface representation of Γ
$\mathcal{T}_{\boldsymbol{s}}\Gamma$	tangent space of Γ at $\boldsymbol{s} \in \Gamma$
$\operatorname{supp} f$	support of a function f
L^p	Lebesgue space
$\boldsymbol{L}^p$	vector-valued Lebesgue space
$H^{1,p}$	first-order Sobolev space
$\boldsymbol{H}(\operatorname{div})$	space of $\boldsymbol{L}^2$-functions with divergence in $\boldsymbol{L}^2$
BV	space of functions with bounded variation
$\lVert \cdot \rVert_V$	norm equipped with function space V
$\lvert \cdot \rvert_2$	euclidean 2-norm
$\lvert \cdot \rvert_{TV}$	total variation seminorm for finite elements
$\lvert \cdot \rvert_{DTV}$	discrete total variation seminorm for finite elements
$\mathcal{P}_r$	space of polynomials of maximum degree r
$\mathcal{CG}_r$	continuous Lagrange finite element space of order r
$\mathcal{DG}_r$	discontinuous Lagrange finite element space of order r
$\mathcal{RT}_r$	Raviart-Thomas finite element space of order r
$\mathcal{S}^2$	manifold 2-sphere
$\mathcal{T}_{\boldsymbol{s}}\mathcal{S}^2$	tangent space of $\mathcal{S}^2$ at $\boldsymbol{s} \in \mathcal{S}^2$
$\mathfrak{g}(\cdot, \cdot)$	Riemannian metric
$\lvert \cdot \rvert_{\mathfrak{g}}$	norm induced by Riemannian metric
$\mathrm{d}J[\boldsymbol{V}]$	directional shape derivative of functional J in direction $\boldsymbol{V}$
$\mathrm{d}g[\boldsymbol{V}]$	material derivative of function g
$g'[\boldsymbol{V}]$	local shape derivative of function g
D_Γ	derivative in tangential directions

Contents

CHAPTER 1

INTRODUCTION

Rudin, Osher, and Fatemi [139] proposed to estimate the denoised image u as the solution of the minimization problem

$$\begin{aligned} \text{Minimize} \quad & \frac{1}{2}\int_\Omega |Ku - f|^2 \, \mathrm{d}\boldsymbol{s} + \beta \int_\Omega |Du| \\ \text{over} \quad & u \in BV(\Omega), \end{aligned} \tag{1.1}$$

with $K = \mathrm{id}$, where $BV(\Omega)$ is the space of functions with bounded variation and the total variation (TV) seminorm

$$\int_\Omega |\nabla u| \tag{1.2}$$

was used as a regularizing functional. The TV-seminorm in the minimization problem discourages the solution from having oscillations, yet it does allow it to have discontinuities and favours it to be piecewise constant. Due to the choice of norms in the fidelity and regularization terms, problem (1.1) is also termed a TV–L^2 model (by contrast to TV–L^1, where the fidelity term consists of a L^1-norm). A large body of literature on this topic has emerged; see for instance [44, 46, 49, 148, 160] and the references therein. The operator K appearing in (1.1) expresses available a-priori knowledge about the relation between the image u to be reconstructed and the observed data f. Common examples include $K = \mathrm{id}$ for classical image denoising, $K = \mathrm{masking}$ for inpainting problems [52, Chapter 6.5], $K = \mathrm{blur}$ for deblurring problems [39, 71], and $K = \mathrm{coarsen}$ for un-zooming problems [118].

The first two Chapters of this thesis deal with the extension of (1.1) to closed surfaces $\Gamma \subset \mathbb{R}^3$ and its discretization. The increasing interest in studying image processing problems *on surfaces* is due to its numerous applications, for instance, in computer vision [102] and geophysics [101]. This is accompanied by the ongoing development in 3D scanning, remote sensing and other data acquisition hardware. In the applications mentioned unavoidable sampling errors from the imaging equipment, or the need to compress large-scale images, e.g., for limited-bandwidth Internet applications, are potential sources of noise, necessitating post processing. The predominant approach in surface image processing so far is based on extensions of the nonlinear, anisotropic diffusion method going back to [127]. In particular, we mention [12, 57, 67] for surface intrinsic concepts, and [29, 30, 122] for volume-based formulations. We also point out [19] who consider an extension of the Mumford–Shah image segmentation problem using the active contour

method on surfaces, with a subsequent restoration phase on the segmented parts driven by linear isotropic diffusion.
As an alternative to diffusion driven image restoration the focus of Chapter 2 is on an analog of the TV–L^2 reconstruction model for images defined on smooth *surfaces*, which was recently proposed in [108]. We establish a rigorous relation between the primal and dual problems in appropriate function spaces. To be precise, we formulate the *predual*, which is a quadratic convex problem with pointwise bound constraints in $\boldsymbol{H}(\mathrm{div};\Gamma)$, the analog on surfaces of the space of vector-valued L^2 functions whose divergence is likewise square integrable. The distinction between dual and predual problems is necessary due to $BV(\Gamma)$ being non-reflexive. A similar analysis has previously been pursued in [99] for the 'flat' case. Notice however that in [99] the TV-seminorm is defined in a way which is *not* rotationally invariant but has the advantage of leading to pointwise simple bounds. By contrast, we propose to use an *interior-point method*, which deals nicely with pointwise *nonlinear* constraints of the form $|\boldsymbol{p}|_2 \leq \beta$ arising in the *coordinate free setting* that naturally comes with surfaces. While Cartesian grids are natural in 'flat' image processing tasks and lend themselves to finite difference approximations, surfaces are naturally *triangulated*, for instance by 3D scanner software. Based on the rigorous formulation of the predual problem we are led to choose a conforming finite element discretization of the space $\boldsymbol{H}(\mathrm{div};\Gamma)$ by the surface analogue of (possibly higher-order) Raviart–Thomas finite element spaces introduced in [133]. When it comes to discretization we observe the inconsistency that the discretization of the primal problem is no longer the dual of the discretization of the predual problem.
To overcome this issue, we present in Chapter 3 a discrete formulation of the TV-seminorm (DTV) based on a nodal quadrature formula, which is defined for piecewise polynomial, globally discontinuous and continuous finite element functions on triangulated surface meshes. We establish that optimization problems utilizing the discrete TV-seminorm as a regularizer, like TV-L^2 and TV-L^1, possess a discrete dual problem with very simple constraints. The structure of the primal and dual problems is in turn essential for the efficient implementation of appropriate solution algorithms. We are able to show that a variety of popular algorithms for TV-L^2 and TV-L^1, originally developed in the context of finite difference discretizations on Cartesian grids, apply with little or no changes to discretizations with low or higher-order finite elements. Specifically, we consider the split Bregman algorithm [85], the primal-dual method of [47] and Chambolle's projection method [44] for TV-L^2 for denoising and inpainting problems, as well as the primal-dual method and the ADMM of [152] for TV-L^1.

In the second half of this thesis we apply our experiences about the total variation framework, received in the previous chapters, to surfaces. Our main goal is archiving a regularization functional for shape optimization problems that favours polyhedral shapes and discrete surface meshes. Meshes are widely employed in computer graphics and computer vision, where they are utilized to model arbitrary shapes and real geometries. Meshes can be produced by 3D scanners and can be efficiently processed numerically with appropriate software. Unfortunately, the process of geometry acquisition by scanning leads to unavoidable errors in the form of noise or missing parts. The process of removing such noise while preserving relevant features is known as *mesh denoising*. When missing parts of the geometry must be reconstructed we speak of *mesh inpainting*. The main difficulty

in removing undesired noise from a mesh is that both noise and sharp geometric features can be considered high frequency signals. This makes it difficult to distinguish between them. The aforementioned problem has been of interest in the community of *image processing* since late in the 1980s; see for instance [43]. Also for mesh denoising, many algorithms exist and we refer the reader, e.g., to [34] for a survey.
In Chapter 4, we introduce the *total variation of the normal field*

$$|\boldsymbol{n}|_{TV(\Gamma)} := \int_\Gamma \left(|(D_\Gamma \boldsymbol{n})\, \boldsymbol{\xi}_1|_{\mathfrak{g}}^2 + |(D_\Gamma \boldsymbol{n})\, \boldsymbol{\xi}_2|_{\mathfrak{g}}^2 \right)^{\frac{1}{2}} \mathrm{d}\boldsymbol{s} \tag{1.3}$$

along a smooth surface Γ in analogy to (1.2), where $\boldsymbol{n}$ is the outer unit normal vector field along Γ and $\{\boldsymbol{\xi}_1(\boldsymbol{s}), \boldsymbol{\xi}_2(\boldsymbol{s})\}$ denotes an orthonormal basis of the tangent spaces $\mathcal{T}_{\boldsymbol{s}}\Gamma$. A thorough introduction to $|\boldsymbol{n}|_{TV(\Gamma)}$ and its properties will be given in Chapter 4. Nevertheless we wish to point out already at this point a number of properties of (1.3) which set it apart from the (1.2):

1. The variable on which (1.3) depends is the surface Γ. Since the normal vector field $\boldsymbol{n}$ in turn depends on Γ, both the integration domain and the integrand in (1.3) have relevant dependencies for shape optimization. By contrast, Ω is fixed in (1.2), where u is the variable.

2. The normal vector field, whose pointwise variation the total variation functional (1.3) seeks to capture, is manifold-valued with values in $\mathcal{S}^2$. By contrast, the function u in (1.2) is real-valued.

3. It is well known that the TV functional penalizes jumps and non-zero gradients of BV functions. Consequently, the minimization of (1.2) avoids unnecessary variations of u and thus favors piecewise constant minimizers in BV. Generally, it does not admit minimizers in spaces of functions of higher smoothness, such as $W^{1,1}(\Omega)$. The situation is slightly different for (1.3) since we are considering closed surfaces Γ, which yields a periodicity constraint for the normal vector field $\boldsymbol{n}$. In this setting, unnecessary variations of $\boldsymbol{n}$ correspond to non-convex regions of the enclosed body of Γ. Consequently, the minimization of (1.3) favors convex shapes and, more precisely, spheres; see Theorem 4.9.

Since (1.3) is non-smoothness and most of its variables are manifold-valued or live in tangent spaces, solving shape optimization problems containing (1.3) is challenging. Although many optimization algorithms have recently been generalized to Riemannian manifolds [10, 25, 26], the split Bregman method for manifolds proposed in Chapter 4 is new to the best of our knowledge. For a general overview of optimization on manifolds, we refer the reader to [1].
In Chapter 5, we discuss a discrete variant of (1.3) tailored to piecewise flat surfaces Γ_h, where (1.3) does not apply. In contrast with the smooth setting, the total variation of the piecewise constant normal vector field $\boldsymbol{n}$ is concentrated in jumps across edges between flat facets. We therefore propose the following *discrete total variation of the normal*

$$|\boldsymbol{n}|_{DTV(\Gamma_h)} := \sum_E d(\boldsymbol{n}_E^+, \boldsymbol{n}_E^-)\, |E|\,, \tag{1.4}$$

where E denotes an edge of length $|E|$ between facets of Γ_h. Here, $d(\boldsymbol{n}_E^+, \boldsymbol{n}_E^-)$ is the geodesic distance, which denotes the shortest distance between the two neighboring normal vectors on $\mathcal{S}^2$. Similarly as for the case of smooth surfaces, solving discrete shape optimization problems is challenging, but can be approached with a discrete version of the split Bregman method for smooth surfaces.
The aforementioned split Bregman method for the *discrete total variation of the normal* will be used in Chapter 6 to solve three different shape optimization problems. We present numerical results for an Electrical impedance tomography (EIT) problem, *mesh denoising* and *mesh inpainting*.
Finally in Chapter 7 we summarize our results and list some possible extensions and modifications for future research.

CHAPTER 2

TOTAL VARIATION IMAGE RECONSTRUCTION ON SMOOTH SURFACES

This Chapter parallels [96], where the image reconstruction problem

$$\left\{ \begin{array}{rl} \text{Minimize} & \dfrac{1}{2}\displaystyle\int_\Gamma |Ku-f|^2 \,\mathrm{d}\boldsymbol{s} + \dfrac{\alpha}{2}\int_\Gamma |u|^2 \,\mathrm{d}\boldsymbol{s} + \beta\int_\Gamma |\nabla u| \\ \text{over} & u \in BV(\Gamma) \end{array} \right. \tag{2.1}$$

is considered. Here, $\Gamma \subset \mathbb{R}^3$ is a smooth, compact, orientable and connected surface without boundary. $BV(\Gamma)$ denotes the space of functions of bounded variation on the surface Γ, and $\int_\Gamma |\nabla u|$ is the surface analog of the total-variation seminorm, both of which are introduced in Section 2.1. Furthermore, the observed data $f \in L^2(\Gamma)$, parameters $\beta > 0$, $\alpha \geq 0$ and the observation operator $K \in \mathcal{L}(L^2(\Gamma))$ are given. By $K^* \in \mathcal{L}(L^2(\Gamma))$ we denote the Hilbert space adjoint of K. It will be shown that $BV(\Gamma) \hookrightarrow L^2(\Gamma)$ so that the integrals in (2.1) are well defined. We assume throughout that either $\alpha > 0$ holds, or else that K is injective and has closed range, i.e., there exists a constant $\gamma > 0$ such that $\|Ku\|_{L^2(\Gamma)} \geq \gamma \|u\|_{L^2(\Gamma)}$ for all $u \in L^2(\Gamma)$. This second case is equivalent to K^*K being a coercive operator in $\mathcal{L}(L^2(\Gamma))$; see for instance [76, Chapter A.2].

This Chapter is organized as follows. In Section 2.1 we introduce the proper functional analytic framework for the discussion of (2.1) and its predual. In particular, we recall the definition of the spaces $BV(\Gamma)$ and $\boldsymbol{H}(\mathrm{div};\Gamma)$ on a smooth surface Γ. Section 2.2 is devoted to the study of the Fenchel predual problem. In Section 2.3 we formulate a function space interior point approach for the solution of the predual problem, analyze the well-posedness of the barrier approximations, and provide necessary and sufficient optimality conditions. Details concerning the discretization by Raviart–Thomas surface finite elements and the implementation of our method are also given in that section. Subsequently, numerical results are presented in Section 2.4. While the presentation focuses on denoising and inpainting of scalar (gray-scale) image data, an extension to multi-channel (color) images is rather straightforward.

2.1 Functional Analytic Framework for Smooth Surfaces

In the following we introduce the necessary analytical framework to extend the definition of functions of bounded variation (BV) as well as functions in $\boldsymbol{H}(\mathrm{div})$ on an open subset of $\mathbb{R}^n$ to functions defined on smooth surfaces.

2.1.1 Concepts of Differential Geometry

In a nutshell, a *smooth surface* Γ is a two-dimensional manifold of class C^∞ embedded in $\mathbb{R}^3$. In the interest of keeping this thesis self-contained, we briefly summarize the required concepts from differential geometry. The interested reader is referred, for instance, to [70, 106, 130] for further background material.

Definition 2.1. *A subset $\Gamma \subset \mathbb{R}^3$, endowed with the relative topology of $\mathbb{R}^3$, is a* smooth surface *if for every point $\boldsymbol{s} \in \Gamma$ there exists an open set $V \subset \Gamma$ containing $\boldsymbol{s}$, an open set $U \subset \mathbb{R}^2$ and a homeomorphism $\boldsymbol{x} : U \to V$ with the additional properties that $\boldsymbol{x} \in C^\infty(U;\mathbb{R}^3)$ holds and that the Jacobian of $\boldsymbol{x}$ has rank 2 on U.*

A mapping $\boldsymbol{x}$ as above is called a *parametrization* at $\boldsymbol{s}$. A collection of parametrizations covering all of Γ is said to be an *atlas* of Γ. We will always associate with a smooth surface an atlas of parametrizations, and it will not matter throughout this thesis which particular atlas is being used. Coordinates in the parameter domain U of a chart $\boldsymbol{x}$ will be denoted by ζ_1 and ζ_2.

Assumption 2.2. *Throughout this thesis we will assume that the smooth surface $\Gamma \subset \mathbb{R}^3$ is compact and connected.*

It can be shown that for smooth surfaces, connectedness implies that any two points can be joined by a smooth path. As a further consequence of Assumption 2.2 the surface Γ is also *orientable*; cf. [9, Prob. 2.43]. That is, the Jacobian of the transition map $x^{-1} \circ y$ between any two intersecting parametrizations has positive determinant on its domain of definition.
A function

$$f : \Gamma \to \mathbb{R}$$

is said to be of *class* C^k if, for any parametrization $\boldsymbol{x}$ in the atlas, the function

$$f \circ \boldsymbol{x} : \mathbb{R}^2 \supset U \to \mathbb{R}$$

is of class C^k. Similarly, this notion can be defined for functions f defined only on an open subset of Γ by appropriately restricting those parametrizations, whose image intersects the domain of definition of f.
We continue with the notions of tangent vectors and the tangent space at a point $\boldsymbol{s} \in \Gamma$. Consider a differentiable curve

$$\gamma : (-\varepsilon, \varepsilon) \to \Gamma, \quad \gamma(0) = \boldsymbol{s}.$$

Then $\boldsymbol{X} := \dot{\gamma}(0) \in \mathbb{R}^3$ is said to be the *tangent vector* to the curve γ at $\boldsymbol{s}$. The *tangent space* at $\boldsymbol{s}$, denoted by $\mathcal{T}_{\boldsymbol{s}}\Gamma$, consists of all tangent vectors of such curves γ at $\boldsymbol{s}$. It is a

vector space of dimension 2. If s belongs to the image of some parametrization x, then it is easy to verify that

$$\left\{ \frac{\partial x}{\partial \zeta_1}(x^{-1}(s)), \frac{\partial x}{\partial \zeta_2}(x^{-1}(s)) \right\}$$

constitutes a basis for $\mathcal{T}_s\Gamma$. Therefore, any tangent vector X at s can be represented as

$$X = X^i \frac{\partial x}{\partial \zeta_i}(x^{-1}(s)). \tag{2.2}$$

Here and in the sequel we use Einstein's summation convention. The coefficients X^i are the *components* of the tangent vector $X \in \mathcal{T}_s\Gamma$ in the local basis induced by the parametrization x.
For a given parametrization x at $s \in \Gamma$ we define the *metric tensor* G by its entries

$$(g_{ij})(s) := \left(\frac{\partial x}{\partial \zeta_i}(x^{-1}(s)) \right)^\top \left(\frac{\partial x}{\partial \zeta_j}(x^{-1}(s)) \right),$$

where $a^\top b$ denotes the Euclidean inner product in the ambient space $\mathbb{R}^3$. Since the vectors $\frac{\partial x}{\partial \zeta_i}(x^{-1}(s))$, $i = 1,2$ are linearly independent, $G(s)$ is positive definite and also symmetric.
Due to the fact that every tangent space to a point s on the surface inherits the standard inner product from the ambient space $\mathbb{R}^3$, we can introduce the *inner product* of two vectors $X, Y \in \mathcal{T}_s\Gamma$ as

$$(X, Y)_2 := X^\top Y = g_{ij} X^i Y^j,$$

where the last equation holds if X and Y are given by representations of type (2.2) w.r.t. a parametrization x. Moreover, the 2-*norm* of a vector $X \in \mathcal{T}_s\Gamma$ will be denoted by

$$|X|_2 := (X, X)_2^{1/2}.$$

Definition 2.3. *The* tangent bundle *of* Γ *is defined as* $\mathcal{T}\Gamma := \bigcup_{s\in\Gamma} \{s\} \times \mathcal{T}_s\Gamma$. *A (tangential)* vector field *of class* C^k *(*$k \geq 0$*) is a map* $X : \Gamma \to \mathcal{T}\Gamma$ *with the following properties:*

(*i*) $X(s) \in \{s\} \times \mathcal{T}_s\Gamma$ *for all* $s \in \Gamma$, *i.e.,* X *is a* section.

(*ii*) *For any parametrization* $x : U \to V$, *the component functions* $s \mapsto X^i(s)$ *in the representation*

$$X(s) = X^i(s) \frac{\partial x}{\partial \zeta_i}(x^{-1}(s)), \quad s \in V \tag{2.3}$$

are of class C^k *on* V.

Finally we recall the notion of *divergence* and *gradient* on a surface Γ, see for instance [93, 138].

Definition 2.4. *Let be* $f : \Gamma \to \mathbb{R}$ *a* C^k *function for* $k \geq 1$. *Define the differential operators* $(\partial_i \cdot)(s)$, $i = 1,2$, *by*

$$(\partial_i f)(s) := \frac{\partial (f \circ x)}{\partial \zeta_i}(x^{-1}(s))$$

and the gradient *of f by*

$$(\nabla f)(\boldsymbol{s}) := g^{ij}(\boldsymbol{s})\,(\partial_i f)(\boldsymbol{s})\,\frac{\partial \boldsymbol{x}}{\partial \zeta_j}(\boldsymbol{x}^{-1}(\boldsymbol{s}))$$

for $\boldsymbol{s} \in V$. Here, g^{ij} are the components of the inverse *of the metric tensor $G = (g_{ij})$.*

The gradient assigns to each point $\boldsymbol{s} \in S$ a vector $(\nabla f)(\boldsymbol{s})$ in $\mathcal{T}_{\boldsymbol{s}}\Gamma \subset \mathbb{R}^3$ verifying

$$\big((\nabla f)(\boldsymbol{s}), v\big)_2 = v^i(\partial_i f)(\boldsymbol{s})$$

for all $v = v^i \frac{\partial \boldsymbol{x}}{\partial \zeta_i}(\boldsymbol{x}^{-1}(\boldsymbol{s})) \in \mathcal{T}_{\boldsymbol{s}}\Gamma$.

Definition 2.5. *Let be $\boldsymbol{X}$ a vector field of class C^k for $k \geq 1$ with representation* (2.3) *w.r.t. the parametrization $\boldsymbol{x}$. We define the divergence operator by*

$$(\operatorname{div} \boldsymbol{X})(\boldsymbol{s}) := \frac{1}{\sqrt{\det G(\boldsymbol{s})}}\,\partial_i\left(X^i\sqrt{\det G}\right)(\boldsymbol{s}), \quad \boldsymbol{s} \in V. \tag{2.4}$$

Notice that the notions of gradient, tangent space, tangent bundle, vector fields and their divergence, as well as the inner product $(\cdot,\,\cdot)_2$ and the norm $|\cdot|_2$ are intrinsic quantities, i.e., independent of the atlas used to describe the surface Γ.

2.1.2 Sobolev Functions and Functions of BV

In this part we recall the notions of Lebesgue and Sobolev spaces $L^p(\Gamma)$ and $H^{1,p}(\Gamma)$ on the surface Γ, as well as the spaces $\boldsymbol{H}(\operatorname{div};\Gamma)$ and $BV(\Gamma)$ required for the subsequent analysis.
For $m \in \mathbb{N}_0$, $C^m(\Gamma)$ denotes the space of C^m functions on the surface Γ. Moreover, $\boldsymbol{C}^m(\Gamma;\mathcal{T}\Gamma)$ denotes the space of C^m vector fields. As usual, the support of a function f is defined as

$$\operatorname{supp} f := \operatorname{cl}\{\boldsymbol{s} \in \Gamma : f(\boldsymbol{s}) \neq 0\}$$

with $\operatorname{cl} C$ denoting the *closure* of a set $C \subset \Gamma$.
We begin with the recollection of the spaces $L^p(\Gamma)$. Let f be a continuous function on Γ with support in the range V of a parametrization $\boldsymbol{x} : U \to V$. Then, we have by definition

$$\int_\Gamma f \,\mathrm{d}\boldsymbol{s} := \int_U f(\boldsymbol{x}(\boldsymbol{u}))\,\sqrt{\det G(\boldsymbol{x}(\boldsymbol{u}))}\,\mathrm{d}\boldsymbol{u}, \tag{2.5}$$

where the measure $\mathrm{d}\boldsymbol{s}$ is defined as $\mathrm{d}\boldsymbol{s} = \sqrt{(\det G)\circ \boldsymbol{x}}\,\mathrm{d}\boldsymbol{u}$, with $\mathrm{d}\boldsymbol{u}$ denoting the Lebesgue measure in $\mathbb{R}^2$. This definition of the integral extends to arbitrary continuous functions on Γ by using a partition of unity; cf. [94, Ch. 1.2]. As it is shown there the integrability of a function and the value of its integral over Γ depend neither on the atlas nor on the partition of unity used.
For $1 \leq p < \infty$ the space $L^p(\Gamma)$ is defined as the completion of $C^\infty(\Gamma)$ w.r.t. the norm

$$\|f\|_{L^p(\Gamma)} := \left(\int_\Gamma |f|^p \,\mathrm{d}\boldsymbol{s}\right)^{1/p}. \tag{2.6}$$

We also recall that $L^\infty(\Gamma)$ is defined as the space of functions such that

$$\|f\|_{L^\infty(\Gamma)} := \operatorname*{ess\,sup}_{\boldsymbol{s}\in\Gamma} |f(\boldsymbol{s})| < \infty.$$

Naturally, these definitions extend to vector fields $\boldsymbol{f} \in \boldsymbol{L}^p(\Gamma;\mathcal{T}\Gamma)$. For instance, we have

$$\|\boldsymbol{f}\|_{\boldsymbol{L}^p(\Gamma;\mathcal{T}\Gamma)} := \left(\int_\Gamma |\boldsymbol{f}|_2^p \, \mathrm{d}\boldsymbol{s}\right)^{1/p}.$$

The spaces $L^2(\Gamma)$ and $\boldsymbol{L}^2(\Gamma;\mathcal{T}\Gamma)$ are Hilbert spaces w.r.t. the usual inner products $(\cdot,\,\cdot)_{L^2(\Gamma)}$ and $(\cdot,\,\cdot)_{\boldsymbol{L}^2(\Gamma;\mathcal{T}\Gamma)}$.
We are now in the position to define functions of bounded variation on surfaces satisfying Assumption 2.2. Background material on BV functions on flat domains can be found, for instance, in [83], [174, Ch. 5] or [8, Ch. 10]. For the definition of BV functions on surfaces, see also [108, Sect. 3.1] or [17, Sect. 4].

Definition 2.6. *A function $u \in L^1(\Gamma)$ belongs to $BV(\Gamma)$ if the TV-seminorm defined by*

$$\int_\Gamma |\nabla u| := \sup\left\{\int_\Gamma u \operatorname{div} \boldsymbol{p}\, \mathrm{d}\boldsymbol{s} : \boldsymbol{p} \in \boldsymbol{V}\right\} \tag{2.7}$$

is finite, where

$$\boldsymbol{V} := \{\boldsymbol{p} \in \boldsymbol{C}^\infty(\Gamma;\mathcal{T}\Gamma) : |\boldsymbol{p}(\boldsymbol{s})|_2 \le 1 \quad \forall \boldsymbol{s} \in \Gamma\}. \tag{2.8}$$

We equip the space $BV(\Gamma)$ with the norm

$$\|u\|_{BV(\Gamma)} = \|u\|_{L^1(\Gamma)} + \int_\Gamma |\nabla u|, \quad u \in BV(\Gamma). \tag{2.9}$$

It is worth remarking that, as in the planar case,

$$\int_\Gamma |\nabla u| = \int_\Gamma |\nabla u|_2 \, \mathrm{d}\boldsymbol{s}$$

holds for all functions $u \in C^\infty(\Gamma)$ and indeed for $u \in H^{1,1}(\Gamma)$; see [138, p.18]. Notice that both contributions to the norm $\|\cdot\|_{BV(\Gamma)}$ are independent of the parametrization. We also remark that the space $\boldsymbol{C}^\infty(\Gamma;\mathcal{T}\Gamma)$ can be replaced by $\boldsymbol{C}^1(\Gamma;\mathcal{T}\Gamma)$ without affecting the definition; compare [8, Def. 10.1.1], [174, p.221] or [17].
According to Definition 2.6, it is clear that the embedding

$$BV(\Gamma) \hookrightarrow L^1(\Gamma)$$

holds. Next, we are going to prove that even

$$BV(\Gamma) \hookrightarrow L^2(\Gamma)$$

is valid, as is known for two-dimensional flat domains; see for instance [8, Th. 10.1.3]. This result is essential to establish the well-posedness of (2.1) in the sequel. Its proof requires the notion of intermediate convergence of $BV(\Gamma)$ functions as well as the concept

of first-order Sobolev spaces $H^{1,p}(\Gamma)$. We summarize only the essential concepts and refer the reader to [93, 94] for an in-depth introduction to Sobolev spaces on manifolds. For $1 \leq p < \infty$ and a function $u \in C^\infty(\Gamma)$, define the norm

$$\|u\|_{H^{1,p}(\Gamma)} := \left(\|u\|^p_{L^p(\Gamma)} + \int_\Gamma |\nabla u|_2^p \, \mathrm{d}\boldsymbol{s} \right)^{1/p}. \tag{2.10}$$

The Sobolev space $H^{1,p}(\Gamma)$ is then given by

$$H^{1,p}(\Gamma) := \mathrm{cl}\left(C^\infty(\Gamma)\right)$$

where the closure is w.r.t. the norm (2.10).
The counterpart of the following definition in the classical framework can be found in [8, Definition 10.1.3].

Definition 2.7. *Let $\{u_n\}$ be a sequence of functions in $BV(\Gamma)$ and suppose $u \in BV(\Gamma)$. We say that $u_n \to u$ in the sense of* intermediate convergence *if*

(*i*) $u_n \to u$ *strongly in* $L^1(\Gamma)$ *and*

(*ii*) $\int_\Gamma |\nabla u_n| \to \int_\Gamma |\nabla u|$.

The following lemma can be proved analogously as in [8, Th. 10.1.2]. The proof uses a partition-of-unity argument as well as mollification.

Lemma 2.8. *For any $u \in BV(\Gamma)$, there exists a sequence $\{u_k\} \subset C^\infty(\Gamma)$ with $u_k \to u$ in the intermediate sense.*

To proof the next theorem, we need the following proposition, see [8, Prop. 10.1.1.]:

Proposition 2.9. *Let $\{u_n\}$ be a sequence of functions in $BV(\Gamma)$, which strongly converges to some $u \in L^1(\Gamma)$ and satisfies*

$$\sup_{n \in \mathbb{N}} \int_\Gamma |\nabla u_n| < \infty.$$

Then $u \in BV(\Gamma)$ and

$$\int_\Gamma |\nabla u| \leq \liminf_{n \to \infty} \int_\Gamma |\nabla u_n|$$

holds.

Proof. For $\boldsymbol{p} \in \boldsymbol{V}$ as defined in (2.8), we have

$$\begin{aligned} \int_\Gamma u \ \mathrm{div}\, \boldsymbol{p} \mathrm{d}\boldsymbol{s} &= \lim_{n \to \infty} \int_\Gamma u_n \ \mathrm{div}\, \boldsymbol{p} \mathrm{d}\boldsymbol{s} \\ &\leq \liminf_{n \to \infty} \int_\Gamma |\nabla u_n| \,. \end{aligned}$$

By taking the supremum over all $\boldsymbol{p} \in \boldsymbol{V}$, we proof our claim. □

Theorem 2.10. *The space $BV(\Gamma)$, equipped with the norm* (2.9)*, is a Banach space and the embedding*

$$BV(\Gamma) \hookrightarrow L^p(\Gamma)$$

holds for all $1 \leq p \leq 2$.

Proof. The proof proceeds along the lines of [8, Th. 10.1.1. and Th. 10.1.3.]. For some Cauchy sequence $\{u_n\}$ in $BV(\Gamma)$, it holds that $\{u_n\}$ is also a Cauchy sequence in $L^1(\Gamma)$ and there exists $u \in L^1(\Gamma)$ with $u_n \to u$ strongly in $L^1(\Gamma)$. Consequently,

$$u_p - u_q \to u - u_q$$

strongly in $L^1(\Gamma)$ for some $q \in \mathbb{N}$ when p goes to $+\infty$. On the other hand, for all $\epsilon > 0$ there exists some $N_\epsilon \in \mathbb{N}$ such that

$$\int_\Gamma \left|\nabla u_p - \nabla u_q\right| < \epsilon \quad \forall p, q > N_\epsilon.$$

Applying Proposition 2.9 on $u_p - u_q$ for $q > N_\epsilon$ yields

$$\begin{aligned}\int_\Gamma \left|\nabla(u - u_q)\right| &\leq \liminf_{p\to\infty} \int_\Gamma \left|\nabla(u_p - u_q)\right| \\ &< \epsilon.\end{aligned}$$

Consequently, $u \in BV(\Gamma)$ and

$$\lim_{q\to\infty} \int_\Gamma \left|\nabla(u - u_q)\right| = 0$$

holds and $u_n \to u$ strongly in $BV(\Gamma)$ follows.
Now, let us focus on the proof of the second claim. To this aim, let us define $\{u_n\} \subset C^\infty(\Gamma)$ which converges to $u \in BV(\Gamma)$ in the sense of intermediate convergence. Due to [94, Th. 2.6], we have that the embedding

$$H^{1,q}(\Gamma) \hookrightarrow L^p(\Gamma)$$

is continuous for all $q \in [1, 2)$ and $p = \frac{2q}{2-q}$. In particular, for $q = 1$ and $p = 2$ we have

$$H^{1,1}(\Gamma) \hookrightarrow L^2(\Gamma),$$

so there exists $c > 0$ such that

$$\left(\int_\Gamma |u_n|^2 \, \mathrm{d}s\right)^{1/2} \leq c \left(\int_\Gamma |u_n| \, \mathrm{d}s + \int_\Gamma |\nabla u_n|_2 \, \mathrm{d}s\right)$$

since $\{u_n\} \subset C^\infty(\Gamma) \subset H^{1,1}(\Gamma)$. The sequence on the right hand side is bounded, and thus a subsequence of $\{u_n\}$ convergences weakly in $L^2(\Gamma)$. Since $u_n \to u$ in $L^1(\Gamma)$, we must have $u_n \rightharpoonup u$ in $L^2(\Gamma)$. By weak sequential lower semicontinuity of the norm,

$$\begin{aligned}\left(\int_\Gamma |u|^2 \, \mathrm{d}s\right)^{1/2} &\leq \liminf_{n\to\infty} \left(\int_\Gamma |u_n|^2 \, \mathrm{d}s\right)^{1/2} \\ &\leq \liminf_{n\to\infty} c \left(\int_\Gamma |u_n| \, \mathrm{d}s + \int_\Gamma |\nabla u_n|_2 \, \mathrm{d}s\right) \\ &= c \left(\|u\|_{L^1(\Gamma)} + \int_\Gamma |\nabla u|\right) \\ &= c \, \|u\|_{BV(\Gamma)}.\end{aligned}$$

Then, applying [94, Cor. 2.1], we have that $BV(\Gamma) \hookrightarrow L^p(\Gamma)$ holds for all $p \in [1,2]$. $\square$

To close this section we introduce the following space of vector fields, which will play a fundamental role throughout the thesis,

$$\boldsymbol{H}(\mathrm{div};\Gamma) := \left\{ \boldsymbol{v} \in \boldsymbol{L}^2(\Gamma;\mathcal{T}\Gamma) : \mathrm{div}\, \boldsymbol{v} \in L^2(\Gamma) \right\}.$$

We equip this space with the norm

$$\|\boldsymbol{v}\|_{\boldsymbol{H}(\mathrm{div};\Gamma)} := \left(\|\boldsymbol{v}\|^2_{\boldsymbol{L}^2(\Gamma;\mathcal{T}\Gamma)} + \|\mathrm{div}\, \boldsymbol{v}\|^2_{L^2(\Gamma)} \right)^{1/2}, \tag{2.11}$$

which is induced by the inner product

$$(\boldsymbol{v}, \boldsymbol{w})_{\boldsymbol{H}(\mathrm{div};\Gamma)} := (\boldsymbol{v}, \boldsymbol{w})_{\boldsymbol{L}^2(\Gamma;\mathcal{T}\Gamma)} + (\mathrm{div}\, \boldsymbol{v}, \mathrm{div}\, \boldsymbol{w})_{L^2(\Gamma)}.$$

$\boldsymbol{H}(\mathrm{div};\Gamma)$ is a Hilbert space.

2.2 The Fenchel Predual on Surfaces

The dual problem of TV–L^2 has been stated in various references; see for instance [41, 44, 51]. In particular, it appears in [108] exactly for problem (2.1) on smooth surfaces. However, the arguments used to derive the dual problem in these references were all *formal*, and in particular no function space was assigned to the problem. To the best of our knowledge [99] is the only reference where this analysis is made rigorously, but only for the flat case. Due to the lack of reflexivity of BV spaces, the dual and predual problems are different. As has been shown in [99] the *predual*, posed as a problem in $\boldsymbol{H}(\mathrm{div})$, is the appropriate concept.

In this section we adapt this rigorous analysis to problem (2.1) on the surface Γ. As expected from [108] the predual problem is a quadratic optimization problem for the predual tangent field $\boldsymbol{p} \in \boldsymbol{H}(\mathrm{div};\Gamma)$ with pointwise constraints on the surface. We will show that both problems are equivalent and that the primal solution can be recovered from the predual solution. We wish to point out that the constraints

$$|\boldsymbol{p}(\boldsymbol{s})|_2 \leq \beta \quad \forall \boldsymbol{s} \in \Gamma$$

arising in our setting are nonlinear. This is in contrast with [99, eq. (2.1)], where simple bounds

$$-\beta \mathbf{1} \leq \boldsymbol{p}(\boldsymbol{s}) \leq \beta \mathbf{1} \quad \forall \boldsymbol{s} \in \Gamma$$

were obtained due to a slightly different definition of the TV-seminorm, which is, however, not invariant under changes of the parametrization.

Solving the predual problem has a number of advantages compared to solving the primal problem directly. First, we do not have to deal with the discretization of the nonsmooth term $\int_\Gamma |\nabla u|$ in the finite element context, nor employ an optimization algorithm for the nonsmooth problem (2.1); we mention however that such a program was carried out in a different context in [13]. Second, as was pointed out in [14], the finite element solution of minimization problems in BV spaces may suffer from low convergence rates. Finally, as

was observed previously in [41,44,51,99], we mention that the predual variable $\boldsymbol{p}$ serves as an edge detector in the image.
Let us recall some preliminary results from convex analysis; see for instance [169, Ch. 2.8]. Given two locally convex Hausdorff spaces X, Y, two proper convex functions

$$F : X \to \mathbb{R} \cup \{\infty\},\ G : Y \to \mathbb{R} \cup \{\infty\}$$

as well as a bounded linear map $\Lambda : X \to Y$ we have, due to the Fenchel-Young inequality, the relation of weak duality

$$\inf_{x \in X} \{F(x) + G(\Lambda x)\} \geq \sup_{y^* \in Y^*} \{-F^*(\Lambda^* y^*) - G^*(-y^*)\}. \tag{2.12}$$

Here $F^* : X^* \to \mathbb{R}$ and $G^* : Y^* \to \mathbb{R}$ are the Fenchel conjugates of F and G, defined by

$$\begin{aligned} F^*(x^*) &= \sup_{x \in X} \{\langle x, x^* \rangle - F(x)\} \\ G^*(y^*) &= \sup_{y \in Y} \{\langle y, y^* \rangle - G(y)\} \end{aligned}$$

and X^* and Y^* are the topological dual spaces of X and Y. Moreover $\Lambda^* : Y^* \to X^*$ stands for the adjoint operator of Λ. Under the assumption

$$\Lambda(\operatorname{dom} F) \cap \{y \in Y : G \text{ is continuous in } y\} \neq \emptyset, \tag{2.13}$$

strong Fenchel duality holds, i.e.,

$$\inf_{x \in X} \{F(x) + G(\Lambda x)\} = \max_{y^* \in Y^*} \{-F^*(\Lambda^* y^*) - G^*(-y^*)\}. \tag{2.14}$$

We now apply this to our specific setting. As in [99], we define the operator B as

$$B := \alpha \operatorname{id} + K^* K \in \mathcal{L}(L^2(\Gamma)), \tag{2.15}$$

where id is the identity mapping. Furthermore, we define

$$\|w\|_{B^{-1}}^2 := (w, B^{-1} w)_{L^2(\Gamma)} =: (w, w)_{B^{-1}}$$

for any $w \in L^2(\Gamma)$. Notice that in view of our standing assumptions ($\alpha > 0$ or K^*K coercive), $\|w\|_{B^{-1}}$ is a norm equivalent to the standard norm of $L^2(\Gamma)$.

Theorem 2.11. *The Fenchel dual problem of*

$$\left\{ \begin{array}{rl} \textit{Minimize} & \dfrac{1}{2} \|\operatorname{div} \boldsymbol{p} + K^* f\|_{B^{-1}}^2 \\ \textit{over} & \boldsymbol{p} \in \boldsymbol{H}(\operatorname{div}; \Gamma) \\ \textit{subject to} & |\boldsymbol{p}|_2 \leq \beta \quad \textit{a.e. on } \Gamma \end{array} \right. \tag{2.16}$$

is equivalent to the optimization problem (2.1)*. In other words,* (2.16) *can be seen as the predual of the primal problem* (2.1)*.*

Proof. The proof proceeds along the lines of [99, Th. 2.2]. We invoke the Fenchel duality theory in the setting

$$\begin{aligned} X &= \boldsymbol{H}(\mathrm{div};\Gamma), \\ Y &= L^2(\Gamma), \\ \Lambda &= -\mathrm{div} : \boldsymbol{H}(\mathrm{div};\Gamma) \to L^2(\Gamma). \end{aligned}$$

It is convenient to identify Y with Y^* so that

$$\Lambda^* = -\mathrm{div}^* : L^2(\Gamma) \to X^*.$$

Define the functions $F : \boldsymbol{H}(\mathrm{div};\Gamma) \to \mathbb{R}$ and $G : L^2(\Gamma) \to \mathbb{R}$ as

$$\begin{aligned} F(\boldsymbol{p}) &:= \begin{cases} 0 & \text{if } |\boldsymbol{p}|_2 \le \beta \text{ a.e. on } \Gamma, \\ \infty & \text{otherwise,} \end{cases} \\ G(v) &:= \frac{1}{2}\|v - K^* f\|^2_{B^{-1}}. \end{aligned} \tag{2.17}$$

From [99] we have

$$\begin{aligned} G^*(v^*) &= \sup_{v \in L^2(\Gamma)} \left\{ (v,\, v^*)_{L^2(\Gamma)} - G(v) \right\} \\ &= \frac{1}{2}\|Kv^* + f\|^2_{L^2(\Gamma)} + \frac{\alpha}{2}\|v^*\|^2_{L^2(\Gamma)} - \frac{1}{2}\|f\|^2_{L^2(\Gamma)} \end{aligned} \tag{2.18}$$

for $v^* \in L^2(\Gamma)$. With regard to $F^* : \boldsymbol{H}(\mathrm{div};\Gamma)^* \to \mathbb{R}$ it is clear that

$$F^*(\boldsymbol{p}^*) = \sup_{\boldsymbol{p} \in \mathcal{B}_0} \langle \boldsymbol{p},\, \boldsymbol{p}^* \rangle_{\boldsymbol{H}(\mathrm{div};\Gamma),\boldsymbol{H}(\mathrm{div};\Gamma)^*} \tag{2.19}$$

holds, where

$$\mathcal{B}_0 := \left\{ \boldsymbol{p} \in \boldsymbol{H}(\mathrm{div};\Gamma) : |\boldsymbol{p}|_2 \le \beta \text{ a.e. on } \Gamma \right\}.$$

Next we argue that the set

$$\mathcal{B}_1 := \left\{ \boldsymbol{p} \in \boldsymbol{C}^\infty(\Gamma;\mathcal{T}\Gamma) : |\boldsymbol{p}|_2 \le \beta \text{ a.e. on } \Gamma \right\}$$

is dense in $\mathcal{B}_0$ in the topology of $\boldsymbol{H}(\mathrm{div};\Gamma)$. In fact, in the case $\Gamma = \mathbb{R}^n$ and in the absence of bounds $|\boldsymbol{p}|_2 \le \beta$, the result is classical; see for instance [82, Theorem I.2.4]. The proof can be done by mollification. Given $\boldsymbol{p} \in \boldsymbol{H}(\mathrm{div};\mathbb{R}^n)$, define

$$\boldsymbol{p}_\varepsilon := \boldsymbol{p} \star \eta_\varepsilon,$$

where $\{\eta_\varepsilon\}$ is a family of Friedrichs mollifiers and $\star$ denotes convolution. Since mollification preserves pointwise bounds, the convergence

$$\boldsymbol{p}_\varepsilon \to \boldsymbol{p} \quad \text{in} \quad \boldsymbol{H}(\mathrm{div};\mathbb{R}^n)$$

remains true under the constraint $|\boldsymbol{p}|_2 \le \beta$. In case that Γ is a compact surface, consider a finite atlas $\{\boldsymbol{x}_\ell\}_{\ell=1}^N$ of parametrizations

$$\boldsymbol{x}_\ell : U_\ell \to V_\ell.$$

Moreover, let $\{\theta_\ell\}_{\ell=1}^N$ denote a partition of unity subordinate to $\{U_\ell\}$. Consider $\boldsymbol{p} \in \mathcal{B}_0$ and write

$$\boldsymbol{p} = \sum_{\ell=1}^{N} \boldsymbol{p}\,\theta_\ell.$$

Then

$$[(\boldsymbol{p}\,\theta_\ell) \circ x_\ell]_\varepsilon \to (\boldsymbol{p}\,\theta_\ell) \circ x_\ell \quad \text{in} \quad L^2(\mathbb{R}^2),$$

which is enough to confirm the convergence

$$\boldsymbol{p}_\varepsilon = \sum_{\ell=1}^{N} [(\boldsymbol{p}\,\theta_\ell) \circ x_\ell]_\varepsilon \circ x_\ell^{-1} \to \sum_{\ell=1}^{N} [(\boldsymbol{p}\,\theta_\ell) \circ x_\ell] \circ x_\ell^{-1} = \boldsymbol{p}$$

in $\boldsymbol{L}^2(\Gamma)$ due to the boundedness of $\det(G(x_\ell))$ for all $\ell = 1, \ldots, N$; see (2.5). By applying an analogous argument, $\operatorname{div} \boldsymbol{p}_\varepsilon$ can likewise be shown to converge to $\operatorname{div} \boldsymbol{p}$ in $L^2(\Gamma)$, which proves the density of $\mathcal{B}_1$ in $\mathcal{B}_0$.
Consequently, it is enough to take the supremum over $\boldsymbol{p} \in \mathcal{B}_1$ in (2.19). Hence, for every $u \in L^2(\Gamma)$ we obtain

$$\begin{aligned} F^*((-\operatorname{div})^* u) &= \sup\{\langle \boldsymbol{p},\, (-\operatorname{div})^* u\rangle_{\boldsymbol{H}(\operatorname{div};\Gamma),\boldsymbol{H}(\operatorname{div};\Gamma)^*} : \boldsymbol{p} \in \mathcal{B}_1\} \\ &= \sup\{(u, -\operatorname{div} \boldsymbol{p})_{L^2(\Gamma)} : \boldsymbol{p} \in \mathcal{B}_1\} \\ &= \beta\, \sup\{(u, \operatorname{div} \boldsymbol{p})_{L^2(\Gamma)} : \boldsymbol{p} \in \boldsymbol{C}^\infty(\Gamma; \mathcal{T}\Gamma) : |\boldsymbol{p}|_2 \le 1 \text{ a.e. on } \Gamma\}. \end{aligned}$$

According to Definition 2.6, we get

$$F^*((-\operatorname{div})^* u) = \begin{cases} \beta \displaystyle\int_\Gamma |\nabla u| & \text{if } u \in BV(\Gamma), \\ \infty & \text{otherwise.} \end{cases} \tag{2.20}$$

Thus, since F and G are proper and convex and condition (2.13) is fulfilled for them, there is no duality gap between the optimal values of (2.1) and (2.16), i.e., (2.12) becomes an equality and

$$\begin{aligned} &\inf_{\boldsymbol{p} \in \boldsymbol{H}(\operatorname{div};\Gamma)} \{F(\boldsymbol{p}) + G(-\operatorname{div} \boldsymbol{p})\} \\ &= \sup_{u \in L^2(\Gamma)} \{-F^*((-\operatorname{div})^* u) - G^*(-u)\} \\ &= \sup_{u \in BV(\Gamma)} \{-F^*((-\operatorname{div})^* u) - G^*(-u)\} \\ &= \sup_{u \in BV(\Gamma)} \left\{ -\frac{1}{2}\|Ku - f\|^2_{L^2(\Gamma)} - \frac{\alpha}{2}\|u\|^2_{L^2(\Gamma)} - \beta \int_\Gamma |\nabla u| \right\} + \frac{1}{2}\|f\|^2_{L^2(\Gamma)}. \end{aligned} \tag{2.21}$$

Finally, it is immediate to check that (2.21) is in turn equivalent to (2.1) . □

Corollary 2.12. *Problem* (2.1) *and its predual* (2.16) *are solvable.*

Proof. It is easy to see that the objective $\frac{1}{2}\|\operatorname{div} \boldsymbol{p} + K^* f\|^2_{B^{-1}}$ is bounded below by 0. Let us consider a minimizing sequence $\{\boldsymbol{p}_n\}$. Owing to the boundedness of the objective as

well as $|\boldsymbol{p}_n|_2 \leq \beta$, $\{\boldsymbol{p}_n\}$ is bounded in $\boldsymbol{H}(\operatorname{div};\Gamma)$. Hence, there exists a subsequence (again denoted by $\{\boldsymbol{p}_n\}$) such that

$$\boldsymbol{p}_n \rightharpoonup \overline{\boldsymbol{p}} \quad \text{in} \quad \boldsymbol{L}^2(\Gamma;\mathcal{T}\Gamma)$$

holds with $|\overline{\boldsymbol{p}}|_2 \leq \beta$ a.e. on Γ, as well as

$$\operatorname{div} \boldsymbol{p}_n \rightharpoonup \operatorname{div} \overline{\boldsymbol{p}} \quad \text{in} \quad L^2(\Gamma).$$

By weak sequential lower semicontinuity of $H(\boldsymbol{p}) := \frac{1}{2}\|\operatorname{div} \boldsymbol{p} + K^* f\|^2_{B^{-1}}$,

$$\frac{1}{2}\|\operatorname{div} \overline{\boldsymbol{p}} + K^* f\|^2_{B^{-1}} \leq \liminf_{n\to\infty} \frac{1}{2}\|\operatorname{div} \boldsymbol{p}_n + K^* f\|^2_{B^{-1}}$$

holds. This implies that (2.16) has the (global) minimizer $\overline{\boldsymbol{p}}$ and is solvable.
Regarding the solvability of (2.1), since condition (2.13) is fulfilled for F and G defined in the proof of Theorem 2.11, we conclude that the supremum in the RHS of (2.21) is attained, so (2.14) holds and the optimization problem (2.1) is solvable. □

The following theorem shows how the optimal solutions to (2.1) and (2.16) are related to each other.

Theorem 2.13. *Suppose that $\overline{\boldsymbol{p}}$ is an optimal solution to* (2.16) *and $\overline{u}$ is optimal to* (2.1). *Then*

$$B\,\overline{u} = \operatorname{div} \overline{\boldsymbol{p}} + K^* f. \tag{2.22}$$

Proof. Suppose that $\overline{\boldsymbol{p}}$ and $\overline{u}$ are optimal to (2.16) and (2.1), respectively. Then the following conditions are fulfilled, see for instance [73, Prop. 4.1],

$$\begin{aligned} (-\operatorname{div})^* \overline{u} &\in \partial F(\overline{\boldsymbol{p}}) \qquad \text{in } \boldsymbol{H}(\operatorname{div};\Gamma)^*, \\ -\operatorname{div} \overline{\boldsymbol{p}} &\in \partial G^*(-\overline{u}) \quad \text{in } L^2(\Gamma), \end{aligned} \tag{2.23}$$

where ∂F stands for the standard representation of the subdifferential of the convex function $F : \boldsymbol{H}(\operatorname{div};\Gamma) \to \mathbb{R}$, and ∂G^* is defined analogously. The second condition in (2.23) is equivalent to

$$G^*(-\overline{u}) + G(-\operatorname{div} \overline{\boldsymbol{p}}) - (-\operatorname{div} \overline{\boldsymbol{p}},\, -\overline{u})_{L^2(\Gamma)} = 0,$$

see [73, Prop. I.5.1]. Using the expressions (2.17) and (2.18) for G and G^*, this becomes

$$\frac{1}{2}\|K(-\overline{u}) + f\|^2_{L^2(\Gamma)} + \frac{\alpha}{2}\|\overline{u}\|^2_{L^2(\Gamma)} - \frac{1}{2}\|f\|^2_{L^2(\Gamma)} + \frac{1}{2}\|\operatorname{div} \overline{\boldsymbol{p}} + K^* f\|^2_{B^{-1}} = (\operatorname{div} \overline{\boldsymbol{p}},\, \overline{u})_{L^2(\Gamma)},$$

or equivalently,

$$\frac{1}{2}\|K\overline{u}\|^2_{L^2(\Gamma)} + \frac{\alpha}{2}\|\overline{u}\|^2_{L^2(\Gamma)} + \frac{1}{2}\|\operatorname{div} \overline{\boldsymbol{p}} + K^* f\|^2_{B^{-1}} = (\operatorname{div} \overline{\boldsymbol{p}} + K^* f,\, \overline{u})_{L^2(\Gamma)}.$$

Applying the definition of B, see (2.15), we obtain

$$\frac{1}{2}\left\|u - B^{-1}(\operatorname{div} \overline{\boldsymbol{p}} + K^* f)\right\|^2_B = 0$$

and (2.22) follows. □

2.3 Algorithmic Approach

In this section we describe a novel approach for solving (2.1) via its predual (2.16). Once again, recall that the pointwise constraints $|\boldsymbol{p}|_2 \leq \beta$ are nonlinear. This is in contrast with $|\boldsymbol{p}|_\infty \leq \beta$ obtained in [99] due to a slightly different definition of the TV-seminorm. The nonlinearity of the constraint would render the analysis and application of a primal-dual active set method more challenging although this has been successfully pursued, for instance, in [98] in different contexts.
Our solution approach is based on a logarithmic barrier method to deal with the inequality constraints. Consequently, we consider the following family of convex problems for a decreasing sequence of barrier parameters $\mu \searrow 0$:

$$\left\{\begin{array}{rl} \text{Minimize} & \dfrac{1}{2}\|\operatorname{div}\boldsymbol{p} + K^*f\|^2_{B^{-1}} - \mu\displaystyle\int_\Gamma \ln\left(\beta^2 - |\boldsymbol{p}|_2^2\right) \mathrm{d}\boldsymbol{s} \\ \text{over} & \boldsymbol{p} \in \boldsymbol{H}(\operatorname{div};\Gamma) \\ \text{subject to} & |\boldsymbol{p}|_2 \leq \beta \text{ a.e. on } \Gamma. \end{array}\right. \tag{2.24}$$

Notice that the constraint $|\boldsymbol{p}|_2 \leq \beta$ is explicitly kept in (2.24) for mathematical convenience and it avoids the need to define the logarithmic barrier term for negative arguments. For any fixed barrier parameter $\mu > 0$, problem (2.24) will be solved using Newton's method. The constraint $|\boldsymbol{p}|_2 \leq \beta$ is not enforced explicitly but its satisfaction will be monitored throughout the Newton iterations. More details concerning the implementation are given in Section 2.4.
For convenience, we use the abbreviations

$$\begin{aligned} H(\boldsymbol{p}) &:= \frac{1}{2}\|\operatorname{div}\boldsymbol{p} + K^*f\|^2_{B^{-1}} \\ b(\boldsymbol{p}) &:= -\mu\int_\Gamma \ln\left(\beta^2 - |\boldsymbol{p}|_2^2\right) \mathrm{d}\boldsymbol{s} \end{aligned} \tag{2.25}$$

in the sequel.

2.3.1 Existence and Uniqueness for the Predual Barrier Problem

The analysis of interior point methods in L^p spaces including a convergence analysis of the central path has been addressed in [131, 156] in the context of optimal control problems. Notice that the presence of the logarithmic barrier term helps to overcome the lack of strict convexity of the objective in (2.16). We therefore obtain the following result.

Proposition 2.14. *For every $\mu > 0$, problem* (2.24) *possesses a unique solution $\overline{\boldsymbol{p}} \in \boldsymbol{H}(\operatorname{div};\Gamma)$.*

Proof. It is easy to check that the objective $H(\boldsymbol{p}) + b(\boldsymbol{p})$ is bounded below by

$$b(\boldsymbol{0}) = -\mu\ |\Gamma|\ \ln(\beta^2),$$

but it may attain the value ∞. Here, $|\Gamma|$ denotes the area of Γ. Let us consider a minimizing sequence $\{\boldsymbol{p}_n\}$. Owing to the boundedness of both terms in the objective as well as

$|\boldsymbol{p}_n|_2 \leq \beta$, $\{\boldsymbol{p}_n\}$ is bounded in $\boldsymbol{H}(\mathrm{div};\Gamma)$. Hence, there exists a subsequence (again denoted by $\{\boldsymbol{p}_n\}$) such that

$$\boldsymbol{p}_n \rightharpoonup \overline{\boldsymbol{p}} \quad \text{in} \quad \boldsymbol{L}^2(\Gamma;\mathcal{T}\Gamma)$$

holds with $|\overline{\boldsymbol{p}}|_2 \leq \beta$ a.e. on Γ, as well as

$$\mathrm{div}\, \boldsymbol{p}_n \rightharpoonup \mathrm{div}\, \overline{\boldsymbol{p}} \quad \text{in} \quad L^2(\Gamma).$$

By weak sequential lower semicontinuity of H,

$$\begin{aligned} H(\overline{\boldsymbol{p}}) &= \frac{1}{2}\|\mathrm{div}\, \overline{\boldsymbol{p}} + K^* f\|_{B^{-1}}^2 \\ &\leq \liminf_{n\to\infty} \frac{1}{2}\|\mathrm{div}\, \boldsymbol{p}_n + K^* f\|_{B^{-1}}^2 \end{aligned}$$

holds. Let us argue that b is also weakly sequentially lower semicontinuous w.r.t. $\boldsymbol{L}^2(\Gamma;\mathcal{T}\Gamma)$. To this end, it suffices to show that b is sequentially lower semicontinuous w.r.t. the strong topology of $\boldsymbol{L}^2(\Gamma;\mathcal{T}\Gamma)$ on

$$\mathcal{B} := \{\boldsymbol{q} \in \boldsymbol{L}^2(\Gamma;\mathcal{T}\Gamma) : |\boldsymbol{q}|_2 \leq \beta \text{ a.e. on } \Gamma\},$$

since $\mathcal{B}$ is closed and convex and b is convex in $\mathcal{B}$. Arguing similarly as in the proof of [156, Proposition 2], suppose that

$$\boldsymbol{q}_n \to \boldsymbol{q} \quad \text{in} \quad \boldsymbol{L}^2(\Gamma;\mathcal{T}\Gamma)$$

holds, where $\boldsymbol{q}_n \in \mathcal{B}$, and thus $\boldsymbol{q} \in \mathcal{B}$ holds as well. We have to show that

$$b(\boldsymbol{q}) \leq \liminf_{n\to\infty} b(\boldsymbol{q}_n),$$

which is clear if the right hand side is ∞. In case

$$\liminf_{n\to\infty} b(\boldsymbol{q}_n) < \infty,$$

we can select a subsequence, denoted by $\{\boldsymbol{q}_j\}$, such that

$$\lim_{j\to\infty} b(\boldsymbol{q}_j) = \liminf_{n\to\infty} b(\boldsymbol{q}_n)$$

and

$$\lim_{j\to\infty} \boldsymbol{q}_j(\boldsymbol{s}) = \boldsymbol{q}(\boldsymbol{s}) \quad \text{a.e. on } \Gamma. \tag{2.26}$$

In particular, the sequence $\{b(\boldsymbol{q}_j)\}$ is bounded and we have

$$b(\boldsymbol{q}_j) \leq C_1 \tag{2.27}$$

with $C_1 \geq 0$. Let us define

$$\begin{aligned} g_n(\boldsymbol{s}) &:= -\mu\, \ln \max\{\beta^2 - |\boldsymbol{q}_n(\boldsymbol{s})|_2^2,\, 1\}, \\ g(\boldsymbol{s}) &:= -\mu\, \ln \max\{\beta^2 - |\boldsymbol{q}(\boldsymbol{s})|_2^2,\, 1\}, \\ h_n(\boldsymbol{s}) &:= -\mu\, \ln \min\{\beta^2 - |\boldsymbol{q}_n(\boldsymbol{s})|_2^2,\, 1\}, \\ h(\boldsymbol{s}) &:= -\mu\, \ln \min\{\beta^2 - |\boldsymbol{q}(\boldsymbol{s})|_2^2,\, 1\}. \end{aligned}$$

for $\boldsymbol{s} \in \Gamma$. Since $\ln(x) < x - 1$ for $x > 1$, we have

$$\begin{aligned} |g_n| &\leq \mu \left| \max\{\beta^2 - |\boldsymbol{q}_n|_2^2,\ 1\} - 1 \right| \\ &\leq \mu \left| \max\{\beta^2 - |\boldsymbol{q}_n|_2^2 - 1,\ 0\} \right| \\ &\leq \mu \left| \beta^2 - |\boldsymbol{q}_n|_2^2 - 1 \right|. \end{aligned} \tag{2.28}$$

Notice that (2.26) and (2.28) imply the pointwise convergence $\lim_{j\to\infty} g_j = g$ as well as the estimate $|g_n| \leq C_2$ for some $C_2 \geq 0$ both a.e. on Γ. Hence Lebesgue's dominated convergence theorem can be applied and gives

$$\lim_{j\to\infty} \int_\Gamma g_j \,\mathrm{d}\boldsymbol{s} = \int_\Gamma g \,\mathrm{d}\boldsymbol{s}.$$

Consequently,

$$\lim_{j\to\infty} \int_\Gamma h_j \,\mathrm{d}\boldsymbol{s} = \lim_{j\to\infty} b(\boldsymbol{q}_j) - \lim_{j\to\infty} \int_\Gamma g_j \,\mathrm{d}\boldsymbol{s}$$

exists as well. Using $h_n \geq 0$, (2.27) and (2.28), we obtain

$$\begin{aligned} 0 \leq & \int_\Gamma h_j \,\mathrm{d}\boldsymbol{s} \\ &\leq C_1 - \int_\Gamma g_j \,\mathrm{d}\boldsymbol{s} \\ &\leq C_1 + \mu \int_\Gamma \left| \left| \boldsymbol{q}_j \right|_2^2 - \beta^2 - 1 \right| \mathrm{d}\boldsymbol{s} \\ &\leq C \end{aligned}$$

with some $C \geq 0$ and for all j. By Fatou's lemma, we thus conclude

$$\begin{aligned} 0 \leq & \int_\Gamma h \,\mathrm{d}\boldsymbol{s} \\ &= \int_\Gamma \lim_{j\to\infty} h_j \,\mathrm{d}\boldsymbol{s} \\ &\leq \lim_{j\to\infty} \int_\Gamma h_j \,\mathrm{d}\boldsymbol{s} \\ &\leq C. \end{aligned}$$

This implies

$$\begin{aligned} \liminf_{n\to\infty} b(\boldsymbol{q}_n) &= \lim_{j\to\infty} b(\boldsymbol{q}_j) \\ &= \lim_{j\to\infty} \int_\Gamma (g_j + h_j) \,\mathrm{d}\boldsymbol{s} \\ &\geq \int_\Gamma (g + h) \,\mathrm{d}\boldsymbol{s} \\ &= b(\boldsymbol{q}). \end{aligned}$$

Consequently, both summands H and b in the objective are weakly sequentially lower semicontinuous, which implies that $\overline{\boldsymbol{p}}$ is a (global) minimizer of (2.24).

To show its uniqueness, we verify that the second part of the objective b is strictly convex where it is finite. To this end, let $\boldsymbol{p}_1, \boldsymbol{p}_2 \in \mathcal{B}$ with

$$b(\boldsymbol{p}_1), b(\boldsymbol{p}_2) < \infty$$

and $\boldsymbol{p}_1$ not equal to $\boldsymbol{p}_2$ a.e. on Γ. Then by classical arguments there exists a set $E \subset \Gamma$ of positive surface measure and $\varepsilon > 0$ such that

$$|\boldsymbol{p}_1 - \boldsymbol{p}_2|_2 \geq \varepsilon \quad \text{a.e. on } E.$$

Let us define

$$\begin{aligned} g(\boldsymbol{p}) &:= |\boldsymbol{p}|_2^2, \\ h(z) &:= -\mu \, \ln(\beta^2 - z), \end{aligned}$$

whence

$$b(\boldsymbol{p}) = \int_\Gamma h(g(\boldsymbol{p})) \, \mathrm{d}\boldsymbol{s}$$

holds. On the set E, we have the following pointwise estimate due to the strong convexity of g,

$$\begin{aligned} g\big(\lambda \, \boldsymbol{p}_1 + (1-\lambda) \, \boldsymbol{p}_2\big) - \lambda \, g(\boldsymbol{p}_1) - (1-\lambda) \, g(\boldsymbol{p}_2) &= -\lambda \, (1-\lambda) \, |\boldsymbol{p}_1 - \boldsymbol{p}_2|_2^2 \\ &\leq -\lambda \, (1-\lambda) \, \varepsilon^2 \end{aligned} \tag{2.29}$$

for all $\lambda \in [0,1]$. Next we use that h is convex and strictly increasing on $[0, \beta^2)$. Its minimal slope is attained at $z = 0$ so we have

$$h'(z) \geq h'(0) = \mu / \beta^2 \quad \forall z \in [0, \beta^2).$$

Consequently, we have

$$\begin{aligned} h(r) &\geq h(\ell) + h'(\ell)(r - \ell) \\ &\geq h(\ell) + h'(0)(r - \ell) \end{aligned}$$

for all $0 \leq \ell \leq r < \beta^2$. Applying this estimate with $\ell = g\big(\lambda \, \boldsymbol{p}_1 + (1-\lambda) \, \boldsymbol{p}_2\big)$ and $r = \lambda \, g(\boldsymbol{p}_1) + (1-\lambda) \, g(\boldsymbol{p}_2)$ and using (2.29), we obtain

$$h\Big(g\big(\lambda \, \boldsymbol{p}_1 + (1-\lambda) \, \boldsymbol{p}_2\big)\Big) \leq h\Big(\lambda \, g(\boldsymbol{p}_1) + (1-\lambda) \, g(\boldsymbol{p}_2)\Big) - \frac{\mu}{\beta^2} \, \lambda \, (1-\lambda) \, \varepsilon^2.$$

Using the convexity of h we can estimate further

$$h\Big(g\big(\lambda \, \boldsymbol{p}_1 + (1-\lambda) \, \boldsymbol{p}_2\big)\Big) \leq \lambda \, h\big(g(\boldsymbol{p}_1)\big) + (1-\lambda) \, h\big(g(\boldsymbol{p}_2)\big) - \frac{\mu}{\beta^2} \, \lambda \, (1-\lambda) \, \varepsilon^2,$$

which holds a.e. on E. Similarly, we obtain the same estimate without the last term on $\Gamma \setminus E$. Integrating these inequalities over Γ, we finally obtain the estimate

$$b\big(\lambda \, \boldsymbol{p}_1 + (1-\lambda) \, \boldsymbol{p}_2\big) \leq \lambda \, b(\boldsymbol{p}_1) + (1-\lambda) \, b(\boldsymbol{p}_2) - \frac{\mu}{\beta^2} \, \lambda \, (1-\lambda) \, \varepsilon^2 \, |E|,$$

which confirms the strict convexity of b on its domain. □

Next we address the first-order necessary and sufficient optimality conditions for (2.24). The main difficulty compared to finite dimensional barrier methods is that one cannot a-priori exclude that the minimizer approaches the bound of the constraint

$$|\boldsymbol{p}|_2 \leq \beta$$

on parts of the surface, which complicates the discussion of differentiability of the barrier term. The proof uses techniques introduced in [143], where optimal control problems with pointwise simple bounds on the control and also the state were discussed. Although the present problem is generally simpler due to the absence of state constraints, but the nonlinearity of the constraint requires modifications.

Theorem 2.15. *The vector field $\boldsymbol{p} \in \boldsymbol{H}(\operatorname{div};\Gamma)$ is the unique solution for* (2.24) *if and only if $|\boldsymbol{p}|_2 \leq \beta$ holds a.e. on Γ and*

$$\big(\operatorname{div}\boldsymbol{p} + K^*f,\ \operatorname{div}\delta\boldsymbol{p}\big)_{B^{-1}} + \mu\int_\Gamma \frac{2\,(\boldsymbol{p},\,\delta\boldsymbol{p})_2}{\beta^2 - |\boldsymbol{p}|_2^2}\,\mathrm{d}\boldsymbol{s} = 0 \tag{2.30}$$

for all $\delta\boldsymbol{p} \in \boldsymbol{H}(\operatorname{div};\Gamma)$.

Before stating the proof of Theorem 2.15 we require some preliminary results. For simplicity, we denote by

$$\ell(\boldsymbol{p}) := \begin{cases} -\mu\,\ln\big(\beta^2 - |\boldsymbol{p}|_2^2\big) & \text{if } |\boldsymbol{p}|_2 < \beta \\ \infty & \text{otherwise} \end{cases}$$

the pointwise barrier term and by

$$\nabla\ell(\boldsymbol{p}) = 2\,\mu\,\frac{\boldsymbol{p}}{\beta^2 - |\boldsymbol{p}|_2^2}$$

its gradient[1], defined for $\boldsymbol{p} \in \mathbb{R}^3$ with $|\boldsymbol{p}|_2 < \beta$ and in particular for $\boldsymbol{p}$ in the tangent space $\mathcal{T}_s\Gamma$ of the surface Γ at some point. Moreover, let

$$b(\boldsymbol{p}) := \int_\Gamma \ell(\boldsymbol{p})\,\mathrm{d}\boldsymbol{s}$$

denote the integrated barrier term, like in (2.25), and

$$\langle b'(\boldsymbol{p}),\,\delta\boldsymbol{p}\rangle := \int_\Gamma \big(\nabla\ell(\boldsymbol{p}),\,\delta\boldsymbol{p}\big)_2\,\mathrm{d}\boldsymbol{s}$$

its *formal* derivative for vector fields $\boldsymbol{p}, \delta\boldsymbol{p} \in \boldsymbol{L}^2(\Gamma;\mathcal{T}\Gamma)$. Let us recall from the proof of Proposition 2.14 that b is convex and it can take values in $\mathbb{R}\cup\{\infty\}$. We denote by

$$\partial b(\boldsymbol{p}) \subset \boldsymbol{L}^2(\Gamma;\mathcal{T}\Gamma)^*$$

the convex subdifferential of b at $\boldsymbol{p}$. Notice that $\boldsymbol{L}^2(\Gamma;\mathcal{T}\Gamma)^*$ can be identified with $\boldsymbol{L}^2(\Gamma;\mathcal{T}\Gamma^*)$ and also with $\boldsymbol{L}^2(\Gamma;\mathcal{T}\Gamma)$.
The following lemma parallels [143, Lemma 3.3].

[1] This should not be confused with the gradient of a scalar function on S in Definition 2.4. In the present context the *gradient* $\nabla\ell(\boldsymbol{p})$ is the transpose of the derivative of the function $\ell : \mathbb{R}^3 \to \mathbb{R}$.

Lemma 2.16. *Consider $\boldsymbol{p}, \delta\boldsymbol{p} \in \boldsymbol{L}^2(\Gamma; \mathcal{T}\Gamma)$ such that all of $b(\boldsymbol{p})$, $b(\boldsymbol{p}+\delta\boldsymbol{p})$ and $\langle b'(\boldsymbol{p}),\, \delta\boldsymbol{p}\rangle$ are finite. Then b is directionally differentiable at $\boldsymbol{p}$ in the direction $\delta\boldsymbol{p}$, and its directional derivative satisfies*

$$b'(\boldsymbol{p};\delta\boldsymbol{p}) = \langle b'(\boldsymbol{p}),\, \delta\boldsymbol{p}\rangle \geq \int_\Gamma (\boldsymbol{m},\, \delta\boldsymbol{p})_2 \,\mathrm{d}\boldsymbol{s} \quad \textit{for all } \boldsymbol{m} \in \partial b(\boldsymbol{p}), \tag{2.31}$$

where the subdifferential is considered a subset of $\boldsymbol{L}^2(\Gamma; \mathcal{T}\Gamma)$.

Proof. To proof the first claim, we have to show that

$$\frac{b(\boldsymbol{p}+h\delta\boldsymbol{p}) - b(\boldsymbol{p})}{h} \to \langle b'(\boldsymbol{p}),\, \delta\boldsymbol{p}\rangle$$

for $h \searrow 0$. Because of the convexity of $\ell(\boldsymbol{p})$,

$$\big(\nabla\ell(\boldsymbol{p}),\, \delta\boldsymbol{p}\big)_2 \leq \frac{\ell(\boldsymbol{p}+h\delta\boldsymbol{p}) + \ell(\boldsymbol{p})}{h}$$

holds pointwise almost everywhere and the RHS is monotonically increasing in h. Since $b(\boldsymbol{p})$, $b(\boldsymbol{p}+\delta\boldsymbol{p})$ and $\langle b'(\boldsymbol{p}),\, \delta\boldsymbol{p}\rangle$ are finite, the function

$$r(\boldsymbol{s},h) := \frac{\ell(\boldsymbol{p}(\boldsymbol{s}) + h\delta\boldsymbol{p}(\boldsymbol{s})) + \ell(\boldsymbol{p}(\boldsymbol{s}))}{h} - \big(\nabla\ell(\boldsymbol{p}(\boldsymbol{s})),\, \delta\boldsymbol{p}(\boldsymbol{s})\big)_2$$

is well defined and non-negative almost everywhere. For every fixed $h \in]0,1]$, $r \in L^1(\Gamma)$ holds and $r(\boldsymbol{s},h)$ is dominated by $r(\boldsymbol{s},1)$ by monotonicity of the difference quotient. Since $\ell(\boldsymbol{p})$ is differentiable with respect to $\boldsymbol{p}$ a.e.,

$$\lim_{h\searrow 0} r(\boldsymbol{s},h) = 0$$

holds pointwise almost everywhere. By applying the convergence theorem of Lebesgue, we obtain

$$\lim_{h\searrow 0} \int_\Gamma r(\boldsymbol{s},h)\,\mathrm{d}\boldsymbol{s} = 0.$$

This shows directional differentiability of b and the relation

$$b'(\boldsymbol{p};\delta\boldsymbol{p}) = \langle b'(\boldsymbol{p}),\, \delta\boldsymbol{p}\rangle.$$

In particular,

$$b(\boldsymbol{p}+h\delta\boldsymbol{p}) - b(\boldsymbol{p}) = \langle b'(\boldsymbol{p}),\, h\delta\boldsymbol{p}\rangle + \mathcal{O}(h)$$

holds. To show the remaining part of (2.31) let $\boldsymbol{m} \in \partial b(\boldsymbol{p})$ and we assume that

$$\int_\Gamma (\boldsymbol{m},\, \delta\boldsymbol{p})_2 \,\mathrm{d}\boldsymbol{s} \geq \langle b'(\boldsymbol{p}),\, \delta\boldsymbol{p}\rangle.$$

Then there exists $\epsilon > 0$ such that

$$\begin{aligned}\int_\Gamma (\boldsymbol{m},\, h\delta\boldsymbol{p})_2 \,\mathrm{d}\boldsymbol{s} &\geq \langle b'(\boldsymbol{p}),\, h\delta\boldsymbol{p}\rangle + \epsilon h \\ &\geq b(\boldsymbol{p}+h\delta\boldsymbol{p}) - b(\boldsymbol{p}) - \mathcal{O}(h) + \epsilon h\end{aligned}$$

But this implies $\int_\Gamma (\boldsymbol{m},\, h\delta\boldsymbol{p})_2 \,\mathrm{d}\boldsymbol{s} \geq b(\boldsymbol{p}+h\delta\boldsymbol{p}) - b(\boldsymbol{p})$ for sufficiently small h. This excludes m from the subdifferential and completes our proof. □

The next result is equal to [143, Prop. 3.4] but the proof requires a number of modifications.

Proposition 2.17. *Let $\boldsymbol{p} \in \boldsymbol{L}^2(\Gamma; \mathcal{T}\Gamma)$ be given. Then we have:*

(i) If $\nabla \ell(\boldsymbol{p})$ belongs to $\boldsymbol{L}^2(\Gamma; \mathcal{T}\Gamma)$, then $\partial b(\boldsymbol{p}) = \{\nabla \ell(\boldsymbol{p})\}$.

(ii) If $\nabla \ell(\boldsymbol{p})$ does not belong to $\boldsymbol{L}^2(\Gamma; \mathcal{T}\Gamma)$, then $\partial b(\boldsymbol{p}) = \emptyset$.

Proof. The proof is split into three parts, which combine to yield the result.
Part A: We begin by considering the case $b(\boldsymbol{p}) < \infty$, which implies $|\boldsymbol{p}|_2 < \beta$ a.e. on Γ. By convexity of ℓ, we obtain

$$(\nabla \ell(\boldsymbol{p}),\, \delta \boldsymbol{p})_2 \leq \ell(\boldsymbol{p} + \delta \boldsymbol{p}) - \ell(\boldsymbol{p})$$

a.e. on Γ and therefore

$$\begin{aligned} \int_\Gamma \big(\nabla \ell(\boldsymbol{p}),\, \delta \boldsymbol{p}\big)_2 \,\mathrm{d}\boldsymbol{s} &= \langle b'(\boldsymbol{p}),\, \delta \boldsymbol{p} \rangle \\ &\leq b(\boldsymbol{p} + \delta \boldsymbol{p}) - b(\boldsymbol{p}) \end{aligned}$$

for all $\delta \boldsymbol{p} \in \boldsymbol{L}^2(\Gamma; \mathcal{T}\Gamma)$, provided that $\nabla \ell(\boldsymbol{p}) \in \boldsymbol{L}^2(\Gamma; \mathcal{T}\Gamma)$ holds. This shows $\nabla \ell(\boldsymbol{p}) \in \partial b(\boldsymbol{p})$ in this case.
Part B: Now suppose that $\boldsymbol{m} \in \partial b(\boldsymbol{p})$ holds and let $M \subset \Gamma$ be an arbitrary measurable subset and $\boldsymbol{v} : \Gamma \to \mathcal{T}\Gamma$ be a vector field of class $\boldsymbol{C}^0$. Due to the compactness of Γ, $\|\boldsymbol{v}\|_{\boldsymbol{L}^\infty(\Gamma; \mathcal{T}\Gamma)}$ is finite. We are going to show that necessarily

$$\int_M \big(\nabla \ell(\boldsymbol{p}),\, \boldsymbol{v}\big)_2 \,\mathrm{d}\boldsymbol{s} = \int_M (\boldsymbol{m},\, \boldsymbol{v})_2 \,\mathrm{d}\boldsymbol{s} \tag{2.32}$$

holds, which then implies $\boldsymbol{m} = \nabla \ell(\boldsymbol{p})$ and $\nabla \ell(\boldsymbol{p}) \in \boldsymbol{L}^2(\Gamma; \mathcal{T}\Gamma)$. To this end, let

$$M_\delta := \{\boldsymbol{s} \in M : \beta - |\boldsymbol{p}(\boldsymbol{s})|_2 > \delta\}$$

for $\delta > 0$. Next we define

$$\boldsymbol{v}_k := \chi_{M_{1/k}} \boldsymbol{v}$$

and

$$\varepsilon_k := \big(2\, k\, \|\boldsymbol{v}\|_{\boldsymbol{L}^\infty(\Gamma; \mathcal{T}\Gamma)}\big)^{-1}$$

for $k \in \mathbb{N}$, where $\chi_{M_{1/k}}$ denotes the characteristic function of $M_{1/k}$. Then, since

$$\nabla \ell(\boldsymbol{p}) = 2\,\mu\, \frac{\boldsymbol{p}}{\beta^2 - |\boldsymbol{p}|_2^2} \in \boldsymbol{L}^\infty(M_\delta; \mathcal{T}\Gamma)$$

for any $\delta > 0$, we have

$$\big|\langle b'(\boldsymbol{p}),\, \pm \varepsilon_k \boldsymbol{v}_k \rangle\big| = \pm 2\,\mu\, \varepsilon_k \int_{M_{1/k}} \frac{(\boldsymbol{p},\, \boldsymbol{v}_k)_2}{\beta^2 - |\boldsymbol{p}|_2^2} \,\mathrm{d}\boldsymbol{s} < \infty.$$

Moreover,

$$\begin{aligned} b(\boldsymbol{p} \pm \varepsilon_k \boldsymbol{v}_k) = & -\mu \int_{S \setminus M_{1/k}} \ln\left(\beta^2 - |\boldsymbol{p}|_2^2\right) \mathrm{d}\boldsymbol{s} \\ & -\mu \int_{M_{1/k}} \ln\left(\beta^2 - |\boldsymbol{p} \pm \varepsilon_k \boldsymbol{v}_k|_2^2\right) \mathrm{d}\boldsymbol{s}. \end{aligned} \tag{2.33}$$

The first integral is finite since $b(\boldsymbol{p})$ is. For the second integral, we use that

$$\begin{aligned} \beta - |\boldsymbol{p} \pm \varepsilon_k \boldsymbol{v}_k|_2 &\geq \beta - |\boldsymbol{p}|_2 - \varepsilon_k \|\boldsymbol{v}\|_{\boldsymbol{L}^\infty(\Gamma;\mathcal{T}\Gamma)} \\ &\geq \frac{1}{k} - \frac{1}{2k} \\ &= \frac{1}{2k} \end{aligned}$$

holds a.e. on $M_{1/k}$. Hence by multiplication with $\beta + |\boldsymbol{p} \pm \varepsilon_k \boldsymbol{v}_k|_2 \geq \beta$ we conclude

$$\beta^2 - |\boldsymbol{p} \pm \varepsilon_k \boldsymbol{v}_k|_2^2 \geq \frac{\beta}{2k} \quad \text{a.e. on } M_{1/k}$$

and thus the second integral in (2.33) is finite as well. So we have shown that for $\delta\boldsymbol{p} = \pm\varepsilon_k \boldsymbol{v}_k$, the terms $b(\boldsymbol{p})$, $b(\boldsymbol{p} + \delta\boldsymbol{p})$ and $\langle b'(\boldsymbol{p}), \delta\boldsymbol{p}\rangle$ are all finite. Hence Lemma 2.16 yields

$$\langle b'(\boldsymbol{p}), \pm\varepsilon_k \boldsymbol{v}_k\rangle \geq \pm\varepsilon_k \int_\Gamma (\boldsymbol{m}, \boldsymbol{v}_k)_2 \,\mathrm{d}\boldsymbol{s} \quad \text{for all } \boldsymbol{m} \in \partial b(\boldsymbol{p}).$$

This implies

$$\begin{aligned} \int_\Gamma \left(\nabla \ell(\boldsymbol{p}), \boldsymbol{v}_k\right)_2 \mathrm{d}\boldsymbol{s} &= \langle b'(\boldsymbol{p}), \boldsymbol{v}_k\rangle \\ &= \int_\Gamma (\boldsymbol{m}, \boldsymbol{v}_k)_2 \,\mathrm{d}\boldsymbol{s} \end{aligned} \tag{2.34}$$

for all $\boldsymbol{m} \in \partial b(\boldsymbol{p})$, $k \in \mathbb{N}$. It remains to pass to the limit in (2.34) to show (2.32). Let us begin with the second term in (2.34) and observe that

$$\chi_M \boldsymbol{v} = \lim_{k\to\infty} \boldsymbol{v}_k$$

holds a.e. on Γ since the set where $|\boldsymbol{p}|_2 = \beta$ holds has zero measure. Moreover, the integrand is dominated pointwise by

$$|(\boldsymbol{m}, \boldsymbol{v}_k)_2| \leq |\boldsymbol{m}|_2 \, \|\boldsymbol{v}\|_{\boldsymbol{L}^\infty(\Gamma;\mathcal{T}\Gamma)} \in L^2(\Gamma).$$

Thus by Lebesgue's dominated convergence theorem we obtain

$$\lim_{k\to\infty} \int_\Gamma (\boldsymbol{m}, \boldsymbol{v}_k)_2 \,\mathrm{d}\boldsymbol{s} = \int_M (\boldsymbol{m}, \boldsymbol{v})_2 \,\mathrm{d}\boldsymbol{s}.$$

We now address the first term in (2.34). Since it is not clear whether or not $\nabla\ell(\boldsymbol{p})$ belongs to $\boldsymbol{L}^2(\Gamma;\mathcal{T}\Gamma)$, we cannot argue by dominated convergence. Instead, let us define

$$\begin{aligned} \Gamma^+ &:= \{\boldsymbol{s} \in \Gamma : (\boldsymbol{p}(\boldsymbol{s}), \boldsymbol{v}(\boldsymbol{s}))_2 \geq 0\} \\ \Gamma^- &:= \Gamma \setminus \Gamma^+. \end{aligned}$$

Then

$$\chi_{\Gamma^+}\big(\nabla\ell(\boldsymbol{p}),\, \boldsymbol{v}_k\big)_2 = \begin{cases} 2\,\mu\,\frac{(\boldsymbol{p},\boldsymbol{v})_2}{\beta^2-|\boldsymbol{p}|_2^2} \geq 0 & \text{on } \Gamma^+ \cap M_{1/k} \\ 0 & \text{elsewhere} \end{cases}$$

and therefore $\{\chi_{\Gamma^+}\big(\nabla\ell(\boldsymbol{p}),\, \boldsymbol{v}_k\big)_2\}_{k\in\mathbb{N}}$ is non-negative and monotone increasing on Γ^+ with pointwise limit $\chi_{\Gamma^+\cap M}\big(\nabla\ell(\boldsymbol{p}),\, \boldsymbol{v}\big)_2$. By the monotone convergence theorem,

$$\lim_{k\to\infty}\int_{\Gamma^+}\big(\nabla\ell(\boldsymbol{p}),\, \boldsymbol{v}_k\big)_2\,\mathrm{d}\boldsymbol{s} = \int_{\Gamma^+\cap M}\big(\nabla\ell(\boldsymbol{p}),\, \boldsymbol{v}\big)_2\,\mathrm{d}\boldsymbol{s}$$

holds. Similarly, this result can be shown with Γ^- as well. We can therefore pass to the limit in (2.34) and conclude (2.32), which in turn proves $\boldsymbol{m} = \nabla\ell(\boldsymbol{p})$ as well as $\nabla\ell(\boldsymbol{p}) \in \boldsymbol{L}^2(\Gamma;\mathcal{T}\Gamma)$.
Part C: If $b(\boldsymbol{p}) = \infty$, then by definition $\partial b(\boldsymbol{p}) = \emptyset$ holds.
The result now follows easily by combining Parts A–C. □

So far we have considered the subdifferential of the barrier term b w.r.t. the $\boldsymbol{L}^2(\Gamma;\mathcal{T}\Gamma)$ topology. This is however not sufficient since problem (2.24) is posed in $\boldsymbol{H}(\mathrm{div};\Gamma)$ and further modifications of the arguments in [143] are required. Let us define by $\widetilde{b}$ the restriction of b to $\boldsymbol{H}(\mathrm{div};\Gamma)$, and let

$$\partial\widetilde{b}(\boldsymbol{p}) := \Big\{\widetilde{\boldsymbol{m}} \in \boldsymbol{H}(\mathrm{div};\Gamma) : \widetilde{b}(\boldsymbol{q}) \geq \widetilde{b}(\boldsymbol{p}) + (\widetilde{\boldsymbol{m}},\, \boldsymbol{q}-\boldsymbol{p})_{\boldsymbol{H}(\mathrm{div};\Gamma)} \quad \forall \boldsymbol{q} \in \boldsymbol{H}(\mathrm{div};\Gamma)\Big\} \tag{2.35}$$

denote the subdifferential of $\widetilde{b}$ at $\boldsymbol{p} \in \boldsymbol{H}(\mathrm{div};\Gamma)$. Finally,

$$\Pi : \boldsymbol{L}^2(\Gamma;\mathcal{T}\Gamma) \to \boldsymbol{H}(\mathrm{div};\Gamma)$$

denotes the $\boldsymbol{H}(\mathrm{div};\Gamma)$-orthogonal projector, defined by

$$\widetilde{\boldsymbol{m}} = \Pi\,\boldsymbol{m} \quad \Leftrightarrow \quad (\widetilde{\boldsymbol{m}},\, \boldsymbol{z})_{\boldsymbol{H}(\mathrm{div};\Gamma)} = (\boldsymbol{m},\, \boldsymbol{z})_{\boldsymbol{L}^2(\Gamma;\mathcal{T}\Gamma)} \quad \forall \boldsymbol{z} \in \boldsymbol{H}(\mathrm{div};\Gamma).$$

Corollary 2.18. *Let $\boldsymbol{p} \in \boldsymbol{H}(\mathrm{div};\Gamma)$ be given. Then we have $\partial\widetilde{b}(\boldsymbol{p}) = \Pi\,\partial b(\boldsymbol{p})$ and consequently:*

(i) If $\nabla\ell(\boldsymbol{p})$ belongs to $\boldsymbol{L}^2(\Gamma;\mathcal{T}\Gamma)$, then $\partial\widetilde{b}(\boldsymbol{p}) = \{\Pi\,\nabla\ell(\boldsymbol{p})\}$.

(ii) If $\nabla\ell(\boldsymbol{p})$ does not belong to $\boldsymbol{L}^2(\Gamma;\mathcal{T}\Gamma)$, then $\partial\widetilde{b}(\boldsymbol{p}) = \emptyset$.

Proof. Let

$$\Lambda : \boldsymbol{H}(\mathrm{div};\Gamma) \to \boldsymbol{L}^2(\Gamma;\mathcal{T}\Gamma)$$

denote the continuous embedding, and let

$$\Lambda^* : \boldsymbol{L}^2(\Gamma;\mathcal{T}\Gamma)^* \to \boldsymbol{H}(\mathrm{div};\Gamma)^*$$

denote its adjoint. Since by definition $\widetilde{b}(\boldsymbol{p}) = b(\Lambda\boldsymbol{p})$ and $\Lambda\boldsymbol{p} = \boldsymbol{p}$ holds for all $\boldsymbol{p} \in \boldsymbol{H}(\mathrm{div};\Gamma)$, we conclude from the chain rule that

$$\begin{aligned}\mathcal{R}_{\boldsymbol{H}(\mathrm{div};\Gamma)}\partial\widetilde{b}(\boldsymbol{p}) &= \Lambda^*\mathcal{R}_{\boldsymbol{L}^2(\Gamma;\mathcal{T}\Gamma)}\partial b(\Lambda\boldsymbol{p}) \\ &= \Lambda^*\mathcal{R}_{\boldsymbol{L}^2(\Gamma;\mathcal{T}\Gamma)}\partial b(\boldsymbol{p})\end{aligned}$$

holds; see for instance [73, Prop. I.5.7]. Notice that the Riesz maps

$$\mathcal{R}_{\boldsymbol{H}(\mathrm{div};\Gamma)} : \boldsymbol{H}(\mathrm{div};\Gamma) \to \boldsymbol{H}(\mathrm{div};\Gamma)^*$$

and

$$\mathcal{R}_{\boldsymbol{L}^2(\Gamma;\mathcal{T}\Gamma)} : \boldsymbol{L}^2(\Gamma;\mathcal{T}\Gamma) \to \boldsymbol{L}^2(\Gamma;\mathcal{T}\Gamma)^*$$

are present here since we identify the subdifferential in both Hilbert spaces with elements from the Hilbert space itself, see (2.35). We have thus shown that

$$\partial\widetilde{b}(\boldsymbol{p}) = \mathcal{R}^{-1}_{\boldsymbol{H}(\mathrm{div};\Gamma)}\Lambda^*\mathcal{R}_{\boldsymbol{L}^2(\Gamma;\mathcal{T}\Gamma)}\partial b(\boldsymbol{p})$$

holds for all $\boldsymbol{p} \in \boldsymbol{H}(\mathrm{div};\Gamma)$. It is now an easy exercise to verify that

$$\mathcal{R}^{-1}_{\boldsymbol{H}(\mathrm{div};\Gamma)}\Lambda^*\mathcal{R}_{\boldsymbol{L}^2(\Gamma;\mathcal{T}\Gamma)} = \Pi$$

. □

Now we can state the proof of Theorem 2.15.

Proof of Theorem 2.15. Recall from (2.25) the definition of H and b and let us denote, as above, by $\widetilde{b}$ the restriction of b to $\boldsymbol{H}(\mathrm{div};\Gamma)$. The (unique) minimizer of (2.24) is characterized by

$$0 \in \partial\big(H(\boldsymbol{p}) + \widetilde{b}(\boldsymbol{p})\big). \tag{2.36}$$

The function H is convex and continuous on all of $\boldsymbol{H}(\mathrm{div};\Gamma)$. Moreover, recall from the proof of Proposition 2.14 that b is convex and weakly sequentially lower semicontinuous w.r.t. $\boldsymbol{L}^2(\Gamma;\mathcal{T}\Gamma)$, and thus $\widetilde{b}$ has the same property w.r.t. $\boldsymbol{H}(\mathrm{div};\Gamma)$. In addition, $\widetilde{b}$ is finite e.g., at $\boldsymbol{p} \equiv \boldsymbol{0}$. Therefore (2.36) is equivalent to

$$0 \in \partial H(\boldsymbol{p}) + \partial\widetilde{b}(\boldsymbol{p})$$

by the sum rule of subdifferentials; see for instance [73, Prop. I.5.6]. Notice that this also implies $|\boldsymbol{p}|_2 \leq \beta$ a.e. on Γ since otherwise $\widetilde{b}(\boldsymbol{p}) = \infty$ and the subdifferential is empty. Having characterized $\partial\widetilde{b}(\boldsymbol{p})$ in Corollary 2.18 and using the obvious Fréchet differentiability of H, we can write equivalently (using the notation from Corollary 2.18)

$$\begin{aligned}
& 0 = \mathcal{R}^{-1}_{\boldsymbol{H}(\mathrm{div};\Gamma)}H'(\boldsymbol{p}) + \Pi\,\nabla\ell(\boldsymbol{p}) \\
\Leftrightarrow\quad & 0 = \mathcal{R}^{-1}_{\boldsymbol{H}(\mathrm{div};\Gamma)}H'(\boldsymbol{p}) + \mathcal{R}^{-1}_{\boldsymbol{H}(\mathrm{div};\Gamma)}\Lambda^*\mathcal{R}_{\boldsymbol{L}^2(\Gamma;\mathcal{T}\Gamma)}\nabla\ell(\boldsymbol{p}) \\
\Leftrightarrow\quad & 0 = H'(\boldsymbol{p})\,\delta\boldsymbol{p} + \langle\Lambda^*\mathcal{R}_{\boldsymbol{L}^2(\Gamma;\mathcal{T}\Gamma)}\nabla\ell(\boldsymbol{p}),\,\delta\boldsymbol{p}\rangle_{\boldsymbol{H}(\mathrm{div};\Gamma)^*,\boldsymbol{H}(\mathrm{div};\Gamma)} \quad \forall\delta\boldsymbol{p} \in \boldsymbol{H}(\mathrm{div};\Gamma) \\
\Leftrightarrow\quad & 0 = H'(\boldsymbol{p})\,\delta\boldsymbol{p} + \langle\mathcal{R}_{\boldsymbol{L}^2(\Gamma;\mathcal{T}\Gamma)}\nabla\ell(\boldsymbol{p}),\,\Lambda\delta\boldsymbol{p}\rangle_{\boldsymbol{L}^2(\Gamma;\mathcal{T}\Gamma)^*,\boldsymbol{L}^2(\Gamma;\mathcal{T}\Gamma)} \quad \forall\delta\boldsymbol{p} \in \boldsymbol{H}(\mathrm{div};\Gamma) \\
\Leftrightarrow\quad & 0 = H'(\boldsymbol{p})\,\delta\boldsymbol{p} + (\nabla\ell(\boldsymbol{p}),\,\Lambda\delta\boldsymbol{p})_{\boldsymbol{L}^2(\Gamma;\mathcal{T}\Gamma)} \quad \forall\delta\boldsymbol{p} \in \boldsymbol{H}(\mathrm{div};\Gamma).
\end{aligned}$$

This is precisely (2.30). □

2.3.2 Implementation Details

All numerical studies are based on two different geometries obtained by scanning physical objects with the Artec Eva 3D scanner. The scanner software provides Wavefront .obj files, which contain a description of the geometry via vertices and triangles. In both examples the surface of the scanned object is closed, i.e., without boundary, in accordance with our analysis. The surface texture is provided by the scanner software as a 2D flat bitmap file, see Figure 2.1, together with a mapping of each physical surface triangle into said bitmap. Thus, originally the textured object is described by a varying number of pixels glued onto each surface triangle. Due to the impossibility of continuously mapping a closed surface onto the flat bitmap, there are necessarily discontinuities in the bitmap and there may also be regions which do not appear on the physical surface. Essentially, two adjacent triangles on the surface can be part of discontinuous regions in the texture file. This data is shown in Figure 2.1 for our first test case.

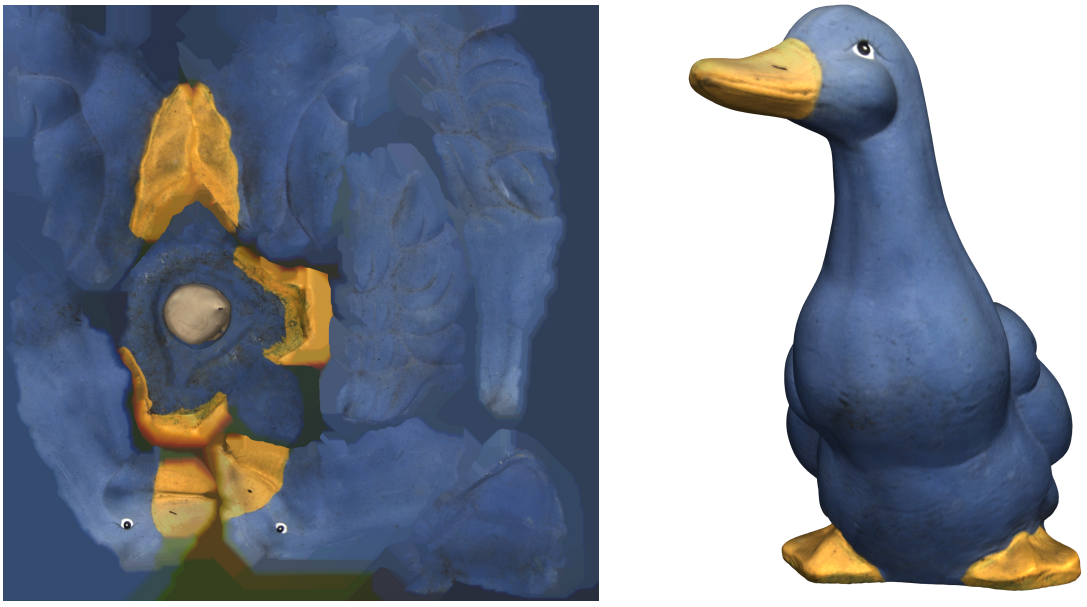

Figure 2.1: Left: Texture bitmap as delivered by the scanner software. Right: Texture mapped onto the geometry.

In order to apply our novel solution scheme, the above mentioned Wavefront object including the texture needs to be made available to the finite element library which is used to discretize the predual barrier problems (2.24). One way of achieving this is to provide the texture data f at each quadrature point. However, for ease of implementation and processing within the finite element framework FEniCS [4], we instead converted the textured object into the finite element setting by interpolation. To account for both natural discontinuities in the texture as well as the discontinuity of the surface-to-texture mapping, we chose a discontinuous Lagrange (DG) finite element representation of the texture data f. To be more precise, let $\mathcal{P}_r$ define the space of polynomials of maximum degree r, then the texture f and the final output u of our scheme are to fulfill $f_{|K}, u_{|K} \in \mathcal{P}_r$ for all triangles K of the scanned surface. Thus, u and f are elements of the $\mathcal{DG}_r$ finite element space on the surface. The image data f is always scaled to the interval $[0, 1]$.

To carry out the texture preprocessing, we compute the spatial location for each degree of freedom of the surface DG function f within the texture bitmap and use the respective gray value at the nearest pixel. For color textures, this is realized via a vector valued DG function on the surfaces with values in the RGB color space. In the original Wavefront object each surface triangle usually obtains data from multiple texture pixels. Thus, in order to maintain an appropriate quality of the texture in the DG setting, higher order finite element spaces are needed, depending on the quality of the scan. Although in the original Wavefront object the number of pixels per triangle may vary significantly, we use a constant finite element order $r = 2$ or $r = 3$ in our examples.

2.3.3 Discretization of the Predual Variable

Before recovering the image u we determine the predual (edge detector) vector field $\boldsymbol{p} \in \boldsymbol{H}(\mathrm{div};\Gamma)$ via a sequence of barrier problems (2.24). For the latter we employ a conforming discretization by surface Raviart–Thomas (RT) finite elements. Although this choice of discretization is natural from the analytical point of view, RT elements seem to be rarely used in the context of image processing; see, however, [14, 68]. We therefore provide details in this section, focusing first on flat domains and later on general orientable surfaces. Notice that a discretization by continuous Lagrangian elements as in [108] would also be conforming but it does not exhaust the space $\boldsymbol{H}(\mathrm{div};\Gamma)$ under mesh refinement. By contrast, only functions in the closed subspace of H^1 vector fields can be approximated.

The Raviart–Thomas element space $\mathcal{RT}_{r+1}$ ($r \geq 0$) on a triangle T is designed to be the smallest vector valued polynomial space with

$$[\mathcal{P}_r]^2 \subset \mathcal{RT}_{r+1|T} \subset [\mathcal{P}_{r+1}]^2$$

such that the divergence maps *onto* $\mathcal{P}_r$; see [133], [76, Chapter 1.4.7] or [4, Ch. 3.4.1]. In more explicit terms, the polynomial space for the $\mathcal{RT}_{r+1}$ FE over a flat triangle T is given by

$$[\mathcal{P}_r]^2 + \boldsymbol{x}\mathcal{P}_r,$$

where $\boldsymbol{x} \in \mathbb{R}^2$ denotes the spatial coordinate. The dimension of this space is

$$(r+1)(r+3) = 3, 8, 15, 24, \ldots$$

In order to obtain an $\boldsymbol{H}(\mathrm{div})$-conforming approximation, continuity of the normal component across all inter-element edges E must be ensured. Let us consider a triangulated flat domain $\Omega \subset \mathbb{R}^2$ endowed with a conforming simplicial triangulation, i.e., any two intersecting triangles intersect either in a common vertex or a common edge. Then the global $\mathcal{RT}_{r+1}$ space on Ω is defined as

$$\big\{\boldsymbol{p} \in [L^1(\Omega)]^2 : \boldsymbol{p}_{|T} \in \mathcal{RT}_{r+1|T} \text{ for all triangles } T, \\ [\![\boldsymbol{p} \cdot \boldsymbol{n}]\!]_E = 0 \text{ for all interior edges } E\big\}.$$

Here $[\![\boldsymbol{p} \cdot \boldsymbol{n}]\!]_E = \boldsymbol{p}_{|T_1} \cdot \boldsymbol{n}_1 + \boldsymbol{p}_{|T_2} \cdot \boldsymbol{n}_2$ denotes the jump of $\boldsymbol{p} \cdot \boldsymbol{n}$ across the edge E between elements T_1 and T_2 with edge normals $\boldsymbol{n}_1$ and $\boldsymbol{n}_2$, respectively. Continuity of the normal components, i.e., $[\![\boldsymbol{p} \cdot \boldsymbol{n}]\!]_E = 0$, is conveniently achieved by observing that the restriction

$(\boldsymbol{p}\cdot\boldsymbol{n})_{|E}$ of any $\boldsymbol{p}\in\mathcal{RT}_{r+1|T}$ to an edge E is a scalar polynomial of degree r in a single variable. $(\boldsymbol{p}\cdot\boldsymbol{n})_{|E}$ is therefore determined by $r+1$ point values along the edge, and the continuity of $\boldsymbol{p}\cdot\boldsymbol{n}$ across E amounts to a coincidence of the degrees of freedom (up to sign) on neighboring triangles. The remaining

$$(r+1)(r+3)-3\,(r+1)=r\,(r+1)$$

degrees of freedom on each triangle are defined as evaluations of $\boldsymbol{p}$ at points inside the triangle.[2] In practical computations, each element $T\subset\mathbb{R}^2$ is obtained as an affine copy of a reference cell $T_0\subset\mathbb{R}^2$ via the affine map $F:T_0\to T$. Local basis functions must be mapped via the associated contravariant Piola transformation in order to preserve normal traces; see [137] for details.

The transition from the $\mathcal{RT}_{r+1}$ space over a flat domain $\Omega\subset\mathbb{R}^2$ to one over a two-dimensional surface Γ is conceptionally straightforward by allowing F to be an affine map of rank 2 from T_0 to a surface triangle $T\subset\Gamma\subset\mathbb{R}^3$. We refer the reader to [136] for details. A similar construction has been described in [108] for the case of linear continuous Lagrange elements, which do not require the Piola transform but which are not dense in $\boldsymbol{H}(\mathrm{div};\Gamma)$. For the purpose of illustration, Figure 2.2 depicts a number of typical basis functions from the lowest-order space $\mathcal{RT}_1$ ($r=0$) on a flat and spherical mesh.

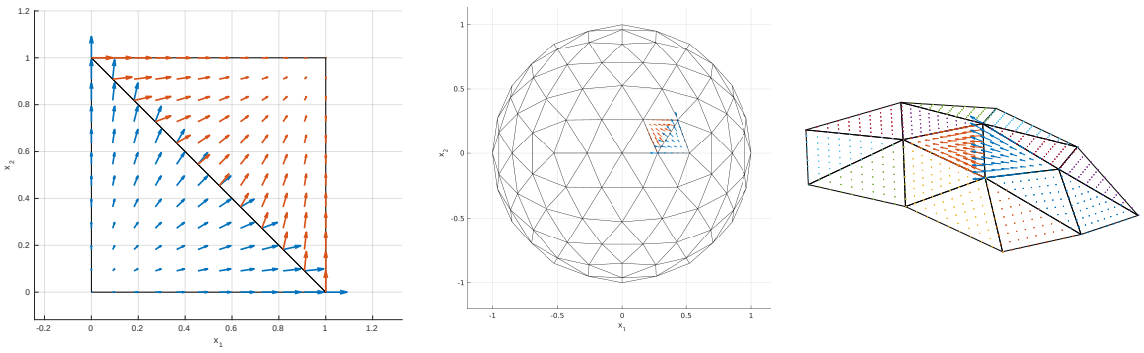

Figure 2.2: Left: global basis function $\boldsymbol{p}$ from $\mathcal{RT}_1$ associated with the degree of freedom located on the edge E adjacent to both triangles in $\mathbb{R}^2$. One clearly sees that $(\boldsymbol{p}\cdot\boldsymbol{n})_{|E}$ is constant, i.e., of degree $r=0$, and continuous, i.e., $[\![\boldsymbol{p}\cdot\boldsymbol{n}]\!]_E=0$ holds. On all other edges we have $\boldsymbol{p}\cdot\boldsymbol{n}=0$. Middle: the same situation on a spherical mesh of topological dimension 2 in $\mathbb{R}^3$. Right: detail.

Recovery of the Image

The last step is to recover the image u from $\boldsymbol{p}$. As proved in Theorem 2.13 we have the relation

$$u=B^{-1}(\mathrm{div}\,\boldsymbol{p}+K^*f). \tag{2.37}$$

[2] Integral moments of $\boldsymbol{p}$ over the edges and triangles are sometimes used as degrees of freedom, in place of point evaluations. This does not change the space $\mathcal{RT}_{r+1}$ but only its representation in terms of global basis functions.

In our examples, which demonstrate denoising and inpainting, K, K^* and therefore

$$B = \alpha\,\mathrm{id} + K^*K$$

are all pointwise operations, which do not involve differentiation. We therefore choose matching polynomial degrees, i.e., $u \in \mathcal{DG}_r$, $\boldsymbol{p} \in \mathcal{RT}_{r+1}$ and $f \in \mathcal{DG}_r$. In terms of finite element functions, (2.37) is realized by solving an orthogonal projection problem in $L^2(\Gamma)$, which is represented by a block-diagonal mass matrix in $\mathcal{DG}_r$ and therefore inexpensive to solve.

2.4 Numerical Results

2.4.1 Gray-Scale Denoising

In this section we consider the classical denoising problem with $K = \mathrm{id}$. The initial test case is the scanned terracotta duck from Figure 2.1 but with the texture data converted to a gray scale. Recall that our image data is scaled to a range $[0, 1]$. The geometry consists of 354 330 triangles and 177 167 vertices. The surface texture is mostly uniform, however there are some details around the eye and a second order DG function ($r = 2$) manages to resolve these quite well. Also there are sharp interfaces between body, beak and feet. As such, this object provides an excellent first test case and we expect that these interfaces are preserved by the total variation approach.

We added artificial noise based on a normal distribution with standard deviation $\sigma = 0.1$ and zero mean to each entry in the coefficient vector representing the image data f. For this and the subsequent color denoising problem described in the following subsection, the value $\alpha = 0.0$ is used and we consider only variations in β. Notice that B in (2.15) is boundedly invertible even for $\alpha = 0$ since $K = \mathrm{id}$ holds.

The denoising results shown in Figure 2.3 were obtained by a rather basic yet effective interior point approach, in which a sequence of barrier approximations (2.24) to the pre-dual problem (2.16) are solved. Each instance of (2.24) is solved by applying Newton's method to the optimality system (2.30); see Algorithm 1. Based on numerical experience and the progress observed in the image u recovered from (2.37), we used $\mu_{\text{start}} = 1.0$, $\mu_{\text{end}} = 0.02$ and $N_{\max} = 8$ in our study. The adjustment of the barrier parameter μ is based on a simple backtracking strategy, depending on the number of Newton iterations necessary to reach the termination criterion $\|\delta\boldsymbol{p}\|_{\boldsymbol{L}^2(\Gamma;T(\Gamma))} \leq 10^{-5}$. Here $\delta\boldsymbol{p}$ denotes the update calculated in each Newton step.

For both $\beta = 0.1$ and $\beta = 0.3$ the terminal value for μ was reached after 4 reductions, necessitating the solution of 5 instances of problem Equation (2.24) with a Newton scheme. As shown in Figure 2.4 each of these required between 3 and 5 Newton steps and this behavior is typical for primal interior point methods. The total wall-clock time on four non-hyper threaded cores of an Intel i5-4690 CPU running at 3.50 Ghz was slightly less than 40 minutes. Comparing the results shown in Figure 2.3 one can see that—as expected—with increasing values of β, the noise is reduced more effectively and although the object looks progressively smoother due to a reduction in contrast, sharp corners are preserved. The convergence plots for different values of β are also shown in Figure 2.4. We expect that the efficiency can be improved and the number of Newton steps reduced by employing a primal-dual interior point method. This is left to future research.

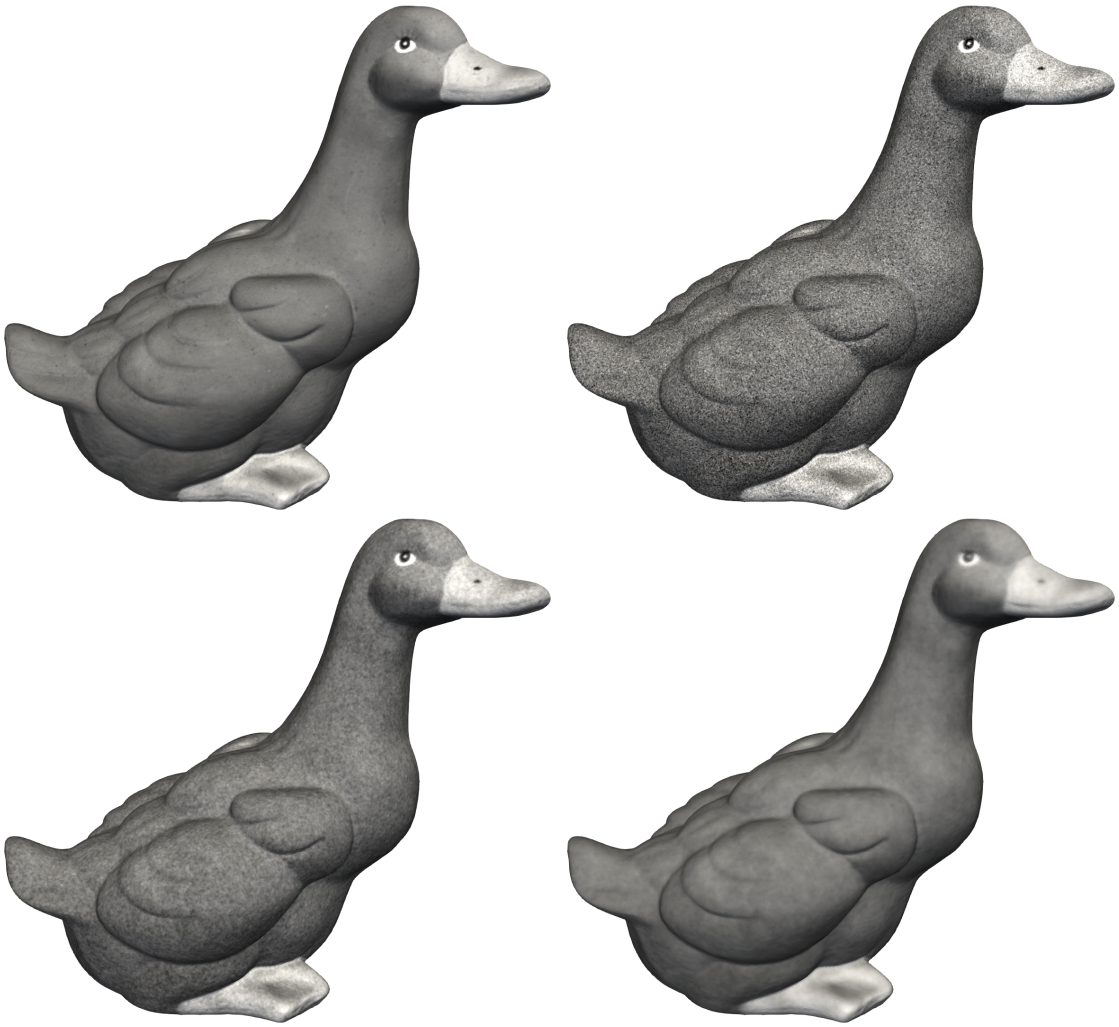

Figure 2.3: Duck test case: noise free and noisy originals (top row) and denoising results for $\beta = 0.1$ and $\beta = 0.3$ (bottom row). The object was kindly scanned by the Rechenzentrum of Würzburg University.

2.4.2 Color Denoising

The second test case consists of a scanned shoe, whose data is provided by the Artec Group Inc.[3] under the Creative Commons Attribution 3.0 Unported License. The shoe consists of exactly 100 000 triangles and 50 002 vertices. It provides an excellent second test case because of discontinuous color changes given by the stripes, while at the same time there are also very fine features on the sole and a leathery texture on the outside. Noise is added in the same way to each of the RGB channels as described for the gray-scale test case above. In this example we chose to represent the color texture in terms of a vector valued discontinuous Galerkin function of order $r = 3$. This amounts to problems with 1.8 million degrees of freedom for the predual variable $\boldsymbol{p}$ associated with a single color channel.
The denoising procedure was conducted individually per RGB channel. Initial, noisy

[3] `https://www.artec3d.com`

Algorithm 1 Basic interior point method

Set $\mu := \mu_{\text{start}}$, $d_\mu := 0.6$, $\boldsymbol{p} := \mathbf{0}$
while $\mu > \mu_{\text{end}}$ **do**
  repeat
    Perform at most $N_{\max}$ steps of Newton's method to solve (2.30) for $\boldsymbol{p}_{\text{new}}$, given the current value of μ, starting from initial guess $\boldsymbol{p}$
    $s \leftarrow$ number of Newton iterations
    $\mu := 1.2\,\mu$, $d_\mu := \min\{0.9,\ 1.2\,d_\mu\}$
  until Newton's method did converge in $N_{\max}$ steps
  $\boldsymbol{p} := \boldsymbol{p}_{\text{new}}$ (accept new approximation)
  if $4 < s$ **then**
    $d_\mu := 1.1\,d_\mu$
  else
    $d_\mu := 0.9\,d_\mu$
  end if
  $\mu := d_\mu\,\mu$ (adapt μ for next instance of (2.30))
end while

and denoised objects are shown in Figure 2.5. The sharp edges between the stripes are preserved for different values of β. Details of the leather's structure, most prominently visible in the yellow stripes in the noise-free image, start reappearing after the bulk of the noise is removed for $\beta = 0.5$. Notice however that some of these features are part of the geometric resolution and not just the texture. On the other hand, the dotted texture in the interior and part of the stitchings seem less discernible due to the reduced contrast for $\beta = 0.5$. As was noted earlier, the predual vector field $\boldsymbol{p}$ can be interpreted as an edge detector, which is shown in Figure 2.6 for each RGB channel.
We also conducted experiments using the *joint* BV-norm, cf. [31]

$$\int_\Gamma |\nabla \boldsymbol{u}| = \sup\left\{ \int_\Gamma \sum_{j=1}^{3} u^j \operatorname{div} \boldsymbol{p}^j \,\mathrm{d}\boldsymbol{s} : \boldsymbol{p} \in \boldsymbol{W} \right\}$$

of the vector-valued unknown $\boldsymbol{u} = (u^1, u^2, u^3) \in [BV(\Gamma)]^3$. In contrast to the scalar case the test space is now defined as

$$\boldsymbol{W} := \left\{ (\boldsymbol{p}^1, \boldsymbol{p}^2, \boldsymbol{p}^3) \in [C^\infty(\Gamma; \mathcal{T}\Gamma)]^3 : \sum_{j=1}^{3} \left| \boldsymbol{p}^j(\boldsymbol{s}) \right|_2^2 \le 1 \quad \forall \boldsymbol{s} \in \Gamma \right\},$$

compare [37, 72]. It can be expected that this modification better suppresses color fringes (similar to chromatic aberration), which occur when the value of two or more color channels have jump discontinuities at neighboring pixels. We refer the reader to [36, Chapter 6.3.4] for a discussion of alternative definitions of vector-valued BV norms in the context of color image restoration.
Use of the joint BV norm leads to the following modified predual problem compared to

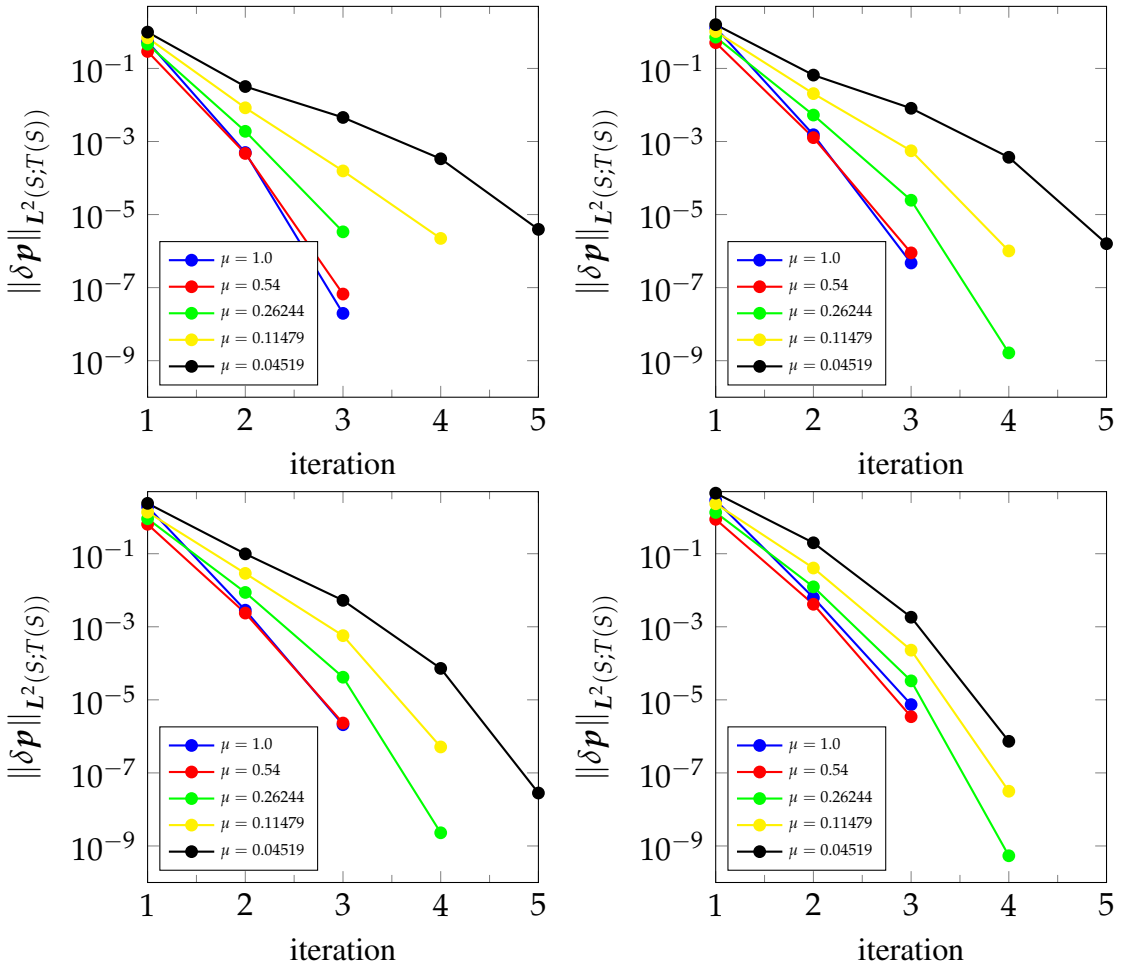

Figure 2.4: Convergence of the inner (Newton) and outer iterations of the interior point method (Algorithm 1) for the duck denoising example. Different colors denote outer iterations and their decreasing barrier parameter μ with a stopping criterion of $\|\delta \boldsymbol{p}\|_{L^2(S;T(S))} \leq 10^{-5}$ for Newton's method. Different subplots for respective denoising parameters $\beta = 0.1, 0.2, 0.3, 0.5$.

(2.16),

$$\begin{cases} \text{Minimize} & \dfrac{1}{2}\left\| \begin{pmatrix} \operatorname{div} \boldsymbol{p}^1 \\ \operatorname{div} \boldsymbol{p}^2 \\ \operatorname{div} \boldsymbol{p}^3 \end{pmatrix} + K^* \boldsymbol{f} \right\|^2_{B^{-1}} \\ \text{over} & (\boldsymbol{p}^1, \boldsymbol{p}^2, \boldsymbol{p}^3) \in [\boldsymbol{H}(\operatorname{div}; \Gamma)]^3 \\ \text{subject to} & \displaystyle\sum_{j=1}^{3} \left|\boldsymbol{p}^j\right|_2^2 \leq \beta^2 \quad \text{a.e. on } \Gamma, \end{cases}$$

see also [37]. Notice that the variables $\boldsymbol{p}^j$ in this problem are *coupled* through the inequality constraints even if — as is the case in our examples — K and K^* act on each color component separately. This leads to an increased complexity of the problem. The conversion of the inequality constraints into a barrier term as in (2.24) is straightforward.

Figure 2.5: Shoe test case: noise free and noisy originals (top row) and denoising results for $\beta = 0.2$ and $\beta = 0.5$ (bottom row).

Figure 2.6: Shoe test case: $|\boldsymbol{p}|_2$ acts as an edge detector for each RGB channel. Solid black corresponds to a value of $|\boldsymbol{p}|_2 \geq 0.4$. Final results for $\beta = 0.5$ are shown. Take note of the different jump amplitudes and positions for each color channel.

In our numerical experiments, we did not experience significantly improved results using this model and therefore do not pursue this further here.

2.4.3 Color Inpainting

The problem of not being able to scan an object completely is quite common, as there might be areas the scanner cannot look into due to its size and the non-convexity and curvature of the object. The inside of the tip of a shoe might be such an example. Data corruption can be another reason for lack or loss of data. Although these issue concern both geometry and texture, the focus of this subsection is on the reconstruction of missing texture information alone.
We simulate the loss of texture data during the scan process on the *outside* of an object by setting to zero all degrees of freedom in the image data which belong to cells with indices in the range 30 000 to 33 000. This corresponds to a data loss of 3%. We denote this erased image region by $\Gamma_0 \subset \Gamma$. Due to the apparently layered scan process the index range chosen corresponds to bands or "stripes" as shown in Figure 2.7, which are better visible than unreachable areas inside the tip.
As usual for TV inpainting problems the mapping K is now chosen so as to ignore the corrupted data. This leads to

$$(Ku)(\boldsymbol{s}) := \chi_{\Gamma\setminus\Gamma_0}(\boldsymbol{s})\, u(\boldsymbol{s}), \tag{2.38}$$

where χ is an indicator function with value 1 in the uncorrupted area $\Gamma \setminus \Gamma_0$. Since K is self-adjoint and idempotent,

$$K^*(Ku) = K(Ku) = Ku.$$

$(Ku)(\boldsymbol{s}) - f(\boldsymbol{s}) = 0$ holds for all $\boldsymbol{s} \in \Gamma_0$ and the (corrupted) value of $f_{|\Gamma_0}$ does not increase the data fidelity part of the objective in Equation (2.1).

Figure 2.7: Shoe with missing texture (top left) and TV-inpainting solutions for $\beta = 0.5$, $\beta = 0.7$ and $\beta = 1.0$.

Contrary to the denoising situation, K^*K is no longer invertible and $\alpha > 0$ is required. Using the definition of K one easily deduces the formula

$$(B\,u)(\boldsymbol{s}) = \begin{cases} \alpha\, u(\boldsymbol{s}) & \text{for } \boldsymbol{s} \in \Gamma_0 \\ (\alpha+1)\, u(\boldsymbol{s}) & \text{for } \boldsymbol{s} \in \Gamma \setminus \Gamma_0. \end{cases}$$

The results of the inpainting test case are shown in Figure 2.7 for different values of β and with $\alpha = 0.1$ constant for each case.

CHAPTER 3

DISCRETE TOTAL VARIATION WITH FINITE ELEMENTS

The total-variation (TV)-seminorm $|\cdot|_{TV}$ is ubiquitous as a regularizing functional in image analysis and related applications; see for instance [45, 50, 77, 139]. When $\Gamma \subset \mathbb{R}^3$ is a smooth surface, which is also compact and connected, this seminorm is defined as in (2.7). It has been observed in [60] that "the rigorous definition of the TV for discrete images has received little attention." In this chapter, which is based on [97], but extends it to surfaces, we go one step further by proposing and analyzing a discrete analogue of (2.7) for functions u belonging to a space $\mathcal{DG}_r(\Gamma_h)$ or $\mathcal{CG}_r(\Gamma_h)$ of globally discontinuous or continuous finite element functions of polynomial degree[1] $0 \leq r \leq 4$ on a geometrically conforming, simplicial triangulation of Γ, consisting of triangles T and interior edges E. In this case, it is not hard to see that the TV-seminorm (2.7) can be evaluated as

$$|u|_{TV(\Gamma_h)} = \sum_T \int_T |\nabla u|_2 \, \mathrm{d}\boldsymbol{s} + \sum_E \int_E \left| u_E^- - u_E^+ \right| \mathrm{d}\boldsymbol{s}, \tag{3.1}$$

where $\left| u_E^- - u_E^+ \right|$ denotes the absolute value of the jump of a function across an edge of the triangulation.

It is intuitively clear that when u is confined to a finite element space such as $\mathcal{DG}_r(\Gamma_h)$ or $\mathcal{CG}_r(\Gamma_h)$, then it ought to be sufficient to consider the supremum in (2.7) over all vector fields $\boldsymbol{p}$ from an appropriate finite dimensional space as well. Indeed, we show that this is the case, provided that the TV-seminorm (3.1) is replaced by its discrete analogue

$$|u|_{DTV(\Gamma_h)} := \sum_T \int_T \mathcal{I}_T \left\{ |\nabla u|_2 \right\} \mathrm{d}\boldsymbol{s} + \sum_E \int_E \mathcal{I}_E \left\{ \left| u_E^- - u_E^+ \right| \right\} \mathrm{d}\boldsymbol{s}, \tag{3.2}$$

which we term the *discrete TV-seminorm*. Here $\mathcal{I}_T$ and $\mathcal{I}_E$ are local interpolation operators into the polynomial spaces $\mathcal{P}_{r-1}(T)$ and $\mathcal{P}_r(E)$, respectively. Therefore, (3.2) amounts to the application of a nodal quadrature formula for the integrals appearing in (3.1). In the lowest-order case ($r = 0$) of piecewise constant functions, the first sum in (3.2) is zero and only edge contributions appear. Moreover, in this case (3.1) and (3.2) coincide since $\left| u_E^- - u_E^+ \right|$ is constant on edges. In general, we will show that the difference between (3.1) and (3.2) is of the order of the mesh size, see Proposition 3.4.

[1] It will become clear in Section 3.2 why the discussion is restricted to polynomial degrees at most 4.

Using (3.2) in place of (3.1) in optimization problems in imaging offers a number of significant advantages. Specifically, we will show in Theorem 3.2 that (3.2) has a discrete dual representation

$$|u|_{DTV(\Gamma_h)} = \max \left\{ \int_{\Gamma_h} u \operatorname{div} \boldsymbol{p} \, \mathrm{d}\boldsymbol{s} : \boldsymbol{p} \in \mathcal{RT}_{r+1}(\Gamma_h) \right. \\ \left. \text{s.t. a number of simple constraints} \right\} \tag{3.3}$$

for $u \in \mathcal{DG}_r(\Gamma_h)$, where $\mathcal{RT}_{r+1}(\Gamma_h)$ denotes the space of Raviart–Thomas finite element functions of order $r+1$. As a consequence of (3.3), we establish that optimization problems utilizing the discrete TV-seminorm (3.2) as a regularizer possess a discrete dual problem with very simple constraints.
This Chapter is structured as follows. We collect some background material on finite elements in Section 3.1. In Section 3.2 we establish the dual representation of the discrete TV-seminorm (3.2). We also derive an estimate of the error between (3.2) and (3.1). We present discrete TV-L^2 and TV-L^1 models along with their duals in Section 3.3. In Section 3.4 we show that a variety of well known algorithms for TV-L^2 image denoising and inpainting can be applied in our (possibly higher-order) finite element setting with little or no changes compared to their classical counterparts in the Cartesian finite difference domain. Further implementation details in the finite element framework FEniCS are given in this section. Afterwards, numerical results for TV-L^2 denoising and inpainting are presented in Section 3.5. In Section 3.6 we briefly also consider two methods for the TV-L^1 case. In Section 3.7 we comment on extensions such as Huber regularized variants of TV-L^2 and TV-L^1, as well as on the simplifications that apply when images belong to globally *continuous* finite element spaces $\mathcal{CG}_r(\Gamma_h)$.

3.1 Finite Element Spaces

Suppose that Γ_h is a triangulated discrete representation of a surface $\Gamma \subset \mathbb{R}^3$ by a geometrically conforming mesh (no hanging nodes) consisting of non-degenerate triangular cells T and edges E. For every edge E we refer with an upper index $+$ and $-$ on the two adjacent triangles T^+ and T^-, where the orientation is arbitrary, but connected to the definition of Raviart-Thomas degrees of freedom given in (3.7b). Also for a finite element function g, we denote with $g_E^{\pm}$ the restriction $g|_{T^{\pm}}$. Throughout, $r \geq 0$ denotes the degree of certain polynomials.

3.1.1 Lagrangian Finite Elements

Let $\mathcal{P}_r(T)$ denote the space of scalar, bivariate polynomials on T with total maximal degree r. The dimension of $\mathcal{P}_r(T)$ is $(r+1)(r+2)/2$. Let $\{\Phi_{T,k}\}$ denote the standard nodal basis of $\mathcal{P}_r(T)$ with associated Lagrange nodes $\{X_{T,k}\}$, $k = 1, \ldots, (r+1)(r+2)/2$. In other words, each $\Phi_{T,k}$ is a function in $\mathcal{P}_r(T)$ satisfying

$$\Phi_{T,k}(X_{T,k'}) = \delta_{kk'},$$

where $\delta_{kk'}$ is the Kronecker Delta. We denote by

$$\mathcal{DG}_r(\Gamma_h) \coloneqq \big\{u \in L^2(\Gamma_h) : u|_T \in \mathcal{P}_r(T)\big\}, \quad r \geq 0, \tag{3.4}$$

$$\mathcal{CG}_r(\Gamma_h) \coloneqq \big\{u \in C(\Gamma_h) : u|_T \in \mathcal{P}_r(T)\big\}, \quad r \geq 1, \tag{3.5}$$

the standard finite element spaces of globally discontinuous (L^2-conforming) or continuous (H^1-conforming) piecewise polynomials of degree r. A finite element function $u \in \mathcal{DG}_r(\Gamma_h)$ or $\mathcal{CG}_r(\Gamma_h)$, restricted to T, is represented by its coefficient vector w.r.t. the basis $\{\Phi_{T,k}\}$, which is simply given by point evaluations. We use the notation

$$u_{T,k} = u|_T(X_{T,k})$$

to denote the elements of the coefficient vector of a function $u \in \mathcal{DG}_r(\Gamma_h)$ or $\mathcal{CG}_r(\Gamma_h)$. Frequently, we will also work with the space $\mathcal{P}_{r-1}(T)$, whose standard nodal basis and Lagrange nodes we denote by $\{\varphi_{T,i}\}$ and $\{x_{T,i}\}$, $i = 1, \ldots, r\,(r+1)/2$. The interpolation operator into this space (used in the definition (3.2) of $|u|_{DTV(\Gamma_h)}$) is defined by

$$\mathcal{I}_T\{v\} \coloneqq \sum_{i=1}^{r\,(r+1)/2} v(x_{T,i})\,\varphi_{T,i}.$$

Similarly, $\mathcal{P}_r(E)$ denotes the space of univariate scalar polynomials on E of maximal degree r, which has dimension $r+1$. Let $\{\varphi_{E,j}\}$ denote the standard nodal basis of $\mathcal{P}_r(E)$ with associated Lagrange nodes $\{x_{E,j}\}$, $j = 1, \ldots, r+1$. The associated interpolation operator becomes

$$\mathcal{I}_E\{v\} \coloneqq \sum_{j=1}^{r+1} v(x_{E,j})\,\varphi_{E,j}.$$

3.1.2 Raviart–Thomas Finite Elements

For $r \geq 0$, we denote by

$$\begin{aligned}\mathcal{RT}_{r+1}(\Gamma_h) \coloneqq \big\{\boldsymbol{p} \in [L^1(\Gamma_h)]^2 : \boldsymbol{p}|_T \in \mathcal{P}_r(T)^3 + \boldsymbol{x}\,\mathcal{P}_r(T) \text{ for all triangles } T,\\ \boldsymbol{p}_E^+ \cdot \boldsymbol{\mu}_E^+ = -\boldsymbol{p}_E^- \cdot \boldsymbol{\mu}_E^- \text{ for all edges } E\big\}\end{aligned} \tag{3.6}$$

the ($\boldsymbol{H}(\mathrm{div})$-conforming) Raviart–Thomas finite element space of order $r+1$.[2] Here, we denote with $\boldsymbol{\mu}_E^{\pm}$ the co-normal of the triangle $T^{\pm}$ at edge E; see also Figure 5.2. Notice again that in order to obtain an $\boldsymbol{H}(\mathrm{div})$-conforming approximation, continuity of the co-normal component across all edges E must be ensured. The dimension of the polynomial space on each cell is $(r+1)\,(r+3)$. Notice that several choices of local bases for $\mathcal{RT}_{r+1}(T)$ are described in the literature, based on either point evaluations or integral moments as degrees of freedom (dofs). Clearly, a change of the basis does not alter the finite element space but only the representation of its members, which can be identified with their coefficient vectors w.r.t. a particular basis. For the purpose of this chapter, it

[2] Notice that while denote the lowest-order $\mathcal{RT}$ space by $\mathcal{RT}_1$, some authors use $\mathcal{RT}_0$ for this purpose.

is convenient to work with the following global degrees of freedom of integral type for $\boldsymbol{p} \in \mathcal{RT}_{r+1}(\Gamma_h)$; see [114, Ch. 3.4.1]:

$$\sigma_{T,i}(\boldsymbol{p}) \coloneqq \int_T \varphi_{T,i}\, \boldsymbol{p}\, \mathrm{d}\boldsymbol{s}, \quad i = 1, \dots, r\,(r+1)/2, \tag{3.7a}$$

$$\sigma_{E,j}(\boldsymbol{p}) \coloneqq \int_E \varphi_{E,j}\, (\boldsymbol{p}_E^+ \cdot \boldsymbol{\mu}_E^+)\, \mathrm{d}\boldsymbol{s}, \quad j = 1, \dots, r+1. \tag{3.7b}$$

We will refer to (3.7a) as triangle-based dofs or interior dofs and to (3.7b) as edge-based dofs. Notice that while the edge-based dofs are scalar, the triangle-based dofs have values in $\mathbb{R}^3$ for notational convenience. The global basis functions for the space $\mathcal{RT}_{r+1}(\Gamma_h)$ are denoted by $\boldsymbol{\psi}_i^T$ and $\boldsymbol{\psi}_j^E$, respectively. Notice that $\boldsymbol{\psi}_i^T$ is $\mathbb{R}^{3\times 3}$-valued. As is the case for all finite element spaces, any dof applied to any of the basis functions evaluates to zero except

$$\sigma_{T,i}(\boldsymbol{\psi}_{i'}^T) = \left(\begin{smallmatrix} 1 & 0 & 0 \\ 0 & 1 & 0 \\ 0 & 0 & 1 \end{smallmatrix}\right) \delta_{ii'} \quad \text{and} \quad \sigma_{E,j}(\boldsymbol{\psi}_{j'}^E) = \delta_{jj'}. \tag{3.8}$$

Let us emphasize that for any function $\boldsymbol{p} \in \mathcal{RT}_{r+1}(\Gamma_h)$, the dof values (3.7) are precisely the coefficients of $\boldsymbol{p}$ w.r.t. the basis, i.e.,

$$\boldsymbol{p} = \sum_T \sum_{i=1}^{r\,(r+1)/2} \boldsymbol{\psi}_i^T\, \sigma_{T,i}(\boldsymbol{p}) + \sum_E \sum_{j=1}^{r+1} \sigma_{E,j}(\boldsymbol{p})\, \boldsymbol{\psi}_j^E. \tag{3.9}$$

3.1.3 Index Conventions

In order to reduce the notational overhead, we are going to associate specific ranges for any occurrence of the indices i, j and k in the sequel:

$i \in \{1, \dots, r\,(r+1)/2\}$ as in the basis functions
$\varphi_{T,i}$ of $\mathcal{P}_{r-1}(T)$ and dofs $\sigma_{T,i}$ in $\mathcal{RT}_{r+1}(\Gamma_h)$,
$j \in \{1, \dots, r+1\}$ as in the basis functions
$\varphi_{E,j}$ of $\mathcal{P}_r(E)$ and dofs of $\sigma_{E,j}$ in $\mathcal{RT}_{r+1}(\Gamma_h)$,
$k \in \{1, \dots, (r+1)(r+2)/2\}$ as in the basis functions
$\Phi_{T,k}$ of $\mathcal{P}_r(T)$.

For instance, (3.9) will simply be written as

$$\boldsymbol{p} = \sum_{T,i} \boldsymbol{\psi}_i^T\, \sigma_{T,i}(\boldsymbol{p}) + \sum_{E,j} \sigma_{E,j}(\boldsymbol{p})\, \boldsymbol{\psi}_j^E$$

in what follows. For convenience, we summarize the notation for the degrees of freedom and basis functions needed throughout this chapter in Table 3.1.

3.2 Properties of the Discrete Total Variation

In this section, we investigate the properties of the discrete total variation seminorm

$$|u|_{DTV(\Gamma_h)} \coloneqq \sum_T \int_T \mathcal{I}_T \{\, |\nabla u|_2 \,\}\, \mathrm{d}\boldsymbol{s} + \sum_E \int_E \mathcal{I}_E \{\, |u_E^- - u_E^+| \,\}\, \mathrm{d}\boldsymbol{s}$$

FE space	local dimension	dofs	basis functions	global dimension
$\mathcal{CG}_r(\Gamma_h)$ $(r \geq 1)$	$(r+1)(r+2)/2$	eval. in $X_{T,k}$	$\{\Phi_{T,k}\}$	$N_T\,(r-2)^+(r-1)/2$ $+ N_E\,(r-1)^+ + N_V$
$\mathcal{DG}_r(\Gamma_h)$	$(r+1)(r+2)/2$	eval. in $X_{T,k}$	$\{\Phi_{T,k}\}$	$N_T\,(r+1)(r+2)/2$
$\mathcal{DG}_{r-1}(\Gamma_h)$	$r\,(r+1)/2$	eval. in $x_{T,i}$	$\{\varphi_{T,i}\}$	$N_T\,r\,(r+1)/2$
$\mathcal{DG}_r(\cup E)$	$r+1$	eval. in $x_{E,j}$	$\{\varphi_{E,j}\}$	$N_E\,(r+1)$
$\mathcal{RT}_{r+1}(\Gamma_h)$	$(r+1)(r+3)$	$\sigma_{T,i}$, see (3.7a) $\sigma_{E,j}$, see (3.7b)	$\{\boldsymbol{\psi}_i^T\}$ $\{\boldsymbol{\psi}_j^E\}$	$N_T\,r\,(r+1)$ $+ N_E\,(r+1)$

Table 3.1: Finite element spaces, their degrees of freedom and corresponding bases. Here N_T, N_E and N_V denote the number of triangles, edges and vertices in the triangular mesh. A term like $(r-a)^+$ should be understood as $\max\{r-a, 0\}$.

for functions $u \in \mathcal{DG}_r(\Gamma_h)$. Recall that $\mathcal{I}_T$ and $\mathcal{I}_E$ are local interpolation operators into the polynomial spaces $\mathcal{P}_{r-1}(T)$ and $\mathcal{P}_r(E)$, respectively. In terms of the Lagrangian bases $\{\varphi_{T,i}\}$ and $\{\varphi_{E,j}\}$ of these spaces, we have

$$\int_T \mathcal{I}_T\{\,|\nabla u|_2\,\}\,\mathrm{d}\boldsymbol{s} = \sum_{i=1}^{r\,(r+1)/2} \big|\nabla u\big|_2(x_{T,i})\,c_{T,i}, \tag{3.10a}$$

$$\int_E \mathcal{I}_E\{\,|u_E^- - u_E^+|\,\}\,\mathrm{d}\boldsymbol{s} = \sum_{j=1}^{r+1} |u_E^- - u_E^+|(x_{E,j})\,c_{E,j}, \tag{3.10b}$$

where the weights are given by

$$\begin{aligned} c_{T,i} &:= \int_T \varphi_{T,i}\,\mathrm{d}\boldsymbol{s} \\ c_{E,j} &:= \int_E \varphi_{E,j}\,\mathrm{d}\boldsymbol{s}. \end{aligned} \tag{3.11}$$

Figure 3.1 provides an illustration of the difference between the contributions

$$\int_E |u_E^- - u_E^+|\,\mathrm{d}\boldsymbol{s}$$

and

$$\int_E \mathcal{I}_E\{|u_E^- - u_E^+|\}\,\mathrm{d}\boldsymbol{s}$$

to $|u|_{TV(\Gamma_h)}$ and $|u|_{DTV(\Gamma_h)}$. In virtue of the fact that

$$\nabla u|_T \in \mathcal{P}_{r-1}(T)^3$$

and

$$(u_E^- - u_E^+) \in \mathcal{P}_r(E),$$

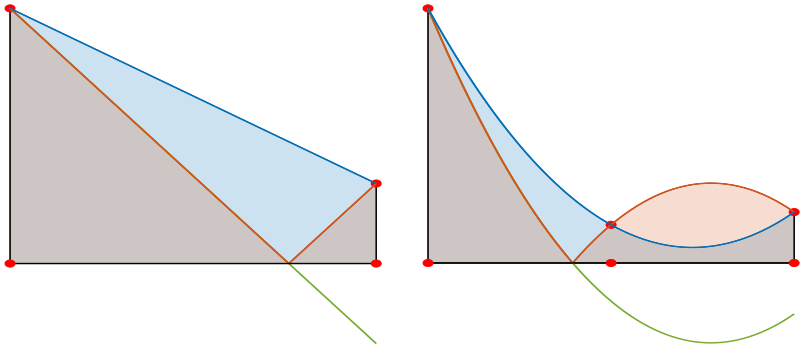

Figure 3.1: Illustration of typical edge-jump contributions to $|u|_{TV(\Gamma_h)}$ and to $|u|_{DTV(\Gamma_h)}$. The green and red curves show $(u_E^- - u_E^+)$ and $\left|u_E^- - u_E^+\right|$, respectively, and the blue curve shows $\mathcal{I}_E\{\,|u_E^- - u_E^+|\,\}$ for polynomial degrees $r = 1$ (left) and $r = 2$ (right). The left picture also confirms $|u|_{TV(\Gamma_h)} \le |u|_{DTV(\Gamma_h)}$ when $r = 1$, see Corollary 3.5, while $|u|_{TV(\Gamma_h)}$ may be larger or smaller than $|u|_{DTV(\Gamma_h)}$ when $r \in \{2,3,4\}$.

it is clear that $|\cdot|_{DTV(\Gamma_h)}$ is indeed a seminorm on $\mathcal{DG}_r(\Gamma_h)$, provided that all weights $c_{T,i}$ and $c_{E,j}$ are non-negative. The following lemma shows that this is the case for polynomial degrees $0 \le r \le 4$.

Lemma 3.1 (Lagrange basis functions with positive integrals)**.**

(*i*) *Let* $T \subset \mathbb{R}^3$ *be a triangle and* $1 \le r \le 4$. *Then* $c_{T,i} \ge 0$ *holds for all* $i = 1,\dots,r\,(r+1)/2$. *When* $r \ne 3$, *then all* $c_{T,i} > 0$.

(*ii*) *Let* $E \subset \mathbb{R}^2$ *be an edge and* $0 \le r \le 7$. *Then* $c_{E,j} > 0$ *holds for all* $j = 1,\dots,r+1$.

Proof. Given that the Lagrange points form a uniform lattice on either T or E, the values of $c_{T,i}$ and $c_{E,j}$ are precisely the integration weights of the closed Newton–Cotes formulas. For triangles, these weights are tabulated, e.g., in [145, Tab. I] for orders $0 \le r \le 8$, and they confirm the first part. For edges (intervals), we refer the reader to, e.g., [63, Ch. 2.5] or [62, Ch. 5.1.5], which confirms the second part. □

We can now give a precise formulation of the dual representation of the discrete TV-seminorm (3.2).

Theorem 3.2 (Dual Representation of $|u|_{DTV(\Gamma_h)}$)**.** *Suppose* $0 \le r \le 4$. *Then for any* $u \in \mathcal{DG}_r(\Gamma_h)$, *the discrete TV-seminorm* (3.2) *satisfies*

$$
\begin{aligned}
|u|_{DTV(\Gamma_h)} = \sup \Bigg\{ \int_{\Gamma_h} u \operatorname{div} \boldsymbol{p}\, \mathrm{d}\boldsymbol{s} : \boldsymbol{p} \in \mathcal{RT}_{r+1}(\Gamma_h), \\
|\sigma_{T,i}(\boldsymbol{p})|_2 \le c_{T,i} \quad \forall T,\ i = 1,\dots,r\,(r+1)/2, \\
\left|\sigma_{E,j}(\boldsymbol{p})\right| \le c_{E,j} \quad \forall E,\ j = 1,\dots,r+1 \Bigg\}.
\end{aligned}
\tag{3.12}
$$

Proof. We begin with the observation that integration by parts and continuity of the co-normal component across all edges E, see (3.6), yields

$$\begin{aligned} -\int_{\Gamma_h} u \operatorname{div} \boldsymbol{p} \, \mathrm{d}\boldsymbol{s} &= -\sum_T \int_T u \operatorname{div} \boldsymbol{p} \, \mathrm{d}\boldsymbol{s} \\ &= \sum_T \int_T \nabla u \cdot \boldsymbol{p} \, \mathrm{d}\boldsymbol{s} - \sum_E \left(\int_E u_E^+ \left(\boldsymbol{p}_E^+ \cdot \boldsymbol{\mu}_E^+ \right) + u_E^- \left(\boldsymbol{p}_E^- \cdot \boldsymbol{\mu}_E^- \right) \mathrm{d}\boldsymbol{s} \right) \\ &= \sum_T \int_T \nabla u \cdot \boldsymbol{p} \, \mathrm{d}\boldsymbol{s} + \sum_E \int_E \left(u_E^- - u_E^+ \right) \left(\boldsymbol{p}_E^+ \cdot \boldsymbol{\mu}_E^+ \right) \mathrm{d}\boldsymbol{s} \end{aligned} \tag{3.13}$$

for any $u \in \mathcal{DG}_r(\Gamma_h)$ and $\boldsymbol{p} \in \mathcal{RT}_{r+1}(\Gamma_h)$.
Let us consider one of the edge integrals first. Notice that

$$\left(u_E^- - u_E^+ \right) \in \mathcal{P}_r(E)$$

holds and thus

$$\left(u_E^- - u_E^+ \right) = \sum_j v_j \, \varphi_{E,j}$$

with coefficients

$$v_j = \left(u_E^-(x_{E,j}) - u_E^+(x_{E,j}) \right).$$

By the definition (3.7b) of the basis of $\mathcal{RT}_{r+1}(\Gamma_h)$, we obtain

$$\begin{aligned} \int_E \left(u_E^- - u_E^+ \right) \left(\boldsymbol{p}_E^+ \cdot \boldsymbol{\mu}_E^+ \right) \mathrm{d}\boldsymbol{s} &= \sum_j v_j \int_E \varphi_{E,j} \left(\boldsymbol{p}_E^+ \cdot \boldsymbol{\mu}_E^+ \right) \mathrm{d}\boldsymbol{s} \\ &= \sum_j v_j \, \sigma_{E,j}(\boldsymbol{p}). \end{aligned}$$

The maximum of this expression w.r.t. $\boldsymbol{p}$ verifying the constraints in (3.12) is attained when

$$\sigma_{E,j}(\boldsymbol{p}) = \operatorname{sgn}(v_j) \, c_{E,j}$$

holds. Here we are using the fact that $c_{E,j} > 0$ holds; see Lemma 3.1. Choosing $\boldsymbol{p}$ as the maximizer yields

$$\begin{aligned} \int_E \left(u_E^- - u_E^+ \right) \left(\boldsymbol{p}_E^+ \cdot \boldsymbol{\mu}_E^+ \right) \mathrm{d}\boldsymbol{s} &= \sum_j \left| v_j \right| \, c_{E,j} \\ &= \sum_j \int_E \left| v_j \right| \, \varphi_{E,j} \, \mathrm{d}\boldsymbol{s} \\ &= \int_E \mathcal{I}_E \left\{ \left| u_E^- - u_E^+ \right| \right\} \mathrm{d}\boldsymbol{s}, \end{aligned}$$

where we used that

$$\begin{aligned} \left| v_j \right| &= \left| u_E^-(x_{E,j}) - u_E^+(x_{E,j}) \right| \\ &= \left| u_E^- - u_E^+ \right|(x_{E,j}) \end{aligned}$$

in the last step.

Next we consider an integral over a triangle, which is relevant only when $r \geq 1$. Since $u \in \mathcal{P}_r(T)$ holds, we have

$$\nabla u \in \mathcal{P}_{r-1}(T)^3$$

and thus

$$\nabla u = \sum_i \varphi_{T,i}\, \boldsymbol{w}_i$$

with vector-valued coefficients

$$\boldsymbol{w}_i = \nabla u(x_{T,i}).$$

Using again the definition of the basis of $\mathcal{RT}_{r+1}(\Gamma_h)$ (3.7b), we obtain

$$\begin{aligned}\int_T \nabla u \cdot \boldsymbol{p}\, \mathrm{d}\boldsymbol{s} &= \sum_i \boldsymbol{w}_i \cdot \int_T \varphi_{T,i}\, \boldsymbol{p}\, \mathrm{d}\boldsymbol{s} \\ &= \sum_i \boldsymbol{w}_i \cdot \boldsymbol{\sigma}_{T,i}(\boldsymbol{p}).\end{aligned}$$

By virtue of Hölder's inequality, the maximum of this expression w.r.t. $\boldsymbol{p}$ satisfying the constraints in (3.12) can be characterized explicitly. When $\boldsymbol{w}_i \neq \boldsymbol{0}$, then the maximum is attained when

$$\boldsymbol{\sigma}_{T,i}(\boldsymbol{p}) = \frac{\boldsymbol{w}_i}{|\boldsymbol{w}_i|_2}\, c_{T,i}.$$

When $\boldsymbol{w}_i = \boldsymbol{0}$ holds, $\boldsymbol{\sigma}_{T,i}(\boldsymbol{p})$ can be chosen arbitrarily but subject to

$$|\boldsymbol{\sigma}_{T,i}(\boldsymbol{p})|_2 \leq c_{T,i}.$$

In any case, we arrive at the optimal value

$$\boldsymbol{w}_i \cdot \boldsymbol{\sigma}_{T,i}(\boldsymbol{p}) = c_{T,i}\ |\boldsymbol{w}_i|_2\,.$$

As before, we are using here the fact that $c_{T,i} \geq 0$ holds; see again Lemma 3.1. For an optimal $\boldsymbol{p}$, we thus have

$$\begin{aligned}\int_T \nabla u \cdot \boldsymbol{p}\, \mathrm{d}\boldsymbol{s} &= \sum_i |\boldsymbol{w}_i|_2\ c_{T,i} \\ &= \sum_i \int_T |\boldsymbol{w}_i|_2\ \varphi_{T,i}\, \mathrm{d}\boldsymbol{s} \\ &= \int_T \mathcal{I}_T\big\{\, |\nabla u|_2 \,\big\}\, \mathrm{d}\boldsymbol{s},\end{aligned}$$

where we used

$$|\boldsymbol{w}_i|_2 = |\nabla u(x_{T,i})|_2$$

in the last step.

Finally, we point out that each summand in (3.13) depends on $\boldsymbol{p}$ only through the dof values $\boldsymbol{\sigma}_{T,i}(\boldsymbol{p})$ or $\sigma_{E,j}(\boldsymbol{p})$ associated with one particular triangle or edge. Consequently, the maximum of (3.13) is attained if and only if each summand attains its maximum subject to the constraints on the dof values set forth in (3.12). Since $-\boldsymbol{p}$ verifies the same constraints as $\boldsymbol{p}$, the maxima over

$$\pm \int_{\Gamma_h} u\, \mathrm{div}\, \boldsymbol{p}\, \mathrm{d}\boldsymbol{s}$$

coincide and (3.12) is proved. □

Remark 3.3 (The lowest-order case)**.** *In the lowest-order case $r = 0$, the only basis function on any edge E is $\varphi_{E,1} \equiv 1$ so that $c_{E,1} = |E|$ holds. Consequently,* (3.12) *reduces to*

$$|u|_{DTV(\Gamma_h)} = \max \left\{ \int_{\Gamma_h} u \operatorname{div} \boldsymbol{p} \, \mathrm{d}\boldsymbol{s} : \boldsymbol{p} \in \mathcal{RT}_1(\Gamma_h), \int_E \left| \boldsymbol{p}_E^+ \cdot \boldsymbol{\mu}_E^+ \right| \, \mathrm{d}\boldsymbol{s} \leq |E| \quad \forall E \right\}.$$

It may appear peculiar that the constraints for the edge dofs in (3.12) are scalar and linear, while the constraints for the triple-wise triangle dofs $\boldsymbol{\sigma}_{T,i}(\boldsymbol{p}) \in \mathbb{R}^3$ are generally nonlinear. Notice, however, that it becomes evident in the proof of Theorem 3.2 that the edge dofs are utilized to measure the contributions in $|u|_{DTV(\Gamma_h)}$ associated with the edge jumps of u, while the triangle dofs account for the contributions attributed to the gradient ∇u. Since the edge jumps are maximal in the direction normal to the edge, scalar dofs suffice in order to determine the unknown jump height. On the other hand, both the norm and direction of the gradient are unknown and must be recovered from integration against suitable functions $\boldsymbol{p}$. To this end, a variation of $\boldsymbol{\sigma}_{T,i}(\boldsymbol{p})$ within a three-dimensional ball (w.r.t. the $|\cdot|_2$-norm) is required, leading to constraints $|\boldsymbol{\sigma}_{T,i}(\boldsymbol{p})|_2 \leq c_{T,i}$ on triple of coefficients of $\boldsymbol{p}$. Notice that those constraints appear for polynomial degrees $r \geq 1$ and they are nonlinear.

We conclude this section by comparing the TV-seminorm (3.1) with our discrete variant (3.2) for $\mathcal{DG}_r(\Gamma_h)$ functions. For the purpose of the following result, let us denote by

$$\left(u_E^- - u_E^+\right)'$$

the tangential derivative (in arbitrary direction of traversal) of the scalar jump of u along an edge E. For a function $u \in \mathcal{DG}_r(\Gamma_h)$, we define

$$\begin{aligned} |u|_{W^{1,\infty}(T)} &= \max_{x \in T} \left\{ \left| \nabla u(\boldsymbol{x}) \cdot \boldsymbol{\xi}_{T,1} \right| \right\} + \max_{x \in T} \left\{ \left| \nabla u(\boldsymbol{x}) \cdot \boldsymbol{\xi}_{T,2} \right| \right\} \\ |u|_{W^{2,\infty}(T)} &= \max_{x \in T} \left\{ \left| \boldsymbol{\xi}_{T,1} \cdot \mathrm{H}(u(\boldsymbol{x})) \boldsymbol{\xi}_{T,1} \right| \right\} + \max_{x \in T} \left\{ \left| \boldsymbol{\xi}_{T,2} \cdot \mathrm{H}(u(\boldsymbol{x})) \boldsymbol{\xi}_{T,2} \right| \right\} \\ &\quad + \max_{x \in T} \left\{ \left| \boldsymbol{\xi}_{T,1} \cdot \mathrm{H}(u(\boldsymbol{x})) \boldsymbol{\xi}_{T,2} \right| \right\} \end{aligned}$$

the $W^{1,\infty}$ and $W^{2,\infty}$-seminorm of u on T. Here, $\mathrm{H}(u)$ denotes the hessian of u and $\boldsymbol{\xi}_{T,1}$ and $\boldsymbol{\xi}_{T,2}$ are two orthogonal tangential vectors of the triangle T with

$$\left|\boldsymbol{\xi}_{T,1}\right|_2 = \left|\boldsymbol{\xi}_{T,2}\right|_2 = 1.$$

Moreover, we recall that the diameter h_T of a triangle T is the euclidean length of its longest edge.

Proposition 3.4. *There is a constant $C > 0$ such that*

$$\left| |u|_{TV(\Gamma_h)} - |u|_{DTV(\Gamma_h)} \right| \leq C h \left(\max_T |u|_{W^{2,\infty}(T)} + \sum_E \left\| \left(u_E^- - u_E^+\right)' \right\|_{L^1(E)} \right) \tag{3.14}$$

holds for all $u \in \mathcal{DG}_r(\Gamma_h)$, $0 \leq r \leq 4$, where

$$h := \max_T h_T$$

is the mesh size. The constant C depends only on r and $|\Gamma_h|$.

Proof. Within the proof, $C > 0$ denotes a generic constant which may change from instance to instance. Note that for $r = 0$, (3.1) and (3.2) are equal, which makes (3.14) true. In case $r \geq 1$, we use (3.10) to interpret the discrete TV-seminorm as a quadrature rule applied to the TV-seminorm (3.1), which yields

$$\begin{aligned}\left||u|_{TV(\Gamma_h)} - |u|_{DTV(\Gamma_h)}\right| \leq{}& \left|\sum_T \left(\int_T |\nabla u|_2 \,\mathrm{d}s - \sum_i \left|\nabla u(x_{T,i})\right|_2 c_{T,i}\right)\right| \\ &+ \left|\sum_E \left(\int_E \left|u_E^- - u_E^+\right| \,\mathrm{d}s - \sum_j \left|u_E^-(x_{E,j}) - u_E^+(x_{E,j})\right| \, c_{E,j}\right)\right| \\ \leq{}& \sum_T \left|\int_T |\nabla u|_2 \,\mathrm{d}s - \sum_i \left|\nabla u(x_{T,i})\right|_2 c_{T,i}\right| \\ &+ \sum_E \left|\int_E \left|u_E^- - u_E^+\right| \,\mathrm{d}s - \sum_j \left|u_E^-(x_{E,j}) - u_E^+(x_{E,j})\right| \, c_{E,j}\right|.\end{aligned} \tag{3.15}$$

For the triangle related summand in (3.15) we use [76, Lem. 8.4] with $d = 2$, $p = \infty$, $k_q = 0$, and $s = 1$ therein. This result yields the existence of a constant $C > 0$ such that

$$\left|\int_T |\nabla u|_2 \,\mathrm{d}s - \sum_i \left|\nabla u(x_{T,i})\right|_2 c_{T,i}\right| \leq C h_T \, |T| \, \left||\nabla u|_2\right|_{W^{1,\infty}(T)}.$$

Summing over T, we find

$$\begin{aligned}\sum_T \left|\int_T |\nabla u|_2 \,\mathrm{d}s - \sum_i \left|\nabla u(x_{T,i})\right|_2 c_{T,i}\right| &\leq C h \, |\Gamma_h| \, \max_T \left||\nabla u|_2\right|_{W^{1,\infty}(T)} \\ &\leq C h \, |\Gamma_h| \, \max_T |u|_{W^{2,\infty}(T)},\end{aligned} \tag{3.16}$$

where the last estimate holds due to $v \mapsto |v|_2$ being globally Lipschitz continuous and therefore

$$\left||\nabla u|_2\right|_{W^{1,\infty}(T)} \leq C \, |u|_{W^{2,\infty}(T)}.$$

Similarly, for each edge related summand in (3.15), we will apply [76, Lem. 8.4] in (3.10b) (using $d = 1$, $p = 1$, $k_q = 0$, and $s = 1$ therein); note that the proof carries over to this limit case with $p = 1$ and $d = s$. This implies the existence of $C > 0$ such that

$$\left|\int_E \left|u_E^- - u_E^+\right| \,\mathrm{d}s - \sum_j \left|u_E^-(x_{E,j}) - u_E^+(x_{E,j})\right| \, c_{E,j}\right| \leq C h \left\|\left(u_E^- - u_E^+\right)'\right\|_{L^1(E)}$$

holds. Notice that

$$\left\|\left|\left(u_E^- - u_E^+\right)\right|'\right\|_{L^1(E)} = \left\|\left(u_E^- - u_E^+\right)'\right\|_{L^1(E)}$$

holds. Summing over E yields

$$\sum_E \left|\int_E \left|u_E^- - u_E^+\right| \,\mathrm{d}s - \sum_j \left|u_E^-(x_{E,j}) - u_E^+(x_{E,j})\right| \, c_{E,j}\right| \leq C h \sum_E \left\|\left(u_E^- - u_E^+\right)'\right\|_{L^1(E)}.$$

By combining this estimate and (3.16), we obtain the desired error bound. □

Corollary 3.5 (Low Order Polynomial Degrees)**.**

(*i*) *For $r = 0$, we have $|u|_{TV(\Gamma_h)} = |u|_{DTV(\Gamma_h)}$ $\forall u \in \mathcal{DG}_r(\Gamma_h)$.*

(*ii*) *For $r = 1$, we have $|u|_{TV(\Gamma_h)} \leq |u|_{DTV(\Gamma_h)}$ $\forall u \in \mathcal{DG}_r(\Gamma_h)$.*

Proof. In case of $r = 0$, the right-hand side of the estimate in Proposition 3.4 vanishes. In case of $r = 1$, ∇u is piecewise constant and the corresponding terms in (3.1) and (3.2) coincide. Moreover, for affine functions $v : E \to \mathbb{R}$ it is easy to check that

$$\int_E |v| \, \mathrm{d}s \leq \frac{1}{2} \left(\left|v(x_{E,1})\right| + \left|v(x_{E,2})\right| \right) \int_E 1 \, \mathrm{d}s,$$

where $x_{E,1}$ and $x_{E,2}$ are the two end points of E. This yields the claim in case $r = 1$. □

We also mention that the boundary perimeter formula

$$\mathrm{Per}(U) := |\chi_U|_{TV(\Gamma_h)} = |\chi_U|_{DTV(\Gamma_h)}$$

holds when U is a union of triangles and thus the characteristic function χ_U belongs to $\mathcal{DG}_0(\Gamma_h)$.

3.3 Discrete Dual Problem

In this section we revisit the classical image denoising and inpainting problems,

$$\text{Minimize} \quad \frac{1}{2}\|u - f\|^2_{L^2(\Gamma_h^0)} + \beta \, |u|_{TV(\Gamma_h)}, \tag{TV-L2}$$

$$\text{Minimize} \quad \|u - f\|_{L^1(\Gamma_h^0)} + \beta \, |u|_{TV(\Gamma_h)}, \tag{TV-L1}$$

see [45, 50, 77, 123, 139]. We introduce their discrete counterparts and establish their Fenchel duals. Here $\Gamma_h^0 \subset \Gamma_h$ is the domain where data is available, and β is a positive parameter. For simplicity, we assume that the inpainting region $\Gamma_h \setminus \Gamma_h^0$ is the union of a number of triangles in the discrete problems.

3.3.1 The TV-L^2 Problem

The discrete counterpart of (TV-L2) we consider is

$$\text{Minimize} \quad \frac{1}{2}\|u - f\|^2_{L^2(\Gamma_h^0)} + \beta \, |u|_{DTV(\Gamma_h)}. \tag{DTV-L2}$$

The reconstructed image u is sought in $\mathcal{DG}_r(\Gamma_h)$ for some $0 \leq r \leq 4$. We can assume that the given data f belongs to $\mathcal{DG}_r(\Gamma_h^0)$ as well, possibly after applying interpolation or quasi-interpolation. Notice that we use the discrete TV-seminorm as regularizer.
The majority of algorithms considered in the literature utilize either the primal or the dual formulations of the problems at hand. The *continuous* (pre-)dual problem for (TV-L2) is well known, see for instance [99]:

$$\begin{aligned} \text{Minimize} \quad & \frac{1}{2}\|\mathrm{div}\, \boldsymbol{p} + f\|^2_{L^2(\Gamma_h^0)} \\ \text{s.t.} \quad & |\boldsymbol{p}|_2 \leq \beta, \end{aligned} \tag{TV-L2-D}$$

with $\boldsymbol{p} \in \boldsymbol{H}(\mathrm{div};\Gamma_h)$. Our first result in this section shows that the dual of the discrete problem (DTV-L2) has a very similar structure as (TV-L2-D), but with the pointwise constraints replaced by coefficient-wise constraints as in (3.12). For future reference, we denote the associated admissible set by

$$\boldsymbol{P} \coloneqq \Big\{ \boldsymbol{p} \in \mathcal{RT}_{r+1}(\Gamma_h) : |\sigma_{T,i}(\boldsymbol{p})|_2 \le c_{T,i} \wedge \big|\sigma_{E,j}(\boldsymbol{p})\big| \le c_{E,j} \quad \forall T, E, i, j \Big\}. \tag{3.17}$$

Theorem 3.6 (Discrete dual problem for (DTV-L2))**.** *Let* $0 \le r \le 4$. *Then the dual problem of* (DTV-L2) *is*

$$\begin{aligned} \textit{Minimize} \quad & \frac{1}{2}\|\mathrm{div}\,\boldsymbol{p} + f\|^2_{L^2(\Gamma_h^0)} \\ \textit{s.t.} \quad & \boldsymbol{p} \in \beta\boldsymbol{P}. \end{aligned} \tag{DTV-L2-D}$$

Here $\boldsymbol{p} \in \beta\boldsymbol{P}$ means that $\boldsymbol{p}$ satisfies constraints as in (3.17) but with $c_{T,i}$ and $c_{E,j}$ replaced by $\beta\, c_{T,i}$ and $\beta\, c_{E,j}$, respectively.

Proof. We cast (DTV-L2) in the common form $F(u) + \beta\, G(\Lambda u)$. Let us define

$$U \coloneqq \mathcal{DG}_r(\Gamma_h)$$

and

$$F(u) \coloneqq \frac{1}{2}\|u - f\|^2_{L^2(\Gamma_h^0)}.$$

The operator Λ represents the gradient of u, which consists of the triangle-wise contributions plus measure-valued contributions due to (normal) edge jumps. We therefore define

$$\Lambda : U \to Y \coloneqq \prod_T \mathcal{P}_{r-1}(T)^2 \times \prod_E \mathcal{P}_r(E). \tag{3.18a}$$

The components of Λu will be addressed by $(\Lambda u)_T$ and $(\Lambda u)_E$ respectively, and they are defined by

$$\begin{aligned} (\Lambda u)_T &\coloneqq \nabla u|_T \\ (\Lambda u)_E &\coloneqq (u_E^- - u_E^+). \end{aligned} \tag{3.18b}$$

Finally, the function $G : Y \to \mathbb{R}$ is defined by

$$G(\boldsymbol{d}) \coloneqq \sum_T \int_T \mathcal{I}_T\{\, |\boldsymbol{d}_T|_2 \,\}\, \mathrm{d}\boldsymbol{s} + \sum_E \int_E \mathcal{I}_E\{\, |d_E| \,\}\, \mathrm{d}\boldsymbol{s}. \tag{3.19}$$

A crucial observation is that now the dual space Y^* of Y can be identified with $\mathcal{RT}_{r+1}(\Gamma_h)$ when the duality product is defined as

$$\langle \boldsymbol{p}, \boldsymbol{d} \rangle \coloneqq \sum_T \int_T \boldsymbol{p} \cdot \boldsymbol{d}_T \,\mathrm{d}\boldsymbol{s} + \sum_E \int_E (\boldsymbol{p}_E^+ \cdot \boldsymbol{\mu}_E^+)\, d_E \,\mathrm{d}\boldsymbol{s}. \tag{3.20}$$

In fact, $\mathcal{RT}_{r+1}(\Gamma_h)$ has the same dimension as Y and, for any $\boldsymbol{p} \in \mathcal{RT}_{r+1}(\Gamma_h)$, (3.20) clearly defines a linear functional on Y. Moreover, the mapping

$$\boldsymbol{p} \mapsto \langle \boldsymbol{p}, \cdot \rangle$$

is injective since

$$\langle \boldsymbol{p}, \boldsymbol{d} \rangle = 0 \quad \forall \boldsymbol{d} \in Y \implies \boldsymbol{p} = \boldsymbol{0},$$

see (3.7). With this representation of Y^* available, we can evaluate

$$\Lambda^* : \mathcal{RT}_{r+1}(\Gamma_h) \to U,$$

where we identify U with its dual space using the Riesz isomorphism induced by the $L^2(\Gamma_h)$ inner product. Consequently, Λ^* is defined by the condition

$$\langle \boldsymbol{p}, \Lambda u \rangle = (u, \Lambda^* \boldsymbol{p})_{L^2(\Gamma_h)}$$

for all $\boldsymbol{p} \in \mathcal{RT}_{r+1}(\Gamma_h)$ and all $u \in \mathcal{DG}_r(\Gamma_h)$. The left hand side is

$$\begin{aligned}
\langle \boldsymbol{p}, \Lambda u \rangle &= \sum_T \int_T \boldsymbol{p} \cdot \nabla u \, \mathrm{d}\boldsymbol{s} + \sum_E \int_E (\boldsymbol{p}_E^+ \cdot \boldsymbol{\mu}_E^+) \, (u_E^- - u_E^+) \, \mathrm{d}\boldsymbol{s} \\
&= -\sum_T \int_T (\operatorname{div} \boldsymbol{p}) \, u \, \mathrm{d}\boldsymbol{s} + \sum_T \int_{\partial T} (\boldsymbol{p} \cdot \boldsymbol{\mu}_T) \, u \, \mathrm{d}\boldsymbol{s} \\
&\quad - \sum_E \left(\int_E u_E^+ \, (\boldsymbol{p}_E^+ \cdot \boldsymbol{\mu}_E^+) + u_E^- \, (\boldsymbol{p}_E^- \cdot \boldsymbol{\mu}_E^-) \, \mathrm{d}\boldsymbol{s} \right) \\
&= -\int_{\Gamma_h} (\operatorname{div} \boldsymbol{p}) \, u \, \mathrm{d}\boldsymbol{s},
\end{aligned} \tag{3.21}$$

hence $\Lambda^* = -\operatorname{div}$ holds. Here $\boldsymbol{\mu}_T$ denotes the outward co-normal along the triangle boundary ∂T.
The dual problem can be cast as

$$\text{Minimize} \quad F^*(-\Lambda^* \boldsymbol{p}) + \beta \, G^*(\boldsymbol{p}/\beta). \tag{3.22}$$

Similar to (2.18), we have that the convex conjugate of

$$F(u) = \frac{1}{2} \|u - f\|^2_{L^2(\Gamma_h^0)}$$

is

$$F^*(u) = \frac{1}{2} \|u + f\|^2_{L^2(\Gamma_h^0)} - \frac{1}{2} \|f\|^2_{L^2(\Gamma_h^0)}. \tag{3.23}$$

It remains to evaluate

$$\begin{aligned}
G^*(\boldsymbol{p}) &= \sup_{\boldsymbol{d} \in Y} \langle \boldsymbol{p}, \boldsymbol{d} \rangle - G(\boldsymbol{d}) \\
&= \sup_{\boldsymbol{d} \in Y} \left\{ \sum_T \int_T \left(\boldsymbol{p} \cdot \boldsymbol{d}_T - \mathcal{I}_T \{ \, |\boldsymbol{d}_T|_2 \, \} \right) \mathrm{d}\boldsymbol{s} \right. \\
&\qquad \left. + \sum_E \int_E \left((\boldsymbol{p}_E^+ \cdot \boldsymbol{\mu}_E^+) \, d_E - \mathcal{I}_E \{ \, |d_E| \, \} \right) \mathrm{d}\boldsymbol{s} \right\}.
\end{aligned}$$

Let us consider the contribution from

$$d_E = \alpha \, \varphi_{E,j}$$

for some $\alpha \in \mathbb{R}$ on a single edge E, and $\boldsymbol{d} \equiv 0$ otherwise. By (3.7b) and (3.11), this contribution is

$$\alpha\, \sigma_{E,j}(\boldsymbol{p}) - |\alpha|\; c_{E,j},$$

which is bounded above if and only if

$$\left|\sigma_{E,j}(\boldsymbol{p})\right| \leq\; c_{E,j}.$$

In this case, the maximum is zero. Similarly, it can be shown that the contribution from

$$\boldsymbol{d}_T = \left(\begin{smallmatrix}\alpha_1\\ \alpha_2\end{smallmatrix}\right) \varphi_{T,i}$$

remains bounded above if and only if

$$\left|\boldsymbol{\sigma}_{T,i}(\boldsymbol{p})\right|_{s^*} \leq c_{T,i},$$

in which case the maximum is zero as well. This shows that

$$G^* = \chi_{\boldsymbol{P}}$$

is the indicator function of the constraint set $\boldsymbol{P}$ defined in (3.17), which combined with (3.23) and (3.22) concludes the proof. □

Notice that the discrete dual problem (DTV-L2-D) features the same, very simple set of constraints, which already appeared in (3.12). As is the case for (TV-L2-D), the solution of the discrete dual problem (DTV-L2-D) is not necessarily unique. However its divergence is unique on Γ_h^0 due to the strong convexity of the objective in terms of $\operatorname{div} \boldsymbol{p}$. Although not needed for Algorithms 2 and 3, we state the following relation between the primal and the dual solutions for completeness.

Lemma 3.7 (Recovery of the Primal Solution in (DTV-L2))**.** *Suppose that $\boldsymbol{p} \in \mathcal{RT}_{r+1}(\Gamma_h)$ is a solution of* (DTV-L2-D) *in case $\Gamma_h^0 = \Gamma_h$. Then the unique solution of* (DTV-L2) *is given by $u \in \mathcal{DG}_r(\Gamma_h)$ with*

$$u|_T = \operatorname{div} \boldsymbol{p}|_T + f|_T \quad \forall T \in \Gamma_h. \tag{3.24}$$

Proof. From (3.22), the pair of optimality conditions to analyze is

$$\begin{aligned} -\Lambda^* \boldsymbol{p} &\in \partial F(u)\\ \boldsymbol{p} &\in \partial(\beta\, G)(\Lambda u), \end{aligned} \tag{3.25}$$

see [73, Ch. III, Sect. 4]. Here it suffices to consider the first condition, which by [73, Prop. I.5.1] is equivalent to

$$F(u) + F^*(-\Lambda^* \boldsymbol{p}) - (u,\, -\Lambda^* \boldsymbol{p})_{L^2(\Gamma_h)} = 0.$$

This equality can be rewritten as

$$\|u - f\|^2_{L^2(\Gamma_h)} + \|\operatorname{div} \boldsymbol{p} + f\|^2_{L^2(\Gamma_h)} - \|f\|^2_{L^2(\Gamma_h)} - 2\,(u,\, \operatorname{div} \boldsymbol{p})_{L^2(\Gamma_h)} = 0.$$

Developing each summand in terms of the inner product $(\cdot,\,\cdot)_{L^2(\Gamma_h)}$ and rearranging appropriately, we obtain

$$\begin{aligned} 0 = (u - f - \operatorname{div} \boldsymbol{p},\, u)_{L^2(\Gamma_h)} &+ (-u + f + \operatorname{div} \boldsymbol{p},\, f)_{L^2(\Gamma_h)} \\ &+ (\operatorname{div} \boldsymbol{p} + f - u,\, \operatorname{div} \boldsymbol{p})_{L^2(\Gamma_h)}, \end{aligned}$$

which amounts to

$$\|u - f - \operatorname{div} \boldsymbol{p}\|^2_{L^2(\Gamma_h)} = 0,$$

and (3.24) is proved. □

Remark 3.8. *In case $\Gamma_h^0 \subsetneq \Gamma_h$, the solution of the primal problem will not be unique in general. An inspection of the proof of Lemma 3.7 shows that in this case, one can derive the relation*

$$\|u - f - \operatorname{div} \boldsymbol{p}\|^2_{L^2(\Gamma_h^0)} = 2 \int_{\Gamma_h \setminus \Gamma_h^0} u \,\operatorname{div} \boldsymbol{p}\, \mathrm{d}\boldsymbol{s}.$$

3.3.2 The TV-L^1 Problem

The continuous (pre-)dual problem associated with

$$\text{Minimize} \quad \|u - f\|_{L^1(\Gamma_h^0)} + \beta\ |u|_{TV(\Gamma_h)} \tag{TV-L1}$$

can be shown along the lines of [99, Thm. 2.2] to be

$$\begin{aligned} \text{Minimize} \quad & \int_{\Gamma_h^0} (\operatorname{div} \boldsymbol{p})\, f \,\mathrm{d}\boldsymbol{s} \\ \text{s.t.} \quad & |\operatorname{div} \boldsymbol{p}| \le \chi_{\Gamma_h^0} \text{ and } |\boldsymbol{p}|_2 \le \beta \end{aligned} \tag{TV-L1-D}$$

with $\boldsymbol{p} \in \boldsymbol{H}(\operatorname{div}; \Gamma_h)$, where $\chi_{\Gamma_h^0}$ is the characteristic function of Γ_h^0.
The definition of an appropriate discrete counterpart of (TV-L1) deserves some attention. Simply replacing $|u|_{TV(\Gamma_h)}$ by $|u|_{DTV(\Gamma_h)}$ would yield a discrete dual problem with an infinite number of pointwise constraints

$$|\operatorname{div} \boldsymbol{p}| \le \chi_{\Gamma_h^0}$$

as in (TV-L1-D), which would render the problem intractable. We therefore advocate to consider

$$\text{Minimize} \quad \sum_{T \subset \Gamma_h^0} \int_T \mathcal{J}_T\{\, |u - f| \,\}\, \mathrm{d}\boldsymbol{s} + \beta\ |u|_{DTV(\Gamma_h)} \tag{DTV-L1}$$

as an appropriate discrete version of (TV-L1) with $u \in \mathcal{DG}_r(\Gamma_h)$. Here $\mathcal{J}_T$ denotes the interpolation operator into $\mathcal{P}_r(T)$, i.e.,

$$\mathcal{J}_T\{\, |u - f| \,\} = \sum_k |u - f|\,(X_{T,k})\, \Phi_{T,k}.$$

This choice of applying an interpolatory quadrature formula to the data fidelity (loss) term as well is a decisive advantage, yielding a favorable dual problem.

Theorem 3.9 (Discrete dual problem for (DTV-L1))**.** *Let* $0 \leq r \leq 3$*. Then the dual problem of* (DTV-L1) *is*

$$\begin{aligned} &\textit{Minimize} && \int_{\Gamma_h^0} (\operatorname{div} \boldsymbol{p})\, f \,\mathrm{d}\boldsymbol{s} \\ &\textit{s.t.} && \left| \int_T (\operatorname{div} \boldsymbol{p})\, \Phi_{T,k} \,\mathrm{d}\boldsymbol{s} \right| \leq C_{T,k} \quad \textit{for } T \subset \Gamma_h^0 \\ &\textit{and} && \left| \int_T (\operatorname{div} \boldsymbol{p})\, \Phi_{T,k} \,\mathrm{d}\boldsymbol{s} \right| = 0 \quad \textit{for } T \subset \Gamma_h \setminus \Gamma_h^0 \\ &\textit{and} && \boldsymbol{p} \in \beta \boldsymbol{P}. \end{aligned} \tag{DTV-L1-D}$$

Proof. We proceed similarly as in the proof of Theorem 3.6. The functions G, G^* and Λ remain unchanged, and we replace F by

$$\begin{aligned} F(u) &= \sum_{T \subset \Gamma_h^0} \int_T \mathcal{J}_T\{\, |u - f| \,\} \,\mathrm{d}\boldsymbol{s} \\ &= \sum_{T \subset \Gamma_h^0, k} |u - f|\,(X_{T,k})\, C_{T,k}, \end{aligned} \tag{3.26}$$

where

$$C_{T,k} \coloneqq \int_T \Phi_{T,k} \,\mathrm{d}\boldsymbol{s}$$

is non-negative due to Lemma 3.1. We identify again

$$U = \mathcal{DG}_r(\Gamma_h)$$

with its dual but this time not via the regular $L^2(\Gamma_h)$ inner product but via its lumped approximation, i.e.,

$$(u,\, v)_{\text{lumped}} \coloneqq \sum_{T,k} u(X_{T,k})\, v(X_{T,k})\, C_{T,k} \tag{3.27}$$

for $u, v \in \mathcal{DG}_r(\Gamma_h)$. Notice that this choice first of all affects the representation of

$$\Lambda^* : \mathcal{RT}_{r+1}(\Gamma_h) \to U.$$

Indeed, using (3.21) it follows that

$$v = \Lambda^* \boldsymbol{p}$$

is now defined by

$$(u,\, v)_{\text{lumped}} = -\int_{\Gamma_h} (\operatorname{div} \boldsymbol{p})\, u \,\mathrm{d}\boldsymbol{s} \quad \forall u \in \mathcal{DG}_r(\Gamma_h). \tag{3.28}$$

For the particular choice $u = \Phi_{T,k}$, this yields

$$\begin{aligned} v(X_{T,k}) &= (\Lambda^* \boldsymbol{p})(X_{T,k}) \\ &= -\frac{1}{C_{T,k}} \int_T (\operatorname{div} \boldsymbol{p})\, \Phi_{T,k} \,\mathrm{d}\boldsymbol{s} \end{aligned} \tag{3.29}$$

when $C_{T,k} > 0$. As a side remark, we mention that (3.29) means that $\Lambda^* \boldsymbol{p}$ is given locally by Carstensen's quasi-interpolant of $-\operatorname{div} \boldsymbol{p}$ into $\mathcal{P}_r(T)$; see [40]. When $C_{T,k} = 0$, then (3.28) can only be satisfied when

$$\int_T (\operatorname{div} \boldsymbol{p})\, \Phi_{T,k}\, \mathrm{d}\boldsymbol{s} = 0$$

holds, in which case $v(X_{T,k})$ is arbitrary.
Next, since F from (3.26) is a weighted ℓ_1-norm, its convex conjugate can be easily seen to be

$$F^*(u) = \sum_{T \subset \Gamma_h^0, k} u(X_{T,k})\, f(X_{T,k})\, C_{T,k}$$

if

$$|u(X_{T,k})| \leq \chi_{\Gamma_h^0}(X_{T,k})$$

for all triangles T and k s.t. $C_{T,k} > 0$; and

$$F^*(u) = \infty$$

otherwise. Consequently, by (3.29),

$$\begin{aligned} F^*(-\Lambda^* \boldsymbol{p}) &= \sum_{T \subset \Gamma_h^0, k} \int_T (\operatorname{div} \boldsymbol{p})\, \Phi_{T,k}\, \mathrm{d}\boldsymbol{s}\, f(X_{T,k}) \\ &= \sum_{T \subset \Gamma_h^0} \int_T (\operatorname{div} \boldsymbol{p})\, f\, \mathrm{d}\boldsymbol{s} \\ &= \int_{\Gamma_h^0} (\operatorname{div} \boldsymbol{p})\, f\, \mathrm{d}\boldsymbol{s} \end{aligned}$$

holds when

$$\left| \int_T (\operatorname{div} \boldsymbol{p})\, \Phi_{T,k}\, \mathrm{d}\boldsymbol{s} \right| \leq C_{T,k}\, \chi_{\Gamma_h^0}(X_{T,k})$$

is satisfied, and

$$F^*(-\Lambda^* \boldsymbol{p}) = \infty$$

otherwise. Plugging this into (3.22) concludes the proof. Notice that in case

$$T \subset \Gamma_h \setminus \Gamma_h^0,$$

the constraints

$$\int_T (\operatorname{div} \boldsymbol{p})\, \Phi_{T,k}\, \mathrm{d}\boldsymbol{s} = 0 \quad \forall k$$

imply that

$$\operatorname{div} \boldsymbol{p} \equiv 0 \quad \text{on T}$$

since $\operatorname{div} \boldsymbol{p} \in \mathcal{P}_r(T)$; see (3.6). □ □

Remark 3.10 (Discrete dual problem (DTV-L1-D))**.**

(*a*) *The replacement of* $\|\cdot\|_{L^1(\Gamma_h)}$ *in the objective as well as of the* $L^2(\Gamma_h)$ *inner product in* U *by lumped versions obtained by interpolatory quadrature has been successful in other contexts before; see for instance [42]. Here, it is essential in converting the otherwise infinitely many* pointwise *constraints*

$$|\operatorname{div} \boldsymbol{p}| \leq \chi_{\Gamma_h^0}$$

into just finitely many constraints on $\operatorname{div} \boldsymbol{p}$.

(*b*) *Notice that the dual* (DTV-L1-D) *is a linear program.*

(*c*) *One may ask what would have happened if we had applied the same quadrature formula to the* $L^2(\Gamma_h)$ *inner product already in* (DTV-L2). *It can be seen by straightforward calculations that the objective in* (DTV-L2-D) *would have been replaced by*

$$\frac{1}{2} \sum_{T \subset \Gamma_h^0, k} \left(\frac{1}{C_{T,k}} \int_T (\operatorname{div} \boldsymbol{p})\, \Phi_{T,k}\, \mathrm{d}s + f(X_{T,k}) \right)^2 C_{T,k}$$

with summands involving $C_{T,k} = 0$ *omitted. There is, however, no structural advantage compared to* (DTV-L2-D).

3.4 Algorithms for DTV-L2

Our goal in this section is to show that two standard algorithms developed for images on Cartesian grids, with finite difference approximations of gradient and divergence operations, are implementable with the same efficiency in our framework of higher-order finite elements on triangular surface meshes. Specifically, we consider in the following the split Bregman iteration [85] and the primal-dual method of Chambolle and Pock [47]. We refer the reader to the extended preprint [97] for a additional discussion of Chambolle's projection method [44] and a primal-dual active set method similar to [99]. Since these algorithms are well known, we only focus on the main steps in each case. Let us recall that we are seeking a solution $u \in \mathcal{DG}_r$. For simplicity, we exclude the case $r = 3$, i.e., we restrict the discussion to the polynomial degrees $r \in \{0, 1, 2, 4\}$ so that all weights $c_{T,i}$ and $c_{E,j}$ are strictly positive.

3.4.1 Split Bregman Method

The split Bregman method (as a special case of the alternating direction method of multipliers (ADMM)) considers the primal problem (DTV-L2). It introduces an additional variable $\boldsymbol{d}$ so that (DTV-L2) becomes

$$\begin{aligned} \text{Minimize} \quad & \frac{1}{2}\|u - f\|^2_{L^2(\Gamma_h^0)} + \beta \sum_{T,i} c_{T,i} \left|\boldsymbol{d}_{T,i}\right|_2 + \beta \sum_{E,j} c_{E,j} \left|d_{E,j}\right| \\ \text{s.t.} \quad & \boldsymbol{d} = \Lambda u \end{aligned} \tag{3.30}$$

and enforces the constraint $\boldsymbol{d} = \Lambda u = \nabla u$ by an augmented Lagrangian approach. As detailed in (3.18), $\boldsymbol{d}$ has contributions $\nabla u|_T$ per triangle, as well as contributions

$(u_E^- - u_E^+)$ per edge. We can thus express $\boldsymbol{d}$ through its coefficients $\{\boldsymbol{d}_{T,i}\}$ and $\{d_{E,j}\}$ w.r.t. the standard Lagrangian bases of $\mathcal{P}_{r-1}(T)^2$ and $\mathcal{P}_r(E)$,

$$\boldsymbol{d} = \sum_i \boldsymbol{d}_{T,i}\, \varphi_{T,i} + \sum_j d_{E,j}\, \varphi_{E,j}. \tag{3.31}$$

Using (3.10) and (3.11), we rewrite the discrete total variation (3.2) in terms of $\boldsymbol{d}$ and adjoin the constraint $\boldsymbol{d} = \nabla u$ by way of an augmented Lagrangian functional,

$$\frac{1}{2}\|u - f\|^2_{L^2(\Gamma_h^0)} + \beta \sum_{T,i} c_{T,i} \left|\boldsymbol{d}_{T,i}\right|_2 + \beta \sum_{E,j} c_{E,j} \left|d_{E,j}\right| + \frac{\lambda}{2}\|\boldsymbol{d} - \Lambda u - \boldsymbol{b}\|^2_Y. \tag{3.32}$$

Here $\boldsymbol{b}$ is an estimate of the Lagrange multiplier associated with the constraint

$$\boldsymbol{d} = \nabla u \in Y,$$

and $\boldsymbol{b}$ is naturally discretized in the same way as $\boldsymbol{d}$.

Remark 3.11 (Inner product on Y)**.**
So far we have not endowed the space

$$Y = \prod_T \mathcal{P}_{r-1}(T)^2 \times \prod_E \mathcal{P}_r(E)$$

with an inner product. Since elements of Y represent (measure-valued) gradients of $\mathcal{DG}_r(\Gamma_h)$ functions, the natural choice would be to endow Y with a total variation norm of vector measures, which would amount to

$$\sum_T \int_T |\boldsymbol{d}_T|_2 \, \mathrm{d}\boldsymbol{s} + \sum_E \int_E |d_E| \, \mathrm{d}\boldsymbol{s}$$

for $\boldsymbol{d} \in Y$. Clearly, this L^1-type norm is not induced by an inner product. Therefore we are using the L^2 inner product instead. For computational efficiency, it is crucial to consider its lumped version, which amounts to

$$(\boldsymbol{d},\, \boldsymbol{e})_Y := S \sum_{T,i} c_{T,i}\, \boldsymbol{d}_{T,i}\, \boldsymbol{e}_{T,i} + \sum_{E,j} c_{E,j}\, d_{E,j}\, e_{E,j} \tag{3.33}$$

for $\boldsymbol{d}, \boldsymbol{e} \in Y$. The associated norm is denoted as

$$\|\boldsymbol{d}\|^2_Y = (\boldsymbol{d},\, \boldsymbol{d})_Y.$$

Notice that $S > 0$ is a scaling parameter which can be used to improve the convergence of the split Bregman and other iterative methods.

The efficiency of the split Bregman iteration depends on the ability to efficiently minimize (3.32) independently for u, $\boldsymbol{d}$ and $\boldsymbol{b}$, respectively. Let us show that this is the case.

The Gradient Operator Λ

The gradient operator Λ evaluates the cell-wise gradient of $u \in \mathcal{DG}_r(\Gamma_h)$ as well as the edge jump contributions, see (3.18). These are standard operations in any finite element toolbox. For computational efficiency, the matrix realizing $u(x_{T,i})$ and $u(x_{E,j})$ in terms of the coefficients of u can be stored once and for all.

Solving the u-problem

We consider the minimization of (3.32), or equivalently, of

$$\begin{aligned}\frac{1}{2}\|u-f\|^2_{L^2(\Gamma_h^0)}+\frac{\lambda S}{2}\sum_{T,i}c_{T,i}\left|\boldsymbol{d}_{T,i}-\nabla u(x_{T,i})-\boldsymbol{b}_{T,i}\right|_2^2\\ +\frac{\lambda}{2}\sum_{E,j}c_{E,j}\left|d_{E,j}-(u_E^- - u_E^+)(x_{E,j})-b_{E,j}\right|^2\end{aligned} \tag{3.34}$$

w.r.t. $u\in\mathcal{DG}_r(\Gamma_h)$. This problem can be interpreted as a DG finite element formulation of the elliptic partial differential equation

$$-\lambda\,\Delta u+\chi_{\Gamma_h^0}u=\chi_{\Gamma_h^0}f+\lambda\,\operatorname{div}(\boldsymbol{b}-\boldsymbol{d})\quad\text{on }\Gamma_h.$$

More precisely, it constitutes a nonsymmetric interior penalty Galerkin (NIPG) method; compare for instance [135] or [134, Ch. 2.4, 2.6]. Specialized preconditioned solvers for such systems are available, see for instance [6]. However, as proposed in [85], a (block) Gauss–Seidel method may be sufficient. It is convenient to group the unknowns of the same triangle together, which leads to local systems of size $(r+1)(r+2)/2$.

Solving the d-problem

The minimization of (3.32), or equivalently, of

$$\begin{aligned}&\beta\sum_{T,i}c_{T,i}\left|\boldsymbol{d}_{T,i}\right|_2+\frac{\lambda S}{2}\sum_{T,i}c_{T,i}\left|\boldsymbol{d}_{T,i}-\nabla u(x_{T,i})-\boldsymbol{b}_{T,i}\right|_2^2\\ &+\beta\sum_{E,j}c_{E,j}\left|d_{E,j}\right|+\frac{\lambda}{2}\sum_{E,j}c_{E,j}\left|d_{E,j}-(u_E^- - u_E^+)(x_{E,j})-b_{E,j}\right|^2\end{aligned} \tag{3.35}$$

decouples into the minimization of

$$\beta\left|\boldsymbol{d}_{T,i}\right|_2+\frac{\lambda S}{2}\left|\boldsymbol{d}_{T,i}-\nabla u(x_{T,i})-\boldsymbol{b}_{T,i}\right|_2^2 \tag{3.36a}$$

and

$$\beta\left|d_{E,j}\right|+\frac{\lambda}{2}\left|d_{E,j}-(u_E^- - u_E^+)(x_{E,j})-b_{E,j}\right|^2 \tag{3.36b}$$

w.r.t. $\boldsymbol{d}_{T,i}\in\mathbb{R}^2$ and $d_{E,j}\in\mathbb{R}$, respectively.
It is well known that the scalar problem (3.36b) is solved via

$$d_{E,j}=\operatorname{shrink}\left((u_E^- - u_E^+)(x_{E,j})+b_{E,j},\ \frac{\beta}{\lambda}\right),$$

where

$$\operatorname{shrink}(\xi,\gamma):=\max\{|\xi|-\gamma,\ 0\}\operatorname{sgn}\xi,$$

while the minimization of (3.36a) defines the (Euclidean) prox mapping of $|\cdot|_2$ and thus we have

$$\boldsymbol{d}_{T,i}=\operatorname{prox}_{\beta/(\lambda S)|\cdot|_2}\left(\nabla u(x_{T,i})+\boldsymbol{b}_{T,i}\right),$$

where

$$\operatorname{prox}_{\beta/(\lambda S)|\cdot|_2}(\boldsymbol{\xi}) = \boldsymbol{\xi} - \frac{\beta}{\lambda S}\operatorname{proj}_{B_{|\cdot|_2}}\left(\frac{\lambda S}{\beta}\boldsymbol{\xi}\right).$$

Here $\operatorname{proj}_{B_{|\cdot|_2}}$ is the Euclidean orthogonal projection onto the closed $|\cdot|_2$-norm unit ball; see or instance [16, Ex. 6.47]. Similar to (3.36b), we have closed-form solutions of (3.36a):

$$\boldsymbol{d}_{T,i} = \max\left\{\left|\nabla u(x_{T,i}) + \boldsymbol{b}_{T,i}\right|_2 - \frac{\beta}{\lambda S},\ 0\right\} \cdot \frac{\nabla u(x_{T,i}) + \boldsymbol{b}_{T,i}}{\left|\nabla u(x_{T,i}) + \boldsymbol{b}_{T,i}\right|_2}$$

When $\nabla u(x_{T,i}) + \boldsymbol{b}_{T,i} = 0$, the formula is understood as $\boldsymbol{d}_{T,i} = 0$.

Updating $\boldsymbol{b}$

This is simply achieved by replacing the current values for $\boldsymbol{b}_{T,i}$ and $b_{E,j}$ by

$$\boldsymbol{b}_{T,i} + \nabla u(x_{T,i}) - \boldsymbol{d}_{T,i}$$

and

$$b_{E,j} + (u_E^- - u_E^+)(x_{E,j}) - d_{E,j},$$

respectively.
The quantities $\boldsymbol{b}_{T,i}$ and $b_{E,j}$ represent discrete multipliers associated with the components of the constraint

$$\boldsymbol{d} = \Lambda u.$$

Here we clarify how these multipliers relate to the dual variable $\boldsymbol{p} \in \mathcal{RT}_{r+1}(\Gamma_h)$ in (DTV-L2-D). In fact, let us interpret $\boldsymbol{b}_{T,i}$ as the coefficients of a function $\boldsymbol{b}_T \in \mathcal{P}_{r-1}(T)$ and $b_{E,j}$ as the coefficients of a function $b_E \in \mathcal{P}_r(E)$ w.r.t. the standard nodal bases, just as in (3.31). Moreover, let us define a function $\bar{\boldsymbol{p}} \in \mathcal{RT}_{r+1}(\Gamma_h)$ by specifying its coefficients as follows,

$$\begin{aligned} \boldsymbol{\sigma}_{T,i}(\bar{\boldsymbol{p}}) &\coloneqq \lambda S\, \boldsymbol{b}_{T,i}\, c_{T,i} \\ \sigma_{E,j}(\bar{\boldsymbol{p}}) &\coloneqq \lambda\, b_{E,j}\, c_{E,j}. \end{aligned} \tag{3.37}$$

Then

$$\begin{aligned} \int_T \bar{\boldsymbol{p}} \cdot (\nabla u - \boldsymbol{d}_T)\,\mathrm{d}\boldsymbol{s} &= \sum_i \int_T \bar{\boldsymbol{p}}\, \varphi_{T,i} \cdot \left(\nabla u(x_{T,i}) - \boldsymbol{d}_{T,i}\right)\mathrm{d}\boldsymbol{s} \\ &= \lambda S \sum_i c_{T,i}\, \boldsymbol{b}_{T,i} \cdot \left(\nabla u(x_{T,i}) - \boldsymbol{d}_{T,i}\right) \end{aligned}$$

and

$$\begin{aligned} \int_E (\bar{\boldsymbol{p}}_E^+ \cdot \boldsymbol{\mu}_E^+)\,((u_E^- - u_E^+) - d_E)\,\mathrm{d}\boldsymbol{s} &= \sum_j \int_E (\bar{\boldsymbol{p}}_E^+ \cdot \boldsymbol{\mu}_E^+)\,\varphi_{E,j}\big((u_E^- - u_E^+)(x_{E,j}) - d_{E,j}\big)\,\mathrm{d}\boldsymbol{s} \\ &= \lambda \sum_j c_{E,j}\, b_{E,j}\,((u_E^- - u_E^+)(x_{E,j}) - d_{E,j}), \end{aligned}$$

and these are precisely the terms appearing in the discrete augmented Lagrangian functional (3.32). Consequently, $\bar{\boldsymbol{p}}$ can be interpreted as the Lagrange multiplier associated with the components of the constraint

$$\boldsymbol{d} = \Lambda u,$$

when the latter are adjoined using the lumped $\boldsymbol{L}^2(T)$ and $L^2(E)$ inner products. It can be shown using the KKT conditions for (3.30) and the optimality conditions (3.25) that $\bar{\boldsymbol{p}}$ defined by (3.37) solves the dual problem (DTV-L2-D). To prove this assertion, suppose that

$$(u, \boldsymbol{d})$$

is optimal for (3.30). We will show that

$$(u, \bar{\boldsymbol{p}})$$

satisfy the necessary and sufficient optimality conditions (3.25). The Lagrangian for (3.30) can be written as

$$F(u) + \beta\, G(\boldsymbol{d}) + \langle \bar{\boldsymbol{p}},\, \Lambda u - \boldsymbol{d} \rangle$$

and the optimality of $(u, \boldsymbol{d})$ implies

$$\bar{\boldsymbol{p}} \in \partial(\beta\, G)(\boldsymbol{d}) = \partial(\beta\, G)(\Lambda u).$$

On the other hand, u is optimal for (DTV-L2), which implies

$$0 \in \partial F(u) + \Lambda^* \partial(\beta\, G)(\Lambda u)$$

and thus

$$-\Lambda^* \bar{\boldsymbol{p}} \in \partial F(u).$$

Altogether, we have verified (3.25), which is necessary and sufficient for $\bar{\boldsymbol{p}}$ to be optimal for (DTV-L2-D).
For convenience, we specify the split Bregman iteration in Algorithm 2.

Algorithm 2 Split Bregman algorithm for (DTV-L2)

1: Set $u^{(0)} := f \in \mathcal{DG}_r(\Gamma_h)$, $\boldsymbol{b}^{(0)} := \mathbf{0} \in Y$ and $\boldsymbol{d}^{(0)} := \mathbf{0} \in Y$
2: Set $n := 0$
3: **while** not converged **do**
4: Minimize (3.34) for $u^{(n+1)}$ with data $\boldsymbol{b}^{(n)}$ and $\boldsymbol{d}^{(n)}$
5: Minimize (3.36) for $\boldsymbol{d}^{(n+1)}$ with data $u^{(n+1)}$ and $\boldsymbol{b}^{(n)}$
6: Set $\boldsymbol{b}_{T,i}^{(n+1)} := \boldsymbol{b}_{T,i}^{(n)} + \nabla u^{(n+1)}(x_{T,i}) - \boldsymbol{d}_{T,i}^{(n+1)}$
7: Set $b_{E,j}^{(n+1)} := b_{E,j}^{(n)} + (u_E^- - u_E^+)^{(n+1)}(x_{E,j}) - d_{E,j}^{(n+1)}$
8: Set $n := n + 1$
9: **end while**
10: Set $\boldsymbol{p}^{(n)}$ by (3.37) with data $\boldsymbol{b}^{(n)}$

3.4.2 Chambolle–Pock Method

The method by [47], also known as primal-dual extragradient method, see [92], is based on a reformulation of the optimality conditions in terms of the prox operators pertaining to F and G^*. We recall that F is defined by

$$F(u) = \frac{1}{2}\|u - f\|^2_{L^2(\Gamma_h^0)}$$

on $U = \mathcal{DG}_r(\Gamma_h)$. Moreover, G^* is defined on $Y^* \cong \mathcal{RT}_{r+1}(\Gamma_h)$ by

$$G^* = I_{\boldsymbol{P}},$$

the indicator function of $\boldsymbol{P}$, see (3.17).
Notice that prox operators depend on the inner product in the respective space. We recall that U has been endowed with the (regular, non-lumped) $L^2(\Gamma_h)$ inner product, see the proof of Theorem 3.6. For the space Y we are using again the inner product defined in (3.33). Exploiting the duality product (3.20) between Y and $Y^* \cong \mathcal{RT}_{r+1}(\Gamma_h)$ it is then straightforward to derive the Riesz map

$$R : Y \ni \boldsymbol{d} \mapsto \boldsymbol{p} \in Y^*.$$

In terms of the coefficients of $\boldsymbol{p}$, we have

$$\begin{aligned} \boldsymbol{\sigma}_{T,i}(\boldsymbol{p}) &= c_{T,i} S\, \boldsymbol{d}_{T,i} \\ \sigma_{E,j}(\boldsymbol{p}) &= c_{E,j}\, d_{E,j}. \end{aligned} \tag{3.38}$$

Consequently, the induced inner product in $\mathcal{RT}_{r+1}(\Gamma_h)$ becomes

$$(\boldsymbol{p}, \boldsymbol{q})_{Y^*} := \sum_{T,i} \frac{1}{c_{T,i} S}\, \boldsymbol{\sigma}_{T,i}(\boldsymbol{p}) \cdot \boldsymbol{\sigma}_{T,i}(\boldsymbol{q}) + \sum_{E,j} \frac{1}{c_{E,j}}\, \sigma_{E,j}(\boldsymbol{p})\, \sigma_{E,j}(\boldsymbol{q}). \tag{3.39}$$

To summarize, the inner products in Y, Y^* as well as the Riesz map are realized efficiently by simple, diagonal operations on the coefficients.

Solving the F-prox

Let $\sigma > 0$. The prox-operator of σF, denoted by

$$\operatorname{prox}_{\sigma F}(\bar{u}) : U \to U,$$

is defined as $u = \operatorname{prox}_{\sigma F}(\bar{u})$ if and only if

$$u = \operatorname*{arg\,min}_{v \in \mathcal{DG}_r(\Gamma_h)} \frac{1}{2}\|v - \bar{u}\|^2_{L^2(\Gamma_h)} + \frac{\sigma}{2}\|v - f\|^2_{L^2(\Gamma_h^0)}.$$

For given data $\bar{u} \in \mathcal{DG}_r(\Gamma_h)$ and $f \in \mathcal{DG}_r(\Gamma_h^0)$, it is easy to see that a necessary and sufficient condition is $u - \bar{u} + \sigma\,(u - f) = 0$, which amounts to the coefficient-wise formula

$$u_{T,k} = \frac{1}{1 + \sigma_{T,k}}\big(\bar{u}_{T,k} + \sigma_{T,k} f_{T,k}\big), \tag{3.40}$$

where $\sigma_{T,k} = \sigma$ if $T \subset \Gamma_h^0$ and $\sigma_{T,k} = 0$ otherwise.

Solving the G^*-prox

Let $\tau > 0$. The prox-operator

$$\operatorname{prox}_{\tau G^*} : Y^* \cong \mathcal{RT}_{r+1}(\Gamma_h) \to Y^*$$

is defined as $\boldsymbol{p} = \operatorname{prox}_{\tau G^*}(\bar{\boldsymbol{p}})$ if and only if

$$\boldsymbol{p} = \operatorname*{arg\,min}_{\boldsymbol{q} \in \mathcal{RT}_{r+1}(\Gamma_h)} \frac{1}{2} \|\boldsymbol{q} - \bar{\boldsymbol{p}}\|_{Y^*}^2 \text{ s.t. } \boldsymbol{q} \in \boldsymbol{P}. \tag{3.41}$$

Similarly, the prox operator for $(\beta G)^*$ is obtained by replacing $\boldsymbol{P}$ by $\beta \boldsymbol{P}$, for any $\tau > 0$. Due to the diagonal structure of the inner product in Y^*, this is efficiently implementable. When $\bar{\boldsymbol{p}} \in \mathcal{RT}_{r+1}(\Gamma_h)$, then we obtain the solution in terms of the coefficients, similar to (3.36), as

$$\begin{aligned} \boldsymbol{\sigma}_{T,i}(\boldsymbol{p}) &= \operatorname{proj}_{\beta c_{T,i} B_{|\cdot|_2}} (\boldsymbol{\sigma}_{T,i}(\bar{\boldsymbol{p}})) \\ &= \min \left\{ |\boldsymbol{\sigma}_{T,i}(\bar{\boldsymbol{p}})|_2 \,,\, \beta\, c_{T,i} \right\} \frac{\boldsymbol{\sigma}_{T,i}(\bar{\boldsymbol{p}})}{|\boldsymbol{\sigma}_{T,i}(\bar{\boldsymbol{p}})|_2} \end{aligned} \tag{3.42a}$$

and

$$\sigma_{E,j}(\boldsymbol{p}) = \min \left\{ \left|\sigma_{E,j}(\bar{\boldsymbol{p}})\right| \,,\, \beta\, c_{E,j} \right\} \frac{\sigma_{E,j}(\bar{\boldsymbol{p}})}{\left|\sigma_{E,j}(\bar{\boldsymbol{p}})\right|}. \tag{3.42b}$$

Both formulas are understood as $\boldsymbol{\sigma}_{T,i}(\boldsymbol{p}) = 0$ and $\sigma_{E,j}(\boldsymbol{p}) = 0$, respectively, when $|\boldsymbol{\sigma}_{T,i}(\bar{\boldsymbol{p}})|_2 = 0$ or $\left|\sigma_{E,j}(\bar{\boldsymbol{p}})\right| = 0$. An implementation of the Chambolle–Pock method is given in Algorithm 3. Notice that the solution of the $\operatorname{prox}_{\tau G^*}$ problem is independent of the scaling parameter $S > 0$. However S enters through the Riesz isomorphism (3.38).

Algorithm 3 Chambolle–Pock algorithm for (DTV-L2)

1: Set $u^{(0)} := f \in \mathcal{DG}_r(\Gamma_h)$, $\boldsymbol{p}^{(0)} := \boldsymbol{0} \in \mathcal{RT}_{r+1}(\Gamma_h)$ and $\bar{\boldsymbol{p}}^{(0)} := \boldsymbol{0} \in \mathcal{RT}_{r+1}(\Gamma_h)$
2: Set $n := 0$
3: **while** not converged **do**
4: Set $v^{(n+1)} := \operatorname{div} \bar{\boldsymbol{p}}^{(n)} \in \mathcal{DG}_r(\Gamma_h)$
5: Set $u^{(n+1)} := \operatorname{prox}_{\sigma F}(u^{(n)} + \sigma\, v^{(n+1)})$, see (3.40)
6: Set $\boldsymbol{d}^{(n+1)} := \Lambda u^{(n+1)} \in Y$
7: Set $\boldsymbol{q}^{(n+1)} := R\, \boldsymbol{d}^{(n+1)} \in \mathcal{RT}_{r+1}(\Gamma_h)$, where R is the Riesz map (3.38)
8: Set $\boldsymbol{p}^{(n+1)} := \operatorname{prox}_{\tau(\beta G)^*}(\boldsymbol{p}^{(n)} + \tau\, \boldsymbol{q}^{(n+1)})$, see (3.42)
9: Set $\bar{\boldsymbol{p}}^{(n+1)} := \boldsymbol{p}^{(n+1)} + \theta\, (\boldsymbol{p}^{(n+1)} - \boldsymbol{p}^{(n)})$
10: Set $n := n + 1$
11: **end while**

3.4.3 Chambolle's Projection Method

Chambolle's method was introduced in [44] and it solves (DTV-L2) via its dual (DTV-L2-D). We also require $\Gamma_h^0 = \Gamma$ here. Squaring the constraints pertaining to $\boldsymbol{p} \in \beta \boldsymbol{P}$, we obtain

the Lagrangian

$$\begin{aligned}\frac{1}{2}\|\operatorname{div} \boldsymbol{p} + f\|^2_{L^2(\Gamma_h)} + \sum_{T,i} \frac{\alpha_{T,i}}{2} \left(|\boldsymbol{\sigma}_{T,i}(\boldsymbol{p})|_2^2 - \beta^2 c_{T,i}^2 \right) \\ + \sum_{E,j} \frac{\alpha_{E,j}}{2} \left(\left|\sigma_{E,j}(\boldsymbol{p})\right|^2 - \beta^2 c_{E,j}^2 \right),\end{aligned} \tag{3.43}$$

where $\alpha_{T,i}$ and $\alpha_{E,j}$ are Lagrange multipliers. Consequently, the KKT conditions associated with this formulation of (DTV-L2-D) are

$$\begin{aligned}(\operatorname{div} \boldsymbol{p} + f,\, \operatorname{div} \delta\boldsymbol{p})_{L^2(\Gamma_h)} + \sum_{T,i} \alpha_{T,i}\, \boldsymbol{\sigma}_{T,i}(\boldsymbol{p}) \cdot \boldsymbol{\sigma}_{T,i}(\delta\boldsymbol{p}) \\ + \sum_{E,j} \alpha_{E,j}\, \sigma_{E,j}(\boldsymbol{p})\, \sigma_{E,j}(\delta\boldsymbol{p}) = 0\end{aligned} \tag{3.44}$$

for all $\delta\boldsymbol{p} \in \mathcal{RT}_{r+1}(\Gamma_h)$, together with the complementarity conditions

$$0 \le \alpha_{T,i} \quad \perp \quad |\boldsymbol{\sigma}_{T,i}(\boldsymbol{p})|_2 - \beta\, c_{T,i} \le 0 \qquad \forall T, i \tag{3.45a}$$

$$0 \le \alpha_{E,j} \quad \perp \quad \left|\sigma_{E,j}(\boldsymbol{p})\right| - \beta\, c_{E,j} \le 0 \qquad \forall E, j \tag{3.45b}$$

Let us observe that the first term in (3.44) can be written as

$$-\langle \Lambda(\operatorname{div} \boldsymbol{p} + f),\, \delta\boldsymbol{p} \rangle_{Y,Y^*},$$

and hence as

$$-\sum_T \int_T \nabla u|_T \cdot \delta\boldsymbol{p}\, \mathrm{d}s - \sum_E \int_E (\delta\boldsymbol{p}_E^+ \cdot \boldsymbol{\mu}_E^+)\, (u_E^- - u_E^+)\, \mathrm{d}s,$$

where we set $u := \operatorname{div} \boldsymbol{p} + f$ as an abbreviation in accordance with (3.24). By selecting directions $\delta\boldsymbol{p}$ from the collections $\{\boldsymbol{\psi}_i^T\}$ and $\{\boldsymbol{\psi}_j^E\}$ of $\mathcal{RT}_{r+1}(\Gamma_h)$ basis functions, see Section 3.1, we infer that (3.44) is equivalent to

$$-\nabla u(x_{T,i}) + \alpha_{T,i}\, \boldsymbol{\sigma}_{T,i}(\boldsymbol{p}) = 0 \qquad \forall T, i \tag{3.46a}$$

$$-(u_E^- - u_E^+)(x_{E,j}) + \alpha_{E,j}\, \sigma_{E,j}(\boldsymbol{p}) = 0 \qquad \forall E, j. \tag{3.46b}$$

A simple calculation similar as in [44] then shows that (3.45) and (3.46) imply

$$\begin{aligned}\beta\, \alpha_{T,i}\, c_{T,i} &= |\nabla u(x_{T,i})|_2, \\ \beta\, \alpha_{E,j}\, c_{E,j} &= \left|(u_E^- - u_E^+)(x_{E,j})\right|.\end{aligned} \tag{3.47}$$

In order to re-derive Chambolle's algorithm for the setting at hand, it remains to rewrite the directional derivative (3.44) in terms of the gradient $\boldsymbol{g} \in Y^*$ w.r.t. the Y^* inner product (3.39). We obtain that $\boldsymbol{g}$ is given by its coefficients

$$\boldsymbol{\sigma}_{T,i}(\boldsymbol{g}) = c_{T,i} \left(\alpha_{T,i}\, \boldsymbol{\sigma}_{T,i}(\boldsymbol{p}) - \nabla u(x_{T,i}) \right), \tag{3.48a}$$

$$\sigma_{E,j}(\boldsymbol{g}) = c_{E,j} \left(\alpha_{E,j}\, \sigma_{E,j}(\boldsymbol{p}) - (u_E^- - u_E^+)(x_{E,j}) \right). \tag{3.48b}$$

Given an iterate for $\boldsymbol{p}$, the main steps of the algorithm are then to update the auxiliary quantity

$$u = \operatorname{div} \boldsymbol{p} + f$$

as well as the multipliers $\alpha_{T,i}$ and $\alpha_{E,j}$ according to (3.47), and take a semi-implicit gradient step with a suitable step length to update $\boldsymbol{p}$. Since all of these steps are inexpensive, Chambolle's method can be implemented just as efficiently as its finite difference version originally given in [44]. For the purpose of comparison, we point out that one step of the method can be written compactly as

$$\boldsymbol{\sigma}_{T,i}(\boldsymbol{p}^{(n+1)}) := \frac{\boldsymbol{\sigma}_{T,i}(\boldsymbol{p}^{(n)}) + \tau\, c_{T,i} \nabla(\operatorname{div} \boldsymbol{p}^{(n)} + f)(x_{T,i})}{1 + \tau\, \beta^{-1} \left| \nabla(\operatorname{div} \boldsymbol{p}^{(n)} + f)(x_{T,i}) \right|_2},$$
$$\sigma_{E,j}(\boldsymbol{p}^{(n+1)}) := \frac{\sigma_{E,j}(\boldsymbol{p}^{(n)}) + \tau\, c_{E,j} [\![\operatorname{div} \boldsymbol{p}^{(n)} + f]\!](x_{E,j})}{1 + \tau\, \beta^{-1} \left| [\![\operatorname{div} \boldsymbol{p}^{(n)} + f]\!](x_{E,j}) \right|}.$$

for all T and i, and for all E and j, respectively. Let us mention that our variable $\boldsymbol{p}$ differs by a factor of β from the one used in [44]. Moreover, in the implementation given as Algorithm 4, we found it convenient to rename $\alpha_{T,i}\, c_{T,i}$ as $\gamma_{T,i}$, and similarly for the edge based quantities. Notice that $\gamma_{T,i}$ and $\gamma_{E,j}$ can be conveniently stored, for instance, as the coefficients of a $\mathcal{DG}_{r-1}(\Gamma_h)$ function, and another $\mathcal{DG}_r$ function on the skeleton of the mesh, i.e., the union of all interior edges.

Algorithm 4 Chambolle's algorithm for (DTV-L2) with $s = 2$

1: Set $\boldsymbol{p}^{(0)} := \mathbf{0} \in \mathcal{RT}_{r+1}(\Gamma_h)$
2: Set $n := 0$
3: **while** not converged **do**
4: Set $u^{(n)} := \operatorname{div} \boldsymbol{p}^{(n)} + f \in \mathcal{DG}_r(\Gamma_h)$
5: Set $\gamma_{T,i} := \beta^{-1} \left| \nabla u^{(n)}(x_{T,i}) \right|_2$ // $\gamma_{T,i} = \alpha_{T,i}\, c_{T,i}$, see (3.47)
6: Set $\gamma_{E,j} := \beta^{-1} \left| (u_E^- - u_E^+)^{(n)}(x_{E,j}) \right|$ // $\gamma_{E,j} = \alpha_{E,j}\, c_{E,j}$, see (3.47)
7: Set $\boldsymbol{\sigma}_{T,i}(\boldsymbol{p}^{(n+1)}) := \dfrac{\boldsymbol{\sigma}_{T,i}(\boldsymbol{p}^{(n)}) + \tau\, c_{T,i} \nabla u^{(n)}(x_{T,i})}{1 + \tau\, \gamma_{T,i}}$
8: Set $\sigma_{E,j}(\boldsymbol{p}^{(n+1)}) := \dfrac{\sigma_{E,j}(\boldsymbol{p}^{(n)}) + \tau\, c_{E,j} (u_E^- - u_E^+)^n(x_{E,j})}{1 + \tau\, \gamma_{E,j}}$
9: Set $n := n + 1$
10: **end while**

3.4.4 Implementation Details

Our implementation was carried out in the finite element framework FENICS (version 2017.2). We refer the reader to [4, 114] for background reading. FENICS supports finite elements of various types on simplicial meshes, including $\mathcal{CG}_r$, $\mathcal{DG}_r$ and $\mathcal{RT}_{r+1}$ elements of arbitrary order. Although we focus on this piece of software, the content of this section will apply to other finite element frameworks as well.

While the bases for the spaces $\mathcal{CG}_r$ and $\mathcal{DG}_r$ in FENICS are given by the standard nodal basis functions as described in Section 3.1, the implementation of $\mathcal{RT}_{r+1}$ elements in FENICS uses degrees of freedom based on point evaluations of $\boldsymbol{p}$ and $\boldsymbol{p}_E^+ \cdot \boldsymbol{\mu}_E^+$, rather than the integral-type dofs in (3.7). Since we wish to take advantage of the simple structure of the constraints in the dual representation (3.12) of $|u|_{DTV(\Gamma_h)}$ however, we rely on the choice of dofs described in (3.7). In order to avoid a global basis transformation, we implemented our own version of the $\mathcal{RT}_{r+1}$ finite element in FENICS.
Our implementation uses the dofs in (3.7) on the reference cell $\widehat{T}$. As usual in finite element methods, an arbitrary cell T is then obtained via an affine geometry transformation, i.e.,

$$G_T : \widehat{T} \to T, \qquad G_T(\widehat{x}) := B_T\,\widehat{x} + b_T,$$

where $B_T \in \mathbb{R}^{3\times 2}$ is a matrix of rank 2 and $b_T \in \mathbb{R}^3$. By defining the matrix

$$\tilde{B}_T = (B_T|\boldsymbol{n}_T) \in \mathbb{R}^{3\times 3},$$

where the oriented normal vector $\boldsymbol{n}_T$ of the triangle T is added as a third column to the matrix B_T, we are able to state G_T differently

$$G_T(\widehat{x}) := \tilde{B}_T \begin{pmatrix} \widehat{x} \\ 0 \end{pmatrix} + b_T.$$

It is easy to see that

$$\sqrt{\det B_T^\top B_T} = \left|\det \tilde{B}_T\right|,$$

but the $\operatorname{sign}\left(\det \tilde{B}_T\right)$, which shows if G_T is orientation preserving, will be important below. Therefore, we can define the matrix

$$B_T^{-1} \in \mathbb{R}^{2\times 3}$$

through

$$B_T^{-1} y = x \iff B_T x = y \quad \forall y \in \operatorname{Im} B_T.$$

In a similar way, the inverse mapping G_T^{-1} of G_T is defined. We mention that the transformation G_T may not necessarily be orientation preserving. In contrast to $\mathcal{CG}$ and $\mathcal{DG}$ elements, a second transformation is required for the ($\boldsymbol{H}(\operatorname{div};\Gamma_h)$-conforming) $\mathcal{RT}$ space to define the dofs and basis functions on the world cell T from the dofs and basis functions on $\widehat{T}$. This is achieved via the (contravariant) Piola transform; see for instance [76, Ch. 1.4.7] or [137]. In terms of functions $\widehat{\boldsymbol{p}}$ from the local polynomial space, we have

$$\begin{aligned} P_T &: \mathcal{P}_r(\widehat{T})^2 + \widehat{\boldsymbol{x}}\,\mathcal{P}_r(\widehat{T}) \to \mathcal{P}_r(T)^2 + \boldsymbol{x}\,\mathcal{P}_r(T), \\ P_T(\widehat{\boldsymbol{p}}) &= \frac{1}{\det \tilde{B}_T}\, B_T\,[\widehat{\boldsymbol{p}} \circ G_T^{-1}]. \end{aligned}$$

The Piola transform preserves tangent directions on edges, as well as co-normal traces of vector fields, up to edge lengths. It satisfies

$$\begin{aligned} \left|\widehat{E}\right| \widehat{\boldsymbol{p}}_{\widehat{E}} \cdot \widehat{\boldsymbol{\mu}}_{\widehat{E}} &= \pm |E|\ \boldsymbol{p}_E^+ \cdot \boldsymbol{\mu}_E^+ \\ \left|\widehat{T}\right| B_T\,\widehat{\boldsymbol{p}} &= \pm |T|\ \boldsymbol{p}, \end{aligned} \tag{3.49}$$

where $\widehat{E}$ is an edge of $\widehat{T}$, $\widehat{\boldsymbol{\mu}}_{\widehat{E}}$ is the corresponding co-normal and $E = G_T(\widehat{E})$; see for instance [76, Lem. 1.84]. The correct choice of the sign in (3.49) depends on orientation preserving of G_T and the relative orientations of $P_T(\widehat{\boldsymbol{\mu}}_{\widehat{E}})$ and $\boldsymbol{\mu}_E^+$. However the sign is not important since all operations depending on the dofs or coefficients, such as $\boldsymbol{\sigma}_{T,i}(\boldsymbol{p})$, are sign invariant, notably the constraint set in (3.17).
We denote by $\widehat{\sigma}_{\widehat{T},i}$ and $\widehat{\sigma}_{\widehat{E},j}$ the degrees of freedom as in (3.7), defined in terms of the nodal basis functions $\widehat{\varphi}_{\widehat{T},i} \in \mathcal{P}_{r-1}(\widehat{T})$ and $\widehat{\varphi}_{\widehat{E},j} \in \mathcal{P}_r(\widehat{E})$ on the reference cell. Let us consider how these degrees of freedom act on the world cell. Indeed, the relations above imply

$$\begin{aligned}
\widehat{\sigma}_{\widehat{T},i}(\widehat{\boldsymbol{p}}) &:= \int_{\widehat{T}} \widehat{\varphi}_{\widehat{T},i}\, \widehat{\boldsymbol{p}}\, \mathrm{d}\widehat{x} \\
&= \operatorname{sign}\left(\det \tilde{B}_T\right) \int_T \varphi_{T,i}\, B_T^{-1}\, \boldsymbol{p}\, \mathrm{d}x \qquad (3.50a) \\
&= \operatorname{sign}\left(\det \tilde{B}_T\right) B_T^{-1} \boldsymbol{\sigma}_{T,i}(\boldsymbol{p}), \\
\widehat{\sigma}_{\widehat{E},j}(\widehat{\boldsymbol{p}}) &:= \int_{\widehat{E}} \widehat{\varphi}_{\widehat{E},j}\, (\widehat{\boldsymbol{p}}_{\widehat{E}} \cdot \widehat{\boldsymbol{\mu}}_{\widehat{E}})\, \mathrm{d}\widehat{s} \\
&= \pm \int_E \varphi_{E,j}\, (\boldsymbol{p}_E^+ \cdot \boldsymbol{\mu}_E^+)\, \mathrm{d}s \qquad (3.50b) \\
&= \pm\, \sigma_{E,j}(\boldsymbol{p}),
\end{aligned}$$

where we used that Lagrangian basis functions are transformed according to

$$\varphi_{T,i} = \widehat{\varphi}_{\widehat{T},i} \circ G_T^{-1},$$

and similarly for the edge-based quantities.
Notice that while (3.50b) agrees (possibly up to the sign) with our preferred set of edge-based dofs (3.7b), the interior dofs $\widehat{\sigma}_{\widehat{T},i}$ are related to the desired dofs $\sigma_{T,i}$ from (3.7a) via

$$\boldsymbol{\sigma}_{T,i}(\boldsymbol{p}) = \operatorname{sign}\left(\det \tilde{B}_T\right) B_T\, \widehat{\boldsymbol{\sigma}}_{\widehat{T},i}(\boldsymbol{p}). \qquad (3.51)$$

Notice that this transformation is impossible to avoid since the dofs (3.7a) are not invariant under the Piola transform. However, (3.51) is completely local to the triangle and inexpensive to evaluate. Although not required for our numerical computations, we mention for completeness that the corresponding dual basis functions are related via

$$\boldsymbol{\psi}_i^T = \frac{1}{\det \tilde{B}_T}\, B_T\, \widehat{\boldsymbol{\psi}}_i^T\, B_T^{-1}. \qquad (3.52)$$

To summarize this discussion, functions $\boldsymbol{p} \in \mathcal{RT}_{r+1}(\Gamma_h)$ will be represented in terms of coefficients w.r.t. the dofs $\{\sigma_{E,j}\}$ and $\{\widetilde{\sigma}_{T,i}\}$ in our FEniCS implementation of the $\mathcal{RT}$ space. Transformations to and from the desired dofs $\{\boldsymbol{\sigma}_{T,i}\}$ will be performed for all operations manipulating directly the coefficients of an $\mathcal{RT}_{r+1}$ function. For instance, the projection operation in (3.42) for the Chambolle–Pock Algorithm 3 would be implemented as

$$\widehat{\boldsymbol{\sigma}}_{\widehat{T},i}(\boldsymbol{p}) = \operatorname{sign}\left(\det \tilde{B}_T\right) B_T^{-1} \min\left\{ \left| B_T\, \widehat{\boldsymbol{\sigma}}_{\widehat{T},i}(\bar{\boldsymbol{p}}) \right|_2,\ \beta\, c_{T,i} \right\} \cdot \frac{B_T\, \widehat{\boldsymbol{\sigma}}_{\widehat{T},i}(\bar{\boldsymbol{p}})}{\left| B_T\, \widehat{\boldsymbol{\sigma}}_{\widehat{T},i}(\bar{\boldsymbol{p}}) \right|_2}.$$

3.5 Numerical Results

In this section we present some numerical results for (DTV-L2). Our goals are to demonstrate computational efficiency of Algorithm 2 w.r.t. varying polynomial degree $r \in \{0,1,2\}$, and to exhibit the benefits of polynomial orders $r \geq 1$ for image quality, both for denoising and inpainting applications. For results of Algorithm 3, we refer to [97].

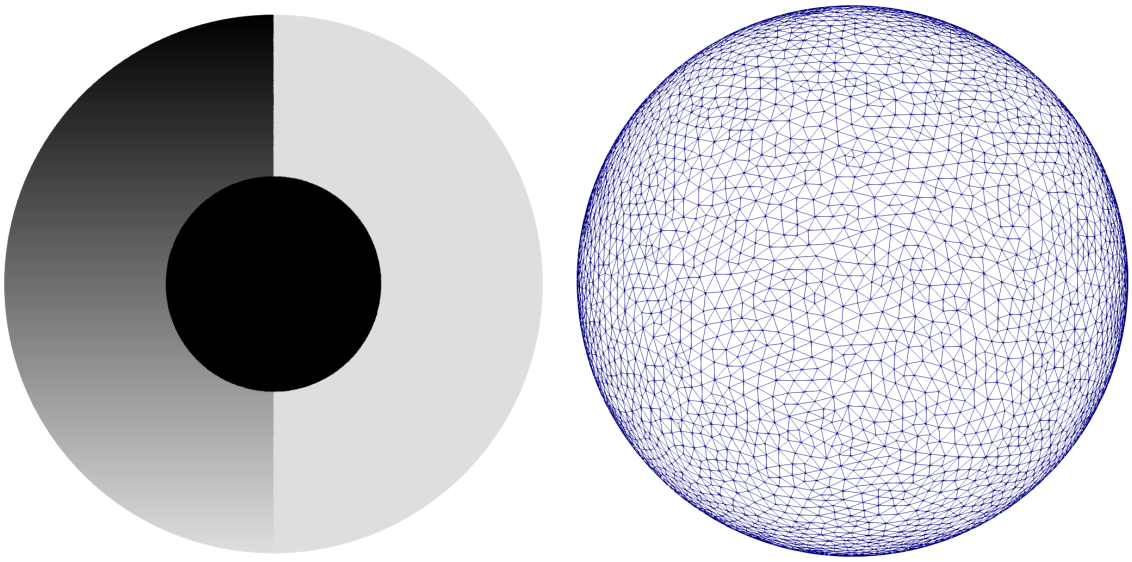

Figure 3.2: Non-discrete test texture (left), which will be projected on the sphere mesh (right) and interpolated into $\mathcal{DG}_r$ with $r = 0,1,2$.

In our tests, we use the a sphere mesh with texture as displayed in Figure 3.2, which has data in the range $[0,1]$. The sphere mesh has radius 1 and consists of 14448 cells and 7226 vertices. In all of the following tests, noise is added to each degree of freedom in the form of a normally distributed random variable with standard deviation $\sigma = 1 \times 10^{-1}$ and zero mean. Our implementation uses the finite element framework FEniCS (version 2017.2) and the visualization was achieved in ParaView.

A stopping criterion for Algorithms 2 to 4 can be based on the primal-dual gap

$$F(u) + \beta\, G(\Lambda u) + F^*(\Lambda^* \boldsymbol{p}) + \beta\, G^*(\boldsymbol{p}/\beta). \tag{3.53}$$

Notice that since $G^* = \chi_{\boldsymbol{P}}$ is the indicator function of the constraint set $\boldsymbol{P}$, the last term is either 0 or ∞, and (3.53) can therefore not directly serve as a meaningful stopping criterion. Instead, we omit the last term in (3.53) and introduce a distance-to-feasibility measure for $\boldsymbol{p}$ as a second criterion. For the latter, we utilize the difference of $\boldsymbol{p}$ and its Y^*-orthogonal projection onto $\beta\boldsymbol{P}$, measured in the Y^*-norm squared. Straightforward calculations then show that we obtain the following specific expressions:

$$\begin{aligned}\mathrm{GAP}(u,\boldsymbol{p}) \coloneqq{}& \frac{1}{2}\|u-f\|^2_{L^2(\Gamma_0)} + \frac{1}{2}\|\operatorname{div}\boldsymbol{p}+f\|^2_{L^2(\Gamma_0)} \\ &- \frac{1}{2}\|f\|^2_{L^2(\Gamma_0)} + \beta\sum_T \int_T \mathcal{I}_T\{\,|\nabla u|_2\,\}\,\mathrm{d}s + \beta\sum_E \int_E \mathcal{I}_E\{\,|u_E^- - u_E^+|_2\,\}\,\mathrm{d}s\end{aligned}$$

and

$$\begin{aligned}\mathrm{INFEAS}(\boldsymbol{p}) := &\sum_{T,i} \frac{1}{c_{T,i} S} \max\left\{ \, |\boldsymbol{\sigma}_{T,i}(\boldsymbol{p})|_2 - \beta \, c_{T,i}, \, 0 \right\}^2 \\ &+ \sum_{E,j} \frac{1}{c_{E,j}} \max\left\{ \, |\sigma_{E,j}(\boldsymbol{p})| - \beta \, c_{E,j}, \, 0 \right\}^2\end{aligned}$$

In our numerical experiments, we stop either algorithm as soon as the iterates $(u, \boldsymbol{p})$ satisfy the following conditions:

$$\begin{aligned}|\mathrm{GAP}(u, \boldsymbol{p})| &\leq \varepsilon_{\mathrm{rel}} \, \mathrm{GAP}(f, \mathbf{0}) \\ \mathrm{INFEAS}_2(\boldsymbol{p}) &\leq 1 \times 10^{-20}\end{aligned} \tag{3.54}$$

with $\varepsilon_{\mathrm{rel}} = 1 \times 10^{-3}$.

3.5.1 Denoising of $\mathcal{DG}_r$-Images

This section addresses the denoising of $\mathcal{DG}_r$ images. We represent (interpolate) the non-discrete texture displayed in Figure 3.2 in the space $\mathcal{DG}_r(\Gamma)$ for $r = 0, 1, 2$. Noise is added to each degree of freedom as described above. We show the denoising results for the split Bregman method (Algorithm 2) in Figure 3.3, where the noise is removed successfully.

Figure 3.3 visualizes the benefits of higher-order finite elements in particular in the case where the discontinuities in the image are not resolved by the computational mesh. In addition, the $\mathcal{DG}_1$ and $\mathcal{DG}_2$ solutions exhibit less staircasing.

Before continuing, we mention that all results in $\mathcal{DG}_1$ were interpolated onto $\mathcal{DG}_0$ on a twice refined mesh merely for visualization since $\mathcal{DG}_1$ functions cannot directly be displayed in PARAVIEW. Likewise, results in $\mathcal{DG}_2$ were interpolated onto $\mathcal{DG}_0$ on a three times refined mesh for visualization.

3.5.2 Inpainting of $\mathcal{DG}_r$-Images

In this and the following section we demonstrate the utility of higher-order polynomial function spaces for the purpose of inpainting. To this end, we consider the same sphere setting as before and randomly delete 70% of all cells, which subsequently serve as the inpainting region $\Gamma \setminus \Gamma^0$. Again, problem (DTV-L2) is solved in $\mathcal{DG}_r(\Gamma_h)$ for $r \in \{0, 1, 2\}$ with Algorithm 2; see Figure 3.4.

The results for this inpainting problem are similar to those for the pure denoising case in Figure 3.3. Clearly, the higher-order results produce images closer to the original than the recovery in $\mathcal{DG}_0$.

3.6 Solving the (DTV-L1) Problem

We briefly discuss the implementation of two algorithms for

$$\text{Minimize} \quad \sum_{T \subset \Gamma_h^0} \int_T \mathcal{J}_T\left\{ \, |u - f| \, \right\} \mathrm{d}\boldsymbol{s} + \beta \, |u|_{DTV(\Gamma_h)} \, . \tag{DTV-L1}$$

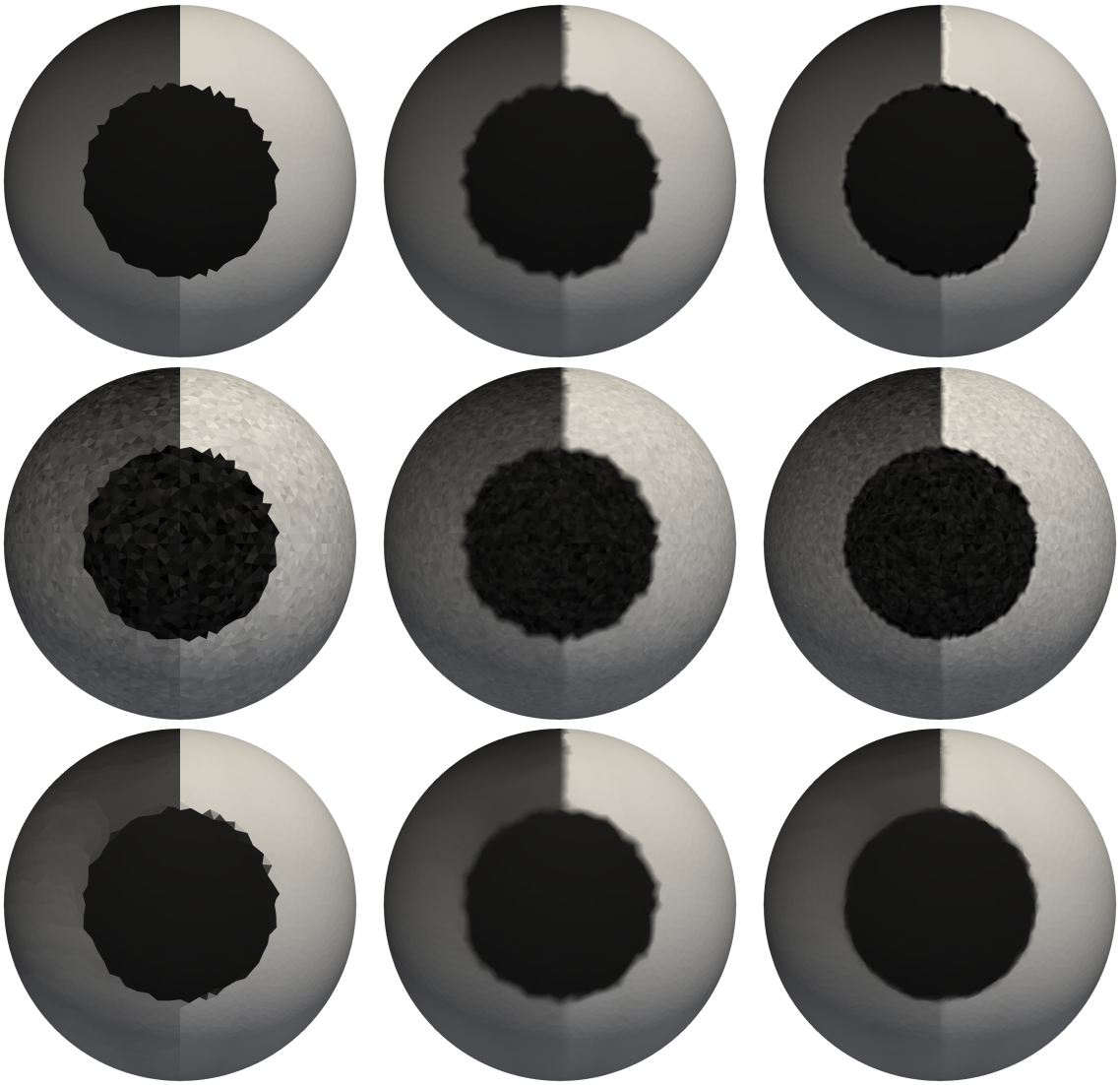

Figure 3.3: Original, noisy and denoised images (top to bottom) for $\mathcal{DG}_0$ (left column), $\mathcal{DG}_1$ (middle column) and $\mathcal{DG}_2$ (right column) for (DTV-L2) with parameters $\beta = 1 \times 10^{-2}$, $\lambda = 1 \times 10^{-1}$ ans $S = 1 \times 10^{-2}$.

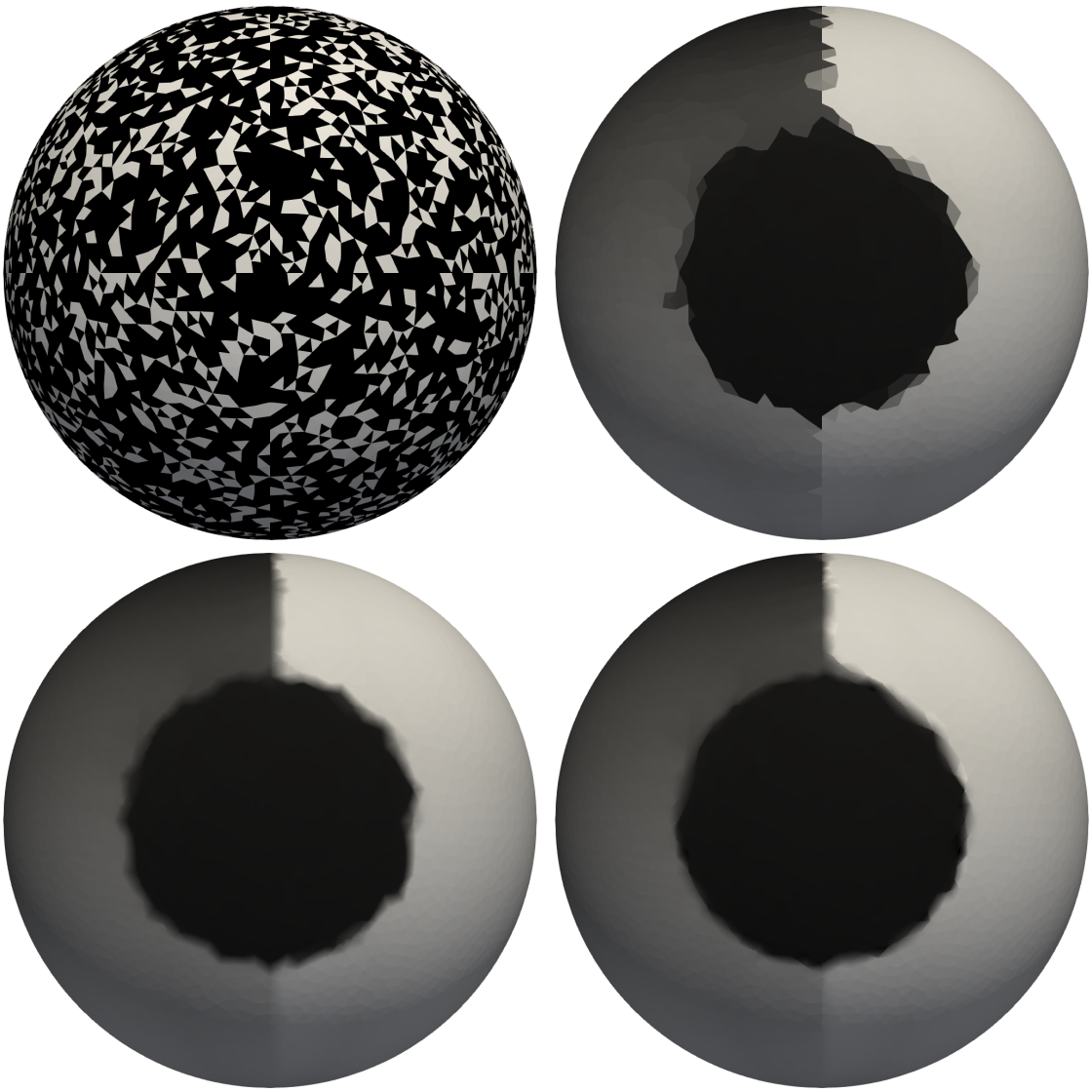

Figure 3.4: Inpainting with 70% of the cells erased (shown in black in the upper left image). Inpainting results for $\mathcal{DG}_0$ (upper right), $\mathcal{DG}_1$ (lower left) and $\mathcal{DG}_2$(lower right) for (DTV-L2) with parameters $\beta = 1 \times 10^{-3}$, $\lambda = 1 \times 10^{-1}$ ans $S = 1 \times 10^{-3}$.

They too can be realized equally efficiently as their original counterparts devised for images on Cartesian grids with low-order finite difference approximations of the gradient and divergence. For simplicity, we restrict the discussion to the polynomial degrees $r \in \{0,1\}$ in this section so that all weights $c_{T,i}$, $c_{E,j}$ as well as $C_{T,k}$ are strictly positive. The cases $r = \{2,3\}$ can be included provided that zero weights are properly treated and we come back to this in Section 3.7.2.

3.6.1 Chambolle–Pock Method

We focus on the changes compared to the method for (DTV-L2) discussed in Section 3.4.2. As in Section 3.3.2, we need to replace F by (3.26) and use the lumped inner product (3.27) in

$$U = \mathcal{DG}_r(\Gamma_h).$$

Due to the diagonal structure of both F and the inner product, the F-prox operator is easily seen to be

$$u = \operatorname{prox}_{\sigma F}(\bar{u})$$

if and only if

$$u_{T,k} = f_{T,k} + \operatorname{shrink}\big(|\bar{u}_{T,k} - f_{T,k}|,\ \sigma\big), \tag{3.55}$$

in case

$$T \subset \Gamma_h^0,$$

similarly as in [47, Sect. 6.2.2]. In case

$$T \subset \Gamma_h \setminus \Gamma_h^0,$$

we have

$$u_{T,k} = \bar{u}_{T,k}.$$

The remaining steps in Algorithm 3 are unaffected.

3.6.2 ADMM Method

Finally we consider the Alternating Direction Method of Multipliers (ADMM) for the primal problem (DTV-L1) as in [152]. In our context, similar as for the split Bregman method (Section 3.4.1), one introduces variables

$$u \in \mathcal{DG}_r(\Gamma_h)$$

and

$$\boldsymbol{d}, \boldsymbol{b} \in Y.$$

A second splitting

$$e = u - f$$

is required, so we additionally introduce

$$e \in \mathcal{DG}_r(\Gamma_h)$$

as well as a multiplier

$$g \in \mathcal{DG}_r(\Gamma_h).$$

The corresponding augmented Lagrangian functional reads

$$\sum_{T\subset\Gamma_h^0,k} C_{T,k}\ |e_{T,k}| + \beta \sum_{T,i} c_{T,i}\ \left|\boldsymbol{d}_{T,i}\right|_s + \beta \sum_{E,j} c_{E,j}\ \left|d_{E,j}\right| + \frac{\lambda}{2}\|\boldsymbol{d} - \Lambda u - \boldsymbol{b}\|_Y^2 + \frac{\lambda S}{2} \sum_{T,k} C_{T,k} \left|e_{T,k} - u_{T,k} + f_{T,k} - g_{T,k}\right|^2. \tag{3.56}$$

Let us briefly consider the individual minimization problems w.r.t. u, $\boldsymbol{d}$, and e. The u-problem is to minimize

$$\frac{\lambda S}{2} \sum_{T,k} C_{T,k} \left|e_{T,k} - u_{T,k} + f_{T,k} - g_{T,k}\right|^2 + \frac{\lambda S}{2} \sum_{T,i} c_{T,i} \left|\boldsymbol{d}_{T,i} - \nabla u(x_{T,i}) - \boldsymbol{b}_{T,i}\right|_2^2 + \frac{\lambda}{2} \sum_{E,j} c_{E,j} \left|d_{E,j} - (u_E^- - u_E^+)(x_{E,j}) - b_{E,j}\right|^2 \tag{3.57}$$

w.r.t. $u \in \mathcal{DG}_r(\Gamma_h)$. This problem is similar to (3.34) and it leads to a coupled linear system for u. The minimization of (3.56) w.r.t. $\boldsymbol{d} \in \mathcal{RT}_{r+1}(\Gamma_h)$ is identical to (3.35) and the e-problem is to minimize

$$\sum_{T\subset\Gamma_h^0,k} |e_{T,k}|\ C_{T,k} + \frac{\lambda S}{2} \sum_{T,k} C_{T,k} \left|e_{T,k} - u_{T,k} + f_{T,k} - g_{T,k}\right|^2. \tag{3.58}$$

This problem can be easily solved via shrinkage, cf. (3.36b). Finally, the multiplier update for $\boldsymbol{b}$ is as in Section 3.4.1, and the update for g is similar; see Algorithm 5. Once again, the solution $\boldsymbol{p}$ of the dual (DTV-L1-D) can be recovered from the multipliers $\boldsymbol{b}_{T,i}$ and $b_{E,j}$ as in (3.37). Moreover, it can be easily checked that

$$\lambda\, g_{T,k} = \frac{1}{C_{T,k}} \int_T (\operatorname{div} \boldsymbol{p})\, \Phi_{T,k}\, \mathrm{d}\boldsymbol{s} \tag{3.59}$$

holds, where the quantity on the right appears as a constraint in (DTV-L1-D) and thus it satisfies

$$|\lambda\, g_{T,k}| \leq 1$$

in the limit where $T \subset \Gamma_h^0$ and

$$|\lambda\, g_{T,k}| = 0$$

where $T \subset \Gamma_h \setminus \Gamma_h^0$.

3.7 Extensions

In this section we collect a number of extensions showing that problems more general than those based on the TV-L^2 and TV-L^1 models and discontinuous functions can be dealt with efficiently by generalizations of the respective algorithms to our higher-order finite element setting.

Algorithm 5 ADMM algorithm for (DTV-L1)

Set $u^{(0)} := f \in \mathcal{DG}_r(\Gamma_h)$, $\boldsymbol{b}^{(0)} := \mathbf{0} \in Y$ and $\boldsymbol{d}^{(0)} := \mathbf{0} \in Y$
Set $e^{(0)} := 0 \in \mathcal{DG}_r(\Gamma_h)$ and $g^{(0)} := 0 \in \mathcal{DG}_r(\Gamma_h)$
Set $n := 0$
while not converged **do**
  Minimize (3.57) for $u^{(n+1)}$ with data $\boldsymbol{b}^{(n)}$, $\boldsymbol{d}^{(n)}$, $e^{(n)}$ and $g^{(n)}$
  Minimize (3.36) for $\boldsymbol{d}^{(n+1)}$ with data $u^{(n+1)}$ and $\boldsymbol{b}^{(n)}$
  Minimize (3.58) for $e^{(n+1)}$ with data $u^{(n+1)}$ and $g^{(n)}$
  Set $\boldsymbol{b}_{T,i}^{(n+1)} := \boldsymbol{b}_{T,i}^{(n)} + \nabla u^{(n+1)}(x_{T,i}) - \boldsymbol{d}_{T,i}^{(n+1)}$
  Set $b_{E,j}^{(n+1)} := b_{E,j}^{(n)} + [\![u^{(n+1)}]\!](x_{E,j}) - d_{E,j}^{(n+1)}$
  Set $g_{T,k}^{(n+1)} := g_{T,k}^{(n)} + u_{T,k}^{(n+1)} - f_{T,k} - e_{T,k}^{(n+1)}$
  Set $n := n + 1$
end while
Set $\boldsymbol{p}^{(n)}$ by (3.37) with data $\boldsymbol{b}^{(n)}$

3.7.1 Huber TV-Seminorm

We consider the replacement of the TV-seminorm by its 'Huberized' variant; see for instance [107, 124] and [142, Ch. 4]. Here, function G in (3.19) can be written as

$$\begin{aligned} G(\boldsymbol{d}) &= \sum_T \int_T \mathcal{I}_T\{\, |\boldsymbol{d}_T|_2 \,\} \,\mathrm{d}\boldsymbol{s} + \sum_E \int_E \mathcal{I}_E\{\, |d_E| \,\} \,\mathrm{d}\boldsymbol{s} \\ &= \sum_{T,i} c_{T,i} \left|\boldsymbol{d}_{T,i}\right|_2 + \sum_{E,j} c_{E,j} \left|d_{E,j}\right|. \end{aligned} \tag{3.60}$$

The corresponding Huber functional with parameter $\varepsilon > 0$ then becomes

$$\begin{aligned} G_\varepsilon(\boldsymbol{d}) = &\sum_{T,i} c_{T,i} \max\left\{ |\boldsymbol{d}_{T,i}|_2 - \frac{\varepsilon}{2},\ \frac{1}{2\varepsilon} |\boldsymbol{d}_{T,i}|_2^2 \right\} \\ &+ \sum_{E,j} c_{E,j} \max\left\{ d_{E,j} - \frac{\varepsilon}{2},\ -d_{E,j} - \frac{\varepsilon}{2},\ \frac{1}{2\varepsilon}(d_{E,j})^2 \right\}. \end{aligned} \tag{3.61}$$

It can be shown by straightforward calculations that the convex conjugate of G_ε is

$$G_\varepsilon^*(\boldsymbol{p}) = \chi_{\boldsymbol{P}}(\boldsymbol{p}) + \frac{\varepsilon}{2}\|\boldsymbol{p}\|_{Y^*}^2. \tag{3.62}$$

We recall that $\chi_{\boldsymbol{P}}$ is the indicator function of the constraint set $\boldsymbol{P}$ in (3.17).
The 'Huberized' discrete TV-seminorm is thus defined by $G_\varepsilon(\Lambda u)$ where Λ is given in (3.18). It can be combined with both the L^2 and L^1 loss terms,

$$F(u) = \frac{1}{2}\|u - f\|_{L^2(\Gamma_h^0)}^2$$

and

$$F(u) = \sum_{T \subset \Gamma_h^0} \int_T \mathcal{J}_T\{\, |u - f| \,\} \,\mathrm{d}\boldsymbol{s}.$$

We refer to the corresponding primal problems, i.e., the minimization of

$$F(u) + \beta\, G_\varepsilon(\Lambda u),$$

as (DTV_ε-L2) and (DTV_ε-L1). The specific form of corresponding dual problems, where

$$F^*(-\Lambda^* \boldsymbol{p}) + \beta\, G_\varepsilon^*(\boldsymbol{p}/\beta)$$

is minimized, should now also be clear.
The Chambolle–Pock method (Algorithm 3) can be adapted in a straightforward way by replacing the G^*-prox by the one involving G_ε^*, i.e., by replacing (3.41) by

$$\boldsymbol{p} = \operatorname*{arg\,min}_{\boldsymbol{q} \in \mathcal{RT}_{r+1}(\Gamma_h)} \frac{1}{2}\|\boldsymbol{q} - \bar{\boldsymbol{p}}\|_{Y^*}^2 + \frac{\varepsilon}{2}\|\boldsymbol{q}\|_{Y^*}^2 \text{ s.t. } \boldsymbol{q} \in \boldsymbol{P}. \tag{3.63}$$

This amounts to

$$\begin{aligned} \sigma_{E,j}(\boldsymbol{p}) &= \min\left\{ \frac{1}{1+\varepsilon}\left|\sigma_{E,j}(\bar{\boldsymbol{p}})\right|,\ \beta\, c_{E,j} \right\} \frac{\sigma_{E,j}(\bar{\boldsymbol{p}})}{\left|\sigma_{E,j}(\bar{\boldsymbol{p}})\right|}, \\ \boldsymbol{\sigma}_{T,i}(\boldsymbol{p}) &= \min\left\{ \frac{1}{1+\varepsilon}\left|\boldsymbol{\sigma}_{T,i}(\bar{\boldsymbol{p}})\right|_2,\ \beta\, c_{T,i} \right\} \frac{\boldsymbol{\sigma}_{T,i}(\bar{\boldsymbol{p}})}{\left|\boldsymbol{\sigma}_{T,i}(\bar{\boldsymbol{p}})\right|_2} \end{aligned} \tag{3.64}$$

in place of (3.42). Chambolle's projection method (Algorithm 4) can also be adapted to (DTV_ε-L2) by modifying (3.47) and (3.48). Similarly, the Chambolle–Pock method for (DTV-L1) (Section 3.6.1) can be adapted to solve (DTV_ε-L1) with the same modification as above.

3.7.2 Polynomial Degrees

We recall that we restricted the discussion of algorithms for (DTV-L2) and its dual (DTV-L2-D) in Section 3.4 to the cases

$$r \in \{0, 1, 2, 4\},$$

each of which ensures that $c_{T,i}$ and $c_{E,j}$ are strictly positive; see Lemma 3.1. In the case $r = 3$, three of the six weights $c_{T,i}$ on each triangle are zero. This is not a major issue but it requires some care when formulating the algorithms in Section 3.4 in this case. Briefly, when $c_{T,i} = 0$, quantities bearing the same index (T, i) are to be ignored. This applies, in particular, to the inner product $(\cdot,\, \cdot)_{Y^*}$ in (3.39).
Similarly, we excluded the cases $r \in \{2, 3\}$ in the discussion of algorithms for (DTV-L1) and its dual problem (DTV-L1-D) in Section 3.6 so that the weights

$$C_{T,k} \coloneqq \int_T \Phi_{T,k}\, \mathrm{d}\boldsymbol{s}$$

pertaining to the basis $\{\Phi_{T,k}\}$ of $\mathcal{P}_r(T)$ are strictly positive as well. In case $r = 3$, we proceed as discussed above, ignoring terms for which the corresponding weights $c_{T,i} = 0$. When $r = 2$, we instead ignore terms for which $C_{T,k} = 0$ in any of the algorithms in Section 3.6.

3.7.3 Textures in $\mathcal{CG}_r(\Gamma_h)$

While we believe that the representation of images as discontinuous functions is rather natural, it is certainly useful to consider also the case when $u \in \mathcal{CG}_r(\Gamma_h)$. This situation is meaningful only for $r \geq 1$, and hence we consider

$$r \in \{1, 2, 3, 4\}$$

in this section. Clearly, for $u \in \mathcal{CG}_r(\Gamma_h)$, the TV-seminorm (3.1) and its discrete counterpart (3.2) reduce to

$$|u|_{TV(\Gamma_h)} = \sum_T \int_T |\nabla u|_2 \, \mathrm{d}s \tag{3.65a}$$

$$|u|_{DTV(\Gamma_h)} = \sum_T \int_T \mathcal{I}_T \{ \, |\nabla u|_2 \, \} \, \mathrm{d}s \tag{3.65b}$$

since the terms related to edge jumps disappear. As was mentioned in the introduction, the lowest-order case $r = 1$ has been considered in [13, 15, 28, 58, 74, 78]. In this case,

$$|u|_{TV(\Gamma_h)} = |u|_{DTV(\Gamma_h)}$$

holds. Similarly as in Corollary 3.5, a simple convexity argument shows that

$$|u|_{TV(\Gamma_h)} \leq |u|_{DTV(\Gamma_h)}$$

holds for all $u \in \mathcal{CG}_2(\Gamma_h)$.
Since $\mathcal{CG}_r(\Gamma_h)$ is a proper subspace of $\mathcal{DG}_r(\Gamma_h)$, it can be expected that it is enough to take the supremum in Theorem 3.2 over a smaller set of test functions. Indeed, as the image of the gradient operator

$$\Lambda : U = \mathcal{CG}_r(\Gamma_h) \to Y$$

reduces to

$$Y = \prod_T \mathcal{P}_{r-1}(T)^2,$$

the edge-based dofs of $\boldsymbol{p} \in \mathcal{RT}_{r+1}(\Gamma_h)$ that can be dispensed with since no edge jumps need to be measured. We thus obtain the following corollary of Theorem 3.2.

Corollary 3.12 (Dual Representation of $|u|_{DTV(\Gamma_h)}$ for $u \in \mathcal{CG}_r(\Gamma_h)$)**.** *Suppose $r \in \{1, 2, 3, 4\}$. Then for any $u \in \mathcal{CG}_r(\Gamma_h)$, the discrete TV-seminorm* (3.2) *reduces to* (3.65) *and it satisfies*

$$\begin{aligned} |u|_{DTV(\Gamma_h)} = \sup \Bigg\{ & \int_{\Gamma_h} u \operatorname{div} \boldsymbol{p} \, \mathrm{d}s : \boldsymbol{p} \in \mathcal{RT}_{r+1}(\Gamma_h), \\ & |\boldsymbol{\sigma}_{T,i}(\boldsymbol{p})|_2 \leq c_{T,i} \quad \forall T, i = 1, \ldots, r\,(r+1)/2, \\ & \sigma_{E,j}(\boldsymbol{p}) = 0 \quad \forall E, j = 1, \ldots, r+1 \Bigg\}. \end{aligned} \tag{3.66}$$

It is straightforward to adopt the algorithms presented in Sections 3.4 and 3.6 to this simpler situation. In a nutshell, all edge-based quantities (such as $d_{E,j}$ and $b_{E,j}$ in the split Bregman method, Algorithm 2) can be ignored, and the edge-based coefficients $\sigma_{E,j}(\boldsymbol{p})$ of any function $\boldsymbol{p} \in \mathcal{RT}_{r+1}(\Gamma_h)$ would be left at zero.
We remark, however, that the gradient operator is not surjective onto Y so that the set of test functions $\boldsymbol{p}$ in (3.66) is unnecessarily large. A more economical formulation for these cases remains open for future investigation.

3.7.4 The 3D-Volume Case

When $\Gamma_h \subset \mathbb{R}^3$ is a volume mesh consisting of tetrahedra K and interior facets F, then the former replace triangles T and the latter replace interior edges E throughout the chapter. For instance, the definition (3.2) of the discrete total variation becomes

$$|u|_{DTV(\Gamma_h)} := \sum_K \int_K \mathcal{I}_K\{\, |\nabla u|_2 \,\}\, \mathrm{d}\boldsymbol{s} + \sum_F \int_F \mathcal{I}_F\{(u_F^- - u_F^+)\}\, \mathrm{d}\boldsymbol{s}. \tag{3.67}$$

The finite element spaces involved remain the same, except that their respective cell domains and thus their dimensions change; see Table 3.2.

FE space	local dimension	global dimension
$\mathcal{CG}_r(\Gamma_h)$ $(r \geq 1)$	$(r+1)(r+2)(r+3)/6$	$N_K\,(r-3)^+(r-2)(r-1)$ $+ N_F\,(r-2)^+(r-1)/2$ $+ N_E\,(r-1)^+ + N_V$
$\mathcal{DG}_r(\Gamma_h)$	$(r+1)(r+2)(r+3)/6$	$N_K\,(r+1)(r+2)(r+3)/6$
$\mathcal{DG}_{r-1}(\Gamma_h)$	$r\,(r+1)(r+2)/6$	$N_K\,r\,(r+1)(r+2)/6$
$\mathcal{DG}_r(\cup F)$	$(r+1)(r+2)/2$	$N_F\,(r+1)(r+2)/2$
$\mathcal{RT}_{r+1}(\Gamma_h)$	$(r+1)(r+2)(r+4)/2$	$N_K\,r\,(r+1)(r+2)/2$ $+ N_F\,(r+1)(r+2)/2$

Table 3.2: Finite element spaces, their degrees of freedom and corresponding bases in 3D. Here N_K, N_F, N_E and N_V denote the number of tetrahedra, interior facets, interior edges and vertices in the triangular mesh; compare Table 3.1.

The operator Λ, which represents the gradient and was defined in (3.18), now maps the space

$$U = \mathcal{DG}_r(\Gamma_h)$$

onto

$$Y = \prod_K \mathcal{P}_{r-1}(K)^3 \times \prod_F \mathcal{P}_r(F).$$

It is important to realize for our approach that Y^* can still be identified with $\mathcal{RT}_{r+1}(\Gamma_h)$ with the duality product given by (3.20), mutatis mutandis. From here, all results can be derived as in the surface case. We only mention that the analogue of Lemma 3.1 in 3D

limits the polynomial degrees with non-negative weights to $r \in \{0, 1, 2, 4\}$ in case of (DTV-L2); see [145, Tab. II]. When (DTV-L1) is considered, only the choices $r \in \{0, 1\}$ remain.

CHAPTER 4

TOTAL VARIATION OF THE NORMAL VECTOR FIELD ON SMOOTH SURFACES

The total variation (TV) functional is popular as a regularizer in imaging and inverse problems; see for instance [11, 51, 110, 139] and [157, Chapter 8]. For a real-valued function $u \in W^{1,1}(\Omega)$ on a bounded domain Ω in $\mathbb{R}^2$, the total variation seminorm is defined as

$$\begin{aligned} |u|_{TV(\Omega)} &:= \int_\Omega |\nabla u|_2 \, \mathrm{d}\boldsymbol{s} \\ &= \int_\Omega \left(|(Du)\, \boldsymbol{e}_1|^2 + |(Du)\, \boldsymbol{e}_2|^2 \right)^{\frac{1}{2}}. \end{aligned} \tag{4.1}$$

Notice that we restrict the discussion to the isotropic case here, i.e., $|\cdot|_2$ denotes the Euclidean norm. Moreover, Du is the derivative of u and $\{\boldsymbol{e}_1, \boldsymbol{e}_2\}$ denotes the standard Euclidean basis. The seminorm (4.1) extends to less regular, so-called BV functions (bounded variation), whose distributional gradient exists only in the sense of measures. We refer the reader to [8, 83] for an extensive discussion of BV functions. The utility of (4.1) as a regularizer, or prior, lies in the fact that it favors piecewise constant solutions.

This chapter parallels [24], where we introduce a novel regularizer based on the total variation, which can be used, for instance, in shape optimization applications as well as geometric inverse problems. In the latter class, the unknown, which one seeks to recover, is a *shape* $\Omega \subset \mathbb{R}^3$, which might represent the location of a source or inclusion inside a given, larger domain, or the geometry of an inclusion or a scatterer. The boundary of Ω will be denoted by Γ.
The novel functional, which we term the *total variation of the normal field* along a smooth surface Γ, is defined by

$$|\boldsymbol{n}|_{TV(\Gamma)} := \int_\Gamma \left(|(D_\Gamma \boldsymbol{n})\, \boldsymbol{\xi}_1|_{\mathfrak{g}}^2 + |(D_\Gamma \boldsymbol{n})\, \boldsymbol{\xi}_2|_{\mathfrak{g}}^2 \right)^{\frac{1}{2}} \mathrm{d}\boldsymbol{s} \tag{4.2}$$

in analogy to (4.1). In (4.2), $\boldsymbol{n}$ is the outer unit normal vector field along Γ, i.e., $\boldsymbol{n}$ belongs to the manifold $\mathcal{S}^2 = \{\boldsymbol{v} \in \mathbb{R}^3 : |\boldsymbol{v}|_2 = 1\}$ pointwise. Moreover, $D_\Gamma \boldsymbol{n}$ denotes the derivative (push-forward) of the normal vector field, and $\{\boldsymbol{\xi}_1(\boldsymbol{s}), \boldsymbol{\xi}_2(\boldsymbol{s})\}$ denotes an

orthonormal basis (w.r.t. the Euclidean inner product in the embedding $\Gamma \subset \mathbb{R}^3$) of the tangent spaces $\mathcal{T}_s\Gamma$ along Γ. Finally, $|\cdot|_{\mathfrak{g}}$ denotes the norm induced by a Riemannian metric on $\mathcal{S}^2$. We will consider the metric induced from embedding $\mathcal{S}^2$ in $\mathbb{R}^3$, i. e., the distance induced by this metric is the arc length distance and the curvature is 1. We write $|\cdot|_{\mathfrak{g}}$ for the norm induced by the Riemannian metric $\mathfrak{g}(\cdot, \cdot)$ on the tangent spaces of $\mathcal{S}^2$.

We are also considering the total variation of the normal (4.2) as a prior in shape optimization problems, which may involve a partial differential equation (PDE). The aforementioned problem can be cast in the form

$$\begin{aligned} &\text{Minimize} \quad \ell(u(\Omega), \Omega) + \beta \, |\boldsymbol{n}|_{TV(\Gamma)} \\ &\text{w.r.t. } \Omega \text{ in a suitable class of domains.} \end{aligned} \tag{4.3}$$

Here $u(\Omega)$ denotes the solution of the problem specific PDE, which depends on the unknown domain Ω. Moreover, ℓ represents a loss function, such as a least squares function. The coupling between Ω and its normal vector field $\boldsymbol{n}$ makes the minimization of (4.3) algorithmically challenging. Moreover, since the integrand in (4.2) is zero on flat regions (with constant normal) of Γ, (4.2) and thus (4.3) cannot be expected to be shape differentiable, although the first (loss function) part pertaining to the PDE often is. We therefore resort to a splitting approach in the spirit of [85] to overcome this issue.

The structure of the chapter is as follows. In Section 4.1 we provide an analysis of (4.2) and its properties. We also compare (4.2) to geometric functionals appearing elsewhere in the literature. In Section 4.2 we discuss the role of (4.2) in optimization problems. Section 4.3 is devoted to the formulation of an ADMM method which generalizes the split Bregman algorithm to the manifold-valued problem (4.3).

4.1 Total Variation of the Normal

In this section we discuss our proposal (4.2) for the total variation of the normal on smooth surfaces in detail and relate it to other geometric functionals used previously in the literature. A minimal background in differential geometry of surfaces is required, which we recall here and refer the reader to [69, 87, 106] for a thorough introduction.

4.1.1 Preliminaries

From this section onwards we assume that the boundary Γ of the unknown bounded domain Ω is a smooth, compact, orientable manifold of dimension 2 without boundary, embedded in $\mathbb{R}^3$. Therefore we can think of tangent vectors at $s \in \Gamma$ to be elements of the appropriate two-dimensional subspace (the tangent plane) of $\mathbb{R}^3$. This tangent plane at s is denoted by $\mathcal{T}_s\Gamma$. Each tangent plane is endowed with the Riemannian metric furnished by the embedding via the pull-back of the Euclidean metric in $\mathbb{R}^3$. In other words, the inner product of two vectors

$$\xi_1, \xi_2 \in \mathcal{T}_s\Gamma$$

is simply given by

$$\mathfrak{g}(\xi_1, \xi_2) = \xi_1^\top \xi_2.$$

In what follows,

$$\{\boldsymbol{\xi}_1(\boldsymbol{s}), \boldsymbol{\xi}_2(\boldsymbol{s})\}$$

denotes an orthonormal basis in $\mathcal{T}_{\boldsymbol{s}}\Gamma$. As the following remark shows, the choice of this basis and how it varies with $\boldsymbol{s}$ will not matter.
Outward pointing unit normal vectors $\boldsymbol{n}$ along Γ will be considered elements of the two-dimensional smooth manifold $\mathcal{S}^2$. The derivative or push-forward of the normal map $\boldsymbol{n}$ is denoted by $D_\Gamma \boldsymbol{n}$. At a given $\boldsymbol{s} \in \Gamma$, $D_\Gamma \boldsymbol{n}$ thus maps tangent vectors $\boldsymbol{\xi} \in \mathcal{T}_{\boldsymbol{s}}\Gamma$ into tangent vectors

$$(D_\Gamma \boldsymbol{n})\, \boldsymbol{\xi} \in \mathcal{T}_{\boldsymbol{n}(\boldsymbol{s})}\mathcal{S}^2.$$

In what follows, we will suppress the dependence on the point $\boldsymbol{s} \in \Gamma$ where possible.

Remark 4.1. *The total variation of the normal* (4.2) *is independent of the choice of the orthonormal basis in the tangent spaces $\mathcal{T}_{\boldsymbol{s}}\Gamma$. To show this, it is enough to consider a point $\boldsymbol{s} \in \Gamma$ and suppose that $\{\boldsymbol{\xi}_1, \boldsymbol{\xi}_2\}$ and $\{\boldsymbol{\eta}_1, \boldsymbol{\eta}_2\}$ are two orthonormal bases of $\mathcal{T}_{\boldsymbol{s}}\Gamma$. Then there exists an orthogonal matrix $Q \in \mathbb{R}^{3\times 3}$ such that*

$$\boldsymbol{\eta}_i = Q\, \boldsymbol{\xi}_i$$

holds for $i = 1, 2$. For

$$J \coloneqq \begin{bmatrix} (D_\Gamma \boldsymbol{n})\, \boldsymbol{\xi}_1 & (D_\Gamma \boldsymbol{n})\, \boldsymbol{\xi}_2 \end{bmatrix}$$

the integrand in (4.2) *satisfies*

$$\begin{aligned} |(D_\Gamma \boldsymbol{n})\, \boldsymbol{\xi}_1|_{\mathfrak{g}}^2 + |(D_\Gamma \boldsymbol{n})\, \boldsymbol{\xi}_2|_{\mathfrak{g}}^2 &= \operatorname{trace}(J^\top J) \\ &= \operatorname{trace}(J^\top J\, Q\, Q^\top) \\ &= \operatorname{trace}(Q^\top J^\top J\, Q) \\ &= |(D_\Gamma \boldsymbol{n})\, Q\, \boldsymbol{\xi}_1|_{\mathfrak{g}}^2 + |(D_\Gamma \boldsymbol{n})\, Q\, \boldsymbol{\xi}_2|_{\mathfrak{g}}^2 \\ &= |(D_\Gamma \boldsymbol{n})\, \boldsymbol{\eta}_1|_{\mathfrak{g}}^2 + |(D_\Gamma \boldsymbol{n})\, \boldsymbol{\eta}_2|_{\mathfrak{g}}^2. \end{aligned}$$

Similarly, as we do for Γ, we consider $\mathcal{S}^2$ embedded into $\mathbb{R}^3$ and therefore we can conceive the tangent space $\mathcal{T}_{\boldsymbol{n}(\boldsymbol{s})}\mathcal{S}^2$ as a two-dimensional plane in $\mathbb{R}^3$ tangent to the sphere $\mathcal{S}^2$. We endow $\mathcal{T}_{\boldsymbol{n}(\boldsymbol{s})}\mathcal{S}^2$ with the Riemannian metric furnished by the pull-back of the Euclidean metric as well, which we denote by $\mathfrak{g}(\cdot, \cdot)$ to distinguish it from the Riemannian metric on $\mathcal{T}_{\boldsymbol{s}}\Gamma$. In fact, $\mathcal{T}_{\boldsymbol{n}(\boldsymbol{s})}\mathcal{S}^2$ is clearly parallel to $\mathcal{T}_{\boldsymbol{s}}\Gamma$, see Figure 4.1. We can therefore identify the two tangent spaces and we write

$$\mathcal{T}_{\boldsymbol{n}(\boldsymbol{s})}\mathcal{S}^2 \cong \mathcal{T}_{\boldsymbol{s}}\Gamma$$

to indicate this.

4.1.2 Relation to Curvature

In order to relate (4.2) with regularizing geometric functionals appearing elsewhere in the literature, we take a second look at the integrand. To this end, we recall that the normal field operator

$$\boldsymbol{N}_\Gamma : \Gamma \to \mathcal{S}^2$$

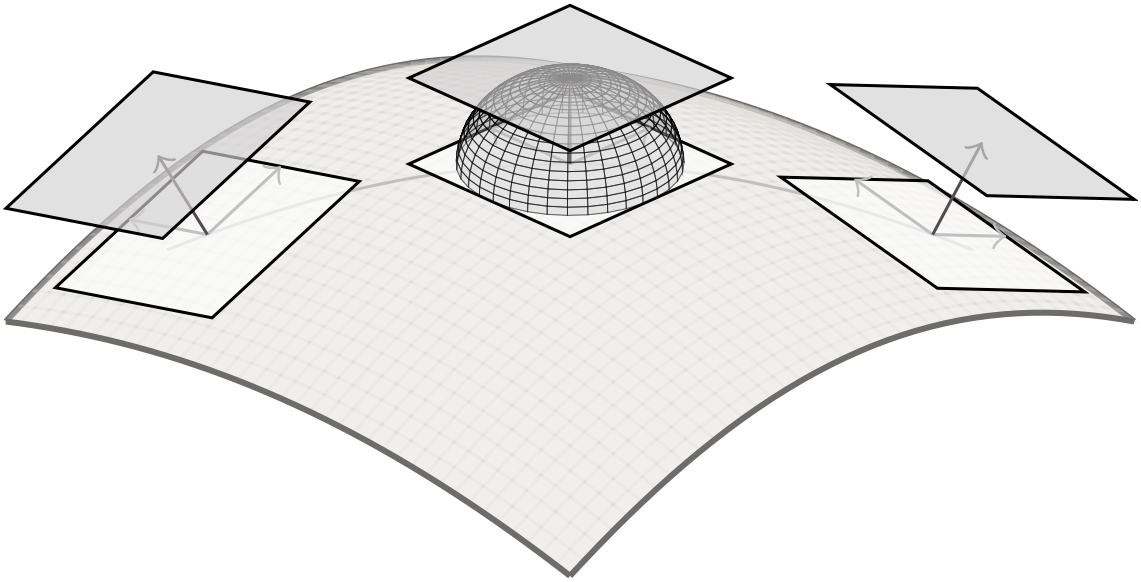

Figure 4.1: The figure shows part of a smooth surface Γ and a representation of its tangent spaces at three points $\boldsymbol{s}$ (light gray). The normal vectors are shown as well. The figure also illustrates that $\mathcal{T}_{\boldsymbol{n}(\boldsymbol{s})}\mathcal{S}^2$ is parallel to $\mathcal{T}_{\boldsymbol{s}}\Gamma$.

is also known as the *Gauss map*; see for instance [106, Chapter 3]. Its derivative at $\boldsymbol{s} \in \Gamma$ maps tangent directions in $\mathcal{T}_{\boldsymbol{s}}\Gamma$ into tangent directions in

$$\mathcal{T}_{\boldsymbol{n}(\boldsymbol{s})}\mathcal{S}^2 \cong \mathcal{T}_{\boldsymbol{s}}\Gamma.$$

With the latter identification, the derivative of the Gauss map is known as the *shape operator*

$$S : \mathcal{T}_{\boldsymbol{s}}\Gamma \to \mathcal{T}_{\boldsymbol{s}}\Gamma.$$

Notice that S is self-adjoint, i.e.,

$$(S\boldsymbol{\xi}_1)^\top \boldsymbol{\xi}_2 = (S\boldsymbol{\xi}_2)^\top \boldsymbol{\xi}_1$$

holds for all $\boldsymbol{s} \in \Gamma$ and all $\boldsymbol{\xi}_1, \boldsymbol{\xi}_2 \in \mathcal{T}_{\boldsymbol{s}}\Gamma$; see for instance [87, Lemma 13.14]. The two eigenvalues of S are the principal curvatures of the surface Γ at $\boldsymbol{s}$, denoted by k_1 and k_2. This insight allows us to interpret the integrand in (4.2) differently.

Proposition 4.2. *The integrand in* (4.2) *satisfies*

$$\left(|(D_\Gamma \boldsymbol{n})\,\boldsymbol{\xi}_1|_{\mathfrak{g}}^2 + |(D_\Gamma \boldsymbol{n})\,\boldsymbol{\xi}_2|_{\mathfrak{g}}^2\right)^{1/2} = \left(k_1^2 + k_2^2\right)^{1/2}. \tag{4.4}$$

Proof. Consider the square of the integrand,

$$|(D_\Gamma \boldsymbol{n})\,\boldsymbol{\xi}_1|_{\mathfrak{g}}^2 + |(D_\Gamma \boldsymbol{n})\,\boldsymbol{\xi}_2|_{\mathfrak{g}}^2 = (S\boldsymbol{\xi}_1)^\top (S\boldsymbol{\xi}_1) + (S\boldsymbol{\xi}_2)^\top (S\boldsymbol{\xi}_2).$$

Due to Remark 4.1 we can choose $\boldsymbol{\xi}_1, \boldsymbol{\xi}_2$ to be normalized eigenvectors in $\mathcal{T}_{\boldsymbol{s}}\Gamma$ corresponding to the eigenvalues k_1, k_2, respectively. Therefore we get

$$\begin{aligned} |(D_\Gamma \boldsymbol{n})\,\boldsymbol{\xi}_1|_{\mathfrak{g}}^2 + |(D_\Gamma \boldsymbol{n})\,\boldsymbol{\xi}_2|_{\mathfrak{g}}^2 &= k_1^2 |\boldsymbol{\xi}_1|_{\mathfrak{g}}^2 + k_2^2 |\boldsymbol{\xi}_2|_{\mathfrak{g}}^2 \\ &= k_1^2 + k_2^2. \end{aligned}$$

□

4.1.3 Comparison with Prior Work

The representation of the integrand from Proposition 4.2 allows us to rewrite (4.2) as the integral over the *root mean square curvature*,

$$|\boldsymbol{n}|_{TV(\Omega)} = \int_\Gamma (k_1^2 + k_2^2)^{1/2} \, \mathrm{d}\boldsymbol{s}, \tag{4.5}$$

and compare it with related functionals appearing in the literature. The quantity

$$\int_\Gamma (k_1^2 + k_2^2) \, \mathrm{d}\boldsymbol{s} \tag{4.6}$$

is known as the integral over the *total curvature* (although this term is also used for other quantities in the literature). The functional (4.6) has a long tradition in surface fairing applications and can be interpreted as a surface strain energy, see for instance [88–90, 116, 153, 163, 164]. In imaging applications, (4.6) corresponds to $\int_\Omega |\nabla u|_2^2 \, \mathrm{d}\boldsymbol{s}$ and it takes the role of a Tikhonov regularization term. Due to the presence of the gradient, the Laplacian appears in the optimality conditions associated with minimization problems involving (4.6), as well as in the corresponding L^2-gradient flow, leading to a smoothed image; see for instance [103], where smoothing by diffusion was employed to $\mathcal{S}^1$-valued images via a mean curvature flow. Similarly, (4.6) tends to smooth the surface and its features.

By contrast, the functional (4.5) seems to have made very few appearances in the mathematical literature. We are aware of the PhD thesis [117, Chapter 6] and the subsequent book publication [125] where it was used to guide mesh generation. In [7, 119] the pointwise root mean square curvature is used as a measure of flatness in biomedical classification problems, in [132] for the purpose of surface segmentation and in [166] it is used as an aid to visualize vascular structures. We also mention that the logarithm of the root mean square curvature is known as the *curvedness* and it plays a role in the classification of intermolecular interactions in crystals; see for instance [120]. We are however not aware of any use of (4.2) or its equivalent form (4.5) as a prior in shape optimization problems.

We regard (4.2) as a natural extension of the total variation seminorm (4.1) to the normal vector on surfaces, measuring surface flatness, but other extensions are certainly possible. Notably, the authors in [75] propose the *total absolute Gaussian curvature*

$$\int_\Gamma |k_1 \, k_2| \, \mathrm{d}\boldsymbol{s} \tag{4.7}$$

for the same purpose. From the Gauss–Bonnet theorem (see for instance [87, Chapter 27] or [106, Chapter 4F]) it follows that the boundaries Γ of *convex* domains Ω will be the global minimizers of (4.7), and they yield a value of 4π. Thus (4.7) promotes domains which are "as convex as possible".

It should be noted that the classical total variation seminorm (4.1) is not invariant with respect to scale. In fact, it is easy to see that when the domain $\Omega \subset \mathbb{R}^d$ is replaced by $\delta\Omega$, and $u(x)$ is replaced by $u_\delta(x) := u(x/\delta)$, then $|u_\delta|_{TV(\delta\Omega)} = \delta^{d-1} \, |u|_{TV(\Omega)}$ holds. Similarly, we can show that the total variation on a 2-dimensional surface Γ scales as follows.

Lemma 4.3. *Suppose that $\delta > 0$. Then*

$$|\boldsymbol{n}_\delta|_{TV(\delta\Gamma)} = \delta \; |\boldsymbol{n}|_{TV(\Gamma)} \,. \tag{4.8}$$

Lemma 4.3 implies that the total variation of the normal (4.2) will go to zero when the domain Ω degenerates to a point as $\delta \to 0$. This is to be expected since the total variation (4.1) behaves in the same way. In practice, this will not be an issue since (4.2) will always be combined with other, e.g., data fidelity terms. By contrast (4.7) proposed in [75] *is invariant* w.r.t. scaling and thus, in this particular respect, does not generalize (4.1).

4.2 Analysis of the Total Variation of the Normal

In this section we discuss some properties of the total variation of the normal functional (4.2). To this end, we begin by briefly recalling some elements of shape calculus, as necessary in order to study optimization problems in which the domain $\Omega \subset \mathbb{R}^3$ appears as an optimization variable. Then we discuss properties of (4.2). In Section 4.2.3 we briefly comment on the case of curves, i.e., when $\Omega \subset \mathbb{R}^2$ and its boundary Γ is a one-dimensional manifold.

4.2.1 Elements of Shape Calculus

Here we follow common practice and define transformations of Ω in terms of perturbations of identity. That is, we consider families of perturbed domains Ω_ε whose material points are given by

$$\begin{aligned} \boldsymbol{x}_\varepsilon &= \boldsymbol{T}_\varepsilon(\boldsymbol{x}) \\ &:= \boldsymbol{x} + \varepsilon \boldsymbol{V}(\boldsymbol{x}). \end{aligned} \tag{4.9}$$

Here

$$\boldsymbol{V} : \mathcal{D} \to \mathbb{R}^3$$

is some smooth vector field defined on a hold-all $\mathcal{D} \supset \Omega$. Suppose that J is a functional depending on the domain. Then we denote by

$$\mathrm{d}J(\Omega)[\boldsymbol{V}]$$

the directional shape derivative (also known as Eulerian derivative) of J in the direction of $\boldsymbol{V}$, i.e.,

$$\mathrm{d}J(\Omega)[\boldsymbol{V}] = \lim_{\varepsilon \searrow 0} \frac{J(\Omega_\varepsilon) - J(\Omega)}{\varepsilon}.$$

Likewise, we write

$$\mathrm{d}J(\Gamma)[\boldsymbol{V}]$$

for functionals J depending on the surface Γ of Ω. In particular, when g is a smooth function and

$$J(\Gamma_\varepsilon) = \int_{\Gamma_\varepsilon} g(\varepsilon, \boldsymbol{s}_\varepsilon) \, \mathrm{d}\boldsymbol{s}_\varepsilon, \tag{4.10}$$

the directional shape derivative is given by [146, Eq. (2.172)]

$$\mathrm{d}J(\Gamma)[\boldsymbol{V}] = \int_\Gamma g(0, \boldsymbol{s}) \, \mathrm{div}_\Gamma \, \boldsymbol{V}(\boldsymbol{s}) + \mathrm{d}g[\boldsymbol{V}](0, \boldsymbol{s}) \, \mathrm{d}\boldsymbol{s}, \tag{4.11}$$

where the material derivative $\mathrm{d}g[\boldsymbol{V}]$ is defined as the total derivative

$$\mathrm{d}g[\boldsymbol{V}](0,\boldsymbol{s}) = \frac{\mathrm{d}}{\mathrm{d}\varepsilon}\bigg|_{\varepsilon=0} g(\varepsilon,\boldsymbol{s}_\varepsilon) = \frac{\mathrm{d}}{\mathrm{d}\varepsilon}\bigg|_{\varepsilon=0} g(\varepsilon,\boldsymbol{T}_\varepsilon(\boldsymbol{s}))$$

and $\operatorname{div}_\Gamma \boldsymbol{V}$ denotes the (tangential) divergence of $\boldsymbol{V}$ along Γ. It is related to the divergence in $\mathbb{R}^3$ via

$$\operatorname{div}_\Gamma \boldsymbol{V} = \sum_{i=1}^{2} \boldsymbol{\xi}_i^\top (D\boldsymbol{V})\,\boldsymbol{\xi}_i = \operatorname{div}\boldsymbol{V} - \boldsymbol{n}^\top (D\boldsymbol{V})\,\boldsymbol{n}.$$

In the following, we simply write g instead of $g(0,\cdot)$ and in addition to the material derivative, we also introduce the (local) shape derivative as the partial derivative

$$g'[\boldsymbol{V}] := (\partial/\partial\varepsilon)|_{\varepsilon=0}\, g(\varepsilon,\cdot).$$

Hence, both are related to each other via

$$g'[\boldsymbol{V}] = \mathrm{d}g[\boldsymbol{V}] - (Dg)\boldsymbol{V}. \tag{4.12}$$

See for instance [146, Eq. (2.163)]. If the shape derivative $g'[\boldsymbol{V}]$ exists, the shape derivative $\mathrm{d}J(\Gamma)[\boldsymbol{V}]$ can alternatively be expressed as

$$\mathrm{d}J(\Gamma)[\boldsymbol{V}] = \int_\Gamma \boldsymbol{V}^\top \boldsymbol{n}\,[(Dg)\boldsymbol{n} + (k_1+k_2)\,g] + g'[\boldsymbol{V}]\,\mathrm{d}\boldsymbol{s}, \tag{4.13}$$

see [146, Eq. (2.174)]. Furthermore, spatial derivatives and material derivatives of differentiable fields $\boldsymbol{F}$ fulfill

$$\begin{aligned} D(\mathrm{d}\boldsymbol{F}[\boldsymbol{V}]) &= D(\boldsymbol{F}'[\boldsymbol{V}]) + D((D\boldsymbol{F})\boldsymbol{V}) \\ &= (D\boldsymbol{F})'[\boldsymbol{V}] + D((D\boldsymbol{F})\boldsymbol{V}) \\ &= (D\boldsymbol{F})'[\boldsymbol{V}] + (D(D\boldsymbol{F})\boldsymbol{V}) + (D\boldsymbol{F})(D\boldsymbol{V}) \\ &= \mathrm{d}(D\boldsymbol{F})[\boldsymbol{V}] + (D\boldsymbol{F})(D\boldsymbol{V}). \end{aligned} \tag{4.14}$$

The symbol Dg in (4.13), which we will need occasionally, stands for the "full" derivative (in all three spatial directions) of a function g defined in a neighborhood of Γ. We recall that we are denoting the derivative in tangential directions of functions defined on Γ by the symbol D_Γ. Notice that Dg and $D_\Gamma g$ are related by

$$Dg = D_\Gamma g + (Dg)\boldsymbol{n}\boldsymbol{n}^\top.$$

Lemma 4.4. *Suppose that $\boldsymbol{a}$, $\boldsymbol{b}$ are C^1-vector fields on Γ with values in $\mathbb{R}^3$, and that $\boldsymbol{V}$ is a C^1-vector field which is normal, i.e.,*

$$\boldsymbol{V} = (\boldsymbol{V}^\top \boldsymbol{n})\,\boldsymbol{n}$$

holds on Γ. Then we have

$$\begin{aligned} &\int_\Gamma \boldsymbol{a}^\top (D_\Gamma \boldsymbol{V})\,\boldsymbol{b}\,\mathrm{d}\boldsymbol{s} \\ &= \int_\Gamma \boldsymbol{V}^\top \boldsymbol{n}\,\Big[-\operatorname{div}_\Gamma((\boldsymbol{a}^\top\boldsymbol{n})\,\boldsymbol{b}) + (\boldsymbol{a}^\top\boldsymbol{n})(\boldsymbol{b}^\top\boldsymbol{n})\,(k_1+k_2) + \boldsymbol{a}^\top (D_\Gamma\boldsymbol{n})\,\boldsymbol{b}\Big]\,\mathrm{d}\boldsymbol{s}. \end{aligned} \tag{4.15}$$

Proof. The general tangential Stokes formula [65, Eq. (5.27)] states that

$$\int_\Gamma c \operatorname{div}_\Gamma \boldsymbol{V} \,\mathrm{d}\boldsymbol{s} = \int_\Gamma \boldsymbol{V}^\top \boldsymbol{n}\, c\,(k_1+k_2)\,\mathrm{d}\boldsymbol{s} - \int_\Gamma (D_\Gamma c)\,\boldsymbol{V}\,\mathrm{d}\boldsymbol{s} \tag{4.16}$$

holds for all C^1-vector fields $\boldsymbol{V}$. We split $\boldsymbol{V}$ into its normal and tangential components according to

$$\boldsymbol{V} = (\boldsymbol{V}^\top \boldsymbol{n})\,\boldsymbol{n} + \sum_{i=1}^{2} (\boldsymbol{V}^\top \boldsymbol{\xi}_i)\,\boldsymbol{\xi}_i$$

and arrive at

$$\begin{aligned}
\int_\Gamma \boldsymbol{a}^\top (D_\Gamma \boldsymbol{V})\,\boldsymbol{b}\,\mathrm{d}\boldsymbol{s} &= \int_\Gamma \boldsymbol{a}^\top D_\Gamma((\boldsymbol{V}^\top \boldsymbol{n})\,\boldsymbol{n})\,\boldsymbol{b} + \sum_{i=1}^{2} \boldsymbol{a}^\top D_\Gamma((\boldsymbol{V}^\top \boldsymbol{\xi}_i)\,\boldsymbol{\xi}_i)\,\boldsymbol{b}\,\mathrm{d}\boldsymbol{s} \\
&= \int_\Gamma D_\Gamma(\boldsymbol{V}^\top \boldsymbol{n})(\boldsymbol{a}^\top \boldsymbol{n})\,\boldsymbol{b} + (\boldsymbol{V}^\top \boldsymbol{n})\,\boldsymbol{a}^\top (D_\Gamma \boldsymbol{n})\,\boldsymbol{b} \\
&\qquad + \sum_{i=1}^{2} D_\Gamma(\boldsymbol{V}^\top \boldsymbol{\xi}_i)(\boldsymbol{a}^\top \boldsymbol{\xi}_i)\,\boldsymbol{b} + (\boldsymbol{V}^\top \boldsymbol{\xi}_i)\,\boldsymbol{a}^\top (D_\Gamma \boldsymbol{\xi}_i)\,\boldsymbol{b}\,\mathrm{d}\boldsymbol{s} \quad \text{(by the product rule)} \\
&= \int_\Gamma \boldsymbol{V}^\top \boldsymbol{n} \left[(\boldsymbol{a}^\top \boldsymbol{n})(\boldsymbol{n}^\top \boldsymbol{b})\,(k_1+k_2) - \operatorname{div}_\Gamma((\boldsymbol{a}^\top \boldsymbol{n})\,\boldsymbol{b}) + \boldsymbol{a}^\top (D_\Gamma \boldsymbol{n})\,\boldsymbol{b} \right] \\
&\qquad + \sum_{i=1}^{2} \boldsymbol{V}^\top \boldsymbol{\xi}_i \left[\boldsymbol{a}^\top (D_\Gamma \boldsymbol{\xi}_i)\,\boldsymbol{b} - \operatorname{div}_\Gamma((\boldsymbol{a}^\top \boldsymbol{\xi}_i)\,\boldsymbol{b}) \right] \mathrm{d}\boldsymbol{s} \quad \text{(by (4.16))} \\
&= \int_\Gamma \boldsymbol{V}^\top \boldsymbol{n} \left[(\boldsymbol{a}^\top \boldsymbol{n})(\boldsymbol{n}^\top \boldsymbol{b})\,(k_1+k_2) - \operatorname{div}_\Gamma((\boldsymbol{a}^\top \boldsymbol{n})\,\boldsymbol{b}) + \boldsymbol{a}^\top (D_\Gamma \boldsymbol{n})\,\boldsymbol{b} \right].
\end{aligned}$$

In the last step we used that $\boldsymbol{V}$ is normal and thus $\boldsymbol{V}^\top \boldsymbol{\xi}_i = 0$ holds. □

4.2.2 Properties of the Total Variation of the Normal

As part of this section, we seek to establish shape differentiability of our novel objective (4.2). To this end, we use that (4.2) is a composition of smooth functions except in the presence of flat regions of positive measure on Γ. Hence, we first present some results of the material derivatives for the quantities involved, which by themselves are also interesting for a wide variety of other problems.
With respect to the outer normal $\boldsymbol{n}$, we first note that under an appropriate regularity assumption, the material derivative exists and is given by

$$\mathrm{d}\boldsymbol{n}[\boldsymbol{V}] = -(D_\Gamma \boldsymbol{V})^\top \boldsymbol{n}. \tag{4.17}$$

This result can be found, for instance, in [146, Eq. (3.168)] or [144, Lemma 3.3.6]. Notice that $\mathrm{d}\boldsymbol{n}[\boldsymbol{V}]$ is tangential because

$$\begin{aligned}
-\boldsymbol{n}^\top \mathrm{d}\boldsymbol{n}[\boldsymbol{V}] &= \boldsymbol{n}^\top (D_\Gamma \boldsymbol{V})^\top \boldsymbol{n} \\
&= \boldsymbol{n}^\top \left[(D\boldsymbol{V})^\top - \boldsymbol{n}\boldsymbol{n}^\top (D\boldsymbol{V})^\top \right] \boldsymbol{n} \\
&= 0.
\end{aligned} \tag{4.18}$$

Theorem 4.5. *Suppose that the orthonormal basis components $\boldsymbol{\xi}_1$ and $\boldsymbol{\xi}_2$ are smooth vector fields on a relatively open part $\Gamma_0 \subset \Gamma$. Then they are shape differentiable and their material derivatives are given by*

$$\begin{aligned} \mathrm{d}\boldsymbol{\xi}_1[\boldsymbol{V}] &= (D\boldsymbol{V})\,\boldsymbol{\xi}_1 - (\boldsymbol{\xi}_1^\top (D\boldsymbol{V})\,\boldsymbol{\xi}_1)\,\boldsymbol{\xi}_1 \\ \mathrm{d}\boldsymbol{\xi}_2[\boldsymbol{V}] &= (D\boldsymbol{V})\,\boldsymbol{\xi}_2 - (\boldsymbol{\xi}_2^\top (D\boldsymbol{V})\,\boldsymbol{\xi}_2)\,\boldsymbol{\xi}_2 - (\boldsymbol{\xi}_1^\top (D\boldsymbol{V} + D\boldsymbol{V}^\top)\,\boldsymbol{\xi}_2)\,\boldsymbol{\xi}_1. \end{aligned} \tag{4.19}$$

The requirement that $\boldsymbol{\xi}_{1,2}$ be smooth is not restrictive. The asymmetry in (4.19) stems from the fact that we chose to transform the first basis vector $\boldsymbol{\xi}_1$ along with (4.9) and then to orthogonalize the second basis vector $\boldsymbol{\xi}_2$ w.r.t. the first.

Proof. The proof is by construction. Beginning from a local parametrization $\boldsymbol{h}$ of the surface, we give an explicit formula for the tangent basis. The perturbed surface Γ_ε is then expressed via a perturbed parametrization

$$\boldsymbol{h}_\varepsilon := \boldsymbol{T}_\varepsilon \circ \boldsymbol{h},$$

where $\boldsymbol{T}_\varepsilon$ is given by (4.9). We derive a formula for the perturbed tangent basis via the Gram–Schmidt process. The desired material derivatives are then given by the total derivative w.r.t. $\varepsilon = 0$.
Let

$$\boldsymbol{h} : U \subset \mathbb{R}^2 \to \mathbb{R}^3$$

be a local smooth orthogonal parametrization of Γ_0, i.e., the derivative $D\boldsymbol{h}$ is a matrix with orthonormal columns, such that $\boldsymbol{s} \in \Gamma$ is locally given by

$$\boldsymbol{s} = \boldsymbol{h}(\boldsymbol{x})$$

for some $\boldsymbol{x} \in U$. Hence, we can define a smooth, orthonormal set of tangent vectors $\boldsymbol{\xi}_1, \boldsymbol{\xi}_2$ via

$$\boldsymbol{\xi}_i(\boldsymbol{s}) := \frac{D\boldsymbol{h}(\boldsymbol{x})\,\boldsymbol{e}_i}{|D\boldsymbol{h}(\boldsymbol{x})\,\boldsymbol{e}_i|_2}, \quad i = 1, 2, \tag{4.20}$$

where $\boldsymbol{e}_i$ is the i-th canonical basis vector of $\mathbb{R}^3$. With respect to $\boldsymbol{\xi}_1$, we arrive at the normalized tangent vector of the perturbed surface as

$$\begin{aligned} \boldsymbol{\xi}_{1,\varepsilon}(\boldsymbol{s}_\varepsilon) &:= \frac{D_{\boldsymbol{x}}\boldsymbol{T}_\varepsilon(\boldsymbol{h}(\boldsymbol{x}))\,\boldsymbol{e}_1}{|D_{\boldsymbol{x}}\boldsymbol{T}_\varepsilon(\boldsymbol{h}(\boldsymbol{x}))\,\boldsymbol{e}_1|_2} \\ &= \frac{D_{\boldsymbol{s}}\boldsymbol{T}_\varepsilon(\boldsymbol{s}) D\boldsymbol{h}(\boldsymbol{x})\,\boldsymbol{e}_1}{|D_{\boldsymbol{s}}\boldsymbol{T}_\varepsilon(\boldsymbol{s}) D\boldsymbol{h}(\boldsymbol{x})\,\boldsymbol{e}_1|_2} \\ &= \frac{D_{\boldsymbol{s}}\boldsymbol{T}_\varepsilon(\boldsymbol{s})\,\boldsymbol{\xi}_1(\boldsymbol{s})}{|D_{\boldsymbol{s}}\boldsymbol{T}_\varepsilon(\boldsymbol{s})\,\boldsymbol{\xi}_1(\boldsymbol{s})|_2} \\ &= \frac{(\mathrm{id} + \varepsilon\, D\boldsymbol{V}(\boldsymbol{s}))\,\boldsymbol{\xi}_1(\boldsymbol{s})}{|(\mathrm{id} + \varepsilon\, D\boldsymbol{V}(\boldsymbol{s}))\,\boldsymbol{\xi}_1(\boldsymbol{s})|_2}. \end{aligned} \tag{4.21}$$

Regarding $\boldsymbol{\xi}_2$, we proceed in a similar way, but have to apply a Gram–Schmidt step to obtain an orthonormal set of perturbed tangent vectors. Hence, $\boldsymbol{\xi}_{2,\varepsilon}$ is given by

$$\begin{aligned}\boldsymbol{\xi}_{2,\varepsilon}(\boldsymbol{s}_\varepsilon) &:= \frac{D_{\boldsymbol{s}}\boldsymbol{T}_\varepsilon(\boldsymbol{s})\,\boldsymbol{\xi}_2 - (\boldsymbol{\xi}_{1,\varepsilon}^\top D_{\boldsymbol{s}}\boldsymbol{T}_\varepsilon(\boldsymbol{s})\,\boldsymbol{\xi}_2)\,\boldsymbol{\xi}_{1,\varepsilon}}{\left|D_{\boldsymbol{s}}\boldsymbol{T}_\varepsilon(\boldsymbol{s})\,\boldsymbol{\xi}_2 - (\boldsymbol{\xi}_{1,\varepsilon}^\top D_{\boldsymbol{s}}\boldsymbol{T}_\varepsilon(\boldsymbol{s})\,\boldsymbol{\xi}_2)\,\boldsymbol{\xi}_{1,\varepsilon}\right|_2} \\ &= \frac{(\mathrm{id}+\varepsilon\,D\boldsymbol{V}(\boldsymbol{s}))\,\boldsymbol{\xi}_2 - (\boldsymbol{\xi}_{1,\varepsilon}^\top(\mathrm{id}+\varepsilon\,D\boldsymbol{V}(\boldsymbol{s}))\,\boldsymbol{\xi}_2)\,\boldsymbol{\xi}_{1,\varepsilon}}{\left|(\mathrm{id}+\varepsilon\,D\boldsymbol{V}(\boldsymbol{s}))\,\boldsymbol{\xi}_2 - (\boldsymbol{\xi}_{1,\varepsilon}^\top(\mathrm{id}+\varepsilon\,D\boldsymbol{V}(\boldsymbol{s}))\,\boldsymbol{\xi}_2)\,\boldsymbol{\xi}_{1,\varepsilon}\right|_2}.\end{aligned} \tag{4.22}$$

A straightforward differentiation with respect to $\varepsilon = 0$ results in the material derivatives given in (4.19). □

Theorem 4.6. *Under the assumptions of the previous theorem, the derivative $D_\Gamma \boldsymbol{n}$ of the normal is shape differentiable. The material derivatives of the directional derivatives of $\boldsymbol{n}$ in the directions of $\boldsymbol{\xi}_{1,2}$ are*

$$\mathrm{d}\left((D_\Gamma \boldsymbol{n})\,\boldsymbol{\xi}_i\right)[\boldsymbol{V}] = D_\Gamma(\mathrm{d}\boldsymbol{n}[\boldsymbol{V}])\,\boldsymbol{\xi}_i - (D_\Gamma \boldsymbol{n})(D_\Gamma \boldsymbol{V})\,\boldsymbol{\xi}_i + (D_\Gamma \boldsymbol{n})\,(\mathrm{d}\boldsymbol{\xi}_i[\boldsymbol{V}]). \tag{4.23}$$

Proof. With the material derivative of both the normal (4.17) and tangent (4.19) at hand, we apply the chain rule and due to the relationship between spatial and material derivatives (4.14) we arrive at

$$\begin{aligned}\mathrm{d}\left((D_\Gamma \boldsymbol{n})\,\boldsymbol{\xi}_i\right)[\boldsymbol{V}] &= \mathrm{d}\left((D\boldsymbol{n})\,\boldsymbol{\xi}_i\right)[\boldsymbol{V}] \\ &= \mathrm{d}(D\boldsymbol{n})[\boldsymbol{V}]\,\boldsymbol{\xi}_i + (D\boldsymbol{n})\,(\mathrm{d}\boldsymbol{\xi}_i[\boldsymbol{V}]) \\ &= D(\mathrm{d}\boldsymbol{n}[\boldsymbol{V}])\,\boldsymbol{\xi}_i - (D\boldsymbol{n})(D\boldsymbol{V})\,\boldsymbol{\xi}_i + (D\boldsymbol{n})\,(\mathrm{d}\boldsymbol{\xi}_i[\boldsymbol{V}]).\end{aligned}$$

Because $\mathrm{d}\boldsymbol{\xi}_i[\boldsymbol{V}]$ is tangential due to (4.19), the reduction of the full derivative D to the intrinsic derivative D_Γ on the surface is straightforward provided that $\boldsymbol{n}$ is assumed to be extended constantly into a tubular neighborhood of Γ, i.e.,

$$(D\boldsymbol{n})\boldsymbol{n} = \boldsymbol{0}.$$

□

Theorem 4.7. *Suppose that the principal curvatures do not vanish simultaneously on Γ except possibly on a set of measure zero. Then* (4.2) *is shape differentiable.*

Proof. Using [146, Sec 2.18 and Sec 2.33], shape differentiability of (4.2) can be established for Γ of class C^1 if the integrand of (4.2), i.e.,

$$\begin{aligned}g(\varepsilon, \boldsymbol{s}_\varepsilon) &:= \left(k_{1,\varepsilon}^2(\boldsymbol{s}_\varepsilon) + k_{2,\varepsilon}^2(\boldsymbol{s}_\varepsilon)\right)^{1/2} \\ &= \left(|(D_\Gamma \boldsymbol{n}_\varepsilon)\,\boldsymbol{\xi}_{1,\varepsilon}|_{\mathfrak{g}}^2 + |(D_\Gamma \boldsymbol{n}_\varepsilon)\,\boldsymbol{\xi}_{2,\varepsilon}|_{\mathfrak{g}}^2\right)^{1/2}\end{aligned} \tag{4.24}$$

fulfills

$$g(\varepsilon, \cdot) \in L^1(\Gamma_\varepsilon).$$

Likewise, the material and local derivatives have to satisfy

$$\mathrm{d}g[\boldsymbol{V}] \in L^1(\Gamma)$$

and

$$g'[\boldsymbol{V}] \in L^1(\Gamma)$$

for all sufficiently smooth vector fields $\boldsymbol{V}$ with compact support in the hold-all $\mathcal{D}$. Since we consider Γ to be a smooth surface and

$$\boldsymbol{V}\colon \mathcal{D} \to \mathbb{R}^3$$

a smooth vector field,

$$\Gamma_\varepsilon \coloneqq T_\varepsilon[\boldsymbol{V}](\Gamma)$$

is smooth. Moreover, since Γ_ε is compact, $g(\varepsilon, \cdot)$ is bounded, and one easily deduces

$$g(\varepsilon, \cdot) \in L^1(\Gamma_\varepsilon).$$

The shape differentiability of the tangent basis is considered in Theorem 4.5 and of the derivative of the normal in Theorem 4.6. Hence, we establish the material derivative of the expression under the square root in (4.24) via the chain rule for a composition of smooth functions. Notice that the local character of the results in Theorems 4.5 and 4.6 is sufficient since (4.24) is independent of the choice of the orthonormal basis, as established in Remark 4.1. Since, by assumption, both principal curvatures do not vanish simultaneously, we have $g \neq 0$ almost everywhere and we arrive at

$$\mathrm{d}g[\boldsymbol{V}] = \frac{1}{g(\boldsymbol{s})} \sum_{i=1}^{2} \mathfrak{g}\big((D_\Gamma \boldsymbol{n})\, \boldsymbol{\xi}_i,\, \mathrm{d}[(D_\Gamma \boldsymbol{n})\, \boldsymbol{\xi}_i][\boldsymbol{V}]\big), \tag{4.25}$$

from where we conclude

$$\mathrm{d}g[\boldsymbol{V}] \in L^1(\Gamma).$$

To establish

$$g'[\boldsymbol{V}] \in L^1(\Gamma),$$

we use (4.12). To this end, we extend g constantly in normal direction into a tubular neighborhood of Γ. As a composition of smooth functions, we conclude $g'[\boldsymbol{V}] \in L^1(\Gamma)$. □

Remark 4.8. *As per [146, Eq. (2.172)], the requirement* $g'[\boldsymbol{V}] \in L^1(\Gamma)$ *can be omitted if one is only interested in the representation* (4.11) *of the shape derivative and not in formulation* (4.13).

We are now in the position to address the minimization of (4.2). In view of Lemma 4.3, this is meaningful only when additional terms are present which prevent the degeneration of the surface to a point. We choose to impose a constraint on the surface area here. We have the following partial result.

Theorem 4.9. *Spheres are stationary points for* (4.2) *among all surfaces* Γ *of constant area.*

Proof. We consider the minimization of (4.2) or equivalently, (4.5), subject to the constraint that the surface area equals the constant $A_0 > 0$. The Lagrangian associated with this problem is given by

$$\int_\Gamma \left(k_1^2(\boldsymbol{s}) + k_2^2(\boldsymbol{s})\right)^{1/2} \mathrm{d}\boldsymbol{s} + \mu \left(\int_\Gamma 1 \,\mathrm{d}\boldsymbol{s} - A_0\right).$$

Here $\mu \in \mathbb{R}$ is the Lagrange multiplier to be determined below. The differentiability of the first summand has been considered in Theorem 4.7. On the perturbed domain with surface Γ_ε with the perturbation according to (4.9), the Lagrangian reads

$$\begin{aligned}\mathcal{L}(\varepsilon,\mu) &:= \int_{\Gamma_\varepsilon} \left(k_{1,\varepsilon}^2(\boldsymbol{s}_\varepsilon) + k_{2,\varepsilon}^2(\boldsymbol{s}_\varepsilon)\right)^{1/2} \mathrm{d}\boldsymbol{s}_\varepsilon + \mu \left(\int_{\Gamma_\varepsilon} 1 \,\mathrm{d}\boldsymbol{s}_\varepsilon - A_0\right) \\ &= \int_{\Gamma_\varepsilon} \left[\left(k_{1,\varepsilon}^2(\boldsymbol{s}_\varepsilon) + k_{2,\varepsilon}^2(\boldsymbol{s}_\varepsilon)\right)^{1/2} + \mu\right] \mathrm{d}\boldsymbol{s}_\varepsilon - \mu\, A_0.\end{aligned}$$

We use the same abbreviation as before in (4.24). The above integral is of type (4.10) and its shape derivative at the unperturbed surface, according to (4.13), is given by

$$\mathrm{d}\mathcal{L}(0,\mu)[\boldsymbol{V}] = \int_\Gamma \boldsymbol{V}^\top \boldsymbol{n} \left[(Dg)\boldsymbol{n} + (k_1 + k_2)\,(g + \mu)\right] + g'[\boldsymbol{V}] \,\mathrm{d}\boldsymbol{s}$$

because μ is a constant.
When Ω is a sphere of radius r, we are going to show that

$$\mathrm{d}\mathcal{L}(0,\mu)[\boldsymbol{V}] = 0$$

holds for all perturbation fields $\boldsymbol{V}$ in normal direction and with

$$\mu = -1/(\sqrt{2}\,r).$$

In this setting, the principal curvatures are

$$k_1(\boldsymbol{s}) = k_2(\boldsymbol{s}) \equiv 1/r;$$

see for instance [87, Chapter 13]. Consequently,

$$g(\boldsymbol{s}) = \left(k_1^2(\boldsymbol{s}) + k_2^2(\boldsymbol{s})\right)^{\frac{1}{2}} \equiv \sqrt{2}/r$$

is spatially constant and thus $Dg \equiv 0$ holds. We obtain from (4.13)

$$\mathrm{d}\mathcal{L}(0,\mu)[\boldsymbol{V}] = \int_\Gamma \boldsymbol{V}^\top \boldsymbol{n}\, \frac{2}{r} \left(\frac{\sqrt{2}}{r} + \mu\right) \mathrm{d}\boldsymbol{s} + \int_\Gamma g'[\boldsymbol{V}] \,\mathrm{d}\boldsymbol{s}.$$

Hence, by (4.12), we also have

$$\mathrm{d}g[\boldsymbol{V}] = g'[\boldsymbol{V}].$$

Using (4.25), we arrive at

$$\begin{aligned} g'[\boldsymbol{V}] &= \mathrm{d}g[\boldsymbol{V}] \\ &= \frac{1}{g(\boldsymbol{s})} \sum_{i=1}^{2} \mathfrak{g}\big((D_\Gamma \boldsymbol{n})\,\boldsymbol{\xi}_i,\, \mathrm{d}[(D_\Gamma \boldsymbol{n})\,\boldsymbol{\xi}_i][\boldsymbol{V}]\big). \end{aligned} \tag{4.26}$$

In order to complete the proof of Theorem 4.9, we need to show that

$$\int_\Gamma \frac{1}{g(\boldsymbol{s})} \sum_{i=1}^{2} \mathfrak{g}\big((D_\Gamma \boldsymbol{n})\, \boldsymbol{\xi}_i,\, \mathrm{d}[(D_\Gamma \boldsymbol{n})\, \boldsymbol{\xi}_i][\boldsymbol{V}]\big)\, \mathrm{d}\boldsymbol{s} = c_0 \int_\Gamma \boldsymbol{V}^\top \boldsymbol{n}\, \mathrm{d}\boldsymbol{s} \tag{4.27}$$

holds with

$$c_0 = -\frac{\sqrt{2}}{r^2}.$$

To this end, we need a tangential Stokes formula as given in Lemma 4.4.
We shall also exploit that

$$g(\boldsymbol{s}) = \sqrt{2}/r$$

is a constant on the sphere of radius r. Finally, we use

$$(D\boldsymbol{n})(\boldsymbol{s}) \equiv \frac{\mathrm{id}}{r} \quad \text{and} \quad (D_\Gamma \boldsymbol{n})(\boldsymbol{s}) = \frac{\mathrm{id}}{r}\left(\mathrm{id} - \boldsymbol{n}\boldsymbol{n}^\top\right) \tag{4.28}$$

and thus

$$(D_\Gamma \boldsymbol{n})\, \boldsymbol{\xi} = \boldsymbol{\xi}/r$$

holds for $i = 1, 2$.
The three terms contributing to the material derivative

$$\mathrm{d}[(D_\Gamma \boldsymbol{n})\, \boldsymbol{\xi}_i][\boldsymbol{V}]$$

in (4.27) are given in (4.23) and we consider them individually. We use that the Riemannian metric on $\mathcal{S}^2$ is the Euclidean inner product of the ambient $\mathbb{R}^3$, i.e.,

$$\mathfrak{g}(\boldsymbol{a}, \boldsymbol{b}) = \boldsymbol{a}^\top \boldsymbol{b}.$$

As noted in Theorem 4.6, there is no need to distinguish between the full derivative D or the intrinsic derivative D_Γ, because they are always actions on objects from the tangent space. As such, we use the symbols in a manner to make the expressions most inline with the previous results.
First Term. The insertion of the first term in (4.23) into the left hand side of (4.27) leads to the expression

$$\begin{aligned}
&\frac{r}{\sqrt{2}} \int_\Gamma \sum_{i=1}^{2} \left[(D_\Gamma \boldsymbol{n})\, \boldsymbol{\xi}_i\right]^\top D_\Gamma(\mathrm{d}\boldsymbol{n}[\boldsymbol{V}])\, \boldsymbol{\xi}_i\, \mathrm{d}\boldsymbol{s} \\
&\quad = \frac{r}{\sqrt{2}} \frac{1}{r} \int_\Gamma \sum_{i=1}^{2} \boldsymbol{\xi}_i^\top D_\Gamma(\mathrm{d}\boldsymbol{n}[\boldsymbol{V}])\, \boldsymbol{\xi}_i\, \mathrm{d}\boldsymbol{s} \quad \text{by (4.28)} \\
&\quad = \frac{1}{\sqrt{2}} \int_\Gamma \mathrm{div}_\Gamma\, \mathrm{d}\boldsymbol{n}[\boldsymbol{V}]\, \mathrm{d}\boldsymbol{s} \qquad (4.29) \\
&\quad = 0. \qquad (4.30)
\end{aligned}$$

The last step follows from (4.16) with $c = 1$. Recall from (4.18) that $\mathrm{d}\boldsymbol{n}[\boldsymbol{V}]$ is tangential.

Second Term. Inserting the second term in (4.23) into the left hand side of (4.27) leads to the expression

$$\begin{aligned}
&-\int_\Gamma \frac{1}{g(s)} \sum_{i=1}^{2} \left[(D_\Gamma \boldsymbol{n})\, \boldsymbol{\xi}_i \right]^\top (D_\Gamma \boldsymbol{n}) (D_\Gamma \boldsymbol{V})\, \boldsymbol{\xi}_i \, \mathrm{d}s \\
&\quad = -\frac{r}{\sqrt{2}} \frac{1}{r^2} \int_\Gamma \sum_{i=1}^{2} \boldsymbol{\xi}_i^\top (D_\Gamma \boldsymbol{V})\, \boldsymbol{\xi}_i \, \mathrm{d}s \quad \text{by (4.28)} \\
&\quad = -\frac{1}{\sqrt{2}\, r} \int_\Gamma \sum_{i=1}^{2} \boldsymbol{V}^\top \boldsymbol{n} \left[\boldsymbol{\xi}_i^\top (D_\Gamma \boldsymbol{n})\, \boldsymbol{\xi}_i \right] \mathrm{d}s \quad \text{by (4.15)} \\
&\quad = -\frac{\sqrt{2}}{r^2} \int_\Gamma \boldsymbol{V}^\top \boldsymbol{n} \, \mathrm{d}s \quad \text{by (4.28).}
\end{aligned} \tag{4.31}$$

Third Term. Finally, inserting the third term in (4.23) into the left hand side of (4.27) yields

$$\int_\Gamma \frac{1}{g(s)} \sum_{i=1}^{2} \left[(D_\Gamma \boldsymbol{n})\, \boldsymbol{\xi}_i \right]^\top (D_\Gamma \boldsymbol{n}) \left(\mathrm{d}\boldsymbol{\xi}_i[\boldsymbol{V}] \right) \mathrm{d}s. \tag{4.32}$$

The first summand ($i = 1$) leads to

$$\begin{aligned}
&\int_\Gamma \frac{1}{g(s)} \left[(D_\Gamma \boldsymbol{n})\, \boldsymbol{\xi}_1 \right]^\top (D_\Gamma \boldsymbol{n}) \left(\mathrm{d}\boldsymbol{\xi}_1[\boldsymbol{V}] \right) \mathrm{d}s \\
&\quad = \frac{r}{\sqrt{2}} \int_\Gamma \left[(D_\Gamma \boldsymbol{n})\, \boldsymbol{\xi}_1 \right]^\top (D_\Gamma \boldsymbol{n}) \left[(D\boldsymbol{V})\, \boldsymbol{\xi}_1 - (\boldsymbol{\xi}_1^\top (D\boldsymbol{V})\, \boldsymbol{\xi}_1)\, \boldsymbol{\xi}_1 \right] \mathrm{d}s \quad \text{by (4.19)} \\
&\quad = \frac{r}{\sqrt{2}} \frac{1}{r^2} \int_\Gamma \boldsymbol{\xi}_1^\top \left[(D\boldsymbol{V})\, \boldsymbol{\xi}_1 - (\boldsymbol{\xi}_1^\top (D\boldsymbol{V})\, \boldsymbol{\xi}_1)\, \boldsymbol{\xi}_1 \right] \mathrm{d}s \\
&\quad = 0.
\end{aligned}$$

For the second summand ($i = 2$), we get one additional term:

$$\begin{aligned}
&\int_\Gamma \frac{1}{g(s)} \left[(D_\Gamma \boldsymbol{n})\, \boldsymbol{\xi}_2 \right]^\top (D_\Gamma \boldsymbol{n}) \left(\mathrm{d}\boldsymbol{\xi}_2[\boldsymbol{V}] \right) \mathrm{d}s \\
&\quad = \frac{r}{\sqrt{2}} \int_\Gamma \left[(D_\Gamma \boldsymbol{n})\, \boldsymbol{\xi}_2 \right]^\top (D_\Gamma \boldsymbol{n}) \left[(D\boldsymbol{V})\, \boldsymbol{\xi}_2 - (\boldsymbol{\xi}_2^\top (D\boldsymbol{V})\, \boldsymbol{\xi}_2)\, \boldsymbol{\xi}_2 \right] \mathrm{d}s \\
&\qquad - \frac{r}{\sqrt{2}} \int_\Gamma \left[(D_\Gamma \boldsymbol{n})\, \boldsymbol{\xi}_2 \right]^\top (D_\Gamma \boldsymbol{n}) \left(\boldsymbol{\xi}_1^\top (D\boldsymbol{V} + D\boldsymbol{V}^\top)\, \boldsymbol{\xi}_2 \right) \boldsymbol{\xi}_1 \quad \text{by (4.19)} \\
&\quad = 0 - \frac{r}{\sqrt{2}} \frac{1}{r^2} \int_\Gamma \boldsymbol{\xi}_2^\top \left[\boldsymbol{\xi}_1^\top (D\boldsymbol{V} + D\boldsymbol{V}^\top)\, \boldsymbol{\xi}_2 \right] \boldsymbol{\xi}_1 \, \mathrm{d}s \\
&\quad = 0.
\end{aligned}$$

Hence expression (4.32) is zero. Collecting terms (4.30)–(4.32), we have shown that the left hand side in (4.27) amounts to

$$\int_\Gamma \frac{1}{g(s)} \sum_{i=1}^{2} \mathfrak{g}\big((D_\Gamma \boldsymbol{n})\, \boldsymbol{\xi}_i,\, \mathrm{d}[(D_\Gamma \boldsymbol{n})\, \boldsymbol{\xi}_i][\boldsymbol{V}] \big) \, \mathrm{d}s = -\frac{\sqrt{2}}{r^2} \int_\Gamma \boldsymbol{V}^\top \boldsymbol{n} \, \mathrm{d}s.$$

Therefore, (4.27) is fulfilled with

$$c_0 = -\frac{\sqrt{2}}{r^2}.$$

As a consequence of (4.27) we obtain the representation

$$\begin{aligned} \mathrm{d}\mathcal{L}(0,\mu)[\boldsymbol{V}] &= \left[\frac{2}{r}\left(\frac{\sqrt{2}}{r}+\mu\right)+c_0\right]\int_\Gamma \boldsymbol{V}^\top \boldsymbol{n}\,\mathrm{d}\boldsymbol{s} \\ &= \left[\frac{2}{r}\left(\frac{1}{\sqrt{2}\,r}+\mu\right)\right]\int_\Gamma \boldsymbol{V}^\top \boldsymbol{n}\,\mathrm{d}\boldsymbol{s} \end{aligned}$$

for all perturbation fields $\boldsymbol{V}$ parallel to $\boldsymbol{n}$. Clearly, the term in brackets vanishes when

$$\mu = -1/(\sqrt{2}\,r)$$

holds. This concludes the proof. □

4.2.3 The Case of Curves

When $\Omega \subset \mathbb{R}^2$ and Γ is a one-dimensional manifold, (4.2) and thus (4.5) reduce to the *total absolute curvature*

$$\int_\Gamma |k|\ \mathrm{d}\boldsymbol{s},$$

where k is the single curvature. It is well known that this integral has a minimal value of 2π, which is attained precisely for the boundaries Γ of convex, smoothly bounded domains $\Omega \subset \mathbb{R}^2$; see [54, Chapter 21.1] or [38]. This case is thus different in two aspects from our setting $\Omega \subset \mathbb{R}^3$. On the one hand, $\int_\Gamma |k|\ \mathrm{d}\boldsymbol{s}$ is invariant to scale while (4.2) is not, as was shown in (4.8). On the other hand, (4.2) appears to have a much smaller set of minimizers; see Theorem 4.9.

4.3 Split Bregman Iteration

In this section we propose an Alternating Direction Method of Multipliers (ADMM) iteration, which generalizes the split Bregman algorithm for total variation problems proposed in [85]. As is well known, ADMM methods introduce a splitting of variables so that minimization over individual variables becomes efficient.

There is very little prior work on ADMM involving manifolds. We are aware of [105, 109, 161, 171], all of which consider particular manifolds and their embeddings into some vector space in order to formulate the splitting constraint. By contrast, in our setting the constraint is formulated pointwise in the tangent bundle of $\mathcal{S}^2$. In addition, and even though we do not emphasize this aspect throughout the chapter, the primary variable Ω in problem (4.33) lives on a *manifold of shapes*. That said, we will not attempt a convergence proof for the proposed split Bregman iteration here but leave it for future research.

In our setting, the primary variable is the unknown domain Ω. Notice that Ω also determines its boundary Γ as well as its normal vector field $\boldsymbol{n}$, and we will always consider Γ and $\boldsymbol{n}$ as a function of Ω. The splitting is achieved through the introduction of a new

variable $\boldsymbol{d}$, which is independent of Ω, Γ and $\boldsymbol{n}$. At the solution, we require the coupling condition

$$\boldsymbol{d} = D_\Gamma \boldsymbol{n}$$

to hold across Γ. We recall that $D_\Gamma \boldsymbol{n}$ denotes the derivative (push-forward) of $\boldsymbol{n}$. At the point $\boldsymbol{s} \in \Gamma$, $(D_\Gamma \boldsymbol{n})(\boldsymbol{s})$ maps $\mathcal{T}_{\boldsymbol{s}}\Gamma$ into $\mathcal{T}_{\boldsymbol{n}(\boldsymbol{s})}\mathcal{S}^2$. Written in terms of Ω and the secondary variable

$$\boldsymbol{d} = (\boldsymbol{d}_1, \boldsymbol{d}_2) \colon \Gamma \to \mathcal{T}_{\boldsymbol{n}(\cdot)}\mathcal{S}^2,$$

problem (4.3) becomes

$$\begin{aligned} \text{Minimize} \quad & \ell(u(\Omega), \Omega) + \beta \int_\Gamma \left(|\boldsymbol{d}_1|_{\mathfrak{g}}^2 + |\boldsymbol{d}_2|_{\mathfrak{g}}^2 \right)^{1/2} \mathrm{d}\boldsymbol{s} \\ \text{s.t.} \quad & \boldsymbol{d}_i = (D_\Gamma \boldsymbol{n})\, \boldsymbol{\xi}_i \quad \text{on } \Gamma \text{ for } i = 1, 2. \end{aligned} \tag{4.33}$$

Notice that for convenience of notation, we represent $D_\Gamma \boldsymbol{n}$ in terms of its actions on the two basis vectors $\boldsymbol{\xi}_i$.
Note also that at the point $\boldsymbol{s} \in \Gamma$, the equality

$$\boldsymbol{d}_i = (D_\Gamma \boldsymbol{n})\, \boldsymbol{\xi}_i$$

is in the tangent space $\mathcal{T}_{\boldsymbol{n}(\boldsymbol{s})}\mathcal{S}^2$. We therefore introduce Lagrange multipliers $\boldsymbol{\lambda} = (\boldsymbol{\lambda}_1, \boldsymbol{\lambda}_2)$, belonging to the same space, and define the augmented Lagrangian associated with (4.3) as follows,

$$\begin{aligned} \widehat{\mathcal{L}}(\Omega, \boldsymbol{d}_1, \boldsymbol{d}_2, \boldsymbol{\lambda}_1, \boldsymbol{\lambda}_2) \coloneqq \ell(u(\Omega), \Omega) &+ \beta \int_\Gamma \left(|\boldsymbol{d}_1|_{\mathfrak{g}}^2 + |\boldsymbol{d}_2|_{\mathfrak{g}}^2 \right)^{1/2} \mathrm{d}\boldsymbol{s} \\ &+ \sum_{i=1}^{2} \left(\int_\Gamma \mathfrak{g}\big(\boldsymbol{\lambda}_i,\, \boldsymbol{d}_i - (D_\Gamma \boldsymbol{n})\, \boldsymbol{\xi}_i\big)\, \mathrm{d}\boldsymbol{s} \right. \\ &\left. + \frac{\lambda}{2} \int_\Gamma \mathfrak{g}\big(\boldsymbol{d}_i - (D_\Gamma \boldsymbol{n})\, \boldsymbol{\xi}_i,\, \boldsymbol{d}_i - (D_\Gamma \boldsymbol{n})\, \boldsymbol{\xi}_i\big)\, \mathrm{d}\boldsymbol{s} \right). \end{aligned} \tag{4.34}$$

Here $\lambda > 0$ is the augmentation parameter. After the usual re-scaling $\boldsymbol{b}_i \coloneqq \boldsymbol{\lambda}_i / \lambda$, we can rewrite (4.34) as

$$\begin{aligned} \mathcal{L}(\Omega, \boldsymbol{d}_1, \boldsymbol{d}_2, \boldsymbol{b}_1, \boldsymbol{b}_2) \coloneqq \ell(u(\Omega), \Omega) &+ \beta \int_\Gamma \left(|\boldsymbol{d}_1|_{\mathfrak{g}}^2 + |\boldsymbol{d}_2|_{\mathfrak{g}}^2 \right)^{1/2} \mathrm{d}\boldsymbol{s} \\ &+ \frac{\lambda}{2} \sum_{i=1}^{2} \int_\Gamma \left| \boldsymbol{d}_i - (D_\Gamma \boldsymbol{n})\, \boldsymbol{\xi}_i - \boldsymbol{b}_i \right|_{\mathfrak{g}}^2 \mathrm{d}\boldsymbol{s}. \end{aligned} \tag{4.35}$$

The main difference to an ADMM method in Euclidean or Hilbert spaces is that the vector fields $\boldsymbol{d}_i$ and $\boldsymbol{b}_i$ have values in the tangent space $\mathcal{T}_{\boldsymbol{n}(\cdot)}\mathcal{S}^2$. Hence they must be updated whenever Ω and thus the normal vector field $\boldsymbol{n}$ are changing.
We outline our proposed method for (4.33) as Algorithm 6. As expected for methods of the ADMM class, we successively optimize with respect to the variables Ω and $(\boldsymbol{d}_1, \boldsymbol{d}_2)$ independently and then perform a simple update step for the multiplier $(\boldsymbol{b}_1, \boldsymbol{b}_2)$. We address each of these steps in the following subsections.

Algorithm 6 Split Bregman method for (4.33)

Require: Initial domain $\Omega^{(0)}$
Ensure: Approximate solution of (4.33)
1: Set $\boldsymbol{b}^{(0)} := \mathbf{0}$, $\boldsymbol{d}^{(0)} := \mathbf{0}$
2: Set $k := 0$
3: **while** not converged **do**
4: Perform some gradient steps for $\Omega \mapsto \mathcal{L}(\Omega, \boldsymbol{d}^{(k)}, \boldsymbol{b}^{(k)})$ starting from $\Omega^{(k)}$, to obtain $\Omega^{(k+1)}$
5: Parallely transport the multiplier estimate $\boldsymbol{b}^{(k)}$ pointwise from $\mathcal{T}_{\boldsymbol{n}^{(k)}(\cdot)}\mathcal{S}^2$ to $\mathcal{T}_{\boldsymbol{n}^{(k+1)}(\cdot)}\mathcal{S}^2$ along the geodesic from $\boldsymbol{n}^{(k)}$ to $\boldsymbol{n}^{(k+1)}$
6: Parallely transport the basis vectors $\boldsymbol{\xi}_i$ pointwise from $\mathcal{T}_{\boldsymbol{n}^{(k)}(\cdot)}\mathcal{S}^2$ to $\mathcal{T}_{\boldsymbol{n}^{(k+1)}(\cdot)}\mathcal{S}^2$ along the geodesic from $\boldsymbol{n}^{(k)}$ to $\boldsymbol{n}^{(k+1)}$ for $i = 1, 2$
7: Set $\boldsymbol{d}^{(k+1)} := \arg\min \mathcal{L}(\Omega^{(k+1)}, \boldsymbol{d}^{(k)}, \boldsymbol{b}^{(k)})$, see (4.41)
8: Update the Lagrange multipliers, i.e., set $\boldsymbol{b}_i^{(k+1)} := \boldsymbol{b}_i^{(k)} + (D_\Gamma \boldsymbol{n}^{(k+1)})\, \boldsymbol{\xi}_i - \boldsymbol{d}_i^{(k+1)}$ for $i = 1, 2$
9: Set $k := k + 1$
10: **end while**

4.3.1 The Shape Optimization Step

We first address the minimization of (4.35) w.r.t. the shape Ω, while the quantities $\boldsymbol{d}_1$, $\boldsymbol{d}_2$, $\boldsymbol{b}_1$ and $\boldsymbol{b}_2$ are fixed, or, more precisely, passively transformed along with Ω. The main effort is to calculate the shape derivative of (4.35).
The derivative of the first term in (4.35), i.e., $\mathrm{d}\ell(u(\Omega), \Omega)[\boldsymbol{V}]$, is not specified here since it depends on the particular PDE underlying the solution operator $u(\Omega)$ and the loss function ℓ considered. This derivative can be obtained by standard shape calculus techniques, which are not our concern here. A concrete example is considered in Section 6.1.
Next we consider the second term in (4.35). Due to the chosen splitting, the vector fields $\boldsymbol{d}_i$ are merely transformed along with Ω according to the perturbation (4.9) and thus we define their perturbed counterparts as

$$\begin{aligned} \boldsymbol{d}_{i,\varepsilon}(s_\varepsilon) &:= \boldsymbol{d}_i(\boldsymbol{T}_\varepsilon^{-1}(s_\varepsilon)) \\ &= \boldsymbol{d}_i(s) \end{aligned} \tag{4.36}$$

and likewise for $\boldsymbol{b}_i$ and

$$\left(|\boldsymbol{d}_1|_{\mathfrak{g}}^2 + |\boldsymbol{d}_2|_{\mathfrak{g}}^2\right)^{1/2}.$$

As a consequence, their material derivatives vanish and the directional derivative of the second term of (4.35) becomes

$$\mathrm{d}\left(\int_\Gamma \left(|\boldsymbol{d}_1|_{\mathfrak{g}}^2 + |\boldsymbol{d}_2|_{\mathfrak{g}}^2\right)^{1/2} \mathrm{d}s\right)[\boldsymbol{V}] = \int_\Gamma (\mathrm{div}_\Gamma \boldsymbol{V}) \left(|\boldsymbol{d}_1|_{\mathfrak{g}}^2 + |\boldsymbol{d}_2|_{\mathfrak{g}}^2\right)^{1/2} \mathrm{d}s.$$

Finally we address the terms

$$\int_\Gamma \left|\boldsymbol{d}_i - (D_\Gamma \boldsymbol{n})\, \boldsymbol{\xi}_i - \boldsymbol{b}_i\right|_{\mathfrak{g}}^2 \mathrm{d}s$$

for $i = 1, 2$. The vector fields $\boldsymbol{d}_i$ and $\boldsymbol{b}_i$ are transformed according to (4.36) and thus we need not consider their material derivatives. However, we do need to track the dependencies of $(D_\Gamma \boldsymbol{n})\,\boldsymbol{\xi}_i$. The respective shape derivative is given in (4.23).
We summarize these findings in the following theorem.

Theorem 4.10. *Suppose that the* $(\boldsymbol{d}_1, \boldsymbol{d}_2)$ *do not vanish simultaneously on* Γ *except possibly on a set of measure zero, and that the loss term* $\ell(u(\Omega), \Omega)$ *is shape differentiable. Then the augmented Lagrangian* (4.35) *is shape differentiable and its shape derivative is given by*

$$\begin{aligned}
&\mathrm{d}\mathcal{L}(\Omega, \boldsymbol{d}_1, \boldsymbol{d}_2, \boldsymbol{b}_1, \boldsymbol{b}_2)[\boldsymbol{V}] \\
&\quad = \mathrm{d}\ell(u(\Omega), \Omega)[\boldsymbol{V}] + \beta \int_\Gamma (\operatorname{div}_\Gamma \boldsymbol{V}) \left(|\boldsymbol{d}_1|_{\mathfrak{g}}^2 + |\boldsymbol{d}_2|_{\mathfrak{g}}^2 \right)^{1/2} \mathrm{d}\boldsymbol{s} \\
&\qquad + \frac{\lambda}{2} \sum_{i=1}^{2} \int_\Gamma (\operatorname{div}_\Gamma \boldsymbol{V}) \left| \boldsymbol{d}_i - (D_\Gamma \boldsymbol{n})\,\boldsymbol{\xi}_i - \boldsymbol{b}_i \right|_{\mathfrak{g}}^2 \mathrm{d}\boldsymbol{s} \\
&\qquad + \lambda \sum_{i=1}^{2} \int_\Gamma \mathfrak{g}\Big(\boldsymbol{d}_i - (D_\Gamma \boldsymbol{n})\,\boldsymbol{\xi}_i - \boldsymbol{b}_i,\ -\mathrm{d}\left((D_\Gamma \boldsymbol{n})\,\boldsymbol{\xi}_i \right)[\boldsymbol{V}] \Big) \mathrm{d}\boldsymbol{s}
\end{aligned} \tag{4.37}$$

with $\mathrm{d}\left((D_\Gamma \boldsymbol{n})\,\boldsymbol{\xi}_i \right)[\boldsymbol{V}]$ *from* (4.23).

The shape derivative in (4.37) is the basis of any shape optimization procedure. After all, the minimization of (4.35) w.r.t. the domain Ω represents a fairly standard shape optimization problem. We convert the shape derivative (4.37) into a shape gradient vector field $\boldsymbol{U}$ by means of an appropriate inner product. Then, instead of minimizing (4.35) w.r.t. Ω to a certain accuracy, in practice we only perform a few gradient steps per ADMM iteration. This is in line with [85], where a Gauss–Seidel sweep is proposed instead of an exact solve.
Still, the terms in (4.23) would be tedious to implement by hand. In our implementation, which is detailed in the next chapter, the shape derivative (4.37) is conveniently evaluated by algorithmic differentiation techniques on the discrete level.

4.3.2 The Total Variation Minimization Step

Before addressing the minimization of (4.35) w.r.t. $\boldsymbol{d}$ we must note that the data $\boldsymbol{b}_i$ at any point $\boldsymbol{s} \in \Gamma$ has to belong to the tangent space $\mathcal{T}_{\boldsymbol{n}(\boldsymbol{s})}\mathcal{S}^2$. Since the surface Γ and hence the field of normal vectors is changing during the shape optimization step, we must first move the data $\boldsymbol{b}_i$ into the new tangent space. This is achieved via parallel transport along geodesics on $\mathcal{S}^2$. Suppose for brevity of notation that $\boldsymbol{n}^-$ denotes the old normal vector field along the boundary Γ^- of the previous iterate Ω^-. Then

$$\boldsymbol{b}_i^- \in \mathcal{T}_{\boldsymbol{n}^-(\cdot)}\mathcal{S}^2$$

needs to be parallely transported into

$$\boldsymbol{b}_i \in \mathcal{T}_{\boldsymbol{n}(\cdot)}\mathcal{S}^2$$

along the geodesic from $\boldsymbol{n}^-$ to $\boldsymbol{n}$. This step is inexpensive since the parallel transport

$$P_{\boldsymbol{n}^- \to \boldsymbol{n}} \colon \mathcal{T}_{\boldsymbol{n}^-}\mathcal{S}^2 \to \mathcal{T}_{\boldsymbol{n}}\mathcal{S}^2$$

on $\mathcal{S}^2$ is available in terms of the following explicit formula

$$P_{n^- \to n}(b_i^-) = b_i^- - \frac{{b_i^-}^\top (\log_{n^-} n)}{\arccos^2(n^\top n^-)} (\log_{n^-} n + \log_n n^-), \tag{4.38}$$

whenever $n \neq -n^-$ holds, see for instance [100] and [128, Section 2.3.1], respectively. Here $\log_{n_E^+} n_E^-$ denotes the logarithmic map

$$\log_a b := \arccos(a^\top b) \frac{b - (a^\top b)\, a}{|b - (a^\top b)\, a|_{\mathfrak{g}}}, \tag{4.39}$$

which specifies the unique tangent vector at the point n_E^+ such that the geodesic departing from n_E^+ in that direction will reach n_E^- at unit time. The logarithmic map on $\mathcal{S}^2$ is well-defined also whenever

$$n_E^+ \neq -n_E^-.$$

Since we explicitly refer to them, also the basis vectors ξ_i^- need to be parallely transported into ξ_i in the same way as above.
We can now address the minimization of (4.35) w.r.t. the field $d = (d_1, d_2)$. Since the first term in (4.35) does not depend on d, we are left with the minimization of

$$\beta \int_\Gamma \left(|d_1|_{\mathfrak{g}}^2 + |d_2|_{\mathfrak{g}}^2 \right)^{1/2} \mathrm{d}s + \frac{\lambda}{2} \sum_{i=1}^{2} \int_\Gamma \left| d_i - (D_\Gamma n)\, \xi_i - b_i \right|_{\mathfrak{g}}^2 \mathrm{d}s, \tag{4.40}$$

where d_1, d_2 are sought pointwise in the tangent spaces $\mathcal{T}_{n(\cdot)}\mathcal{S}^2$. We recall that the latter are two-dimensional subspaces of $\mathbb{R}^3$. At this point it is important to note that the data

$$(D_\Gamma n)\, \xi_i + b_i$$

belongs to the same tangent spaces. Therefore, just like in the Euclidean setting, the minimizer of (4.40) can be evaluated explicitly and inexpensively via a pointwise, vectorial shrinkage operation, i.e.,

$$\begin{aligned} d &= \begin{pmatrix} d_1 \\ d_2 \end{pmatrix} \\ &:= \max\left\{ \left| (D_\Gamma n)\, \xi + b \right|_{\mathfrak{g}} - \frac{\beta}{\lambda},\ 0 \right\} \frac{(D_\Gamma n)\, \xi + b}{\left| (D_\Gamma n)\, \xi + b \right|_{\mathfrak{g}}} \in \left[\mathcal{T}_{n(\cdot)}\mathcal{S}^2 \right]^2. \end{aligned} \tag{4.41}$$

Here we abbreviated

$$(D_\Gamma n)\, \xi := \begin{pmatrix} (D_\Gamma n)\, \xi_1 \\ (D_\Gamma n)\, \xi_2 \end{pmatrix}$$

and

$$\left| (D_\Gamma n)\, \xi + b \right|_{\mathfrak{g}} = \left(|(D_\Gamma n)\, \xi_1 + b_1|_{\mathfrak{g}}^2 + |(D_\Gamma n)\, \xi_2 + b_2|_{\mathfrak{g}}^2 \right)^{1/2}.$$

4.3.3 The Multiplier Update

An update of the Lagrange multiplier fields (b_1, b_2) is achieved, analogously to the Euclidean setting, by replacing b_i with

$$b_i + (D_\Gamma n)\, \xi_i - d_i, \quad i = 1, 2.$$

Notice again that all quantities belong to the subspace $\mathcal{T}_{n(\cdot)}\mathcal{S}^2$ of $\mathbb{R}^3$.

CHAPTER 5

DISCRETE TOTAL VARIATION OF THE NORMAL FOR TRIANGULATED SURFACES

In this chapter, we discuss a discrete variant of (4.2) tailored to piecewise flat surfaces Γ_h, where (4.2) does not apply. In contrast with the smooth setting, the total variation of the piecewise constant normal vector field $\boldsymbol{n}$ is concentrated in jumps across edges between flat facets. We therefore propose the following *discrete total variation of the normal*,

$$|\boldsymbol{n}|_{DTV(\Gamma_h)} := \sum_E d(\boldsymbol{n}_E^+, \boldsymbol{n}_E^-)\,|E|\,. \tag{5.1}$$

Here E denotes an edge of length $|E|$ between facets, and $d(\boldsymbol{n}_E^+, \boldsymbol{n}_E^-)$ is the geodesic distance between the two neighboring normal vectors.

We investigate (5.1) in Section 5.1. It turns out to coincide with the *discrete total mean curvature* known in discrete differential geometry. Subsequently, we discuss the utility of this functional as a prior in shape optimization problems cast in the form

$$\begin{aligned} &\text{Minimize} \quad \ell(u(\Omega_h), \Omega_h) + \beta\ |\boldsymbol{n}|_{DTV(\Gamma_h)} \\ &\text{w.r.t. the vertex positions of the discrete shape } \Omega_h \text{ with boundary } \Gamma_h. \end{aligned} \tag{5.2}$$

Here $u(\Omega_h)$ denotes the solution of the problem specific partial differential equation (PDE), which depends on the unknown domain Ω_h. Moreover, ℓ represents a loss function, such as a least squares function. In particular, (5.2) includes geometric inverse problems, where one seeks to recover a *shape* $\Omega_h \subset \mathbb{R}^3$ representing, e.g., the location of a source or inclusion inside a given, larger domain, or the geometry of an inclusion or a scatterer. Numerical experiments in Chapter 6 confirm that $|\boldsymbol{n}|_{DTV(\Gamma_h)}$, as a shape prior, can help to identify polyhedral shapes.

This chapter is based on [23] and has a similar structure. In the following section we provide an analysis of the discrete total variation of the normal (5.1) and its properties. We also compare it to geometric functionals appearing elsewhere in the literature. In particular, we provide a numerical comparison between (5.1) and surface regularization for a *mesh denoising* problem. Section 5.2 is devoted to the formulation of an ADMM

method which generalizes the split Bregman algorithm to the manifold-valued problem (5.2).

5.1 Discrete Total Variation of the Normal

From this section onwards we assume that $\Gamma_h \subset \mathbb{R}^3$ is a piecewise flat, compact, orientable surface without boundary, which consists of a finite number of flat facets with straight sided edges between facets. Consequently, Γ_h can be thought of as a mesh consisting of polyhedral cells with a consistently oriented outer unit normal. We also assume this mesh to be geometrically conforming, i.e., there are no hanging nodes. A frequent situation is that Γ_h is the boundary mesh of a geometrically conforming volume mesh with polyhedral cells, representing a volume domain $\Omega_h \subset \mathbb{R}^3$. In our numerical example in Chapter 6, we will use a volume mesh consisting of tetrahedra, whose surface mesh consists of triangles; see Figure 5.1.

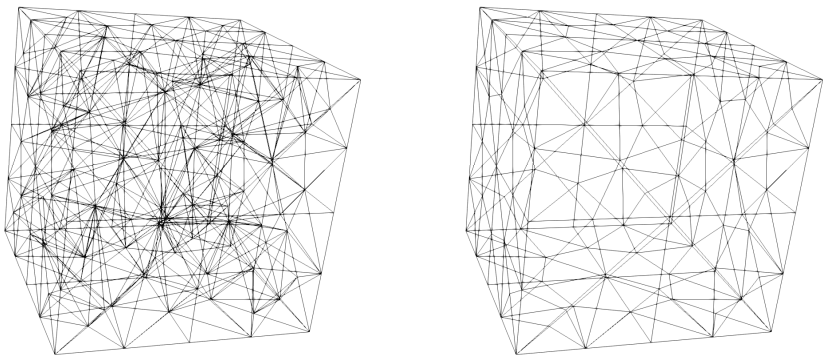

Figure 5.1: Volume mesh of a cube domain Ω_h consisting of tetrahedra (left) and corresponding triangular mesh of the boundary Γ_h (right).

Since the surface Γ_h is non-smooth, the definition (4.2) of the total variation of the normal proposed in Chapter 4 for smooth surfaces does not apply. Since the normal vector field $\boldsymbol{n}$ is piecewise constant here, its variation is concentrated in spontaneous changes across edges between facets, rather than gradual changes expressed by the derivative $D_\Gamma \boldsymbol{n}$. We therefore propose to replace (4.2) by (5.1), where E denotes an edge of Euclidean length $|E|$ between facets. Each edge has an arbitrary but fixed orientation, so that its two neighboring facets can be addressed as F_E^+ and F_E^-. The normal vectors, constant on each facet, are denoted by $\boldsymbol{n}_E^+$ and $\boldsymbol{n}_E^-$. Moreover,

$$\begin{aligned} d(\boldsymbol{n}_E^+, \boldsymbol{n}_E^-) &= \arccos\left((\boldsymbol{n}_E^+)^\top \boldsymbol{n}_E^-\right) \\ &= \sphericalangle\left(\boldsymbol{n}_E^+, \boldsymbol{n}_E^-\right) \end{aligned} \tag{5.3}$$

denotes the geodesic distance on $\mathcal{S}^2$, i.e., the angle between the two unit vectors $\boldsymbol{n}_E^+$ and $\boldsymbol{n}_E^-$; see also Figure 5.2.

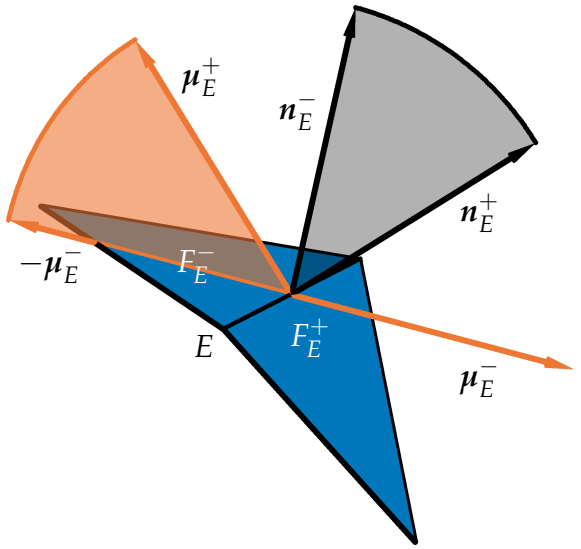

Figure 5.2: The geodesic distance between normals n_E^+ and n_E^- (shown in black) of two Facets F_E^+, F_E^- which share the edge E agrees with the geodesic distance between the co-normals μ_E^+ and $-\mu_E^-$ (shown in orange).

Compared to the common definition of the discrete total variation semi-norm in imaging, which involves the absolute value of the difference of neighboring function values, the arccos in (5.3) appears to be highly non-linear. However, it agrees with the geodesic distance and is thus the natural extension of the absolute value of the difference for $\mathcal{S}^2$-valued data. To illustrate this behavior, let $\alpha \in (-\pi, \pi)$ be the angle between the normal vectors of two neighboring facets F^+ and F^-, such that $\alpha = 0$ refers to the case where the two facets are co-planar, $\alpha < 0$ represents the concave situation and $\alpha > 0$ the convex one. Without loss of generality, the two normal vectors can be parametrized by

$$n^+ = (\sin\alpha, \cos\alpha, 0)^\top \quad \text{and} \quad n^- = (0, 1, 0)^\top,$$

which yields

$$\mu^+ = (-\cos\alpha, \sin\alpha, 0)^\top.$$

Then (5.3) is simplified to

$$\arccos\left(n^+ \cdot n^-\right) = \arccos\left(\cos\alpha\right) = |\alpha|$$

To motivate the definition (5.1), consider a family of smooth approximations Γ_ε of the piecewise flat surface Γ_h. The approximations are supposed to be of class C^2 such that the flat facets are preserved up to a collar of order ε, and smoothing occurs in bands of width 2ε around the edges. Such an approximation can be constructed, for instance, by a level-set representation of Γ_h by means of a signed distance function Φ. Then a family of smooth approximations Γ_ε can be obtained as zero level sets of mollifications

$$\Phi \circledast \varphi_\varepsilon$$

for sufficiently small ε. Here φ_ε is the standard Friedrichs mollifier in 3D and $\circledast$ denotes convolution. A construction of this type is used, for instance, in [33, 86]. An alternative

to this procedure is the so-called Steiner smoothing, where Γ_ε is taken to be the boundary of the Minkowski sum of Ω_h with the ball

$$B_\varepsilon(0) \subset \mathbb{R}^3;$$

see for instance [151, Section 4.4].

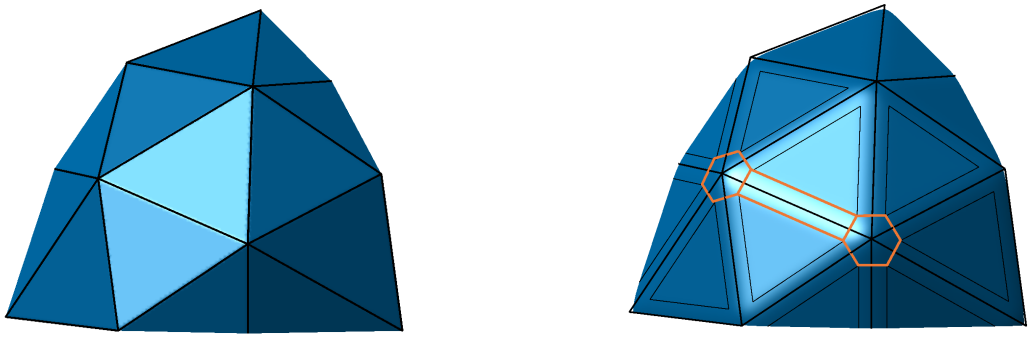

Figure 5.3: Illustration of the approximation of a portion of a triangulated surface Γ_h (left) by a family of smooth surfaces Γ_ε (right). Two vertex caps $B_{V,\varepsilon}$ and one transition region along an edge $I_{E,\varepsilon}$ are highlighted, see the proof of Theorem 5.1.

Theorem 5.1. *Let $\{\Gamma_\varepsilon\}$ denote a family of smooth approximations of Γ_h obtained by mollification, with normal vector fields $\boldsymbol{n}_\varepsilon$. Then*

$$|\boldsymbol{n}_\varepsilon|_{TV(\Gamma_\varepsilon)} \to |\boldsymbol{n}|_{DTV(\Gamma_h)} \quad \text{as } \varepsilon \searrow 0. \tag{5.4}$$

Proof. Let us denote the vertices in Γ_h by V and its edges by E. Since mollification is local, the normal vector is constant in the interior of each facet minus its collar, which is of order ε. Consequently, changes in the normal vector are confined to a neighborhood of the skeleton. We decompose this area into the disjoint union

$$\dot{\bigcup}_E I_{E,\varepsilon} \,\dot{\cup}\, \dot{\bigcup}_V B_{V,\varepsilon}.$$

Here $I_{E,\varepsilon}$ are the transition regions around edge E where the normal vector is modified due to mollification, and $B_{V,\varepsilon}$ are the regions around vertex V. On $I_{E,\varepsilon}$, we can arrange the basis $\boldsymbol{\xi}_{1,2}$ to be aligned and orthogonal to E so that

$$\int_{I_{E,\varepsilon}} \left(|(D_{\Gamma_\varepsilon}\boldsymbol{n}_\varepsilon)\,\boldsymbol{\xi}_1|_{\mathfrak{g}}^2 + |(D_{\Gamma_\varepsilon}\boldsymbol{n}_\varepsilon)\,\boldsymbol{\xi}_2|_{\mathfrak{g}}^2 \right)^{1/2} \mathrm{d}\boldsymbol{s} = \int_{I_{E,\varepsilon}} |(D_{\Gamma_\varepsilon}\boldsymbol{n}_\varepsilon)\,\boldsymbol{\xi}_1|_{\mathfrak{g}}\,\mathrm{d}\boldsymbol{s}$$

holds, which can be easily evaluated as an iterated integral. In each stripe in $I_{E,\varepsilon}$ perpendicular to E, $\boldsymbol{n}_\varepsilon$ changes monotonically along the geodesic path between $\boldsymbol{n}_E^+$ and $\boldsymbol{n}_E^-$, so that the integral along this stripe yields the constant $d(\boldsymbol{n}_E^+, \boldsymbol{n}_E^-)$. Since the length of $I_{E,\varepsilon}$ parallel to E is $|E|$ up to terms of order ε, we obtain

$$\int_{I_{E,\varepsilon}} \left(|(D_{\Gamma_\varepsilon}\boldsymbol{n}_\varepsilon)\,\boldsymbol{\xi}_1|_{\mathfrak{g}}^2 + |(D_{\Gamma_\varepsilon}\boldsymbol{n}_\varepsilon)\,\boldsymbol{\xi}_2|_{\mathfrak{g}}^2 \right)^{1/2} \mathrm{d}\boldsymbol{s} = d(\boldsymbol{n}_E^+, \boldsymbol{n}_E^-)\,(|E| + \mathcal{O}(\varepsilon))\,.$$

The contributions to $|\boldsymbol{n}_\varepsilon|_{TV(\Gamma_\varepsilon)}$ from integration over $B_{V,\varepsilon}$ are of order ε since

$$\left(|(D_{\Gamma_\varepsilon}\boldsymbol{n}_\varepsilon)\,\boldsymbol{\xi}_1|_{\mathfrak{g}}^2+|(D_{\Gamma_\varepsilon}\boldsymbol{n}_\varepsilon)\,\boldsymbol{\xi}_2|_{\mathfrak{g}}^2\right)^{1/2}$$

is of order ε^{-1} and the area of $B_{V,\varepsilon}$ is of order ε^2. This yields the claim. □

5.1.1 Comparison with Prior Work for Discrete Surfaces

The functional (5.1) has been used previously in the literature. We mention that it fits into the framework of total variation of manifold-valued functions defined in [81, 112]. Specifically in the context of discrete surfaces, we mention [150] where the term

$$H_E \coloneqq |E|\;\Theta_E$$

appears as the *total mean curvature* of the edge E. Here Θ_E is the exterior dihedral angle, which agrees with $d(\boldsymbol{n}_E^+,\boldsymbol{n}_E^-)$, see (5.3). Consequently, (5.1) can be written as

$$\sum_E H_E.$$

Moreover, (5.1) appears as a regularizer in [167] within a variational model for *mesh denoising* but the geodesic distances are approximated for the purpose of numerical solution. We also mention the recent [126] where (5.1) appears as a measure of visual smoothness of discrete surfaces. Particular emphasis is given to the impact of the mesh connectivity. In our study, the mesh connectivity will remain fixed and only triangular surface meshes are considered in the numerical experiments.
In addition, we are aware of [170, 173], where

$$\sum_E \left|\boldsymbol{n}_E^+-\boldsymbol{n}_E^-\right|_2|E|\,, \tag{5.5}$$

was proposed in the context of variational *mesh denoising*. Notice that in contrast to (5.1), (5.5) uses the Euclidean as opposed to the geodesic distance between neighboring normals and is therefore an underestimator for (5.1).
Once again, we are not aware of any work in which (5.1) or its continuous counterpart (4.2) were used as a prior in shape optimization or geometric inverse problems involving partial differential equations.

5.1.2 Properties of the Discrete Total Variation of the Normal

In this section we investigate some properties of the discrete total variation of the normal. As can be seen directly from (5.1), a scaling in which Γ_h is replaced by $\delta\Gamma_h$ for some $\delta>0$ yields

$$|\boldsymbol{n}_\delta|_{DTV(\delta\Gamma_h)}=\delta\;|\boldsymbol{n}|_{DTV(\Gamma_h)}\,.$$

This is the same behavior observed, e.g., for the total variation of scalar functions defined on two-dimensional domains. Consequently, when studying optimization problems involving (5.1), we need to take precautions to avoid that Γ_h degenerates to a point. This can be archived either by imposing a constraint, e.g., on the surface area, or by considering tracking problems in which an additional loss term appears.

Simple Minimizers of the Discrete Total Variation of the Normal

In this section, we investigate minimizers of $|\boldsymbol{n}|_{DTV(\Gamma_h)}$ subject to an area constraint. More precisely, we consider the following problem. Given a triangulated surface mesh consisting of vertices V, edges E and facets F, find the mesh with the same connectivity, which

$$\begin{aligned} \text{minimizes} \quad & \sum_E d(\boldsymbol{n}_E^+, \boldsymbol{n}_E^-)\,|E| \\ \text{s.t.} \quad & \sum_F |F| = A_0. \end{aligned} \tag{5.6}$$

To the best of our knowledge, a precise characterization of the minimizers of (5.6) is an open problem and the solution depends on the connectivity; compare the observations in [126, Section 4]. That is, different triangulations of the same (initial) mesh, e.g., a cube, may yield different minimizers. We also refer the reader to [2] for a related observation in discrete mean curvature flow.
We do have, however, the following partial result. For the proof, we exploit that (5.1) coincides with the discrete total mean curvature and use results from discrete differential geometry. The reader may wish to consult [32, 61, 121, 129, 162].

Theorem 5.2. *The icosahedron and the cube with crossed diagonals are stationary for* (5.6) *within the class of triangulated surfaces* Γ_h *of constant area and identical connectivity.*

Proof. Let us consider the Lagrangian associated with (5.6),

$$\mathcal{L}(\boldsymbol{x}_1, \dots, \boldsymbol{x}_{N_V}, \mu) := \sum_E d(\boldsymbol{n}_E^+, \boldsymbol{n}_E^-)\,|E| + \mu \left(\sum_F |F| - A_0 \right). \tag{5.7}$$

Here $\boldsymbol{x}_i \in \mathbb{R}^3$ denote the coordinates of vertex #i and N_V is the total number of vertices of the triangular surface mesh. Notice that the normal vectors $\boldsymbol{n}_E^{\pm}$, edge lengths $|E|$ and facet areas $|F|$ depend on these coordinates. The gradient of (5.7) w.r.t. $\boldsymbol{x}_i$ can be represented as

$$\nabla_{\boldsymbol{x}_i} \mathcal{L}(\boldsymbol{x}_1, \dots, \boldsymbol{x}_{N_V}, \mu) \;=\; \sum_{j \in \mathcal{N}(i)} \left(\frac{d(\boldsymbol{n}_{E_{ij}}^+, \boldsymbol{n}_{E_{ij}}^-)}{|E_{ij}|} + \frac{\mu}{2} \big(\cot \alpha_{ij} + \cot \beta_{ij} \big) \right) (\boldsymbol{x}_i - \boldsymbol{x}_j), \tag{5.8}$$

see for instance [61]. Here $\mathcal{N}(i)$ denotes the index set of vertices adjacent to vertex #i. For any

$$j \in \mathcal{N}(i),$$

E_{ij} denotes the edge between vertices #i and #j. Moreover, α_{ij} and β_{ij} are the angles as illustrated in Figure 5.4.
For the icosahedron with surface area A_0, all edges have length

$$|E_{ij}| = \Big(\frac{A_0}{5\sqrt{3}}\Big)^{1/2}.$$

Moreover, since all facets are equilateral triangles,

$$\alpha_{ij} = \beta_{ij} = \pi/3$$

holds. Finally, the exterior dihedral angles are all equal to

$$d(\boldsymbol{n}_{E_{ij}}^{+}, \boldsymbol{n}_{E_{ij}}^{-}) = \arccos(\sqrt{5}/3) \approx 41.81^{\circ}.$$

Consequently, the Lagrangian is stationary for the Lagrange multiplier

$$\mu = -\sqrt{3}\arccos(\sqrt{5}/3)\left(\frac{5\sqrt{3}}{A_0}\right)^{1/2}.$$

We remark that (5.1) and thus (5.8) is not differentiable when one or more of the angles $d(\boldsymbol{n}_{E_{ij}}^{+}, \boldsymbol{n}_{E_{ij}}^{-})$ are zero. This is the case for the cube with crossed diagonals, see Figure 5.4. However, the right hand side in (5.8) still provides a generalized derivative of $\mathcal{L}$ in the sense of Clarke.
In contrast to the icosahedron, the cube has two types of vertices. When $\boldsymbol{x}_i$ is the center vertex of one of the lateral surfaces, then

$$d(\boldsymbol{n}_{E_{ij}}^{+}, \boldsymbol{n}_{E_{ij}}^{-}) = 0$$

and

$$\alpha_{ij} = \beta_{ij} = \pi/4$$

for all $j \in \mathcal{N}(i)$. Moreover, since

$$\sum_{j \in \mathcal{N}(i)} (\boldsymbol{x}_i - \boldsymbol{x}_j) = \boldsymbol{0}$$

holds, $\boldsymbol{0}$ is an element of the generalized (partial) differential of $\mathcal{L}$ at

$$(\boldsymbol{x}_1, \ldots, \boldsymbol{x}_{N_V}, \mu)$$

w.r.t. $\boldsymbol{x}_i$, independently of the value of the Lagrange multiplier μ. Now when $\boldsymbol{x}_i$ is a vertex of "corner type", we need to distinguish two types of edges. Along the three edges leading to neighbors of the same type, we have an exterior dihedral angle of

$$d(\boldsymbol{n}_{E_{ij}}^{+}, \boldsymbol{n}_{E_{ij}}^{-}) = \pi/2,$$

length

$$\left|E_{ij}\right| = (A_0/6)^{1/2}$$

and

$$\alpha_{ij} = \beta_{ij} = \pi/2.$$

Along the three remaining edges leading to surface centers, we have

$$d(\boldsymbol{n}_{E_{ij}}^{+}, \boldsymbol{n}_{E_{ij}}^{-}) = 0$$

and

$$\alpha_{ij} = \beta_{ij} = \pi/4.$$

Thus for vertices of "corner type", it is straightforward to verify that $\boldsymbol{0}$ belongs to the generalized (partial) differential of $\mathcal{L}$ at

$$(\boldsymbol{x}_1, \ldots, \boldsymbol{x}_{N_V}, \mu)$$

	unit cube	tetrahedron	icosahedron
edge length $\lvert E\rvert$	1	≈ 1.8612	≈ 0.8324
number of edges	12	6	30
exterior dihedral angle	$\pi/2$	≈ 1.9106	≈ 0.7297
$\lvert \boldsymbol{n}\rvert_{DTV(\Gamma_h)}$	$6\pi \approx 18.8496$	≈ 21.3365	≈ 18.2218

Table 5.1: Values of the discrete total variation of the normal functional (5.1) for the cube with edge length 1, as well as the regular tetrahedron and the icosahedron with the same surface area as the cube.

w.r.t. $\boldsymbol{x}_i$ if

$$\left(\frac{\pi\sqrt{2}/2}{(A_0/6)^{1/2}} + 2\mu\right)\begin{pmatrix}1\\1\\1\end{pmatrix} = \mathbf{0}$$

holds, which is true for the obvious choice of μ. □

Numerical experiments indicate that the icosahedron as well as the cube are not only stationary points, but also local minimizers of (5.6). We can thus conclude that the discrete objective (5.1) exhibits different minimizers than its continuous counterpart (4.2) for smooth surfaces. In particular, (5.1) admits and promotes piecewise flat minimizers such as the cube. This is in accordance with observations made in [126, Section 3.2] that optimal meshes typically exhibit a number of zero dihedral angles. This property sets our functional apart from other functionals previously used as priors in shape optimization and geometric inverse problems. For instance, the popular surface area prior is well known to produce smooth shapes; see the numerical experiments in Section 5.1.2 below.

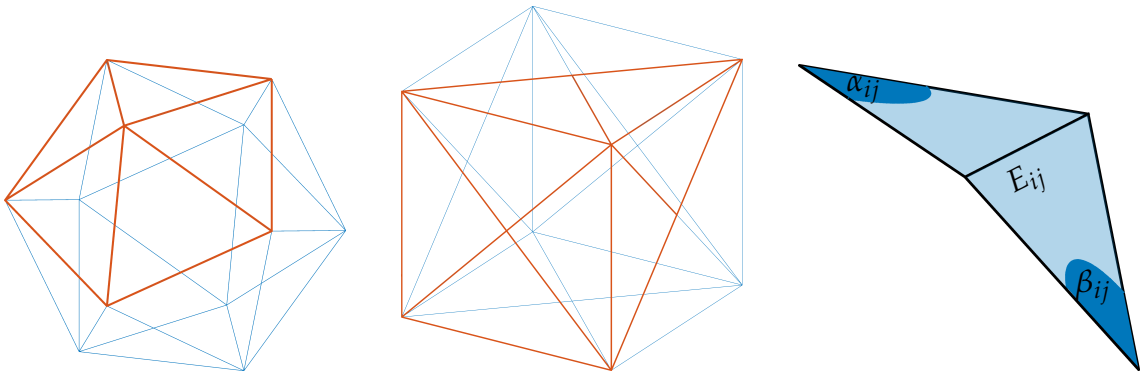

Figure 5.4: The icosahedron and the cube with crossed diagonals, two stationary surfaces for (5.6). The highlighted regions as well as the figure on the right illustrate the proof of Theorem 5.2.

Comparison of Discrete and Continuous Total Variation of the Normal

In this section we compare the values of (4.2) and (5.1) for a sphere Γ, and a sequence of discretized spheres Γ_h. For comparison, we choose Γ to have the same surface area as the

cube in the previous section, i.e., we use $r = \sqrt{3/(2\pi)}$ as the radius. It is easy to see that since the principal curvatures of a sphere Γ of radius r are

$$k_1 = k_2 = 1/r,$$

(4.2) becomes

$$\begin{aligned} |\boldsymbol{n}|_{TV(\Gamma)} &= \int_\Gamma \left(k_1^2 + k_2^2\right)^{1/2} \, \mathrm{d}\boldsymbol{s} \\ &= 4\,\pi\, r^2 \frac{\sqrt{2}}{r} \\ &= 4\,\sqrt{2}\,\pi\, r \\ &= 4\sqrt{3\pi} \\ &\approx 12.2799. \end{aligned}$$

To compare this to the discrete total variation of the normal, we created a sequence of triangular meshes Γ_h of this sphere with various resolutions using GMSH and evaluated (5.1) numerically. The results are shown in Table 5.2. They reveal a factor of approximately $\sqrt{2}$ between the discrete and continuous functionals for the sphere. To explain this discrepancy, recall that the principal curvatures of the sphere are

$$k_1 = k_2 = 1/r.$$

This implies that the derivative map $D_\Gamma \boldsymbol{n}$ has rank two everywhere. Discretized surfaces behave fundamentally different in the following respect. Their curvature is concentrated on the edges, and one of the principal curvatures (the one in the direction along the edge) is always zero. So even for successively refined meshes, e.g., of the sphere, one is still measuring only one principal curvature at a time. We are thus led to the conjecture that the limit of (5.1) for successively refined meshes is the "anisotropic", yet still intrinsic measure

$$\int_\Gamma |k_1| + |k_2| \, \mathrm{d}\boldsymbol{s},$$

whose value for the sphere in Table 5.1 is

$$4\sqrt{6\pi} \approx 17.3664$$

The factor $\sqrt{2}$ can thus be attributed to the ratio between the ℓ_1- and ℓ_2-norms of the vector $(1,1)^\top$. This observation is in accordance with the findings in [126, Section 1.2]. One could consider an "isotropic" version of (5.1) in which the dihedral angles across all edges meeting at any given vertex are measured jointly. These alternatives will be considered elsewhere.

Discrete Total Variation Compared to Surface Area Regularization

In this section we consider a specific instance of the general problem (5.2) and compare our discrete TV functional with the surface area regularizer. We begin with a triangular surface mesh Γ_h of a box

$$\Omega = (-1,1) \times (-1.5,1.5) \times (-2,2)$$

N_V	N_E	N_T	$\|\boldsymbol{n}\|_{DTV(\Gamma_h)}$	$\|\boldsymbol{n}\|_{DTV(\Gamma_h)} \,/\, \|\boldsymbol{n}\|_{TV(\Gamma_h)}$
54	156	104	17.01045	1.38522
270	804	536	17.47614	1.42315
871	2,607	1,738	17.34861	1.41276
1,812	5,430	3,620	17.35852	1.41357
3,314	9,936	6,624	17.36350	1.41398
9,530	28,584	19,056	17.36855	1.41439
82,665	247,989	165,326	17.37524	1.41493
101,935	305,799	203,866	17.37341	1.41478
335,216	1,005,642	670,428	17.37389	1.41482
958,022	2,874,060	1,916,040	17.37410	1.41484

Table 5.2: Various triangulations Γ_h of a sphere Γ with radius $r = \sqrt{3/(2\pi)}$, their values of (5.1) and the ratio between (5.1) and (4.2). The value of the latter is $|\boldsymbol{n}|_{TV(\Gamma)} = 4\sqrt{3\pi} \approx 12.2799$. N_V, N_E and N_T denote the number of vertices, edges, and triangles of the respective mesh.

and add normally distributed noise to the coordinate vector of each vertex in average normal direction of the adjacent triangles with zero mean and standard deviation

$$\sigma = 0.2$$

times the average edge length. We denote the noisy vertex positions as $\widetilde{\boldsymbol{x}}_V$ and use a simple least-squares functional as our loss function and consider the following *mesh denoising* problem,

$$\begin{aligned} &\text{Minimize} \quad \frac{1}{2}\sum_V |\boldsymbol{x}_V - \widetilde{\boldsymbol{x}}_V|_2^2 + \beta \, |\boldsymbol{n}|_{DTV(\Gamma_h)} \\ &\text{w.r.t. the vertex positions } \boldsymbol{x}_V \text{ of the discrete surface } \Gamma_h. \end{aligned} \tag{5.9}$$

Here the sum runs over the vertices of Γ_h. For comparison, we also consider a variant

$$\begin{aligned} &\text{Minimize} \quad \frac{1}{2}\sum_V |\boldsymbol{x}_V - \widetilde{\boldsymbol{x}}_V|_2^2 + \gamma \sum_F |F| \\ &\text{w.r.t. the vertex positions } \boldsymbol{x}_V \text{ of the discrete surface } \Gamma_h, \end{aligned} \tag{5.10}$$

where we use the total surface area as prior.
A numerical approach to solve the non-smooth problem (5.9) will be discussed in Section 5.2. By contrast, problem (5.10) is a fairly standard smooth discrete shape optimization problem and we solve it using a simple shape gradient descent scheme. The details how to obtain the shape derivative and shape gradient are the same as described in Section 6.1.2 for problem (5.9).
Figure 5.5 shows the numerical solutions of (5.9) and (5.10) for various choices of the regularization parameters β and γ, respectively. The initial guess for both problems is a sphere with the same connectivity as Γ_h. We can clearly see that our functional (5.1)

achieves a very good reconstruction of the original shape for a proper choice of β. By contrast, the surface area regularization requires a relatively large choice of γ in order to reasonably reduce the noise, which in turn leads to a significant shrinkage of the surface and a rounding of the sharp features.

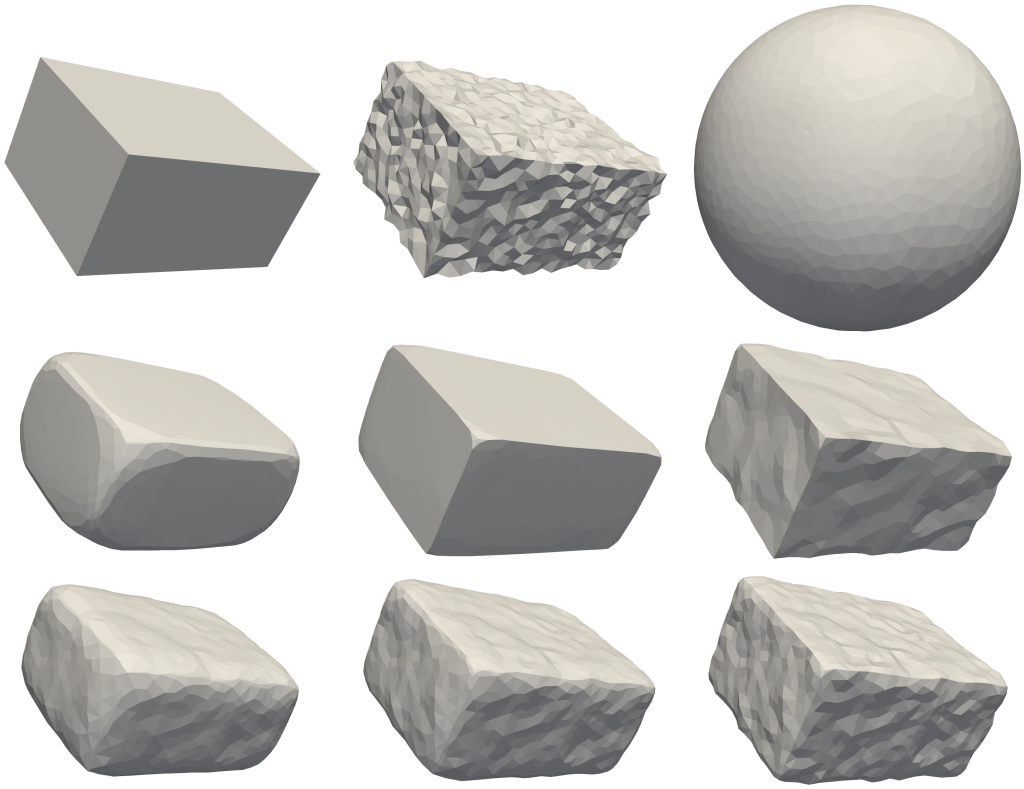

Figure 5.5: Top row: original box and desired outcome of the noise reduction, noisy box with vertex coordinates $\widetilde{x}_V$ used for the data fidelity term, and sphere with same connectivity used as the initial guess; middle row: results for total variation of the normal (5.9) with $\beta = 10^{-2},\ 10^{-3}, 10^{-4}$; bottom row: results for surface area regularization (5.10) with $\gamma = 0.02,\ 0.01,\ 0.005$.

5.2 Discrete Split Bregman Iteration

In this section, we develop an optimization scheme to solve the non-smooth problem (5.1). To this end, we adapt the well-known split Bregman method to our setting. This leads to a discrete realization of the approach presented in Section 4.3, which will be slightly simplified to make the parallel transport unnecessary. Recall that combining (5.1) with (5.2) results in the problem

$$\begin{aligned} &\text{Minimize} \quad \ell(u(\Omega_h), \Omega_h) + \beta \sum_E d(\boldsymbol{n}_E^+, \boldsymbol{n}_E^-)\,|E| \\ &\text{w.r.t. the vertex positions of } \Omega_h, \end{aligned} \tag{5.11}$$

where E are the edges of the unknown part Γ_h of the boundary $\partial\Omega_h$. We will consider a concrete example in Section 6.1.

Notice that the second term in the objective in (5.11) is non-differentiable whenever

$$\boldsymbol{n}_E^+ = \boldsymbol{n}_E^-$$

occurs on at least one edge. Following the classical split Bregman approach, we introduce a splitting in which the variation of the normal vector becomes an independent variable. Since this variation is confined to edges, where the normal vector jumps (without loss of generality) from $\boldsymbol{n}_E^+$ to $\boldsymbol{n}_E^-$, this new variable becomes

$$\boldsymbol{d}_E = \log_{\boldsymbol{n}_E^+} \boldsymbol{n}_E^- \in \mathcal{T}_{\boldsymbol{n}_E^+}\mathcal{S}^2. \tag{5.12}$$

Here $\log_{\boldsymbol{n}_E^+} \boldsymbol{n}_E^-$ denotes again the logarithmic map as in (4.39). Moreover,

$$|\log_{\boldsymbol{n}_E^+} \boldsymbol{n}_E^-|_{\mathfrak{g}} = d(\boldsymbol{n}_E^+, \boldsymbol{n}_E^-)$$

holds. Together with the set of Lagrange multipliers

$$\boldsymbol{b}_E \in \mathcal{T}_{\boldsymbol{n}_E^+}\mathcal{S}^2,$$

we define the Augmented Lagrangian pertaining to (5.2) and (5.12) as

$$\begin{aligned}\mathcal{L}(\Omega_h, \boldsymbol{d}, \boldsymbol{b}) := \ell(u(\Omega_h), \Omega_h) + \beta \sum_E |\boldsymbol{d}_E|_{\mathfrak{g}} \, |E| \\ + \frac{\lambda}{2} \sum_E |E| \left| \boldsymbol{d}_E - \log_{\boldsymbol{n}_E^+} \boldsymbol{n}_E^- - \boldsymbol{b}_E \right|_{\mathfrak{g}}^2.\end{aligned} \tag{5.13}$$

Here $\lambda > 0$ is the augmentation parameter. The vectors $\boldsymbol{d}$ and $\boldsymbol{b}$ are simply the collections of their entries

$$\boldsymbol{d}_E, \boldsymbol{b}_E \in \mathcal{T}_{\boldsymbol{n}_E^+}\mathcal{S}^2,$$

three components per edge E. Hence, since the tangent space $\mathcal{T}_{\boldsymbol{n}_E^+}\mathcal{S}^2$ changes between shape updates, the respective quantities have to be parallely transported, see (4.38), which is a major difference to ADMM methods in Euclidean or Hilbert spaces.

We state the split Bregman iteration in Algorithm 7 and address now its individual steps in more detail, i.e., the successive minimization with respect to the unknown vertices of Ω_h and $\boldsymbol{d}$, followed by an explicit update for the multiplier $\boldsymbol{b}$.

Step 4 is the minimization of (5.13) with respect to the unknown vertex positions of Ω_h. To this end, we employ a gradient descent scheme, where we compute the sensitivities with respect to those node positions discretely, see Section 6.1.2 for more details. Following [85], an approximate minimization suffices, and thus only a certain number of steepest descent steps are performed.
After $\Omega_h^{(k)}$ has been updated to $\Omega_h^{(k+1)}$, the quantity $\boldsymbol{b}_E^{(k)} \in \mathcal{T}_{\boldsymbol{n}_E^{+,(k)}}\mathcal{S}^2$ has to be parallely transported into the new tangent space $\mathcal{T}_{\boldsymbol{n}_E^{+,(k+1)}}\mathcal{S}^2$, see step 5.
Step 6 is the optimization of (5.13) with respect to $\boldsymbol{d}$, which is a non-smooth problem. It can be solved explicitly by one vectorial shrinkage operation per edge E. Given the data

Algorithm 7 Split Bregman method for (5.2)

Require: Initial domain $\Omega_h^{(0)}$
Ensure: Approximate solution of (5.2)
1: Set $\boldsymbol{b}^{(0)} := \mathbf{0}$, $\boldsymbol{d}^{(0)} := \mathbf{0}$
2: Set $k := 0$
3: **while** not converged **do**
4: Perform several gradient steps for $\Omega_h \mapsto \mathcal{L}(\Omega_h, \boldsymbol{d}^{(k)}, \boldsymbol{b}^{(k)})$ at $\Omega_h^{(k)}$ to obtain $\Omega_h^{(k+1)}$
5: Parallely transport the multiplier estimate $\boldsymbol{b}_E^{(k)}$ on each edge E from $\mathcal{T}_{\boldsymbol{n}_E^{+,(k)}}\mathcal{S}^2$ to $\mathcal{T}_{\boldsymbol{n}_E^{+,(k+1)}}\mathcal{S}^2$ along the geodesic from $\boldsymbol{n}_E^{+,(k)}$ to $\boldsymbol{n}_E^{+,(k+1)}$, see (4.38)
6: Set $\boldsymbol{d}^{(k+1)} := \arg\min \mathcal{L}(\Omega_h^{(k+1)}, \boldsymbol{d}^{(k)}, \boldsymbol{b}^{(k)})$, see (5.14)
7: Update the Lagrange multipliers, i.e., set $\boldsymbol{b}_E^{(k+1)} := \boldsymbol{b}_E^{(k)} + \log_{\boldsymbol{n}_E^{+,(k+1)}} \boldsymbol{n}_E^{-,(k+1)} - \boldsymbol{d}_E^{(k+1)}$ for all edges E
8: Set $k := k + 1$
9: **end while**

$\Omega_h^{(k+1)}$ and associated normal field $\boldsymbol{n}^{(k+1)}$, as well as multiplier $\boldsymbol{b}_E^{(k)}$ parallely transported into $\mathcal{T}_{\boldsymbol{n}_E^{+,(k+1)}}\mathcal{S}^2$, the minimizer of (5.13) is given by

$$\boldsymbol{d}_E^{(k+1)} := \max\left\{ \left|\boldsymbol{w}_E + \boldsymbol{b}_E^{(k)}\right|_{\mathfrak{g}} - \frac{\beta}{\lambda},\ 0 \right\} \frac{\boldsymbol{w}_E + \boldsymbol{b}_E^{(k)}}{\left|\boldsymbol{w}_E + \boldsymbol{b}_E^{(k)}\right|_{\mathfrak{g}}} \tag{5.14}$$

for each edge E with

$$\boldsymbol{w}_E = \log_{\boldsymbol{n}_E^{+,(k+1)}} \boldsymbol{n}_E^{-,(k+1)}.$$

Notice that (5.14) is independent of the previous value $\boldsymbol{d}_E^{(k)}$ and thus a parallel transport of $\boldsymbol{d}_E^{(k)}$ into the updated tangent space is not necessary.
Step 7 is the multiplier update for $\boldsymbol{b}$, which is done explicitly via

$$\boldsymbol{b}_E^{(k+1)} = \boldsymbol{b}_E^{(k)} + \log_{\boldsymbol{n}_E^{+,(k+1)}} \boldsymbol{n}_E^{-,(k+1)} - \boldsymbol{d}_E^{(k+1)}$$

for each edge E.

CHAPTER 6

APPLICATIONS USING THE DISCRETE TOTAL VARIATION OF THE NORMAL

In this Chapter we present some numerical results for three different type of problems applied to Algorithm 7. First, we introduce an Electrical impedance tomography (EIT) problem, which is in a prototypical class of inverse problems and we show the results for our new shape prior (5.1) compared to the well known surface area regularization. Second, we focus on *mesh denoising*, which is the process of removing noise while preserving relevant features like edges and corners. The main difficulty in removing undesired noise from a mesh is that both noise and sharp geometric features can be considered high frequency signals. This makes it difficult to distinguish between them. Finally, we apply Algorithm 7 on two *mesh inpainting* problems, where vertex positions of some mesh areas are corrupted and therefore unknown. The *mesh inpainting* problem deals with the reconstruction of these vertex positions.

6.1 An EIT Model Problem and its Implementation in FENICS

In the following, we address some details concerning the implementation of Algorithm 7 in the finite element framework FENICS (version 2018.2.dev0), [4, 114]. For concreteness, we elaborate on a particular reduced loss function $\ell(u(\Omega_h), \Omega_h)$ where the state $u(\Omega_h)$ arises from a PDE modeling a geological electrical impedance tomography (EIT) problem with Robin-type far field boundary conditions. We introduce the problem under consideration first and discuss implementation details and derivative computations later on, completed by some numerical results.

6.1.1 EIT Model Problem

Electrical impedance tomography problems are a prototypical class of inverse problems. Common to these problems is the task of reconstructing the internal conductivity inside a volume from boundary measurements of electric potentials or currents. These problems are both nonlinear and severely ill-posed and require appropriate regularization; see for instance [55, 56, 140].

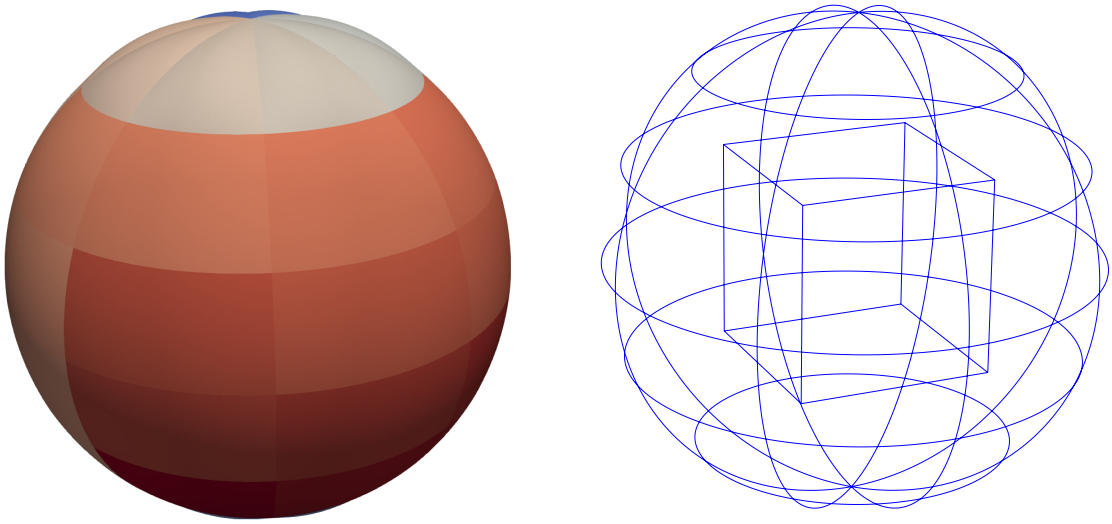

Figure 6.1: The left plot shows the domain Ω_h considered in the numerical example. Each colour on the outer boundary represents the support of one out of $r = 48$ electric sources f_i. The right figure shows a wireframe plot revealing the true inclusion Γ_1, i.e., the boundary of the cube.

Traditionally, EIT problems are modeled with Neumann (current) boundary conditions and the internal conductivity is an unknown function across the entire domain. In order to focus on the demonstration of the utility of (5.1) as a regularizer in geometric inverse problems, we consider a simplified situation in which we seek to reconstruct a perfect conductor inside a domain of otherwise homogeneous electrical properties.
Consequently, the unknowns are the vertex positions of the interface of the inclusion. As a perfect conductor shields its interior from the electric field, there is no necessity to mesh and simulate the interior of the inclusion. However, we mention that our methodology can be extended also to interface problems, non-perfect conductors and other geometric inverse problems.
The perfect conductor is modeled via a homogeneous Neumann condition on the unknown interior boundary Γ_1 of the domain Ω_h. To overcome the non-uniqueness of the electric potential, we employ Robin boundary conditions on the exterior boundary Γ_2. The use of homogeneous Robin boundary conditions to model the far field is well-established for geological EIT problems; see, e.g., [95]. We use them here also for current injection.
The geometry of our model is shown in Figure 6.1, where Γ_1 is the unknown boundary of the perfect conductor and Γ_2 is a fixed boundary where currents are injected and measurements are taken. We assume that

$$i = 1, \dots, r \in \mathbb{N}$$

experiments are conducted, each resulting in a measured electric potential $z_i \in \mathcal{CG}_1(\Gamma_2)$, the finite element space consisting of piecewise linear, globally continuous functions on the outer boundary Γ_2. Experiment $\#i$ is conducted by applying the right hand side source $f_i \in \mathcal{DG}_0(\Gamma_2)$, which is the characteristic function of one of the colored regions shown in Figure 6.1. Here, $\mathcal{DG}_0$ denotes the space of piecewise constant functions. We then

seek to reconstruct the interface of the inclusion Γ_1 by solving the following regularized least-squares problem of type (5.2),

$$\begin{aligned} \text{Minimize} \quad & \frac{1}{2}\sum_{i=1}^{r}\int_{\Gamma_2} |u_i - z_i|^2 \, \mathrm{d}\boldsymbol{s} + \beta \, |\boldsymbol{n}|_{DTV(\Gamma_1)} \\ \text{s.t.} \quad & \begin{cases} -\Delta u_i = 0 & \text{in } \Omega_h, \\ \dfrac{\partial u_i}{\partial \boldsymbol{n}} = 0 & \text{on } \Gamma_1, \\ \dfrac{\partial u_i}{\partial \boldsymbol{n}} + \alpha \, u_i = f_i & \text{on } \Gamma_2 \end{cases} \end{aligned} \tag{6.1}$$

with respect to the vertex positions of Γ_1. Here $u_i \in \mathcal{CG}_1(\Omega_h)$ is the computed electric field for source f_i. Hence, the problem features r PDE constraints with identical operator but different right hand sides.
As detailed in Section 6.1.2, we compute the shape derivative of the least-squares objective and the PDE constraint separately from the shape derivative of the regularization term. To evaluate the former, we employ a classical adjoint approach. To this end, we consider the Lagrangian

$$\begin{aligned} &F(u_1, \dots, u_r, p_1, \dots, p_r, \Omega_h) := \\ &\qquad \sum_{i=1}^{r} \left[\int_{\Gamma_2} \frac{1}{2} |u_i - z_i|^2 \, \mathrm{d}\boldsymbol{s} + \int_{\Omega_h} \nabla p_i \cdot \nabla u_i \, \mathrm{d}\boldsymbol{x} + \int_{\Gamma_2} p_i(\alpha \, u_i - f_i) \, \mathrm{d}\boldsymbol{s} \right] \end{aligned} \tag{6.2}$$

for $p_i \in \mathcal{CG}_1(\Omega_h)$. The differentiation w.r.t. u_i leads to the following adjoint problem for p_i:

$$\begin{cases} -\Delta p_i = 0 & \text{in } \Omega_h, \\ \dfrac{\partial p_i}{\partial \boldsymbol{n}} = 0 & \text{on } \Gamma_1, \\ \dfrac{\partial p_i}{\partial \boldsymbol{n}} + \alpha \, p_i = -(u_i - z_i) & \text{on } \Gamma_2. \end{cases} \tag{6.3}$$

The above adjoint PDE was implemented by hand. Since all forward and adjoint problems are governed by the same differential operator, we assemble the associated stiffness matrix once and solve the state and adjoint equations via an ILU-preconditioned conjugate gradient method.
Provided that u_i and p_i solve the respective state and adjoint equations, the directional derivative of $\ell(u(\Omega_h), \Omega_h)$ coincides with the partial directional derivative of

$$F(u_1, \dots, u_r, p_1, \dots, p_r, \Omega_h),$$

both with respect to the vertex positions. In practice, we evaluate the latter using the coordinate derivative functionality of FEniCS as described in the following subsection.

6.1.2 Discrete Shape Derivative

We now focus on computing the sensitivity of finite element functionals, when mesh vertices $\boldsymbol{x}$ of Ω_h are moved in accordance to

$$\boldsymbol{x}_\varepsilon = \boldsymbol{x} + \varepsilon \boldsymbol{V}_{\Omega_h}$$

with

$$\boldsymbol{V}_{\Omega_h} \in \mathcal{CG}_1^3(\Omega_h).$$

As discussed in [91], a convenient way to compute this within the finite element world is by tapping into the transformation of the reference element to the physical one. Hence, we use the symbol

$$\mathrm{d}\ell(u(\Omega_h), \Omega_h)[\boldsymbol{V}_{\Omega_h}]$$

for this object and we obtain it using the coordinate derivative functionality, first introduced in FEniCS release 2018.2.dev0.
Our split Bregman scheme requires the shape derivative of (5.13), which is given by

$$\mathrm{d}\mathcal{L}(\Omega_h, \boldsymbol{d}, \boldsymbol{b})[P_{\Omega_h}(\boldsymbol{V}_{\Gamma_1})] = \mathrm{d}\ell(u(\Omega_h), \Omega_h)[P_{\Omega_h}(\boldsymbol{V}_{\Gamma_1})] + \mathrm{d}m(\Gamma_1)[\boldsymbol{V}_{\Gamma_1}], \tag{6.4}$$

where

$$m(\Gamma_1) \coloneqq \beta \sum_E |\boldsymbol{d}_E|_{\mathfrak{g}} \, |E| + \frac{\lambda}{2} \sum_E |E| \, \left| \boldsymbol{d}_E - \log_{\boldsymbol{n}_E^+} \boldsymbol{n}_E^- - \boldsymbol{b}_E \right|_{\mathfrak{g}}^2 \tag{6.5}$$

originates from the splitting approach (5.13). Because our design variable is Γ_1 only, we introduce the extension

$$P_{\Omega_h}(\boldsymbol{V}_{\Gamma_1})$$

of $\boldsymbol{V}_{\Gamma_1} \in \mathcal{CG}_1^3(\Gamma_1)$ to the volume Ω_h by padding with zeros. Furthermore, a reduction to boundary only sensitivities can also be motivated from considering shape derivatives in the continuous setting, see [22, Section 3].
The term

$$\mathrm{d}\ell(u(\Omega_h), \Omega_h)[P_{\Omega_h}(\boldsymbol{V}_{\Gamma_1})]$$

is computed via the adjoint approach as explained above,

$$\mathrm{d}\ell(u(\Omega_h), \Omega_h)[P_{\Omega_h}(\boldsymbol{V}_{\Gamma_1})] = \partial_{\Omega_h} F(u_1, \ldots, u_r, p_1, \ldots, p_r, \Omega_h)[P_{\Omega_h}(\boldsymbol{V}_{\Gamma_1})].$$

In order to employ this AD functionality, (6.5) needs to be given as a form in Unified Form Language (UFL), a domain specific language based on Python, which forms the native language of the FEniCS framework, see [5]. Such a UFL representation is easy to achieve if all mathematical expressions are finite element functions. Notice that $\boldsymbol{d}$ and $\boldsymbol{b}$ in (6.5) are constant functions on the edges of the boundary mesh representing Γ_1. We can thus represent them in the so called *HDivTrace* space of lowest order in FEniCS.
From the directional derivatives (6.4), we pass to a shape gradient on the surface w.r.t. a scaled $H^1(\Gamma_1)$ scalar product by solving a variational problem. This problem involves the weak form of a Laplace–Beltrami operator with potential term and it finds

$$\boldsymbol{W}_{\Gamma_1} \in \mathcal{CG}_1(\Gamma_1)^3$$

such that

$$\begin{aligned} \int_{\Gamma_1} 10^{-4} (\nabla \boldsymbol{W}_{\Gamma_1}, \nabla \boldsymbol{V}_{\Gamma_1})_2 + (\boldsymbol{W}_{\Gamma_1}, \boldsymbol{V}_{\Gamma_1})_2 \, \mathrm{d}\boldsymbol{s} \\ = \mathrm{d}\ell(u(\Omega_h), \Omega_h)[P_{\Omega_h}(\boldsymbol{V}_{\Gamma_1})] + \mathrm{d}m(\Gamma_1)[\boldsymbol{V}_{\Gamma_1}] \end{aligned} \tag{6.6}$$

holds for all test functions $\boldsymbol{V}_{\Gamma_1} \in \mathcal{CG}_1(\Gamma_1)^3$.

The previous procedure provides us with a shape gradient $\boldsymbol{W}_{\Gamma_1}$ on the surface Γ_1 alone. In order to propagate this information into the volume Ω_h, we solve the following mesh deformation equation: find

$$\boldsymbol{W}_{\Omega_h} \in \mathcal{CG}_1(\Omega_h)^3$$

such that

$$\int_{\Omega_h} (\nabla \boldsymbol{W}_{\Omega_h}, \nabla \boldsymbol{V}_{\Omega_h})_2 + (\boldsymbol{W}_{\Omega_h}, \boldsymbol{V}_{\Omega_h})_2 \, \mathrm{d}\boldsymbol{s} = 0 \tag{6.7}$$

for all test functions

$$\boldsymbol{V}_{\Omega_h} \in \mathcal{CG}_1(\Omega_h)^3$$

with zero Dirichlet boundary conditions, where $\boldsymbol{W}_{\Omega_h}$ is subject to the Dirichlet boundary condition

$$\boldsymbol{W}_{\Omega_h} = \boldsymbol{W}_{\Gamma_1}$$

on Γ_1 and

$$\boldsymbol{W}_{\Omega_h} = \boldsymbol{0}$$

on Γ_2. Subsequently, the vertices of the mesh are moved in the direction of $\boldsymbol{W}_{\Omega_h}$.

6.1.3 Intrinsic Formulation Using Co-Normal Vectors

We recall that our functional of interest (5.1) is formulated in terms of the unit outer normal $\boldsymbol{n}$ of the oriented surface Γ_1. This leads to the term (6.5) inside the augmented Lagrangian (5.13). In order to exploit the differentiation capability of FEniCS w.r.t. vertex coordinates, we need to represent (6.5) in terms of an integral. Since the edges are the interior facets of the surface mesh for Γ_1, and $\boldsymbol{d}$ and $\boldsymbol{b}$ can be represented as constant on edges as explained above, (6.5) can indeed be written as a UFL integral w.r.t. the so-called interior facet measure `dS` on Γ_1. Then, however, the outer normal vectors appearing in the term $\log_{\boldsymbol{n}_E^+} \boldsymbol{n}_E^-$ are not available. We remedy the situation by observing that the geodesic distance between two normal vectors $\boldsymbol{n}_E^+$ and $\boldsymbol{n}_E^-$ on the two triangles T_1 and T_2 sharing the edge E can also be expressed via the co-normal (or in-plane normal) vectors $\boldsymbol{\mu}_E^+, \boldsymbol{\mu}_E^-$, as is shown in Figure 5.2. Indeed, one has

$$\left|\log_{\boldsymbol{n}_E^+} \boldsymbol{n}_E^-\right|_{\mathfrak{g}} = \left|\log_{\boldsymbol{\mu}_E^+}(-\boldsymbol{\mu}_E^-)\right|_{\mathfrak{g}}.$$

Since the co-normal vectors are intrinsic to the surface Γ_1, they are available on Γ_1 while $\boldsymbol{n}_E^+$ and $\boldsymbol{n}_E^-$ are not.

6.1.4 Numerical Results

In this section we present numerical results obtained with Algorithm 7 for the geological impedance tomography model problem described before. The data of the problem are given in Table 6.1 and the initial guess of the inclusion Γ_1, as well as the true inclusion, are shown in Figure 6.2. The state u and adjoint state p were discretized using piecewise linear, globally continuous finite elements on a tetrahedral grid of Ω_h minus the volume enclosed by Γ_1. The mesh has 4429 vertices and 19 384 tetrahedra. Regarding the shape optimization problem of Algorithm 7, we perform 10 gradient steps per split Bregman

domain Ω_h	unit sphere $B_1(0) \setminus [-0.4, 0.4]^3 \subset \mathbb{R}^3$
measurement boundary Γ_2	boundary of Ω_h
boundary of true inclusion Γ_1	boundary of $[-0.4, 0.4]^3$
initial guess for Γ_1	boundary of $B_{0.5}(0) \subset \mathbb{R}^3$
number of measurements	$r = 48$
Robin coefficient in (6.1)	$\alpha = 10^{-5}$
split Bregman parameter	$\lambda = 10^{-5}$
standard deviation of noise	$\sigma = 0$ or $\sigma = 0.34 \cdot 10^{-2}$
regularization parameter ...	
for total variation regularization	$\beta = 10^{-6}$
for surface area regularization	$\gamma = 5 \cdot 10^{-5}, 2 \cdot 10^{-5}$
shape step size	10^2

Table 6.1: Setting of the numerical experiments for (6.1).

iteration combined with an Armijo linesearch with starting step size of 10^2. Also, we stop the whole algorithm, i.e., the outer Bregman iteration, when the initial gradient of the above mentioned shape optimization problem has a norm below 10^{-7} in the sense of (6.6).

In Figure 6.3, we show the results obtained in the noise-free setting (top row) and with noise (bottom row). In the latter case, normally distributed random noise is added with zero mean and standard deviation $\sigma = 0.34 \cdot 10^{-2}$ per degree of freedom of z_i on Γ_2 for each of the $r = 48$ simulations of the forward model (6.1). The amount of noise is considerable when put in relation to the average range of values for the simulated states, which is

$$\frac{\sum_{i=1}^{r} \left(\max_{\boldsymbol{s} \in \Gamma_2} z_i(\boldsymbol{s}) - \min_{\boldsymbol{s} \in \Gamma_2} z_i(\boldsymbol{s}) \right)}{r} \approx 0.34, \quad i = 1, \ldots, r.$$

Due to mesh corruption, we have to remesh Ω_h at some point in the cases with noise. Afterwards, we start again Algorithm 7 with the remeshed Ω_h as new initial guess.

For comparison, we also provide results obtained for a related problem in Figure 6.3, using the popular surface area regularization with the same data otherwise. For the surface area regularization, $\beta \ |\boldsymbol{n}|_{TV(\Gamma_1)}$ is replaced by

$$\gamma \int_{\Gamma_1} \mathrm{d}\boldsymbol{s} = \gamma \sum_{F} |F| \,,$$

where F are the facets of Γ_1. Because the problem is smooth in this case, we apply a shape gradient scheme directly rather than a split Bregman scheme and terminate as soon as the norm of the gradient falls below $5 \cdot 10^{-8}$. The regularization parameters β and γ are selected by hand in each case. Automatic parameter selection strategies can clearly be applied here as well, but this is out of the scope of the present thesis. We refer the reader to [64, 110] for examples of such strategies.

As is expected and well known, the use of surface area regularization leads to results in which the identified inclusion Γ_1 is smoothed out. This can be explained by the observation that the gradient based minimization of the surface area yields a mean curvature flow.

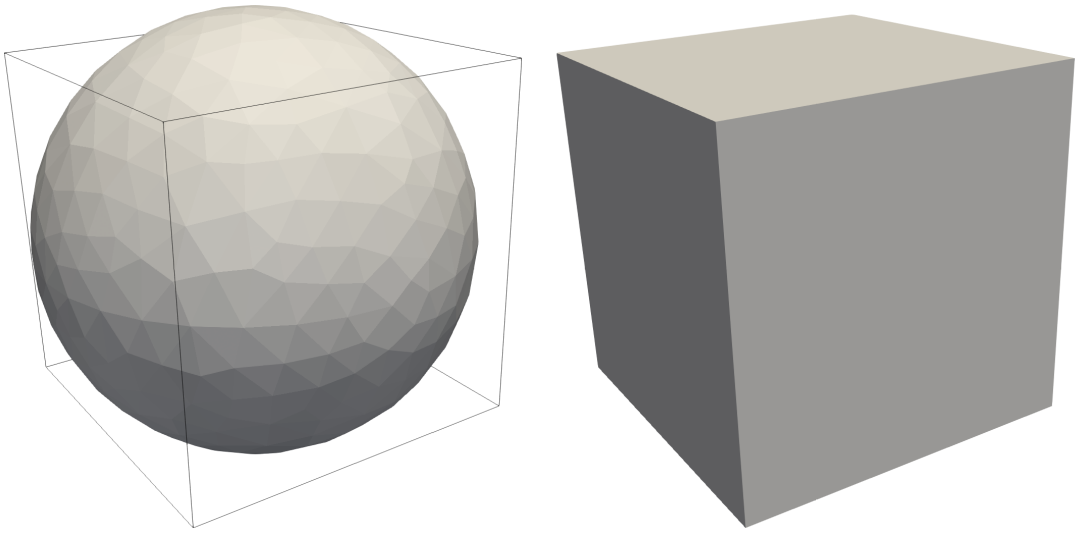

Figure 6.2: Initial guess for the inclusion Γ_1 on the left and the true inclusion on the right.

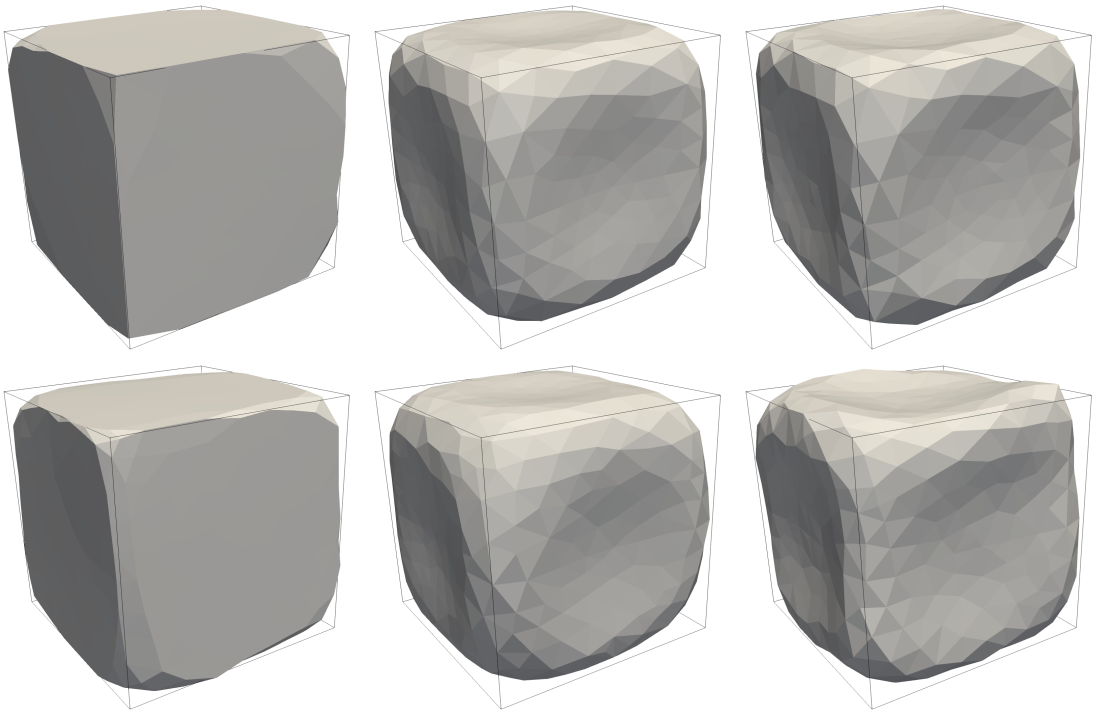

Figure 6.3: Top row: setting without noise; left: total variation regularization, $\beta = 10^{-6}$ and 90 iterations; middle: surface area regularization with $\gamma = 5 \cdot 10^{-5}$ and 1129 iterations; right: surface area regularization with $\gamma = 2 \cdot 10^{-5}$ and 978 iterations. Bottom row: setting with noise; left: total variation regularization with $\beta = 10^{-6}$ and 173 iterations with remeshing after iteration 121; middle: surface area regularization with $\gamma = 5 \cdot 10^{-5}$ and 1016 iterations with remeshing after iteration 539; right: surface area regularization with $\gamma = 2 \cdot 10^{-5}$ and 987 iterations with remeshing after iteration 308.

By contrast, our novel prior (5.1) allows for piecewise flat shapes and thus the interface Γ_1 is closely reconstructed in the noise-free situation. Even in the presence of noise, the reconstruction is remarkably good. In particular, the flat lateral surfaces and sharp edges can be identified quite well.

6.2 Mesh Denoising

In this section we consider an analogue of the ROF model for *mesh denoising*. The vertex positions $\boldsymbol{x}_V \in \mathbb{R}^3$ serve as optimization variables, and they implicitly determine the facets' normal and co-normal vectors. We consider the following variational model:

$$\text{Minimize } \frac{1}{2}\sum_V |\boldsymbol{X}_V - \boldsymbol{x}_V|_2^2 + \beta \sum_E |\log_{\boldsymbol{n}_E^+} \boldsymbol{n}_E^-|_{\mathfrak{g}} \; |E|_2 \,. \tag{6.8}$$

Here $\boldsymbol{X}_V \in \mathbb{R}^3$ are the given, noisy vertex positions which serve as data in the fidelity term in (6.8) and therefore, the associated augmented Lagrangian reads

$$\begin{aligned} \mathcal{L}(\boldsymbol{x}, \boldsymbol{d}, \boldsymbol{b}) \coloneqq \frac{1}{2}\sum_V |\boldsymbol{X}_V - \boldsymbol{x}_V|_2^2 + \beta \sum_E |\boldsymbol{d}_E|_{\mathfrak{g}} \; |E|_2 \\ + \frac{\lambda}{2}\sum_E \left|\boldsymbol{d}_E - \log_{\boldsymbol{n}_E^+} \boldsymbol{n}_E^- - \boldsymbol{b}_E\right|^2 \; |E|_2 \,. \end{aligned} \tag{6.9}$$

Figure 6.4 shows two denoising results obtained using (6.8) and Algorithm 7. For the first result, noise at a vertex was added in average normal direction using a Gaussian distribution with standard deviation $\sigma = 0.2$ times the average length of all edges. 100 outer iterations were needed, while performing one gradient step with step length 0.01 per outer iteration. In the second result, noise was added in arbitrary direction and it took 200 outer iterations. Never the less, Algorithm 7 removed noise very well, while preserving sharp features like edges and corners.

6.3 Mesh Inpainting

This section is devoted to a modification of (6.8) for *mesh inpainting* problems. These problems differ from (6.8) in that there is no fidelity term. Instead, the exact positions of a number of vertices are given beforehand, while the positions of the remaining vertices are unknown and there is no reference value known for them. In this setting, (6.9) is replaced by

$$\mathcal{L}(\boldsymbol{x}, \boldsymbol{d}, \boldsymbol{b}) \coloneqq \beta \sum_E |\boldsymbol{d}_E|_{\mathfrak{g}} \; |E|_2 + \frac{\lambda}{2}\sum_E \left|\boldsymbol{d}_E - \log_{\boldsymbol{n}_E^+} \boldsymbol{n}_E^- - \boldsymbol{b}_E\right|_{\mathfrak{g}}^2 \; |E|_2 \,. \tag{6.10}$$

Step 4 in Algorithm 7 now minimizes only w.r.t. the unknown vertex positions. Note that this assumes that a mesh connectivity is either given or has been constructed to span the missing parts as well. Usually, unknown vertex positions come in contiguous sections rather than single vertices.

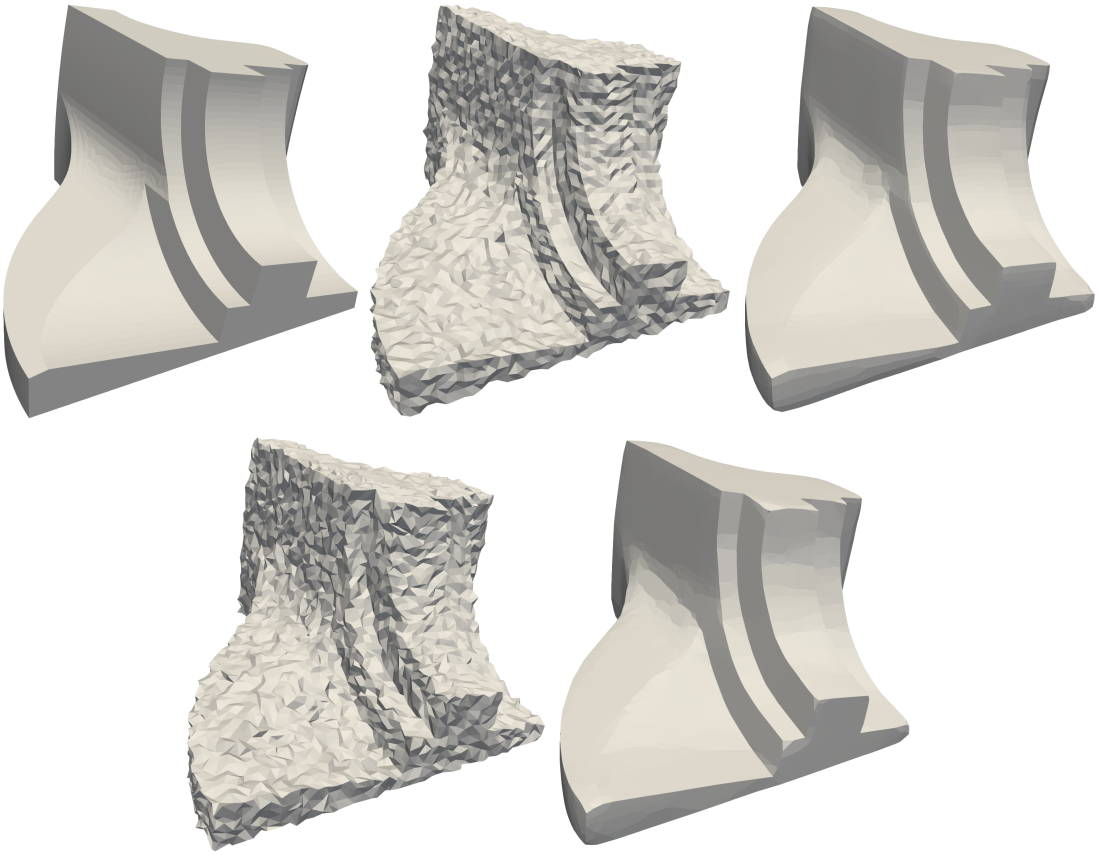

Figure 6.4: *Mesh denoising* using the split Bregman iteration on (6.8) with $\beta = 10^{-2}$ and $\lambda = 10^{-1}$. Original geometry (top left), with noise in normal direction (top middle) and reconstruction (top right). Geometry with noise in arbitrary direction (bottom left) and reconstruction (bottom right).

As a first test we consider a unit cube mesh with $10 \times 10 \times 2$ triangles on each side. After selecting a subdomain to simulate the loss of data, a surface area minimization problem is solved on this subdomain, which ensures that geometric information from the original mesh is removed. Note that the original mesh connectivity is maintained in this process, which might possibly add information that would help the reconstruction. Since usually such information is not available, the affected area is, for the purpose of this test, remeshed using the open source software Gmsh (version 3.0.6). The inpainting results obtained using FEniCS, once starting from the original and once from the newly generated mesh, are shown in Figure 6.5. To show the performance of our algorithm, another inpainting problem is solved on the more complex geometry *fandisk*. The corresponding results are shown in Figure 6.6.

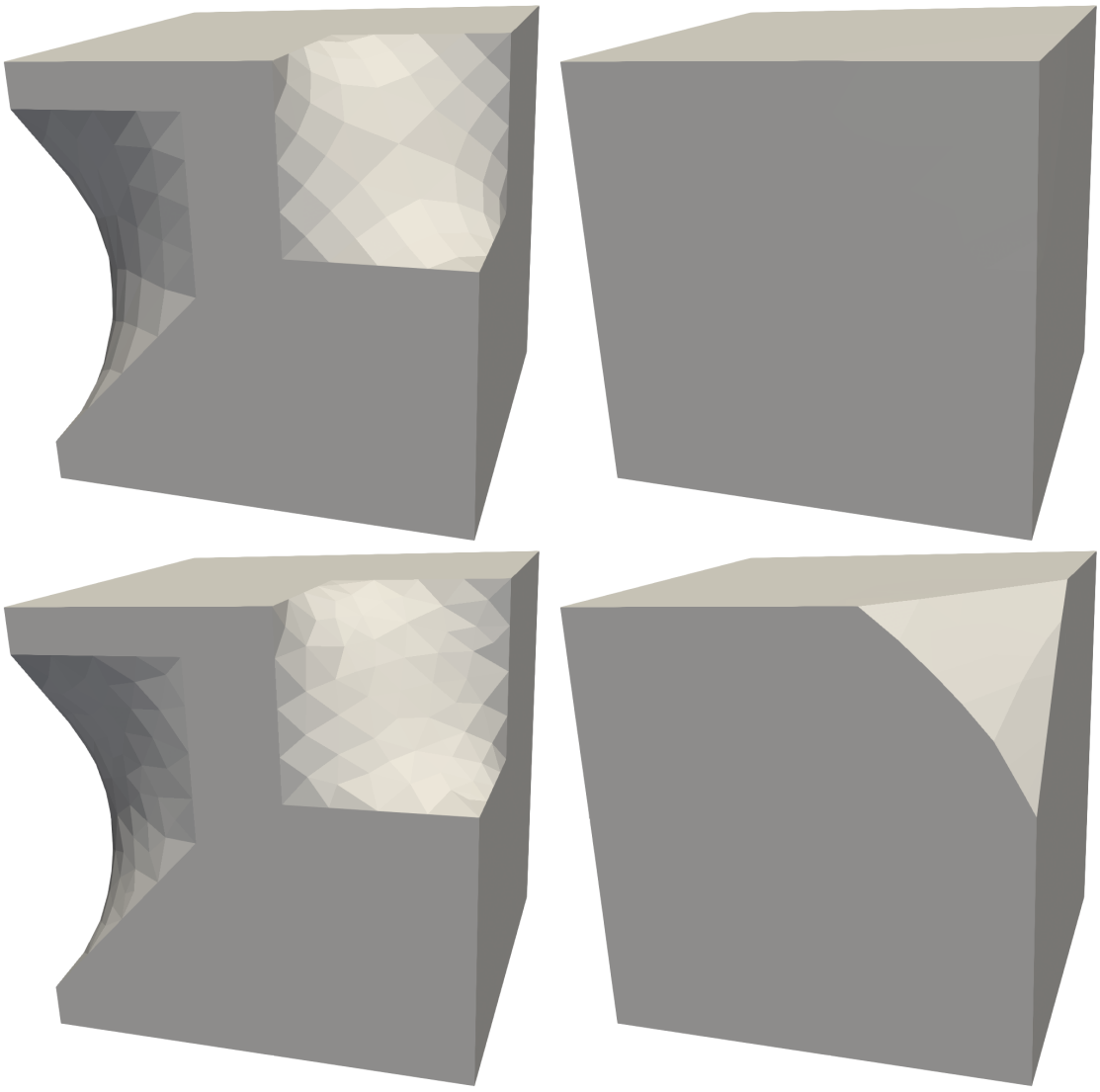

Figure 6.5: Using Algorithm 7 for *mesh inpainting*, based on (6.10) with $\beta = 10^{-3}$ and $\lambda = 10^{-2}$. Starting mesh with original mesh connectivity (top left) and corresponding reconstruction (top right), previous starting mesh after remesh with Gmsh (bottom left) and corresponding reconstruction (bottom right). The step size was 10^{-1} and it took 3000 outer iterations for the first and 900 for the second result with 10 inner iteration per outer iteration.

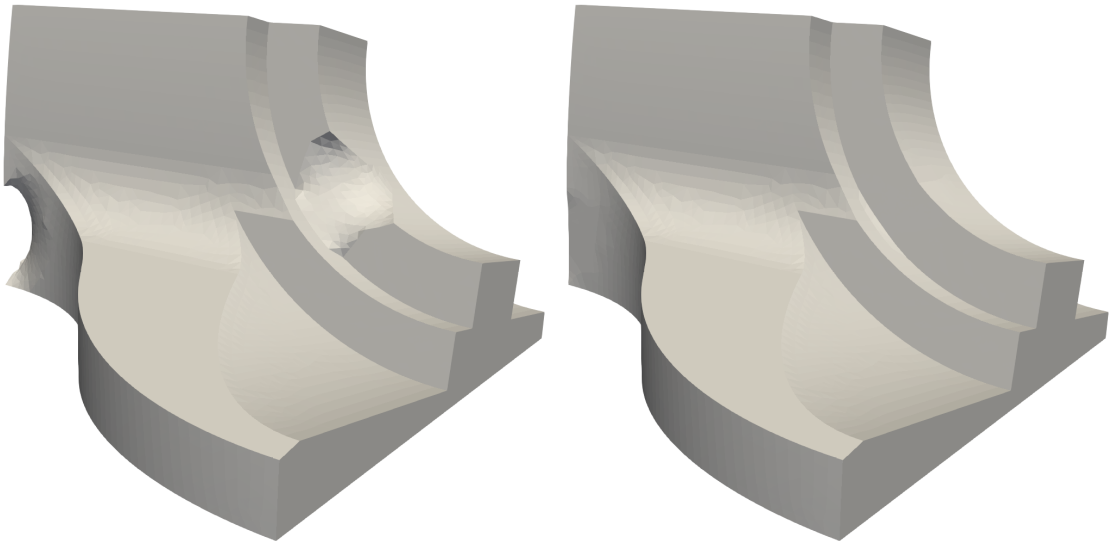

Figure 6.6: Using Algorithm 7 for *mesh inpainting*, based on (6.10) with $\beta = 10^{-3}$ and $\lambda = 10^{-2}$, after an initial remeshing was done on the affected area. Starting mesh (left) and reconstruction (right). The step size was 10^{-2} and it took 3500 outer iterations with 10 inner iteration per outer iteration.

CHAPTER 7

CONCLUSION

We successfully investigated the well-known total variation regularizer on surfaces in the context of textures and introduced an extension for shape optimization problems. In this chapter, we conclude the thesis by summarizing the main results and discussing possible topics of future research.

The Total Variation on Surfaces

We considered an analogue of the TV–L^2 image reconstruction approach for images on smooth surfaces. Complementary to [108], we proved the well-posedness of the model and its predual, and rigorously established strong duality with the predual in function space. The predual problem is a quadratic optimization problem for the vector field $\boldsymbol{p} \in \boldsymbol{H}(\mathrm{div};\Gamma)$ with pointwise nonlinear inequality constraints on the surface. As in the flat case, $\boldsymbol{p}$ serves as an edge detector. We proposed and analyzed a function space interior point method for the predual problem. Based on the finding that the latter is posed in $\boldsymbol{H}(\mathrm{div};\Gamma)$, we are led to choose a conforming finite element discretization by the surface analogue of first- or higher-order Raviart–Thomas finite element spaces. In contrast to linear Lagrangian elements employed in [108], our discretization exhausts the space when the surface mesh is refined. Numerical examples, which comprise denoising and inpainting problems, show the viability of the approach for real-world geometries consisting of more than 350 000 and 175 000 vertices. Our method can be easily adapted to surfaces with boundary, by replacing $\boldsymbol{H}(\mathrm{div};\Gamma)$ with $\boldsymbol{H}_0(\mathrm{div};\Gamma)$. This amounts to imposing the boundary condition $\boldsymbol{p} \cdot \boldsymbol{\mu} = 0$ along the boundary ∂S. The analysis presented carries over with minor changes.

There is room for improvement in various directions. For instance, the polynomial order r of the finite element space $\mathcal{DG}_r$ for the image data f could be adjusted locally to reflect the level of detail present in each surface cell. This would then naturally lead to discretizations of $\boldsymbol{p}$ and u with varying polynomial degree as well. Moreover, we have so far been solving the predual problem with a basic primal interior point approach, running Newton's method to convergence for each value of the barrier parameter μ. A more sophisticated primal-dual interior-point method with inexact system solves might help reduce the computational cost for high-dimensional problems. While we are exploiting the MPI-based parallelism of the FENICS library for system assembly and direct system solves already, more efficiency might be gained by preconditioned iterative solvers

with tailored preconditioners. This appears particularly promising in order to treat also problems with non-local operators K efficiently. This is left for future research.
Since we admit higher-order polynomial functions, it would be natural to extend our analysis to a discrete version of the total generalized variation (TGV) functional introduced in [35]. Another generalization that could be of interest is to consider finite element functions defined on more general cells than the simplices considered here. Clearly rectangles are of particular interest in imaging applications, but also hexagons; see [59, 104], as mentioned in the introduction. We remark that $\mathcal{RT}$ finite element spaces on parallelograms were already discussed in the original contribution [133], and we refer to [111] for an application to imaging, but only for the lowest-order case. The generalization to higher-order finite elements, as well as to more general element geometries, is left for future research.

Afterwards, we have introduced a discrete version (DTV) of the TV-seminorm for globally discontinuous ($\mathcal{DG}_r$) Lagrangian finite element functions on triangulated surface meshes in $\mathbb{R}^3$. Since continuous ($\mathcal{CG}_r$) functions form a subspace of $\mathcal{DG}_r$, all considerations apply to images represented as continuous finite element functions as well. We have shown that $|\cdot|_{DTV(\Gamma_h)}$ has a convenient dual representation in terms of the supremum over the space of Raviart–Thomas finite element functions, subject to a set of simple constraints. This allows for the efficient realization of a variety of algorithms, e.g., (DTV-L2-D) and (DTV-L1-D) for image denoising and inpainting, both with low and higher-order finite element functions available in finite element libraries.
The polynomial degree in our study was limited to $0 \leq r \leq 4$ (or $0 \leq r \leq 3$ for (DTV-L1)), which should be sufficient for most applications. The limitation in the degree arises due to the requirement that the quadrature weights, i.e., the integrals over the standard Lagrangian basis functions, have to be non-negative; see Lemma 3.1. This brings up the question whether a Lagrangian basis for higher-order polynomial functions on triangles or tetrahedra exists, such that the integrals of the basis functions are (strictly) positive. This is answered in the affirmative by results in [155, 159] for the triangle and [80, 172] for tetrahedra, where interpolatory quadrature formulas with positive weights are constructed. However, it remains to be investigated whether a Lagrangian finite element with a modified basis admits an appropriate Raviart–Thomas type counterpart such that a dual representation of $|\cdot|_{DTV(\Gamma_h)}$ parallel to Theorem 3.2 continues to hold. Moreover, such non-standard finite element spaces certainly incur an overhead in implementation.
One may also envision applications where it would be beneficial to allow for locally varying polynomial degrees and mesh sizes in imaging applications, so that the resolution can be chosen adaptively. Finally, we mention possible extensions to vectorial TV-seminorms, see for instance [84]. These topics remain for future research.

The Total Variation of Surfaces

In the second part of this thesis, we introduced an analogue of the total variation prior for the normal vector field (4.2) defined on the boundary Γ of smooth domains $\Omega \subset \mathbb{R}^3$. This functional is also known as the total root mean square curvature (4.5). We have shown in Theorem 4.9 that it admits spheres as stationary points under an area constraint and we conjecture that spheres are in fact global minimizers. We proposed a split Bregman

(ADMM) scheme for the numerical solution of shape optimization problems (4.3) involving the total variation of the normal. In contrast to a Euclidean ADMM, as proposed for instance in [85], the normal vector data belongs to the sphere $\mathcal{S}^2$. Therefore, the formulation of the ADMM method requires concepts from differential geometry. An analysis of the Riemannian ADMM scheme is beyond the scope of this thesis and will be presented elsewhere.

Finally, a discrete analogue of the total variation prior for the normal vector field was presented. While we are currently unable to characterize all minimizers of its discrete counterpart, we showed that the icosahedron and a cube with crossed diagonals are stationary under an area constraint. We conjecture that the full set of minimizers is much richer than this, in particular when the connectivity is included as design unknown. It has been argued in [126, Section 3.3] that minimal energy is achieved for meshes which are not triangular, but whose faces are approximately rectangular.
We proposed, described and implemented a split Bregman (ADMM) scheme, similar to the continuous case, for the numerical solution of shape optimization problems involving the discrete total variation of the normal.
We demonstrate the utility of the discrete total variation of the normal as a shape prior in a geometric inverse problem, in which we aim to detect a polyhedral inclusion. Unlike the popular surface area regularization, our prior allows for piecewise flat shapes.

BIBLIOGRAPHY

[1] P.-A. Absil, R. Mahony, and R. Sepulchre. *Optimization Algorithms on Matrix Manifolds*. Princeton University Press, 2008. doi:10.1515/9781400830244.

[2] M. Alexa and M. Wardetzky. Discrete laplacians on general polygonal meshes. In *ACM Transactions on Graphics (TOG)*, volume 30, page 102. ACM, 2011. doi:10.1145/2010324.1964997.

[3] M. Alkämper and A. Langer. Using DUNE-ACFem for non-smooth minimization of bounded variation functions. *Archive of Numerical Software*, 5(1):3–19, 2017. doi:10.11588/ans.2017.1.27475.

[4] M. Alnæs, J. Blechta, J. Hake, A. Johansson, B. Kehlet, A. Logg, C. Richardson, J. Ring, M. E. Rognes, and G. N. Wells. The FEniCS project version 1.5. *Archive of Numerical Software*, 3(100):9–23, 2015. doi:10.11588/ans.2015.100.20553.

[5] M. S. Alnæs, A. Logg, K. B. Ølgaard, M. E. Rognes, and G. N. Wells. Unified form language: a domain-specific language for weak formulations and partial differential equations. *Association for Computing Machinery. Transactions on Mathematical Software*, 40(2):Art. 9, 37, 2014. doi:10.1145/2566630.

[6] P. F. Antonietti and B. Ayuso. Schwarz domain decomposition preconditioners for discontinuous Galerkin approximations of elliptic problems: non-overlapping case. *M2AN. Mathematical Modelling and Numerical Analysis*, 41(1):21–54, 2007. doi:10.1051/m2an:2007006.

[7] G. Ateshian, M. Rosenwasser, and V. Mow. Curvature characteristics and congruence of the thumb carpometacarpal joint: Differences between female and male joints. *Journal of Biomechanics*, 25(6):591–607, jun 1992. doi:10.1016/0021-9290(92)90102-7.

[8] H. Attouch, G. Buttazzo, and G. Michaille. *Variational Analysis in Sobolev and BV Spaces*, volume 6 of *MPS/SIAM Series on Optimization*. Society for Industrial and Applied Mathematics (SIAM), Philadelphia, PA, 2006.

[9] T. Aubin. *A Course in Differential Geometry*, volume 27 of *Graduate Studies in Mathematics*. American Mathematical Society, Providence, RI, 2001.

[10] M. Bačák. Computing medians and means in Hadamard spaces. *SIAM Journal on Optimization*, 24(3):1542–1566, 2014. doi:10.1137/140953393.

[11] M. Bachmayr and M. Burger. Iterative total variation schemes for nonlinear inverse problems. *Inverse Problems*, 25(10):105004, 26, 2009. doi:10.1088/0266-5611/25/10/105004.

[12] C. L. Bajaj and G. Xu. Anisotropic diffusion of surfaces and functions on surfaces. *ACM Transactions on Graphics*, 22(1):4–32, jan 2003. doi:10.1145/588272.588276.

[13] S. Bartels. Total variation minimization with finite elements: convergence and iterative solution. *SIAM Journal on Numerical Analysis*, 50(3):1162–1180, 2012. doi:10.1137/11083277X.

[14] S. Bartels. Error control and adaptivity for a variational model problem defined on functions of bounded variation. *Mathematics of Computation*, 84(293):1217–1240, 2015. doi:10.1090/S0025-5718-2014-02893-7.

[15] S. Bartels, R. H. Nochetto, and A. J. Salgado. Discrete total variation flows without regularization. *SIAM Journal on Numerical Analysis*, 52(1):363–385, 2014. doi:10.1137/120901544.

[16] A. Beck. *First-Order Methods in Optimization*. Society for Industrial and Applied Mathematics, Philadelphia, PA, 2017. doi:10.1137/1.9781611974997.

[17] M. Ben-Artzi and P. G. LeFloch. Well-posedness theory for geometry-compatible hyperbolic conservation laws on manifolds. *Annales de l'Institut Henri Poincaré. Analyse Non Linéaire*, 24(6):989–1008, 2007. doi:10.1016/j.anihpc.2006.10.004.

[18] M. Ben-Ezra, Z. Lin, B. Wilburn, and W. Zhang. Penrose pixels for super-resolution. *IEEE Transactions on Pattern Analysis and Machine Intelligence*, 33(7):1370–1383, jul 2011. doi:10.1109/tpami.2010.213.

[19] H. Benninghoff and H. Garcke. Segmentation and restoration of images on surfaces by parametric active contours with topology changes. *Journal of Mathematical Imaging and Vision*, 55(1):105–124, 2016. doi:10.1007/s10851-015-0616-6.

[20] R. Bergmann, R. H. Chan, R. Hielscher, J. Persch, and G. Steidl. Restoration of manifold-valued images by half-quadratic minimization. *Inverse Problems in Imaging*, 10(2):281–304, 2016. doi:10.3934/ipi.2016001.

[21] R. Bergmann, M. Herrmann, R. Herzog, S. Schmidt, and J. Vidal-Núñez. Discrete total variation of the normal vector field as shape prior with applications in geometric inverse problems, 2019, 1908.07916.

[22] R. Bergmann, M. Herrmann, R. Herzog, S. Schmidt, and J. Vidal-Núñez. Total variation of the normal vector field as shape prior, 2019, 1902.07240.

[23] R. Bergmann, M. Herrmann, R. Herzog, S. Schmidt, and J. Vidal-Núñez. Discrete total variation of the normal vector field as shape prior with applications in geometric inverse problems. *Inverse Problems*, submitted.

[24] R. Bergmann, M. Herrmann, R. Herzog, S. Schmidt, and J. Vidal-Núñez. Total variation of the normal vector field as shape prior. *Inverse Problems*, submitted.

[25] R. Bergmann, R. Herzog, D. Tenbrinck, and J. Vidal-Núñez. Fenchel duality theory and a primal-dual algorithm on riemannian manifolds, 2019, 1908.02022.

[26] R. Bergmann, J. Persch, and G. Steidl. A parallel Douglas Rachford algorithm for minimizing ROF-like functionals on images with values in symmetric Hadamard manifolds. *SIAM Journal on Imaging Sciences*, 9(4):901–937, 2016. doi:10.1137/15M1052858.

[27] R. Bergmann and D. Tenbrinck. A graph framework for manifold-valued data. *SIAM Journal on Imaging Sciences*, 11(1):325–360, 2018. doi:10.1137/17M1118567.

[28] B. Berkels, A. Effland, and M. Rumpf. A posteriori error control for the binary Mumford-Shah model. *Mathematics of Computation*, 86(306):1769–1791, 2017. doi:10.1090/mcom/3138.

[29] M. Bertalmío, L.-T. Cheng, S. Osher, and G. Sapiro. Variational problems and partial differential equations on implicit surfaces. *Journal of Computational Physics*, 174(2):759–780, 2001. doi:10.1006/jcph.2001.6937.

[30] H. Biddle, I. von Glehn, C. B. Macdonald, and T. März. A volume-based method for denoising on curved surfaces. In *2013 IEEE International Conference on Image Processing*, pages 529–533. IEEE, sep 2013. doi:10.1109/icip.2013.6738109.

[31] P. Blomgren and T. Chan. Color TV: total variation methods for restoration of vector-valued images. *IEEE Transactions on Image Processing*, 7(3):304–309, mar 1998. doi:10.1109/83.661180.

[32] A. I. Bobenko and B. A. Springborn. A discrete Laplace-Beltrami operator for simplicial surfaces. *Discrete & Computational Geometry. An International Journal of Mathematics and Computer Science*, 38(4):740–756, 2007. doi:10.1007/s00454-007-9006-1.

[33] A. Bonito, A. Demlow, and R. H. Nochetto. Finite element methods for the laplace-beltrami operator, 2019, 1906.02786.

[34] M. Botsch, M. Pauly, L. Kobbelt, P. Alliez, B. Lévy, S. Bischoff, and C. Rössl. Geometric modeling based on polygonal meshes. In *ACM SIGGRAPH 2007 Courses*, SIGGRAPH '07. ACM, 2007. doi:10.1145/1281500.1281640.

[35] K. Bredies, K. Kunisch, and T. Pock. Total generalized variation. *SIAM Journal on Imaging Sciences*, 3(3):492–526, 2010. doi:10.1137/090769521.

[36] K. Bredies and D. Lorenz. *Mathematische Bildverarbeitung*. Vieweg & Teubner, 2011. doi:10.1007/978-3-8348-9814-2.

[37] X. Bresson and T. F. Chan. Fast dual minimization of the vectorial total variation norm and applications to color image processing. *Inverse Problems and Imaging*, 2(4):455–484, 2008. doi:10.3934/ipi.2008.2.455.

[38] A. Brook, A. M. Bruckstein, and R. Kimmel. On similarity-invariant fairness measures. In *International Conference on Scale-Space Theories in Computer Vision*, pages 456–467. Springer, 2005. doi:10.1007/11408031_39.

[39] J.-F. Cai, S. Osher, and Z. Shen. Linearized Bregman iterations for frame-based image deblurring. *SIAM Journal on Imaging Sciences*, 2(1):226–252, 2009. doi:10.1137/080733371.

[40] C. Carstensen. Quasi-interpolation and a posteriori error analysis in finite element methods. *M2AN. Mathematical Modelling and Numerical Analysis*, 33(6):1187–1202, 1999. doi:10.1051/m2an:1999140.

[41] J. L. Carter. *Dual Methods for Total Variation-Based Image Restoration*. PhD thesis, UCLA, 2001.

[42] E. Casas, R. Herzog, and G. Wachsmuth. Approximation of sparse controls in semilinear equations by piecewise linear functions. *Numerische Mathematik*, 122(4):645–669, 2012. doi:10.1007/s00211-012-0475-7.

[43] V. Caselles, A. Chambolle, and M. Novaga. Total variation in imaging. In O. Scherzer, editor, *Handbook of Mathematical Methods in Imaging*, pages 1455–1499. Springer New York, 2015. doi:10.1007/978-1-4939-0790-8_23.

[44] A. Chambolle. An algorithm for total variation minimization and applications. *Journal of Mathematical Imaging and Vision*, 20(1-2):89–97, 2004. doi:10.1023/B:JMIV.0000011325.36760.1e. Special issue on mathematics and image analysis.

[45] A. Chambolle, V. Caselles, D. Cremers, M. Novaga, and T. Pock. An introduction to total variation for image analysis. In *Theoretical foundations and numerical methods for sparse recovery*, volume 9 of *Radon Series on Computational and Applied Mathematics*, pages 263–340. Walter de Gruyter, Berlin, 2010. doi:10.1515/9783110226157.263.

[46] A. Chambolle and P.-L. Lions. Image recovery via total variation minimization and related problems. *Numerische Mathematik*, 76(2):167–188, 1997. doi:10.1007/s002110050258.

[47] A. Chambolle and T. Pock. A first-order primal-dual algorithm for convex problems with applications to imaging. *Journal of Mathematical Imaging and Vision*, 40(1):120–145, 2011. doi:10.1007/s10851-010-0251-1.

[48] A. Chambolle and T. Pock. Crouzeix–Raviart approximation of the total variation on simplicial meshes, 2018. URL `https://hal.archives-ouvertes.fr/hal-01787012`.

[49] T. Chan, S. Esedoglu, F. Park, and A. Yip. Total variation image restoration: overview and recent developments. In *Handbook of mathematical models in computer vision*, pages 17–31. Springer, New York, 2006. doi:10.1007/0-387-28831-7_2.

[50] T. F. Chan and S. Esedoglu. Aspects of total variation regularized L^1 function approximation. *SIAM Journal on Applied Mathematics*, 65(5):1817–1837, 2005. doi:10.1137/040604297.

[51] T. F. Chan, G. H. Golub, and P. Mulet. A nonlinear primal-dual method for total variation-based image restoration. *SIAM Journal on Scientific Computing*, 20(6):1964–1977, 1999. doi:10.1137/S1064827596299767.

[52] T. F. Chan and J. Shen. *Image processing and analysis*. Society for Industrial and Applied Mathematics (SIAM), Philadelphia, PA, 2005. doi:10.1137/1.9780898717877. Variational, PDE, wavelet, and stochastic methods.

[53] T. F. Chan and X.-C. Tai. Level set and total variation regularization for elliptic inverse problems with discontinuous coefficients. *Journal of Computational Physics*, 193(1):40–66, 2004. doi:10.1016/j.jcp.2003.08.003.

[54] B.-Y. Chen. Riemannian submanifolds. In *Handbook of differential geometry, Vol. I*, pages 187–418. North-Holland, Amsterdam, 2000. doi:10.1016/S1874-5741(00)80006-0.

[55] M. Cheney, D. Isaacson, and J. C. Newell. Electrical impedance tomography. *SIAM Review*, 41(1):85–101 (electronic), 1999. doi:10.1137/S0036144598333613.

[56] E. T. Chung, T. F. Chan, and X.-C. Tai. Electrical impedance tomography using level set representation and total variational regularization. *Journal of Computational Physics*, 205(1):357–372, 2005. doi:10.1016/j.jcp.2004.11.022.

[57] U. Clarenz, U. Diewald, and M. Rumpf. Processing textured surfaces via anisotropic geometric diffusion. *IEEE Transactions on Image Processing*, 13(2):248–261, feb 2004. doi:10.1109/tip.2003.819863.

[58] C. Clason, F. Kruse, and K. Kunisch. Total variation regularization of multi-material topology optimization. *ESAIM. Control, Optimisation and Calculus of Variations*, 52(1):275–303, 2018. doi:10.1051/m2an/2017061.

[59] S. Coleman, B. Scotney, and B. Gardiner. Tri-directional gradient operators for hexagonal image processing. *Journal of Visual Communication and Image Representation*, 38:614–626, jul 2016. doi:10.1016/j.jvcir.2016.04.001.

[60] L. Condat. Discrete total variation: New definition and minimization. *SIAM Journal on Imaging Sciences*, 10(3):1258–1290, jan 2017. doi:10.1137/16m1075247.

[61] K. Crane, F. De Goes, M. Desbrun, and P. Schröder. Digital geometry processing with discrete exterior calculus. In *ACM SIGGRAPH 2013 Courses*, page 7. ACM, 2013. doi:10.1145/2504435.2504442.

[62] G. Dahlquist and A. Björck. *Numerical methods in scientific computing. Vol. I*. Society for Industrial and Applied Mathematics (SIAM), Philadelphia, PA, 2008. doi:10.1137/1.9780898717785.

[63] P. J. Davis and P. Rabinowitz. *Methods of numerical integration*. Computer Science and Applied Mathematics. Academic Press, Inc., Orlando, FL, 2 edition, 1984.

[64] J. C. de los Reyes, C.-B. Schönlieb, and T. Valkonen. Bilevel parameter learning for higher-order total variation regularisation models. *Journal of Mathematical Imaging and Vision*, 57(1):1–25, 2017. doi:10.1007/s10851-016-0662-8.

[65] M. Delfour and J.-P. Zolésio. *Shapes and Geometries*. Society for Industrial and Applied Mathematics, 2 edition, 2011. doi:10.1137/1.9780898719826.

[66] M. Desbrun, M. Meyer, P. Schröder, and A. H. Barr. Implicit fairing of irregular meshes using diffusion and curvature flow. In *Proceedings of the 26th Annual Conference on Computer Graphics and Interactive Techniques*, SIGGRAPH '99, pages 317–324, 1999. doi:10.1145/311535.311576.

[67] M. Desbrun, M. Meyer, P. Schröder, and A. H. Barr. Anisotropic feature-preserving denoising of height fields and bivariate data. In *Proceedings of Graphics Interface 2000*, pages 145–152, Toronto, Ontario, Canada, 2000. Canadian Human-Computer Communications Society. doi:10.20380/GI2000.20.

[68] P. Destuynder, M. Jaoua, and H. Sellami. A dual algorithm for denoising and preserving edges in image processing. *Journal of Inverse and Ill-Posed Problems*, 15(2):149–165, 2007. doi:10.1515/JIIP.2007.008.

[69] M. P. do Carmo. *Differential geometry of curves and surfaces*. Prentice-Hall, Inc., Englewood Cliffs, N.J., 1976. Translated from the Portuguese.

[70] M. P. do Carmo. *Riemannian Geometry*. Mathematics: Theory & Applications. Birkhäuser Boston, Inc., Boston, MA, 1992.

[71] D. C. Dobson and F. Santosa. Recovery of blocky images from noisy and blurred data. *SIAM Journal on Applied Mathematics*, 56(4):1181–1198, 1996. doi:10.1137/S003613999427560X.

[72] Y. Dong, M. Hintermüller, and M. M. Rincon-Camacho. A multi-scale vectorial L^τ-TV framework for color image restoration. *International Journal of Computer Vision*, 92(3):296–307, 2011. doi:10.1007/s11263-010-0359-1.

[73] I. Ekeland and R. Temam. *Convex Analysis and Variational Problems*, volume 28 of *Classics in Applied Mathematics*. SIAM, Philadelphia, 1999.

[74] C. M. Elliott and S. A. Smitheman. Numerical analysis of the TV regularization and H^{-1} fidelity model for decomposing an image into cartoon plus texture. *IMA Journal of Numerical Analysis*, 29(3):651–689, 2009. doi:10.1093/imanum/drn025.

[75] M. Elsey and S. Esedoglu. Analogue of the total variation denoising model in the context of geometry processing. *Multiscale Modeling & Simulation. A SIAM Interdisciplinary Journal*, 7(4):1549–1573, 2009. doi:10.1137/080736612.

[76] A. Ern and J.-L. Guermond. *Theory and Practice of Finite Elements*. Springer, Berlin, 2004.

[77] S. Esedoglu and S. J. Osher. Decomposition of images by the anisotropic Rudin-Osher-Fatemi model. *Communications on Pure and Applied Mathematics*, 57(12):1609–1626, 2004. doi:10.1002/cpa.20045.

[78] X. Feng and A. Prohl. Analysis of total variation flow and its finite element approximations. *M2AN. Mathematical Modelling and Numerical Analysis*, 37(3):533–556, 2003. doi:10.1051/m2an:2003041.

[79] D. A. Field. Laplacian smoothing and Delaunay triangulations. *Communications in Applied Numerical Methods*, 4(6):709–712, 1988. doi:10.1002/cnm.1630040603.

[80] M. Gellert and R. Harbord. Moderate degree cubature formulas for 3-d tetrahedral finite-element approximations. *Communications in Applied Numerical Methods*, 7(6):487–495, sep 1991. doi:10.1002/cnm.1630070609.

[81] M. Giaquinta and D. Mucci. Maps of bounded variation with values into a manifold: total variation and relaxed energy. *Pure and Applied Mathematics Quarterly*, 3(2, Special Issue: In honor of Leon Simon. Part 1):513–538, 2007. doi:10.4310/PAMQ.2007.v3.n2.a6.

[82] V. Girault and P.-A. Raviart. *Finite Element Methods for Navier-Stokes Equations*. Springer, 1986.

[83] E. Giusti. *Minimal Surfaces and Functions of Bounded Variation*, volume 80 of *Monographs in Mathematics*. Birkhäuser Verlag, Basel, 1984. doi:10.1007/978-1-4684-9486-0.

[84] B. Goldluecke, E. Strekalovskiy, and D. Cremers. The natural vectorial total variation which arises from geometric measure theory. *SIAM Journal on Imaging Sciences*, 5(2):537–564, 2012. doi:10.1137/110823766.

[85] T. Goldstein and S. Osher. The split Bregman method for $L1$-regularized problems. *SIAM Journal on Imaging Sciences*, 2(2):323–343, 2009. doi:10.1137/080725891.

[86] P. Gómez, J. Hernández, and J. López. On the reinitialization procedure in a narrow-band locally refined level set method for interfacial flows. *International Journal for Numerical Methods in Engineering*, 63(10):1478–1512, 2005. doi:10.1002/nme.1324.

[87] A. Gray, E. Abbena, and S. Salamon. *Modern differential geometry of curves and surfaces with Mathematica®*. Studies in Advanced Mathematics. Chapman & Hall/CRC, Boca Raton, FL, third edition, 2006.

[88] G. Greiner. Variational design and fairing of spline surfaces. volume 13, pages 143–154. 1994. doi:10.1111/1467-8659.1330143.

[89] H. Hagen and G. Schulze. Automatic smoothing with geometric surface patches. *Computer Aided Geometric Design*, 4(3):231–235, nov 1987. doi:10.1016/0167-8396(87)90014-8.

[90] M. Halstead, M. Kass, and T. DeRose. Efficient, fair interpolation using catmull-clark surfaces. In *Proceedings of the 20th annual conference on Computer graphics and interactive techniques - SIGGRAPH '93*. ACM Press, 1993. doi:10.1145/166117.166121.

[91] D. A. Ham, L. Mitchell, A. Paganini, and F. Wechsung. Automated shape differentiation in the unified form language. Technical report, 2018, 1808.08083.

[92] B. He and X. Yuan. Convergence analysis of primal-dual algorithms for a saddle-point problem: from contraction perspective. *SIAM Journal on Imaging Sciences*, 5(1):119–149, 2012. doi:10.1137/100814494.

[93] E. Hebey. *Sobolev spaces on Riemannian manifolds*, volume 1635 of *Lecture Notes in Mathematics*. Springer-Verlag, Berlin, 1996. doi:10.1007/BFb0092907.

[94] E. Hebey. *Nonlinear Analysis on Manifolds*, volume 5 of *American Mathematical Society*. Courant Lectures Notes in Mathematics, 2000.

[95] A. Helfrich-Schkarbanenko. *Elektrische Impedanztomografie in der Geoelektrik*. Dissertation, 2011, urn:nbn:de:swb:90-224216.

[96] M. Herrmann, R. Herzog, H. Kröner, S. Schmidt, and J. Vidal-Núñez. Analysis and an interior point approach for TV image reconstruction problems on smooth surfaces. *SIAM Journal on Imaging Sciences*, 11(2):889–922, 2018. doi:10.1137/17M1128022.

[97] M. Herrmann, R. Herzog, S. Schmidt, J. Vidal-Núñez, and G. Wachsmuth. Discrete total variation with finite elements and applications to imaging, 2018, 1804.07477. Extended preprint.

[98] R. Herzog, G. Stadler, and G. Wachsmuth. Directional sparsity in optimal control of partial differential equations. *SIAM Journal on Control and Optimization*, 50(2):943–963, 2012. doi:10.1137/100815037.

[99] M. Hintermüller and K. Kunisch. Total bounded variation regularization as a bilaterally constrained optimization problem. *SIAM Journal on Applied Mathematics*, 64(4):1311–1333, 2004. doi:10.1137/S0036139903422784.

[100] S. Hosseini and A. Uschmajew. A Riemannian gradient sampling algorithm for nonsmooth optimization on manifolds. *SIAM Journal on Optimization*, 27(1):173–189, 2017. doi:10.1137/16M1069298.

[101] J. R. Jensen. *Introductory Digital Image Processing: A Remote Sensing Perspective*. Prentice-Hall Inc., Englewood Cliffs, N.J., 4th edition, 2015.

[102] J. John and M. Wilscy. Image processing techniques for surface characterization of nanostructures. In *2016 International Conference on Circuit, Power and Computing Technologies (ICCPCT)*. IEEE, mar 2016. doi:10.1109/iccpct.2016.7530317.

[103] R. Kimmel and N. Sochen. Orientation diffusion or how to comb a porcupine. *Journal of Visual Communication and Image Representation*, 13(1-2):238–248, 2002. doi:10.1006/jvci.2001.0501.

[104] M. Knaup, S. Steckmann, O. Bockenbach, and M. Kachelrieß. CT image reconstruction using hexagonal grids. In *2007 IEEE Nuclear Science Symposium Conference Record*, pages 3074–3076. IEEE, 2007. doi:10.1109/nssmic.2007.4436779.

[105] A. Kovnatsky, K. Glashoff, and M. M. Bronstein. MADMM: A generic algorithm for non-smooth optimization on manifolds. In *Computer Vision – ECCV 2016*, pages 680–696. Springer International Publishing, 2016. doi:10.1007/978-3-319-46454-1_41.

[106] W. Kühnel. *Differentialgeometrie*. Aufbaukurs Mathematik. [Mathematics Course]. Springer Spektrum, Wiesbaden, 2013. doi:10.1007/978-3-658-00615-0.

[107] H. R. Künsch. Robust priors for smoothing and image restoration. *Annals of the Institute of Statistical Mathematics*, 46(1):1–19, 1994. doi:10.1007/BF00773588.

[108] R. Lai and T. F. Chan. A framework for intrinsic image processing on surfaces. *Computer Vision and Image Understanding*, 115(12):1647–1661, dec 2011. doi:10.1016/j.cviu.2011.05.011.

[109] R. Lai and S. Osher. A splitting method for orthogonality constrained problems. *Journal of Scientific Computing*, 58(2):431–449, 2014. doi:10.1007/s10915-013-9740-x.

[110] A. Langer. Automated parameter selection in the L^1-L^2-TV model for removing Gaussian plus impulse noise. *Inverse Problems. An International Journal on the Theory and Practice of Inverse Problems, Inverse Methods and Computerized Inversion of Data*, 33(7):074002, 41, 2017. doi:10.1088/1361-6420/33/7/074002.

[111] C.-O. Lee, E.-H. Park, and J. Park. A finite element approach for the dual total variation minimization and its nonoverlapping domain decomposition methods, 2018, 1805.02562.

[112] J. Lellmann, E. Strekalovskiy, S. Koetter, and D. Cremers. Total variation regularization for functions with values in a manifold. In *IEEE ICCV 2013*, pages 2944–2951, 2013. doi:10.1109/ICCV.2013.366.

[113] J. Li, C. Bai, Z. Lin, and J. Yu. Penrose high-dynamic-range imaging. *Journal of Electronic Imaging*, 25(3):033024, jun 2016. doi:10.1117/1.jei.25.3.033024.

[114] A. Logg, K.-A. Mardal, G. N. Wells, et al. *Automated Solution of Differential Equations by the Finite Element Method*. Springer, 2012. doi:10.1007/978-3-642-23099-8.

[115] L. D. López Pérez. *Régularisation d'images sur des surfaces non planes*. PhD thesis, Université de Nice-Sophia Antipolis, 2006. URL `https://tel.archives-ouvertes.fr/tel-00141417v1`.

[116] N. Lott and D. Pullin. Method for fairing b-spline surfaces. *Computer-Aided Design*, 20(10):597–600, dec 1988. doi:10.1016/0010-4485(88)90206-0.

[117] T. Maekawa. *Robust Computational Methods for Shape Interrogation*. PhD thesis, Massachusetts Institute of Technology, 1993. URL `http://deslab.mit.edu/DesignLab/tmaekawa/phd.pdf`.

[118] F. Malgouyres and F. Guichard. Edge direction preserving image zooming: a mathematical and numerical analysis. *SIAM Journal on Numerical Analysis*, 39(1):1–37 (electronic), 2001. doi:10.1137/S0036142999362286.

[119] M. W. Marzke, M. W. Tocheri, R. F. Marzke, and J. D. Femiani. Three-dimensional quantitative comparative analysis of trapezial-metacarpal joint surface curvatures in human populations. *The Journal of Hand Surgery*, 37(1):72–76, jan 2012. doi:10.1016/j.jhsa.2011.09.007.

[120] J. J. McKinnon, M. A. Spackman, and A. S. Mitchell. Novel tools for visualizing and exploring intermolecular interactions in molecular crystals. *Acta Crystallographica Section B Structural Science*, 60(6):627–668, nov 2004. doi:10.1107/s0108768104020300.

[121] M. Meyer, M. Desbrun, P. Schröder, and A. H. Barr. Discrete differential-geometry operators for triangulated 2-manifolds. In *Visualization and mathematics III*, Math. Vis., pages 35–57. Springer, Berlin, 2003.

[122] E. Naden, T. März, and C. B. MacDonald. Anisotropic diffusion filtering of images on curved surfaces. Technical report, 2014, 1403.2131.

[123] M. Nikolova. A variational approach to remove outliers and impulse noise. *Journal of Mathematical Imaging and Vision*, 20(1-2):99–120, 2004. doi:10.1023/B:JMIV.0000011920.58935.9c. Special issue on mathematics and image analysis.

[124] R. Pan and S. J. Reeves. Efficient Huber-Markov edge-preserving image restoration. *IEEE Transactions on Image Processing*, 15(12):3728–3735, dec 2006. doi:10.1109/tip.2006.881971.

[125] N. M. Patrikalakis and T. Maekawa. *Shape interrogation for computer aided design and manufacturing*. Springer-Verlag, Berlin, 2001.

[126] D. Pellis, M. Kilian, F. Dellinger, J. Wallner, and H. Pottmann. Visual smoothness of polyhedral surfaces. In *ACM Transactions on Graphics (TOG)*. ACM, 2019. doi:10.1145/3306346.3322975.

[127] P. Perona and J. Malik. Scale-space and edge detection using anisotropic diffusion. *IEEE Transactions on pattern analysis and machine intelligence*, 12(7):629–639, 1990. doi:10.1109/34.56205.

[128] J. Persch. *Optimization Methods in Manifold-Valued Image Processing*. Dissertation, 2018.

[129] K. Polthier. Computational aspects of discrete minimal surfaces. In *Global theory of minimal surfaces*, volume 2 of *Clay Math. Proc.*, pages 65–111. Amer. Math. Soc., Providence, RI, 2005.

[130] A. Pressley. *Elementary differential geometry*. Springer Undergraduate Mathematics Series. Springer-Verlag London, Ltd., London, 2 edition, 2010. doi:10.1007/978-1-84882-891-9.

[131] U. Prüfert, F. Tröltzsch, and M. Weiser. The convergence of an interior point method for an elliptic control problem with mixed control-state constraints. *Computational Optimization and Applications. An International Journal*, 39(2):183–218, 2008. doi:10.1007/s10589-007-9063-7.

[132] S. Pulla, A. Razdan, and G. Farin. Improved curvature estimation for watershed segmentation of 3-dimensional meshes. Technical report, 2001.

[133] P.-A. Raviart and J. M. Thomas. A mixed finite element method for 2nd order elliptic problems. In *Mathematical aspects of finite element methods (Proc. Conf., Consiglio Naz. delle Ricerche (C.N.R.), Rome, 1975)*, volume 606 of *Lecture Notes in Mathematics*, pages 292–315. Springer, Berlin, 1977.

[134] B. Rivière. *Discontinuous Galerkin Methods for Solving Elliptic and Parabolic Equations*. Society for Industrial and Applied Mathematics, jan 2008. doi:10.1137/1.9780898717440.

[135] B. Rivière, M. F. Wheeler, and V. Girault. Improved energy estimates for interior penalty, constrained and discontinuous Galerkin methods for elliptic problems. I. *Computational Geosciences*, 3(3-4):337–360 (2000), 1999. doi:10.1023/A:1011591328604.

[136] M. E. Rognes, D. A. Ham, C. J. Cotter, and A. T. T. McRae. Automating the solution of PDEs on the sphere and other manifolds in FEniCS 1.2. *Geoscientific Model Development*, 6(6):2099–2119, dec 2013. doi:10.5194/gmd-6-2099-2013.

[137] M. E. Rognes, R. C. Kirby, and A. Logg. Efficient assembly of H(div) and H(curl) conforming finite elements. *SIAM Journal on Scientific Computing*, 31(6):4130–4151, 2009. doi:10.1137/08073901X.

[138] S. Rosenberg. *The Laplacian on a Riemannian manifold*, volume 31 of *London Mathematical Society Student Texts*. Cambridge University Press, Cambridge, 1997. doi:10.1017/CBO9780511623783. An introduction to analysis on manifolds.

[139] L. I. Rudin, S. Osher, and E. Fatemi. Nonlinear total variation based noise removal algorithms. *Physica D*, 60(1–4):259–268, 1992. doi:10.1016/0167-2789(92)90242-F.

[140] F. Santosa and M. Vogelius. A backprojection algorithm for electrical impedance imaging. *SIAM Journal on Applied Mathematics*, 50(1):216–243, 1990. doi:10.1137/0150014.

[141] T. Sasao, S. Hiura, and K. Sato. Super-resolution with randomly shaped pixels and sparse regularization. In *IEEE International Conference on Computational Photography (ICCP)*. IEEE, apr 2013. doi:10.1109/iccphot.2013.6528310.

[142] O. Scherzer, M. Grasmair, H. Grossauer, M. Haltmeier, and F. Lenzen. *Variational methods in imaging*, volume 167 of *Applied Mathematical Sciences*. Springer, New York, 2009.

[143] A. Schiela. Barrier methods for optimal control problems with state constraints. *SIAM Journal on Optimization*, 20(2):1002–1031, 2009. doi:10.1137/070692789.

[144] S. Schmidt. *Efficient large scale aerodynamic design based on shape calculus*. PhD thesis, Universität Trier, 2010, urn:nbn:de:hbz:385-5695.

[145] P. Silvester. Symmetric quadrature formulae for simplexes. *Mathematics of Computation*, 24:95–100, 1970. doi:10.2307/2004880.

[146] J. Sokołowski and J.-P. Zolésio. *Introduction to Shape Optimization*. Springer, New York, 1992.

[147] B. Stamm and T. P. Wihler. A total variation discontinuous Galerkin approach for image restoration. *International Journal of Numerical Analysis and Modeling*, 12(1):81–93, 2015.

[148] D. Strong and T. Chan. Edge-preserving and scale-dependent properties of total variation regularization. *Inverse Problems. An International Journal on the Theory and Practice of Inverse Problems, Inverse Methods and Computerized Inversion of Data*, 19(6):S165–S187, 2003. doi:10.1088/0266-5611/19/6/059. Special section on imaging.

[149] S. Sugathan, R. Scaria, and A. P. James. Adaptive digital scan variable pixels. In *2015 International Conference on Advances in Computing, Communications and Informatics (ICACCI)*. IEEE, aug 2015. doi:10.1109/icacci.2015.7275772.

[150] J. M. Sullivan. Curvature measures for discrete surfaces. In *ACM SIGGRAPH 2005 Courses*, SIGGRAPH '05, 2005. doi:10.1145/1198555.1198662.

[151] J. M. Sullivan. Curvatures of smooth and discrete surfaces. In *Discrete Differential Geometry*, pages 175–188. Birkhäuser Basel, 2008. doi:10.1007/978-3-7643-8621-4_9.

[152] M. Tao and J. Yang. Alternating direction algorithms for total variation deconvolution in image reconstruction. Technical Report 2463, Optimization Online, 2009. URL `http://www.optimization-online.org/DB_HTML/2009/11/2463.html`.

[153] T. Tasdizen, R. Whitaker, P. Burchard, and S. Osher. Geometric surface processing via normal maps. *ACM Transactions on Graphics*, 22(4):1012–1033, 2003. doi:10.1145/944020.944024.

[154] G. Taubin. A signal processing approach to fair surface design. In *Proceedings of the 22Nd Annual Conference on Computer Graphics and Interactive Techniques*, SIGGRAPH '95, pages 351–358. ACM, 1995. doi:10.1145/218380.218473.

[155] M. A. Taylor, B. A. Wingate, and L. P. Bos. A cardinal function algorithm for computing multivariate quadrature points. *SIAM Journal on Numerical Analysis*, 45(1):193–205, 2007. doi:10.1137/050625801.

[156] M. Ulbrich and S. Ulbrich. Primal-dual interior point methods for PDE-constrained optimization. *Mathematical Programming*, 117(1–2):435–485, 2009. doi:10.1007/s10107-007-0168-7.

[157] C. R. Vogel. *Computational Methods for Inverse Problems*. SIAM, Philadelphia, 2002.

[158] J. Vollmer, R. Mencl, and H. Müller. Improved Laplacian smoothing of noisy surface meshes. *Computer Graphics Forum*, 18(3):131–138, 1999. doi:10.1111/1467-8659.00334.

[159] S. Wandzura and H. Xiao. Symmetric quadrature rules on a triangle. *Computers & Mathematics with Applications. An International Journal*, 45(12):1829–1840, 2003. doi:10.1016/S0898-1221(03)90004-6.

[160] Y. Wang, J. Yang, W. Yin, and Y. Zhang. A new alternating minimization algorithm for total variation image reconstruction. *SIAM Journal on Imaging Sciences*, 1(3):248–272, 2008. doi:10.1137/080724265.

[161] Y. Wang, W. Yin, and J. Zeng. Global convergence of ADMM in nonconvex nonsmooth optimization. *Journal of Scientific Computing*, jun 2018. doi:10.1007/s10915-018-0757-z.

[162] M. Wardetzky. *Discrete Differential Operators on Polyhedral Surfaces — Convergence and Approximation*. PhD thesis, Freie Universität Berlin, 2006.

[163] W. Welch and A. Witkin. Variational surface modeling. In *Proceedings of the 19th annual conference on Computer graphics and interactive techniques - SIGGRAPH '92*. ACM Press, 1992. doi:10.1145/133994.134033.

[164] W. Welch and A. Witkin. Free-form shape design using triangulated surfaces. In *Proceedings of the 21st annual conference on Computer graphics and interactive techniques - SIGGRAPH '94*. ACM Press, 1994. doi:10.1145/192161.192216.

[165] C. Wu, J. Zhang, Y. Duan, and X.-C. Tai. Augmented Lagrangian method for total variation based image restoration and segmentation over triangulated surfaces. *Journal of Scientific Computing*, 50(1):145–166, 2012. doi:10.1007/s10915-011-9477-3.

[166] J. Wu, R. Ma, X. Ma, F. Jia, and Q. Hu. Curvature-dependent surface visualization of vascular structures. *Computerized Medical Imaging and Graphics*, 34(8):651–658, 2010. doi:https://doi.org/10.1016/j.compmedimag.2010.07.006.

[167] X. Wu, J. Zheng, Y. Cai, and C.-W. Fu. Mesh denoising using extended ROF model with L1 fidelity. *Computer Graphics Forum*, 34(7):35–45, 2015. doi:10.1111/cgf.12743.

[168] L. Yue, H. Shen, J. Li, Q. Yuan, H. Zhang, and L. Zhang. Image super-resolution: The techniques, applications, and future. *Signal Processing*, 128:389–408, nov 2016. doi:10.1016/j.sigpro.2016.05.002.

[169] C. Zălinescu. *Convex analysis in general vector spaces*. World Scientific Publishing Co., Inc., River Edge, NJ, 2002. doi:10.1142/9789812777096.

[170] H. Zhang, C. Wu, J. Zhang, and J. Deng. Variational mesh denoising using total variation and piecewise constant function space. *IEEE Transactions on Visualization and Computer Graphics*, 21(7):873–886, 2015. doi:10.1109/TVCG.2015.2398432.

[171] J. Zhang, S. Ma, and S. Zhang. Primal-dual optimization algorithms over riemannian manifolds: an iteration complexity analysis, 2017, 1710.02236.

[172] L. Zhang, T. Cui, and H. Liu. A set of symmetric quadrature rules on triangles and tetrahedra. *Journal of Computational Mathematics*, 27(1):89–96, 2009.

[173] S. Zhong, Z. Xie, W. Wang, Z. Liu, and L. Liu. Mesh denoising via total variation and weighted laplacian regularizations. *Computer Animation and Virtual Worlds*, 29(3-4):e1827, 2018. doi:10.1002/cav.1827.

[174] W. P. Ziemer. *Weakly differentiable functions*, volume 120 of *Graduate Texts in Mathematics*. Springer-Verlag, New York, 1989. doi:10.1007/978-1-4612-1015-3. Sobolev spaces and functions of bounded variation.